ELECTRON SCATTERING FROM ATOMS (IONS) AND PLASMA MODELING

Ph.D. THESIS

by

PRITI

DEPARTMENT OF PHYSICS
INDIAN INSTITUTE OF TECHNOLOGY ROORKEE
ROORKEE – 247 667 (INDIA)
AUGUST, 2018

ELECTRON SCATTERING FROM ATOMS (IONS) AND PLASMA MODELING

A THESIS

Submitted in partial fulfilment of the
requirements for the award of the degree

of

DOCTOR OF PHILOSOPHY

in

PHYSICS

by

PRITI

DEPARTMENT OF PHYSICS
INDIAN INSTITUTE OF TECHNOLOGY ROORKEE
ROORKEE – 247 667 (INDIA)
AUGUST, 2018

INDIAN INSTITUTE OF TECHNOLOGY ROORKEE
ROORKEE

CANDIDATE'S DECLARATION

I hereby certify that the work which is being presented in the thesis entitled "**ELECTRON SCATTERING FROM ATOMS (IONS) AND PLASMA MODELING**" in partial fulfilment of the requirements for the award of the Degree of Doctor of Philosophy and submitted in the Department of Physics of the Indian Institute of Technology Roorkee, Roorkee is an authentic record of my own work carried out during a period from July, 2013 to August, 2018 under the supervision of Prof. Rajesh Srivastava, Professor, Department of Physics, Indian Institute of Technology Roorkee, Roorkee.

The matter presented in this thesis has not been submitted by me for the award of any other degree of this or any other Institution.

(PRITI)

This is to certify that the above statement made by the candidate is correct to the best of my knowledge.

Date: August 10, 2018

(R. Srivastava)
Supervisor

Dedicated to my beloved parents & family

ABSTRACT

Study of electron collisions with atoms, ions and molecules is fundamentally important subject and has numerous applications related to the different branches of science such as plasma physics, astrophysics, laser physics, fusion research, material sciences and medical science etc. Electron collision processes enhances our knowledge about the structure and collisional dynamics of atomic systems. Currently, it is one of the most active research areas due to the growing demand of the electron collision atomic data in various fields and in particular in the modeling and characterization of verity of plasmas.

For the diagnostics of any plasma, optical emission spectroscopy (OES) is one of the most straightforward and non-invasive techniques. In such experiments, the intensities of the emitted lines from the plasma are recorded which give the information about the local environment of the plasma. Therefore, combining the emission intensities to an appropriate collisional radiative (C-R) model provides the plasma characterization parameters such as electron density and temperature. However, in the C-R model, all the collisional and radiative process should be included in proper manner for reliable diagnostics. Since electron impact excitation is one of the dominant collision processes, the availability of its reliable and detailed cross section data for all various fine structure transitions in the wide range of energy is necessary to get the correct plasma parameters.

In the recent years, due to the advancement of technology, many experimental techniques have emerged which can provide atomic data with a very high precision. However, the electron collision experiments are quite sophisticated and have thus provided very limited set of e^--atom collision data for only selected electron impact energies. Also the available experimental studies have mainly focused on the electron excitation from ground level to few excited levels. While for plasma modeling, there is requirement of large set of collision data for several fine structure transitions in the wide range of electron energies. Consequently, available reliable theoretical methods have to meet such requirements. On the theoretical front, largely available theories are the non-relativistic approaches which have been found totally in adequate to describe the fine structure transitions. Therefore, one needs to adopt only fully relativistic perturbative and non-

perturbative approaches. The relativistic versions of the non-perturbative approaches *viz.* R-matrix and CCC methods are supposed to be very accurate but their applications are limited to the low impact energies due to computationally complexities. However, among the perturbative methods *viz.* the relativistic distorted wave approximation has proved to be very reliable and practical to adopt considering the need of large-scale production of atomic data for modeling of plasmas. In the light of the present context, the work of the thesis focuses on the calculations of the electron impact excitation cross sections required for the various fine structure atomic transitions important to plasma and utilizing them in developing the suitable collisional radiative models to characterize it.

Thus the thesis has mainly two objectives. First is to obtain electron impact excitation cross section of various transitions from ground as well as from the exited states in wide range of electron incident energy for neutral atoms. Thereafter, to incorporate these cross sections to development of C-R model to diagnose the variety of low temperature plasma. Second objective is to study the electron impact excitation of highly charged tungsten ions and to study the polarization of their photon emissions which is needed for the diagnostics of high temperature plasma such as of the ITER tokomak. The entire work of the thesis is presented through eight Chapters as briefly described below:

Chapter 1 introduces the subject of the thesis and gives the current status of the work related to the thesis work. This chapter also provides briefly the different available theoretical methods to describe electron atom collisions as well as an overview of C-R plasma model for non-local thermodynamic equilibrium (non-LTE) plasma. Finally, outlines the chapter wise thesis work.

In Chapter 2, a C-R model developed to characterize the hydrogen-cesium plasma is given. Such a study is relevant to the negative ion based neutral beam injectors for the ITER project. A complete set of data for electron impact excitation cross-sections and rate coefficients for several fine-structure transitions from the ground as well as excited states of cesium atom in the wide range of incident electron energy has been calculated using fully relativistic distorted wave theory. These cross sections are then incorporated in the C-R model. The calculated cross-sections and the extracted plasma parameters from the present model are compared with the available experimental and theoretical results.

Chapter 3 describes a C-R model developed for Ar-O_2 mixture plasma. The model has been applied to diagnose the *rf* generated Ar-O_2 (0-5%) mixture plasma at low temperature. The detailed cross sections for the fine structure transitions involving ground and excited levels of argon obtained from fully relativistic distorted wave (RDW) theory have been used. Processes which account for the coupling of argon with the oxygen molecules have been further added in the model. Through coupling of C-R model to the optical spectroscopic measurements reported by Jogi *et. al.* [J. Phys. D: Appl. Phys. **47** 335206 (2014)], the plasma parameters *viz.* electron density (n_e) and electron temperature (T_e) as a function of O_2 concentration have been obtained using thirteen intense emission lines out of $3p^5 4p \rightarrow 3p^5 4s$ transitions observed in their spectroscopic measurements. The Ar-$3p^5 4s$ ($1s_i$) fine-structure level populations at our extracted plasma parameters were found to be in very good agreement with those obtained from the measurements. Furthermore, the estimation of individual contributions coming from the ground state, $1s_i$ manifolds and cascade contributions to the population of the radiating Ar-$3p^5 4p$ ($2p_i$) states as a function of a trace amount of O_2 has been reported and discussed.

Chapter 4 presents detailed electron impact excitation cross section results for xenon in the wide range of incident energy from threshold to 1000eV are calculated using relativistic distorted wave (RDW) theory. Various transitions from the ground $5p^6$ state to the excited $5p^5 6s$, $5p^5 6p$, $5p^5 5d$, $5p^5 7s$ and $5p^5 7p$ as well as among these excited states are considered. Where available the calculated cross section results are compared with previously reported measurements and other calculations. The fitting of the obtained cross section to suitable analytical expressions is also provided for the plasma modeling applications. As an application a collisional Radiative (C-R) model has been developed using our calculated cross sections to characterize a inductively coupled Xe plasma. The plasma parameters obtained from model are reported and discussed.

Chapter 5 reports a systematic study of the N-shell electron impact excitation of highly charged tungsten ions viz. Rb-like W^{37+} through Br-like W^{39+} in the framework of a fully relativistic distorted wave approach. The cross sections are calculated for various transitions in the electron impact energy range from the excitation threshold to 20 keV. Analytic fitting of the calculated cross sections are also provided so that these can be directly used in any plasma model. Linear polarization of the emitted photons, due to decay of the different electron excited states of the tungsten ions has also been obtained and reported. The present calculations are useful for the diagnostics of the ITER plasmas.

Chapter 6 presents the RDW calculations for electron impact excitation cross-sections of the M- and L-shell transitions in the tungsten ions *viz.* Fe-like W^{48+}, K-like through Ne-like (W^{55+}-W^{64+}). This calculation are carried out in the light of wavelength measurements performed at Super EBIT facility at Livermore for the $n = 3 \rightarrow 3$ transitions in 19–25 Å soft X-ray range for these ions. The fitting of the obtained cross section are also provided for the modeling purposes. The polarizations of the decay of photons from the excited tungsten ions are calculated and reported.

Chapter 7 finally aids the concluding remarks about the present thesis work.

ACKNOWLEDGEMENTS

I am confident that my life as a PhD student has been and will be one of the best periods of my life. It is the people surrounding me that are responsible for my wonderful experience here. I am glad to have this opportunity to show my gratitude to these people.

Foremost, I would like to express my sincere gratitude to my advisor Prof. Rajesh Srivastava for the continuous support during the five years of my Ph.D and research, for his patience, motivation and enthusiasm. His assistance and dedicated involvement at every step throughout this venture helped me in all the time of research and completion of this thesis. I also want to thank Dr. Vandita Srivastava for her love and the delicious homemade food at time when I missed home.

I wish to express my sincere thanks to all the members of my student's research committee (SRC) for their valuable comments and constructive criticism throughout my research work. I am thankful to the Head, Department of Physics for providing me the basic infrastructural facilities and support for carrying out my research work and all the faculty members of the Physics Department for their encouragement. I would also like to thank technical staff and office members of the physics department for their cooperation.

I gratefully acknowledge Dr. Wünderlich and Prof. Fantz for the fruitful discussions. I extend my sincere gratitude to Prof. Zatsarinny and Prof. Bartschat for proving their cross section results in tabular form. I express my gratitude to Dr. Jogi for providing the OES measurements in the electronic form and also for the valuable discussions.

I am grateful to Dr. Lalita Sharma, Department of Physics, IIT Roorkee for providing valuable suggestions in the presentation of our joint publications. I gratefully acknowledge Dr. R. K. Gangwar, National Institute of Technology (NIT) Nagpur for publishing work together and for long discussions which helped me a lot. I would like to express my special thanks to Dr. Dipti, National Institute of standard technology (NIST), USA for working together, for helping me always with a smile and for all the fun we had in the last few years. In addition, I would like to thank all my other colleagues: Neelam, Shivam, Shubham and Debyendu for their active cooperation and the overall atmosphere which remained friendly.

My time at IITR was made enjoyable in large part due to many friends and groups that became a part of my life. I am grateful for the time spent with them. I want to especially thank Himalayans explorer club (HEC) of IITR for some memorable trips into the mountains and long road cycling.

Out of all the people in my life, those who have the greatest influence on my life are my family. I want to express my thanks to my late grandmother and grandfather for their blessings. I would like to thank my elder sister Aradhana and Richa bua for their care and love. I thank my elder brother Chandrakant and sister-in-law Sneha for their encouragement and motivations through my tough time. I want to thank my younger siblings Shruti and Shashank for giving me lot of love and affection. I especially want to thank Raja for bearing this capricious girl. Last but not the least; I want to thank my parents, whom I cannot thank enough, for all their love, support, and kindness. My mother offered her care and encouragement through phone calls every day despite my own limited devotion to correspondence. They gave me immense freedom to take my own decisions and always encourage me to be independent, which is priceless.

Lastly I want to thank Almighty God for all the things and giving me strength in every moment of my life.

(PRITI)

LIST OF PUBLICATIONS

The work presented in this thesis has also been presented in the following Journals and Conferences:

Journals:

[1] **Priti**, Gangwar RK and Srivastava R,Collisional radiative model for Ar-O_2 mixtur plasma with fully relativistic fine structure cross sections", Phys. Plasmas **25** 04351 (2018)

[2] **Priti**, Sharma L and Srivastava R,"Study of electron excitation of Rb-like to Br-like tungsten ions and polarization of their photon emission", *Eur. Phys. J. D.* **71**: 100 (2017)

[3] **Priti**, Dipti, Gangwar R K and Srivastava R,"Calculation of fully relativistic cross sections for electron excitation of cesium atom and its application to the diagnostics of hydrogen-cesium plasma",*J. Quant. Spectrosc. Radiat. Transf.* **187**, 426 (2017)

[4] **Priti**, Dipti, Sharma L and Srivastava R,"Electron Impact Excitation of Fe-like Tungsten Ion",*Journal of Atomic, Molecular, Condensate & Nano Physics* **3,** 89 (2016)

[5] **Priti**, Dipti and Sharma L and Srivastava R"Fully relativistic electron impact excitation cross-section and polarization for tungsten ions",*Atoms* **3,** 53 (2015).

[6] **Priti**, Gangwar R K and Srivastava R,"Electron Impact Excitation of Xenon: Fine Structure Cross sections and its Application in Plasma Modeling", (Communicated)

Conferences

[1] **Priti**, R K Gangwar and R Srivastava, "Electron Excitation Cross sections of Fine-Structure ($5p^56s$ -$5p^56p$) Transitions in Xenon", *7th Topical Conference of the Indian Socitey of Atomic and Molecular Physics (ISAMP-TC)",* held at IISER & IIT Tirupati, Andhra Pradesh during January 6-8, 2018.

[2] **Priti**, R K Gangewar, R Srivastava, “Collisional radiative model for Ar-O_2 plasma with reliable fine structure resolved cross sections”, *70th Annual Gaseous Electronics Conference* at Pittsburgh, PA, U.S.A. during November 6-10, 2017.

[3] R. K. Gangwar, **Priti**, S. Gupta, Dipti and R. Srivastava, “Optical diagnostic of gas mixture plasmas with fine-structure resolved population-kinetic models”, *49th Conference of the European Group on Atomic Systems (EGAS)* held at Durham University, United Kingdom July 17-21, 2017.

[4] R Srivastava, **Priti**, Dipti, R K Gangwar, “Electron excitation of Cesium and its application to plasma modeling, *48th Annual Meeting of the APS Division of Atomic, Molecular and Optical Physics (DAMOP-2017),* Sacramento, California, June 5–9, 2017.

[5] **Priti**, Dipti,Gangwar R K and Srivastava R, “Fine structure Resolved C-R Model for the diagnostic of H-Cs Plasma relevant to ITER negative ion based NBI systems”, *Joint ICTP-IAEA School on Atomic Processes in Plasmas,* at International Center for Theoretical Physics (ICTP), Trieste Italy, Feb 27-March 3, 2017.

[6] **Priti**, L sharma, S Gupta and R Srivastava, “Electron impact excitation of W^{37+} to W^{39+} ions: Cross section and polarization”, *21th National Conference on Atomic and Molecular Physics (NCAMP-2017)* held at Physical Research Laboratory (PRL), Ahmedabad during January 3-6, 2017.

[7] **Priti**, L sharma, N Shukla and R Srivastava, “A new approach to study elastic scattering of electrons from methane, *21th National Conference on Atomic and Molecular Physics (NCAMP-2017)* held at Physical Research Laboratory (PRL), Ahmedabad during January 3-6, 2017.

[8] **Priti**, Gangwar R K and Srivastava R, “Calculation of Detailed Relativistic Electron Excitation Cross Sections and Application to Hydrogen-Caesium Plasma”, *IAEA Technical Meeting on Uncertainty Assessment and Benchmark Experiments for Atomic and Molecular Data for Fusion Applications*, during 19-21 December 2016, IAEA Headquarters, Vienna, Austria.

[9] **Priti**, Dipti and Sharma L and Srivastava R, “Cross-sections and polarization of

the electron impact M-shell transitions in tungsten ions" *Topical conference on charged particle collisions and electronic processes in atoms, molecules and materials (qPaCE-2016)* held at ISM, Dhanbad, India during January 9-11, 2016.

[10] Dipti, Das T, **Priti**, Sharma L and Srivastava R, "Polarization of emissions from electron excited highly charged tungsten ions", , *4th International Conference on Current Developments in Atomic, Molecular, Optical and Nano Physics with Applications (CDAMOP-2015)* held at Delhi University during March 11-15, 2015.

[11] **Priti**, Dipti, Sharma L and Srivastava R, "M-shell Electron Impact Excitation and polarization of emission for w^{48+}-w^{51+} tungsten ions",*20th National Conference on Atomic and Molecular Physics (NCAMP-XX)* held at Indian Institute of Space Science and Technology (IIST), Thiruvananthapuram during December 9-12, 2014.

CONTENTS

CHAPTER 1

INTRODUCTION

1.1 General remarks

Scattering of electrons with atoms, ions and molecules are the most essential atomic processes. Study of these collision processes enhances our understanding of fundamental science by providing the knowledge about the structure and collisional dynamics of atomic systems. Electron collision data is used in many applications in various fields such as astrophysics, laser physics, fusion science, material sciences and medical science etc. [1–5]. For understanding and modeling of natural processes (like aurora, lightening) as well as man-made technologies which contain plasma require a large set of atomic data. One of the admissible uses of collision data is in the modeling of fusion plasma. Energy generated from the fusion is cleaner and safer source of energy. Therefore, building fusion reactors and modeling of plasma present therein is currently a major area of research. Further, the electron collision processes that include excitations, ionization, dielectric recombination etc. are found to be the most important and their cross sections are very crucial to model these plasmas.

The properties of plasma change significantly depending on whether it is fusion plasma, astrophysics plasma, laser plasma or industrial plasma and the related plasma parameters such as temperature of the plasma, electron density and density of constituent atoms and ions vary over many orders of magnitude (as can be seen from figure 1). However, property which is common in most of the plasma is the plasma glow i.e. radiation emissions from the plasma due to the subsequent decay of the exited atoms or ions which are constituents of the plasma. Measurement of such emitted radiation intensities is termed as optical emission spectroscopy (OES), which is one of the most useful diagnostics techniques [6–11]. Comparing the measured line intensities coming out from the plasma, with that of an appropriately developed collisional-radiative (C-R) model for the plasma provides the information about the actual plasma conditions such as temperature and plasma electron density etc. This OES based plasma diagnostics have great advantages over the traditional way to measure the plasma parameters via Langmuir probe as in contrast to probe measurements it provides the plasma parameters without perturbation in any plasma conditions.

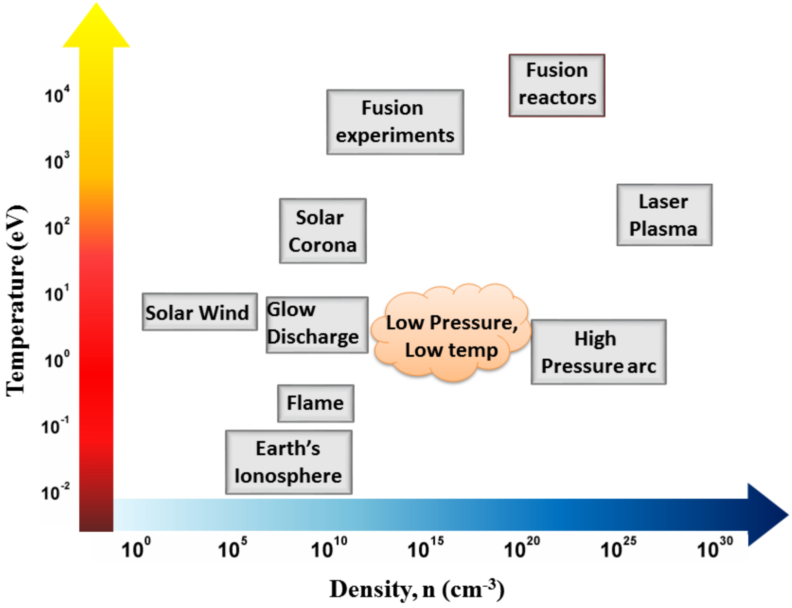

Figure1. Density and temperature range of various natural occurring and man-made plasma.

However, the proper inclusion of all the relevant processes occurring in the plasma is necessary to develop a reliable C-R model[12–14]. Therefore, the primary challenge to develop a reliable plasma model is the requirement of both accurate and large atomic data set such as transition energies, transition probabilities and cross section for various collisional and radiative processes occurring in the plasma[12, 14–18]. Since the spectral lines used for diagnostics are originated due to decay of electron from an excited state to other lower states, the processes which populate and depopulate the emitting state are very important and hence understanding of these processes are the connecting link between atomic physics and the study of plasma properties. Moreover, the electrons having kinetic energy greater than the threshold of any transition are present in the plasma and their inelastic collisions with the plasma constituent atoms or ions populate them to any emitting state. Therefore, among all the processes, the electron impact excitations are one of the most dominant populating or depopulating channel of an atomic state[14, 15, 19]. Thus, in a C-R model, electron impact excitation cross sections are one of the main inputs and their accurate knowledge for different fine structure transitions is necessary to obtain the reliable plasma parameters[14, 15, 20].

Over the few years, due to the advancement in technology, many experimental measurements have provided electron-atom collision data with a very high accuracy [21–28]. However, these being sophisticated experiments could produce only limited set of e^--atom collision cross sections which are for selected transitions and at certain range of electron impact energies. Also the available experimental studies have so far focused mainly on the electron excitation from the ground state of the atoms or ions to their few selected excited levels. While for practical application purposes, such as plasma modeling one requires large set of collision cross sections for several transitions involving ground and excited levels in the wide range of incident electron energies. Consequently, theoretical methods have to meet such requirements, resulting in the development and applications of variety of theories which led it to dominant research area. In the last few decades continuous progress can be seen in theoretical methods and computational approaches to study the collisional dynamics. Among the theoretical methods, the earlier classical approaches have totally failed and one needed to adopt only quantum mechanical approaches. However, in quantum mechanics, the exact solution of even electron-hydrogen scattering problem is not possible. Therefore, various theoretical approximations have been developed to determine the scattering amplitudes [29] [30–36].[37–42].[43–47]. Broadly, the approximation methods used to study e^--atom (ion) collisions can be categorized into two main perturbative and non-perturbative approaches. The Born approximation, distorted-wave approximation (DW) and their variants are the few perturbative methods [30–34, 48, 49]. The R-matrix[37–42] and convergent close-coupling (CCC)[43–47, 50] methods are the most commonly used non-perturbative methods.

The methods fall into the category of non-perturbative approaches are based on coupled channel approximation [51]. In this approach, the total scattering wave function for the electro-atom system is expanded as sum over all the individual channel wave functions involving projectile electron and atomic state wave functions. Hence, square of the wave functions not only give the probability of individual channel but also the coupling among them. This approach includes some of the important effects *viz.* resonance and coupling effect in atomic processes inherently. However, these methods are found to be good for low incident electron energy where only few channels are open. At higher energies when more number of channels open, it is practically impossible to include all of them. Therefore, more recently, the convergent close-coupling (CCC) method [43–47, 50], *R*-matrix and its variant [37–42] have been developed and extended to make them applicable for intermediate energies as well.

In the *CCC* method, the higher discrete and continuum states are included without approximation. Both the discrete and continuum target states are represented by diagonalizing the target Hamiltonian in a large Laguerre basis set. The convergence of this method depends on collisional energy as well as on the observables to be calculated. Many studies [44, 46, 47, 52–54] are available for lighter atoms based on CCC approximations. The *R-matrix* method is based on partition of configuration space. In this method, the configuration space i.e. target-projectile interaction space is divided into two regions. In the inner region, interactions including exchange between the projectile and target electron are very strong as in coupled channel approximation. Therefore, the free electron is indistinguishable from the other N target electrons. Essentially the problem reduces to an atomic structure calculation for an N + 1 electron system. N+1 electron wave functions are constructed from a complete orthonormal set of bound and continuum one-electron functions. While in outer region, the interactions are long range and weak (mainly exchange) and therefore, may be considered via asymptotic approximations. Various forms of R-matrix methods such as B-spline *R*-matrix [39] and Breit-Pauli *R*-matrix [55, 56] have been developed, and these are applied to study many scattering problems [57–65].

Relativistic versions of the R-matrix [59, 66] and CCC [44, 45, 67] methods are developed recently and supposed to be very accurate in low impact energies. However, it is well known that relativistic multi-channel CC calculations are numerically very difficult in the presence of strongly coupled channels and they need very heavy computational work such as massive parallelization on high-performance supercomputing platforms and thus these methods have limitations, especially when used for complex targets. Thus, these are not easy to practically adopt due to computational complexity. Hence, the applicability of these methods are restricted to low impact energies [44, 47, 52, 57, 58, 61–63].

Since there is a need of large-scale production of atomic data for modeling of various kind of plasmas, the perturbative methods remain in common usages. However, among the perturbative methods, relativistic distorted wave (RDW) approximation has been proven to be very successful in explaining the experiments especially, at intermediate and high energies. The RDW method has been applied and tested to calculate reliable electron. impact cross sections for lighter to heavier atoms in the wide range of electron incident energy [68–98]. This method though includes the coupling between initial and final channel only but by representing the target states through multi-configuration wave functions more channels get automatically included. For representing the target the multi-configuration Dirac-Fock wave functions are used while the wave function for the projectile electrons are calculated by solving the Dirac equations numerically, which is the natural way of taking the relativistic effects in to account. For calculating MCDF target bound state wave functions one can use the available GRASP2K [99–101] code. Many other codes based on coupled cluster theory are also available to calculate the atomic structures and related properties[102, 103].

The present thesis primarily deals with the study of electron impact excitation of different fine-structure transitions of various atoms (ions) and reports their excitation cross sections in the wide range of electron incident energies. For the calculations of excitation cross sections we use the fully relativistic distorted wave theory which is therefore will be explained and described in more details here in this Chapter. Further, the calculated cross sections are used in some cases for plasma diagnostic studies by developing a suitable collision radiative model which we will also discuss here in this Chapter briefly. The next two sections (1.2) and (1.3) respectively, describe the evaluation of electron impact excitation T-matrix in RDW approximation and collisional radiative (C-R) model in brief. Finally, Section (1.4) presents the outline of the work reported in the thesis.

1.2 Relativistic distorted wave theory for electron excitation of atoms

Considering the electron impact excitation of an atom with nuclear charge ‘Z’ and having ‘N’ electrons, the total Hamiltonian for (electron + atom) i.e. (N+1) electron system can be written as

$$H = H_0 + V \tag{1.2.1}$$

$$H_0 = H_{atom} + K_{N+1} \tag{1.2.2}$$

Here H_0 is the Hamiltonian for the unperturbed system i.e. non-interacting projectile electron and atom. H_{atom} is the Hamiltonian of the target atom in the relativistic Dirac form and K_{N+1} represents the kinetic energy operator for the projectile electron. V is the total projectile-target atom interaction given by

$$V=-\frac{Z}{r_{N+1}}+\sum_{j=1}^{N}\frac{1}{\left|\mathbf{r_j}-\mathbf{r_{N+1}}\right|} \qquad (1.2.3)$$

Here, r_j and r_{N+1} refer respectively, the position vectors of the jth atomic electron and projectile electron with respect to the target nucleus.

Following the elementary theory of scattering, the T-matrix for electron impact excitation of atom from initial state '*i*' to final state '*f*' can be written as

$$T_{i\to f}=\left\langle \psi_f(1,\ 2,\ .....,\ \mathrm{N}+1)\middle|V\middle|\Psi_i^+(1,\ 2,\ .....,\ \mathrm{N}+1)\right\rangle \qquad (1.2.4)$$

Here, $\psi_f(1,\ 2,\ .....,\ \mathrm{N}+1)$ is the total unperturbed wave function of the (electron + target atom) system in final channel. $\Psi_i^+(1,\ 2,\ .....,\ \mathrm{N}+1)$ is the wave functions for the total system in the initial channel and the '+' sign refers to the usual outgoing wave boundary condition. The numbers 1, 2,….N+1 denote the combined spin and position co-ordinates of the electrons. The wave functions ψ_f and Ψ_i^+ satisfy the following equations

$$(H_0-E)\psi_f=0 \qquad (1.2.5)$$

$$(H-E)\Psi_i^+=0 \qquad (1.2.6)$$

'*E*' is the total energy of the target-projectile system given by

$$E=E_i+\varepsilon_i=E_f+\varepsilon_f \qquad (1.2.7)$$

here, $E_{i(f)}$ and $\varepsilon_{i(f)}$ are the energy of the projectile electron and target in the initial (final) state, respectively.

From equation (1.2.4), it is clear that the exact calculation of the T-matrix for an electron impact excitation process requires exact evaluation of Ψ. Following the quantum mechanics, it is well known that Ψ cannot be obtained exactly for the present problem being many body systems. Therefore, various approximations have been adopted to evaluate Ψ with which then the T-matrix can be evaluated. We introduce "Relativistic distorted wave (RDW) approximation" and discuss here briefly. More details can be followed from the references [30–33, 96, 104].

In the RDW approximation, the interaction V is split as below into two parts such that one part is solved exactly while the rest part is treated in an approximate manner.

$$V = U + W \tag{1.2.8}$$

Here *U* is referred as the distortion potential with which the solution is obtained exactly. Defining a new Hamiltonian $\bar{H} = H_0 + U$ such that

$$\bar{H}\chi = E\chi \tag{1.2.9}$$

Where, the solution χ represents the combined wave function of the target atom and distorted projectile electron wave travelling in the presence of distortion potential *U*.

Further, using two potential formulation, the T-matrix (equation (1.2.4)) within the first order relativistic distorted wave approximation [30–33, 91, 105] can be written as,

$$\begin{aligned} T_{i\to f}^{RDW} &= \left\langle \chi_f^-(1,\ 2,\ .....,\ \mathrm{N}+1) \middle| U_f \middle| \psi_i(1,\ 2,\ .....,\ \mathrm{N}+1) \right\rangle \\ &\quad + \left\langle \chi_f^-(1,\ 2,\ .....,\ \mathrm{N}+1) \middle| V - U_f \middle| \chi_i^+(1,\ 2,\ .....,\ \mathrm{N}+1) \right\rangle \end{aligned} \tag{1.2.10}$$

Further, distortion potential can be chosen such that it depends only on the co-ordinate of the projectile electron. Therefore, for the excitation process (i.e. inelastic scattering), the first term of the *T*-matrix becomes zero due to orthogonality of the atomic wave functions being different in the initial and final states. Thus the *T*-matrix can be written in the following form.

$$T_{i\to f}^{RDW} = \left\langle \chi_f^-(1,\ 2,\ .....,\ \mathrm{N}+1) \middle| V - U_f \middle| \chi_i^+(1,\ 2,\ .....,\ \mathrm{N}+1) \right\rangle \tag{1.2.11}$$

Here, $\chi_{i(f)}^{+(-)}$ is expressed as the product of the atomic N-electron wave function of the target and the relativistic distorted wave functions of the projectile electron as,

$$\chi_{i(f)}^{+(-)}(1,\ 2,\ .....,\ \mathrm{N}+1) = \mathcal{A}\,\Phi_{i(f)}^{rel}(1,\ 2,\ .....,\ \mathrm{N})\mathrm{F}_{i(f),\mu_{i(f)}}^{RDW+(-)}(\mathrm{k}_{i(f)}, \mathrm{N}+1) \tag{1.2.12}$$

Where, $\Phi_{i(f)}^{rel}(1,\ 2,\ .....,\ \mathrm{N})$ and $\mathrm{F}_{i(f),\mu_{i(f)}}^{RDW+(-)}(\mathrm{k}_{i(f)}, \mathrm{N}+1)$ represent respectively, the relativistic N-electron wave atomic function and distorted wave functions of the projectile electron in the initial (final) channel. $\mu_{i(f)}$ and $\mathrm{k}_{i(f)}$ denote the spin projection and wave vector of the incident (scattered) electron. '+' and '-' signs refer the outgoing and incoming waves. $\mathcal{A}$ .is anti-symmetrization operator, that takes into account the exchange of the projectile electron with the atomic target electrons.

Further, the T-matrix can be expressed as a sum of direct $T^{d}_{i\to f}$ and exchange $T^{ex}_{i\to f}$ matrices as follows,

$$T^{d}_{i\to f} = \left\langle \Phi^{rel}_{f}(1,\,2,\,...,\,\mathrm{N})\mathrm{F}^{RDW-}_{f,\mu_f}(\mathrm{k}_f,\mathrm{N}+1)\right| V - U_f(N+1) \\ \times \left|\Phi^{rel}_{i}(1,\,2,\,...,\,\mathrm{N})\mathrm{F}^{RDW+}_{i,\,\mu_i}(\mathrm{k}_i,\mathrm{N}+1)\right\rangle \tag{1.2.13}$$

$$T^{ex}_{i\to f} = \left\langle \Phi^{rel}_{f}(1,\,2,\,...,\,\mathrm{N})\mathrm{F}^{RDW-}_{f,\,\mu_f}(\mathrm{k}_f,\mathrm{N}+1)\right| V - U_f(N+1) \\ \times \left|\sum_{j=1}^{N}(-1)^{N+1-j}\,\Phi^{rel}_{i}(-\mathrm{j})\mathrm{F}^{RDW+}_{\mathrm{i},\,\mu_i}(\mathrm{k}_i,\mathrm{j})\right\rangle \tag{1.2.14}$$

Here $\Phi^{rel}_{a}(-\mathbf{j})$ denotes atomic wave function with co-ordinate **j** absent and **(N+1)** included.

In order to evaluate the T-matrices given by equations (1.2.13) and (1.2.14), we require the wave functions of the initial and final bound states of the target atom, distortion potential and continuum distorted wave function of projectile electron in the initial and final channels. The calculations of these are described further.

1.2.1 Relativistic atomic wave functions

The Dirac-Coulomb Hamiltonian for an atom having N-electrons can be written as [106–108],

$$H_{atom} = \sum_{i=1}^{N} H_i + \sum_{i<j}^{N} \frac{1}{\left|\mathrm{r}_\mathrm{i} - \mathrm{r}_\mathrm{j}\right|} \tag{1.2.15}$$

$$H_i = -ic\alpha.\nabla_i + \beta c^2 + V_{nuc}(r_i) \tag{1.2.16}$$

Here, H_i is the Dirac Hamiltonian for the particle i, α and β are the Dirac matrices and the operator $-i\nabla_i$ represents the momentum operator of ith electron of the atom. $V_{nuc}(r)$ is the potential due to nucleus and for point nucleus $V_{nuc}(r) = -Z/r$.

The N-electron bound state wave function for the target is taken as a Slater determent of single electron Dirac-Fock orbitals $\varphi_{n\kappa m}$. Here we represent the N-electron bound state wave function by a compact notation $\frac{1}{\sqrt{N!}}\{1\mathrm{s}\ \frac{1}{2}\ \frac{1}{2}........n\kappa m\}$, given by,

$$\Phi^{rel}(1,\,2,\,...,\,\mathrm{N}) = \frac{1}{\sqrt{N!}}\begin{vmatrix} \varphi_{1s\frac{1}{2}\frac{1}{2}}(1) & \varphi_{1s\frac{1}{2}\frac{-1}{2}}(1) & .... & \varphi_{n\kappa m}(1) \\ \varphi_{1s\frac{1}{2}\frac{1}{2}}(2) & \varphi_{1s\frac{1}{2}\frac{-1}{2}}(2) & .... & \varphi_{n\kappa m}(2) \\ . & . & & . \\ . & . & & . \\ \varphi_{1s\frac{1}{2}\frac{1}{2}}(\mathrm{N}) & \varphi_{1s\frac{1}{2}\frac{-1}{2}}(\mathrm{N}) & .... & \varphi_{n\kappa m}(\mathrm{N}) \end{vmatrix} \tag{1.2.17}$$

Here, $n\kappa m$ represent the quantum numbers corresponding to the outermost electron. The quantum number κ corresponds to the spin-angular state, defined as

$$\kappa \;=\; \begin{cases} l & if \quad j = l - 1/2 \\ -l-1 & if \quad j = l + 1/2 \end{cases} \tag{1.2.18}$$

The single electron central field Dirac orbitals are given by,

$$\phi_{n\kappa m}(\mathbf{r},\sigma) = \frac{1}{r}\begin{pmatrix} P_{n\kappa}(r)\,\zeta_{\kappa m}(\hat{\mathbf{r}},\sigma) \\ iQ_{n\kappa}(r)\,\zeta_{-\kappa m}(\hat{\mathbf{r}},\sigma) \end{pmatrix} \tag{1.2.19}$$

$P_{n\kappa}$ and $Q_{n\kappa}$ are the large and small components of the radial wave function and $\zeta_{\pm\kappa m}$ represents the spin angular wave function given by,

$$\zeta_{\kappa m}(\hat{\mathbf{r}},\sigma) = \sum_{\mu\nu} (l\;\mu\;\frac{1}{2}\nu|\;j\;m) Y_{l\,\mu}(\hat{\mathbf{r}})\xi_{\frac{1}{2}\nu}(\sigma) \tag{1.2.20}$$

and $$\zeta_{-\kappa m}(\hat{\mathbf{r}},\sigma) = \sum_{\mu\nu} (\tilde{l}\;\mu\;\frac{1}{2}\nu|\;j\;m) Y_{\tilde{l}\,\mu}(\hat{\mathbf{r}})\xi_{\frac{1}{2}\nu}(\sigma) \tag{1.2.21}$$

Where $\tilde{l} = 2j\text{-}l$, $\left(l_1 m_1 l_2 m_2 \,|\, jm\right)$ is the Clebsch-Gordan coefficient and $\xi_{\frac{1}{2}\nu}(\sigma)$ is a spinor basis function.

The bound state orbitals are orthogonal and satisfy the following orthogonality conditions,

$$\int_0^\infty dr\left[P_{n'\kappa}(r)P_{n\kappa}(r) + Q_{n'\kappa}(r)Q_{n\kappa}(r)\right] = \delta_{n'n} \tag{1.2.22}$$

$$\left\langle \zeta_{\kappa m}(\hat{\mathbf{r}},\sigma) \middle| \zeta_{\kappa' m'}(\hat{\mathbf{r}},\sigma) \right\rangle = \delta_{\kappa'\kappa}\;\delta_{m'm} \tag{1.2.23}$$

We use multi-configuration Dirac-Fock (MCDF) approximation to calculate the wave functions of the target atom. Within the multi-configuration Dirac-Fock (MCDF) approximation, the wave function for an atomic state is approximated by an atomic state function (ASF). Further, an ASF can be expressed as linear combination of configuration state functions (CSFs) which have same angular momentum *J* and parity. We use GRASP2K[99–101] code to calculate MCDF target bound state wave functions. In this code, the higher order quantum electrodynamics (QED) modifications due to the transverse electromagnetic interaction and the radiative corrections are also included via perturbation theory.

1.2.2 Distortion potential

In order to obtain the distorted wave for projectile electron, first we evaluate distortion potential using the obtained $P_{n\kappa}$ and $Q_{n\kappa}$ radial atomic wave functions. The distortion potential is chosen to be the spherically averaged static potential V_{static} *i.e.* the spherical average of the static interaction between the projectile electron and the target atom and can be obtained using the following expression,

$$V_{static}(r_{N+1}) = -\frac{Z}{r_{N+1}} + \sum_{\substack{j\in all\\ \text{subshells}}} \omega_j \int_0^\infty \left[P^2_{n_j\kappa_j}(r) + Q^2_{n_j\kappa_j}(r)\right]\frac{1}{r_>}\,dr \qquad (1.2.24)$$

where, ω_j is the occupation number of the j^{th} subshell and the electron in it is represented by quantum numbers $n_j\kappa_j$.

1.2.3 Relativistic distorted wave functions

The relativistic partial wave expansion of the continuum projectile electron distorted waves [109] $\mathrm{F}^{RDW+(-)}_{i(f),\mu_{i(f)}}$ can be expressed as,

$$\mathrm{F}^{RDW\pm}_{\mathrm{ch},\,\mu_{\mathrm{ch}}}(\mathrm{k}_{\mathrm{ch}},\mathrm{r}) = \frac{1}{(2\pi)^{3/2}}\sum_{\kappa m}\mathrm{e}^{\pm \mathrm{i}\eta_\kappa}\,\mathrm{a}^{\mu_{\mathrm{ch}}}_{\mathrm{ch},\kappa m}(\hat{\mathrm{k}}_{\mathrm{ch}})\frac{1}{r}\begin{pmatrix} f_\kappa(r)\ \zeta_{\kappa m}(\hat{\mathrm{r}}) \\ ig_\kappa(r)\ \zeta_{-\kappa m}(\hat{\mathrm{r}}) \end{pmatrix} \qquad (1.2.25)$$

with

$$\mathrm{a}^{\mu_{\mathrm{ch}}}_{\mathrm{ch},\kappa m}(\hat{\mathbf{k}}_{ch}) = 4\pi i^l\left[\frac{E_{ch}+c^2}{2E_{ch}}\right]^{1/2}\sum_{\mathrm{m}_l}(l\ m_l\ \ \tfrac{1}{2}\ \mu_{\mathrm{ch}}|\ \ j\ m)Y^*_{l\,m_l}(\hat{\mathbf{k}}_{\mathbf{ch}}) \qquad (1.2.26)$$

where, '*ch*' refers to the two channels, initial '*i*' and final '*f*'. E_{ch} is the relativistic energy of the projectile electron with linear momenta k_{ch} such that $E_{ch} = ({k_{ch}}^2 c^2 + c^4)^{1/2}$. η_κ is the phase shift of the partial wave.

The radial parts of distorted waves $f_\kappa(r)$ and $g_\kappa(r)$ are obtained by solving the following coupled integro-differential equations

$$\left(\frac{d}{dr} + \frac{\kappa}{r}\right) f_\kappa(r) - \frac{1}{c}(c^2 - U_{ch} + E_{ch}) g_\kappa(r) - \frac{1}{cr} W_Q(\kappa; r) = 0 \tag{1.2.27a}$$

$$\left(\frac{d}{dr} - \frac{\kappa}{r}\right) g_\kappa(r) + \frac{1}{c}(-c^2 - U_{ch} + E_{ch}) f_\kappa(r) + \frac{1}{cr} W_P(\kappa; r) = 0 \tag{1.2.27b}$$

These coupled equation are solved by subjecting to the boundary conditions given below

$$f_\kappa(r) \xrightarrow[r\to\infty]{} \frac{1}{k_{ch}} \sin(k_{ch} r - \frac{l\pi}{2} + \eta_\kappa) \tag{1.2.28a}$$

$$g_\kappa(r) \xrightarrow[r\to\infty]{} \frac{c}{c^2 + E_{ch}} \cos(k_{ch} r - \frac{l\pi}{2} + \eta_\kappa) \tag{1.2.28b}$$

where W_P and W_Q are the non-local exchange Kernels. The details for the solving above coupled integro-diferential equations (1.2.28) can be followed from Zuo [105].

1.2.4 Excitation cross section

The magnetic sublevel cross section cross section σ_{M_f} for the excitation (*i→f*) in terms of the calculated T-matrix (1.2.11) can be obtained by the following expression,

$$\sigma(\alpha_f J_f M_f) = \sigma_{M_f} = (2\pi)^4 \frac{k_f}{2(2J_i + 1)k_i} \int \left| T_{i-f}^{RDW}(J_i, M_i, \mu_i; J_f, M_f, \mu_f, \theta) \right|^2 d\Omega \tag{1.2.29}$$

here, integration has been carried over the solid angle of the scattered electron. Summing the σ_{M_f} for all the magnetic sub levels of final state of the atom i.e. $\sigma(\alpha_f J_f) = \sum_{M_f} \sigma(\alpha_f J_f M_f)$ we can get the total excitation cross section. Here all the calculations are performed in *Collision frame of reference* which is a standard choice for numerical calculations, where the quantization axis (*z*-axis) is parallel to the incident electron beam direction while the *y*-axis is perpendicular to the scattering (*x*-*z*) plane which consists of the direction of incident as well as scattered electron.

1.3 Collisional Radiative (C-R) Model

Collisional radiative model is the most general kinetic plasma model used to determine the atomic state population densities of the constituent species of plasma as a function of electron temperature and electron density. Since the recorded intensities coming out from any plasma are directly proportional to the population of the emitting state, therefore, the state population densities of excited levels are used to model the spectral measurements. More specifically, comparison of the C-R model calculated intensities with experimentally measured intensities provides the information about plasma parameters such as electron temperature and electron density etc.

In the C-R model, the change in population densities of atomic states is considered mainly due to the electron collisional and radiative transitions occurring in plasma. The population density of any level can be obtained by solving the particle-balance equation or rate equation which interconnects the different populating and depopulating channels among the fine-structure levels. Before discussing the rate equation, first, we explore the various collisional and radiative processes responsible for the population transfer among the levels of the plasma.

1.3.1 Collisional processes

Collisional excitation and de-excitation by electron impact:

When electrons collide with atoms in the plasma these go to their higher excited states by gaining energy equal to the transition energy E_{ij} or de-excite to lower states by losing the same amount of energy.

$$X_i + e^- + (E_{ij}) \leftrightarrow X_j + e^-$$

Electron impact ionization and three-particle recombination:

If the electron energy is high enough, its collision with an atom may cause the ionization of atom. In reverse process, the three-particle recombination, collision of two electrons and an atom causes the recombination of an electron with the atom, and energy gained by capture is transferred to another electron.

$$X_i + e^- + (E_{i+}) \leftrightarrow X^+ + e^- + e^-$$

Dielectric recombination and auto-ionization:

Dielectric recombination is a two-step process. In this process, an electron is captured by ion resulting in doubly excited bound state, further an excited state decays to another lower lying bound state by releasing a photon and reverse of this process is auto ionization.

$$X^+ + e^- \rightarrow X^{**} \rightarrow X_i + hv$$

$$X_i + hv \rightarrow X^{**} \rightarrow X^+ + e^-$$

1.3.2 Radiative processes

Spontaneous emission and photo excitation:

In an atom due to bound-bound transition from upper excited state to lower level a photon of energy E_{ij} is emitted. Reversely, a photon hits an atom and atom goes to its excited state by taking the equal amount of energy.

$$X_j \leftrightarrow X_i + hv$$

Photo-ionization and radiative recombination:

In radiative recombination, an ion captures an electron to one of its bound state with a simultaneous decay of a photon. On the other hand, reversely, an atom in any excited state can absorb a photon which results in ionization of the atom.

$$X_i + hv \leftrightarrow X^+ + e^-$$

1.3.3 Rate Balance Equation

The population density of any level can be obtained by solving the rate equation which interconnects the different populating and depopulating channels among the fine-structure levels. Under the assumption that time taken for collisional and radiative processes in atomic systems are very small in comparison to changes in plasma conditions *i.e.* typically $dn_j/dt = 0$, in the steady state, rate balance equation for an excited state j can be written as follows [11, 12, 110, 111]

$$\sum_{i\neq j} k_{ij}(T_e)n_i n_e + \sum_{i>j} A_{ij}n_i + n_e n_+\left\{\alpha_j + n_e\beta_j\right\}n_e - \sum_{i\neq j} k_{ji}(T_e)n_j n_e - \sum_{i<j} A_{ji}n_j - n_j n_e k_{j+}(T_e) = 0 \qquad (1.3.1)$$

here,. n_i represents the population density of i^{th} level, T_e is the electron temperature. n_e and n_+ are the electron density and ion density, respectively. k_{ij} is the rate coefficient for the electron impact excitation from level $i \rightarrow j$ and A_{ij} is the transition probability for spontaneous decay from any upper level to j. α_j and β_j are the rate coefficients for the two particle and three particle recombination, respectively. All the positive terms in the equation represent production and negative terms represent the destruction channel for state j

The required rate coefficients for all the collisional and radiative process can be calculated by integration over respective cross section and electron distribution function or radiation distribution[11, 110, 111]. The electron distribution function can be considered as Maxwellian or non-Maxwellian depending on the plasma conditions such as if the gas pressure is too high or plasma contains hot electrons, distribution function may differ from Maxwellian nature [13, 112, 113]. Under the thermal equilibrium condition, all the rates are balanced by inverse rates i.e. of the inverse processes such as electron de-excitation, recombination, radiative recombination and electron capture. The inverse rate coefficients can be obtained from the direct rate through the principle of detailed balance[111].

Further, to get the atomic level population densities we solve this nonlinear coupled equation (1.3.1) for all atomic levels simultaneously[111]. However, the solution is not so straightforward, as it involves lot of reliable data of energy levels, transition probabilities and rates for various processes in the wide range of plasma temperature. The knowledge of accurate and complete data set for various processes is a big challenge while reliability and validity of the model depends majorly on accuracy of these atomic parameters[12]. In addition, the model size is often limited by the available computational resources. Hence, to reduce the complexity of the model, we limit the number of atomic states and the various populating and depopulating processes according to the field of application and plasma condition. Conclusively, the above rate equation is not universal, C-R models may vary according to the regime of plasma parameters and different atomic (ionic) and molecular species presented in the plasma. For example, in fusion plasma auto-ionization, photo-ionization, dielectronic recombination, radiative recombination play important role in addition to the electron impact excitation[16]. Atom-atom or atom-ion collision and diffusion may be important for plasmas at very high pressure[114]. While in the low temperature and low pressure plasma, the dominant process are the electron impact excitations and spontaneous decay[1, 2, 15]. In this thesis, we deal with the low temperature plasma. Detailed description of the rate calculation and solution of the rate calculation and solution of rate equation will be discussed later in the Chapter 2 while considering a specific plasma study.

1.4 Outline of the thesis

The work reported in this thesis is mainly based on two aspects. First aspect is to study the electron impact excitation cross section of various transitions from ground as well as from the exited states for neutral atoms. Thereafter, incorporate the obtained cross sections to development of C-R model to diagnose the variety of low temperature plasma. Second aspect is to study the electron impact excitation of highly charged tungsten and their photon emission which are needed for the diagnostics of high temperature international thermonuclear reactor (ITER) fusion plasma. The entire work of the thesis is presented through seven chapters including this introductory chapter as briefly described below:

In Chapter 2, a C-R model has been developed to characterize the hydrogen-cesium plasma which is relevant to the negative ion based neutral beam injectors for the ITER project. A complete set of results for electron impact excitation cross sections and rate coefficients for several fine-structure transitions from the ground as well as excited states of cesium atom has been calculated using fully relativistic distorted wave theory. Further, these cross sections are then incorporated in the C-R model along with the other processes such as radiative population transfer, electron impact ionization and mutual neutralization of Cs^+ ion with negative hydrogen ion along with their reverse processes. The calculated cross sections and the extracted plasma parameters from the present model are compared with the available experimental and theoretical results.

Chapter 3 describes a C-R model developed for Ar-O_2 mixture plasma. The model has been applied to diagnose the *rf* generated Ar-O_2 (0-5%) mixture plasma at low temperature. The detailed cross sections for the fine structure transitions involving ground and excited levels of argon obtained from fully relativistic distorted wave (RDW) theory have been used. Processes which account for the coupling of argon with the oxygen molecules have been further added in the model. The model is coupled to the optical spectroscopic measurements reported by Jogi *et. al.* [J. Phys. D: Appl. Phys. **47** 335206 (2014)]. The plasma parameters *viz.* electron density (n_e) and electron temperature (T_e) as a function of O_2 concentration have been obtained. Further, the estimation of individual contributions coming from the ground state, $1s_i$ manifolds and cascade contributions to the population of the radiating Ar-$3p^5 4p$ ($2p_i$) states as a function of a trace amount of O_2 has been reported and discussed.

Chapter 4 presents detailed electron impact excitation cross section results for xenon in the energy range from threshold to 1000 eV are calculated using relativistic distorted wave (RDW) theory. Various transitions from the ground $5p^6$ state to the excited $5p^5 6s$, $5p^5 6p$, $5p^5 5d$, $5p^5 7s$ and $5p^5 7p$ as well as among these excited states are considered. The fitting of the obtained cross section to suitable analytical expressions is also provided for the plasma modeling applications. As an application a collisional Radiative (C-R) model has been developed using our calculated cross sections to characterize inductively coupled Xe plasma. The plasma parameters obtained from model are reported and discussed.

Chapter 5 reports a systematic study of the electron impact N-shell excitation of highly charged tungsten ions viz. Rb-like W^{37+} through Br-like W^{39+} in the framework of a fully relativistic distorted wave approach. The cross sections are calculated for various transitions in the electron impact energy range from the excitation threshold to 20 keV. Analytic fitting of the calculated cross sections are also provided so that these can be directly used in any plasma model. Linear polarization of the emitted photons, due to decay of the different electron excited states of the tungsten ions has also been obtained and reported.

Chapter 6 presents the electron impact M-shell excitation cross sections for the transitions in K-like through Ne-like (W^{55+}-W^{64+}) tungsten ions and polarization of the decay of photons from the excited tungsten ions. These calculations are carried out in the light of wavelength measurements performed at Super EBIT facility at Livermore for the $n = 3 \rightarrow 3$ transitions in 19–25 Å soft X-ray range for these ions. We have also fitted the obtained cross section for the modeling purposes.

Chapter 7 gives the overall concluding remarks on the present thesis work.

CHAPTER 2

ELECTRON EXCITATION OF CESIUM AND MODELING OF LOW TEMPERATURE H_2-Cs PLASMA

2.1 Introduction

The present Chapter deals with the study of electron impact fine-structure excitation cross-section for various transitions in cesium (Cs) and its application in the development of a C-R model to characterize the hydrogen-cesium plasma. This study is relevant to the negative ion based neutral beam injectors for the international thermonuclear rector (ITER) project. The ITER is aimed at demonstrating the scientific and technical feasibility of fusion energy [115] However, many scientific and technological challenges are needed to be addressed before the steady state operation of this huge reactor can be realized. Among these issues, the heating of the plasma up to a temperature of the order of hundreds of millions of degrees centigrade (ten times the temperature of the sun) is the prime requirement to initiate the nuclear fusion reaction between the two hydrogen isotopes *viz.* deuterium and tritium. In all tokamaks (fusion plasma), it is not possible to achieve the desired large temperature only through traditional Ohmic heating. It is due to the fact that the plasma resistivity decreases with the increase in plasma temperature as $T^{-3/2}$, making this mechanism less effective at higher temperature. Therefore, for ITER some external heating systems to achieve such high temperatures are required. For this purpose, in ITER it is planned to install high performance neutral beam injection (NBI) systems and two sources of high-frequency electromagnetic wave systems externally [116–118]. Deuterium neutral beam injectors of power 16.5 MW with particle energies of 1MeV and a diagnostic beam of 100 KV are anticipated for the ITER [119–121].

The acceleration of negative hydrogen or deuterium ions in the fusion device can be achieved through the formation of negative ions by surface effect[122]. Surface with low work function will transfer electrons to generate negative hydrogen or deuterium ions [123]. Cs-seeded negative ion source is expected to fulfill the requirement of ITER project [118, 124, 125]. For high performance, achieving the low work function with cesium layer is a crucial aspect as it is highly dependent on the injected Cs amount and also on its population distribution inside the plasma [126–130]. Thus, an accurate numerical population model to simulate the population of Cs atom in ground as well as excited states is highly needed for the optimization purposes.

For the pure Cs plasma, various collisional radiative (C-R) models have been proposed [131–133]. However, these models are not applicable to the hydrogen-cesium plasmas relevant to ITER NBI systems as the mutual neutralization of Cs^+ ions with H^- ions has not been included which is an important channel for the production of Cs atom in the different states along with the hydrogen atom. Recently Wünderlich *et al.* [134] developed a proper C-R model for the low pressure hydrogen–cesium plasma. Their C-R model includes the channel of mutual neutralization in addition to the other populating and depopulating mechanisms for the excited Cs atom. However, in their model, electron impact excitation processes from the ground and the excited states have been considered in the framework of non-relativistic Born-approximation [135, 136]. Electron impact excitation cross sections for the excitation from the 6^2S, 6^2P, 5^2D states to the excited states up to 6^2D were taken from the compilation of Sobel'man *et al.* [135] with the correction in the lower incident electron energy range. Excitations from the states 6^2S, 6^2P and 5^2D to the 8^2S, 8^2P and 7^2D states were not available which they have determined by extrapolation method using classical Gryzinski method [137]. Cross sections for the inter connecting excited states above 5^2D were taken from the first Born approximation results of Krishnan and Stumpf [136]. Electron impact ionization cross sections of different sates were taken where available from the literature [138–141]. For the unavailable data, the cross sections were obtained by using simple classical Gryzinski method [137].

For the cesium atom, being a heavier element with atomic number Z=55, the relativistic effect such as spin-orbit interaction with *j–j* coupling are supposed to play significant role and hence, should not be ignored in the calculation of electron impact excitation as well as ionization cross sections[63]. In contrast to the C-R model of Wünderlich *et al.* [134], one has to take into account the various electron-impact excitation processes using relativistic approach in order to properly describe the population densities of Cs (ground as well as excited states) by using a suitable C-R model. Overall, the data for relativistic cross sections are scarce and thus insufficient for modeling purposes. Only one recent calculations using relativistic theoretical approaches were reported for selected transitions in a different context [63, 142]. It is therefore desirable to first develop a consistent data set of relativistic cross sections for electron impact excitation processes as well as for ionization process in cesium and then apply these for developing a suitable C-R model.

In this Chapter we performed the calculations in a detailed manner to obtain the relativistic cross sections for various fine-structure excitations using distorted wave (RDW) theory [33] in a for wide range of incident electron energies. For ionization cross section results of all considered fine structure states, available flexible atomic code (FAC) [143] is utilized. To ascertain the reliability of all obtained cross sections, present results are compared with the previous theoretical as well as experimental results available in a selected range of energy for the few transitions. Further, by incorporating these obtained cross sections, a C-R model has been developed for the hydrogen-cesium plasma relevant to Cs-seeded ITER negative ion based NBI systems. The present C-R model is developed on the line of our earlier models which we had used to describe low pressure Ar and Kr plasma successfully [13, 112, 144]. In addition to the electron impact excitation, other important processes such as spontaneous emission, electron impact de-excitation, ionization, three-body recombination as well as the mutual neutralization of Cs^+ ion with negative hydrogen ions have also been taken into account in the present C-R model. The population distribution results obtained from present model are compared with the previous measurements and calculations [134]. These population results are further coupled with the OES measurements [134] to extract the plasma parameters.

The present C-R model considers all the excitation processes as considered by Wünderlich *et al.* [134], thus, it would be worth pointing out here as how our RDW calculations for electron impact excitation are improved and different from their work. This is perhaps simple to understand as the non-relativistic Born-approximation [135, 136] or extrapolation scheme [137] (as used in [134]) does not take into account the distortion of the projectile electron (represented by plane waves) due to the target atom as well as the exchange with the target electrons. On the other hand our RDW theory incorporates these effects. Since spectroscopy based diagnostic approaches are highly dependent on the accuracy of the used cross sections in the model [14], the comparison of our modeling results with those of Wünderlich *et al.* [134] should directly reflect the significance of used relativistic cross sections of the electron impact excitation processes. One can expect that with the inclusion of RDW cross sections, the predicted plasma parameters from our model will be an improvement over the earlier results in [134].

2.2 Electron excitation cross sections and rate coefficients of Cesium

First, we discuss the various electron impact excitation processes which are involved in our CR model. The energy level diagram of Cs is shown in the figure 2.1. Electron impact excitation processes considered among the various fine-structure levels are also shown in the same figure. In particular, the electron-impact excitations for 82 transitions from the ground and various excited states are considered, *viz.* transitions from the ground state $6^2S_{1/2}$ to $n^2P_{1/2,\ 3/2}$, $n'^2D_{3/2,\ 5/2}$, $n''^2S_{1/2}$ states(where n=6-8, n'=5-7 and n''=7, 8), from the states $6^2P_{1/2/3/2}$ to $n^2P_{1/2,\ 3/2}$, $n'^2D_{3/2,\ 5/2}$, $n''^2S_{1/2}$ (where n=7, 8, n'=5-7 and n''=7, 8) states, from the states $5^2D_{3/2,\ 5/2}$ to $n^2P_{1/2,\ 3/2}$, $n'^2D_{3/2,\ 5/2}$, $n''^2S_{1/2}$ (where n=7, 8, n'=6, 7 and n''=7, 8) states, from $7^2S_{1/2}$ to $n^2P_{1/2,\ 3/2}$ (where n=7, 8), from $7^2P_{1/2/3/2}$ to $n'^2D_{3/2,\ 5/2}$, $8^2S_{1/2}$ (where n'=6, 7), from $6^2D_{3/2,\ 5/2}$ to $8^2P_{1/2,\ 3/2}$, from $8^2S_{1/2}$ to $8^2P_{1/2,\ 3/2}$ and from $8^2P_{1/2,\ 3/2}$ to $7^2D_{3/2,\ 5/2}$.

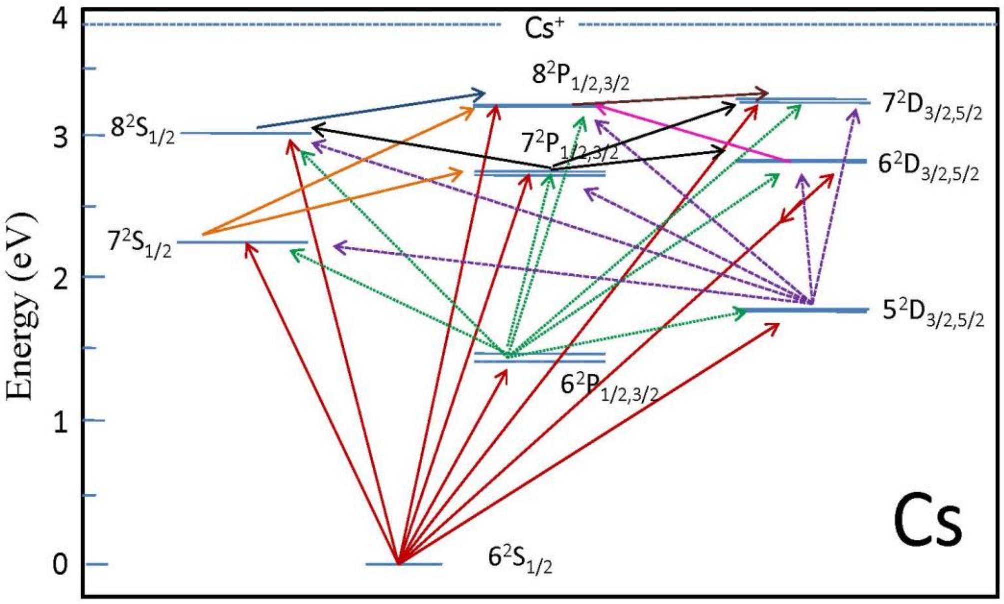

Figure 2.1: Energy level diagram for the cesium atom showing various fine-structure states included in the C-R model. The electron impact excitation processes for 82 transitions among the various states considered in the present work are displayed by arrows.

The electron impact excitation cross sections for all the considered fine structure transitions are obtained by calculating the T-matrix (equation (1.2.29)). The results for the cross sections are obtained in the incident electron energy range from the excitation threshold to 1 keV. Further, utilizing these cross sections $\sigma_{if}(E)$ for the excitation *i→f*, the excitation rate coefficient of each transition is calculated by using the following expression [79]

$$k_{if} = \sqrt{2}\int_{E_{if}}^{\infty} \sigma_{if}\left(E\right)\sqrt{E}\,f\left(E\right)dE \tag{2.2.1}$$

here, E_{if} is the excitation energy and $f\left(E\right)$ is the Maxwellian electron energy distribution function given by,

$$f\left(E\right)=\frac{2\pi}{\left(\pi kT_e\right)^{3/2}}\sqrt{E}\,exp\left(-\frac{E}{kT_e}\right) \tag{2.2.2}$$

here, T_e is the electron temperature and k is the Boltzmann constant.

2.2.1 Dirac-Fock wave functions of Cesium atom

For evaluating the T-matrix (equation (1.2.29)), the required atomic target wave functions of different states have been calculated within the multi configuration Dirac-Fock approach using the GRASP2K code [99]. The various configurations *viz.* involving the orbitals 5*d*, n*s*, n*p* and n*d* (n=6-8), 9*s* and 9*p* have been included in the evaluation of target wave functions. In order to check the reliability of the present wave functions, the oscillator strengths for various dipole allowed transitions are calculated and compared with the other available results.

The Table 2.1 presents the calculated oscillator strengths for all the possible dipole allowed transitions among the different considered fine-structure states and compared them with the available previous theoretical as well as experimental results for $6^2S_{1/2}$ → $n^2P_{1/2,3/2}$ (n=6-8), $6^2P_{1/2}$ → $5^2D_{3/2}$ and $6^2P_{3/2}$ → $5^2D_{3/2,5/2}$ transitions. Discussion of comparison for different results is given transition wise. For $6^2S_{1/2}$ → $6^2P_{1/2,3/2}$ transitions, there are two experimental data set reported by Rafac *et al.* [145, 146]. Note that the NIST data base [147] refers their first experimental data [145]. Another set of the recent experimental data was also reported by Derevianko and Porsev [148]. From the Table 2.1, it is found that these all experimental values [146–148] are in good agreement among themselves. The theoretical calculations [149, 150] as well as ours are obtained using similar Dirac-Fock configuration wavefunctions and on comparing them with the experiment [146–148] we find that our values as well as of Zilitis [149] are slightly higher than the experimental data by 6% and 3% respectively while the results of Glowacki [150] are slightly lower by 1%. On the other hand the values of Bostock *et al.* [151] are relatively much higher by 16% who used entirely different approach i.e. relativistic convergent close-coupling (RCCC) method. In fact, the oscillator strengths depend not only on the calculated wave functions but also on the associated values of the calculated transition energies. Therefore, these two factors can cause such small deviations in the oscillator strengths calculated from different theoretical approaches.

For the transitions $6^2S_{1/2} \rightarrow 7^2P_{1/2,\,3/2}$ and $6^2S_{1/2} \rightarrow 8^2P_{1/2,\,3/2}$, the NIST database [147] values were taken from the measurements of Vasilyev *et al.* [152], and Morton [153], respectively. The theoretical values from Glowacki [150] are also available for these transitions. From the Table 2.1, we find that the overall comparison is somewhat similar as seen for $6^2S_{1/2} \rightarrow 6^2P_{1/2,\,3/2}$. Our values are slightly higher by ~6% than the experimental values while that of Glowacki [150] are much lower by 22%. However, for $6^2S_{1/2} \rightarrow 8^2P_{1/2}$ transition, the theoretical results (present and [150]) seem to deviate more than 50% from the experiment [153] but one should note that the value of the oscillator strength is itself of the order of 10^{-4} therefore, this deviation may be said reasonable. For $6^2P_{1/2,/3/2} \rightarrow 5^2D_{3/2}$ transitions, the NIST values are taken from the theoretical Dirac- Fock calculations of Safronova *et al.* [154] and on comparison of our results with theirs we find that the our oscillator strengths for $6^2P_{1/2,/3/2} \rightarrow 5^2D_{3/2}$ are higher by 44% and 56% respectively from the calculations of Safronova *et al.* [154]. This large difference in the oscillator strengths of the two theoretical calculations can be due to the different approaches adopted for the calculations of the wave-functions and their associated energies. Since there are no experimental data available for comparison it is difficult to assess the accuracy of the oscillator strengths for these transitions. For $6^2P_{3/2} \rightarrow 5^2D_{5/2}$ transition the available NIST data is the measurement of DiBerardino *et al.* [155] and on comparison with their value we find that the present oscillator strength is in reasonable agreement.

Table 2.1: Comparison of present oscillator strengths (*f*) of the transitions between the different states of Cs with the available measured and the other theoretically values. The number in the parenthesis stands for the multiplying power of 10.

Lower level	***Upper level***	f_{present}	f_{NIST} [147]	$f_{previous}$(Exp.)	$f_{previous}$(Theory)
$6\,^2S_{1/2}$	$6\,^2P_{1/2}$	3.64(-1)	3.43(-1) †	3.42(-1)[a] 3.45(-1)[b]	3.53(-1)[c] 3.40(-1)[d] 3.98(-1)[e]
$6\,^2S_{1/2}$	$6\,^2P_{3/2}$	7.27(-1)	7.14(-1)	7.13(-1)[a] 7.17(-1)[b]	7.26(-1)[c] 7.07(-1)[d] 8.19(-1)[e]
$6\,^2S_{1/2}$	$7\,^2P_{1/2}$	2.36(-3)	2.51(-3)		2.01(-3)[c]
$6\,^2S_{1/2}$	$7\,^2P_{3/2}$	1.20(-2)	1.15(-2)		9.28(-3)[c]
$6\,^2S_{1/2}$	$8\,^2P_{1/2}$	3.85(-4)	2.04(-4)		1.37(-4)[c]
$6\,^2S_{1/2}$	$8\,^2P_{3/2}$	1.78(-3)	1.74(-3)		1.35(-3)[c]
$6\,^2P_{1/2}$	$5\,^2D_{3/2}$	3.59(-1)	2.48(-1)		
$6\,^2P_{3/2}$	$5\,^2D_{3/2}$	3.30(-2)	2.10(-2)		
$6\,^2P_{3/2}$	$5\,^2D_{5/2}$	2.97(-1)	2.14(-1)		
$6\,^2P_{1/2}$	$7\,^2S_{1/2}$	1.75(-1)			
$6\,^2P_{3/2}$	$7\,^2S_{1/2}$	1.89(-1)			
$6\,^2P_{1/2}$	$6\,^2D_{3/2}$	2.51(-1)			
$6\,^2P_{3/2}$	$6\,^2D_{3/2}$	2.86(-2)			
$6\,^2P_{3/2}$	$6\,^2D_{5/2}$	2.50(-1)			
$6\,^2P_{1/2}$	$8\,^2S_{1/2}$	2.03(-2)			
$6\,^2P_{3/2}$	$8\,^2S_{1/2}$	2.17(-2)			
$6\,^2P_{1/2}$	$7\,^2D_{3/2}$	8.76(-2)			
$6\,^2P_{3/2}$	$7\,^2D_{3/2}$	8.93(-3)			
$6\,^2P_{3/2}$	$7\,^2D_{5/2}$	7.83(-2)			
$5\,^2D_{3/2}$	$7\,^2P_{1/2}$	1.99(-2)			
$5\,^2D_{3/2}$	$7\,^2P_{3/2}$	3.44(-3)			

$5\,^2D_{5/2}$	$7\,^2P_{3/2}$	2.70(-2)			
$5\,^2D_{3/2}$	$8\,^2P_{1/2}$	2.59(-3)			
$5\,^2D_{3/2}$	$8\,^2P_{3/2}$	4.59(-4)			
$5\,^2D_{5/2}$	$8\,^2P_{3/2}$	2.21(-3)			
$7\,^2S_{1/2}$	$7\,^2P_{1/2}$	5.05(-1)			
$7\,^2S_{1/2}$	$7\,^2P_{3/2}$	1.03(+0)			
$7\,^2S_{1/2}$	$8\,^2P_{1/2}$	8.83(-3)			
$7\,^2S_{1/2}$	$8\,^2P_{3/2}$	2.60(-2)			
$7\,^2P_{1/2}$	$6\,^2D_{3/2}$	4.48(-1)			
$7\,^2P_{3/2}$	$6\,^2D_{3/2}$	3.74(-2)			
$7\,^2P_{3/2}$	$6\,^2D_{5/2}$	3.52(-1)			
$7\,^2P_{1/2}$	$8\,^2S_{1/2}$	3.61(-1)			
$7\,^2P_{3/2}$	$8\,^2S_{1/2}$	4.05(-1)			
$7\,^2P_{1/2}$	$7\,^2D_{3/2}$	2.88(-1)			
$7\,^2P_{3/2}$	$7\,^2D_{3/2}$	3.34(-2)			
$7\,^2P_{3/2}$	$7\,^2D_{5/2}$	2.86(-1)			
$6\,^2D_{3/2}$	$8\,^2P_{1/2}$	6.18(-2)			
$6\,^2D_{3/2}$	$8\,^2P_{3/2}$	1.00(-2)			
$6\,^2D_{5/2}$	$8\,^2P_{3/2}$	6.08(-2)			
$8\,^2S_{1/2}$	$8\,^2P_{1/2}$	5.78(-1)			
$8\,^2S_{1/2}$	$8\,^2P_{3/2}$	1.15(+0)			
$8\,^2P_{1/2}$	$7\,^2D_{3/2}$	9.61(-1)			
$8\,^2P_{3/2}$	$7\,^2D_{3/2}$	9.03(-2)			
$8\,^2P_{3/2}$	$7\,^2D_{5/2}$	8.15(-1)			

[†]Rafac *et al.* [145], [a]Rafac *et al.* [146], [b]Derevianko and Porsev [148], [c]Zilitis [149], [d]Głowacki [150] and [e]Bostock *et al.* [151].

2.2.2. Cross sections and rates

Most of the earlier theoretical calculations reported on electron impact excitation of cesium atom are from the 6^2S state and they have used non-relativistic approximations [135, 136, 156, 157] which do not resolve the fine-structure levels. Thus such calculations are not directly comparable to any fully relativistic calculation, in particular, for a heavier atom like Cs (see Zatsarinny *et al.* [63]). Also no experimental electron impact direct excitation cross section results are reported in the literature. However, Chen and Gallagher [158] reported their normalized optical cross sections for the $6^2S \rightarrow 6^2P$ excitation which includes direct excitation cross section along with cascade contribution. In fact, they measured optical excitation functions for $6^2P_{3/2}$ and normalized their cross sections to the sum of Born direct and cascade excitation cross sections but these cannot be compared until the cascade contributions are separately known and excluded. However if there would have been some suitable measurements even for the unresolved $6^2S \rightarrow 6^2P$ excitation one can compare the fine structure resolved results by combining them. Also majority of the available unresolved theoretical results reported are obtained using simple Born approximation and impact parameter methods [135, 136]. The available relativistic calculations include the work of Zemen *et al.* [159] who reported differential and integrated cross sections using the relativistic distorted wave theory for the electron impact excitation from the ground state 6^2S to the $6\ ^2P_{1/2,3/2}$ states only. Though their RDW theory is similar to ours but they used simple single configuration Cs target wavefunctions which were obtained from the older version of MCDF code [160]. Recently, Zatsarinny *et al.* [63] reported fully relativistic Dirac B-spline R-matrix (DBSR) with pseudo states calculations for the electron impact cross sections for the excitation from the ground $6^2S_{1/2}$ as well as from the excited states $6^2P_{1/2/3/2}$ to the different higher lying states.

Comparisons of present RDW results with the DBSR-311 calculations [63] for the excitation from the fine structure states $6^2S_{1/2}$ and $6^2P_{1/2,3/2}$ to few higher lying states are presented through figures 2.2, 2.3 and 2.4. Figure 2.2 shows the comparison of present RDW and DBSR results available up to 150 eV for the electron impact excitation cross sections from the ground state $6^2S_{1/2}$ to $6^2P_{1/2,\ 3/2,}$ $5^2D_{3/2,\ 5/2}$, $7^2S_{1/2}$ and $7^2P_{1/2,\ 3/2}$. On comparison of these two set of calculations i.e. present RDW and DBSR [63] for the fine-structure excitation cross sections from the ground state $6^2S_{1/2}$ to $6^2P_{1/2,\ 3/2}$ levels, it is found that their natures are different and the magnitudes differ maximum by factor of 2-3 and, similar can be said for the excitation to $7^2S_{1/2}$. The cross section curves for the excitations to the $5^2D_{3/2,\ 5/2}$ and $7^2P_{1/2,\ 3/2}$ states show similar behavior and are in reasonable agreement. Figures 2.3 and 2.4 present the comparison of our RDW and DBSR [63] cross section results for the excitation from the states $6^2P_{1/2}$ and $6^2P_{3/2}$ respectively to the states $5^2D_{3/2,\ 5/2}$, $7^2S_{1/2}$ and $7^2P_{1/2,\ 3/2}$. It can be seen from the figures that the two set of calculations for all these transitions show reasonable agreement.

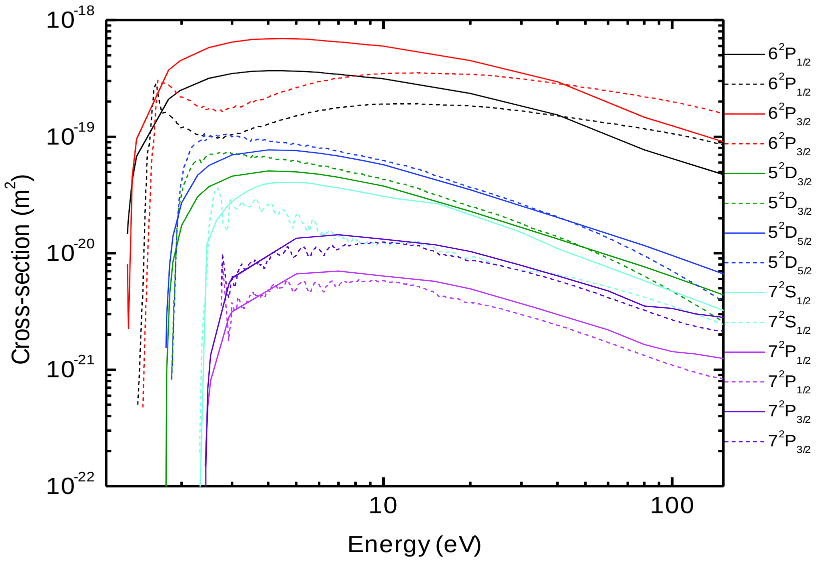

Figure 2.2: Comparison of the present RDW electron impact excitation cross sections (solid line) from the ground state $6^2S_{1/2}$ of cesium with the DBSR calculations of Zatsarinny *et al.* [63] (dashed line).

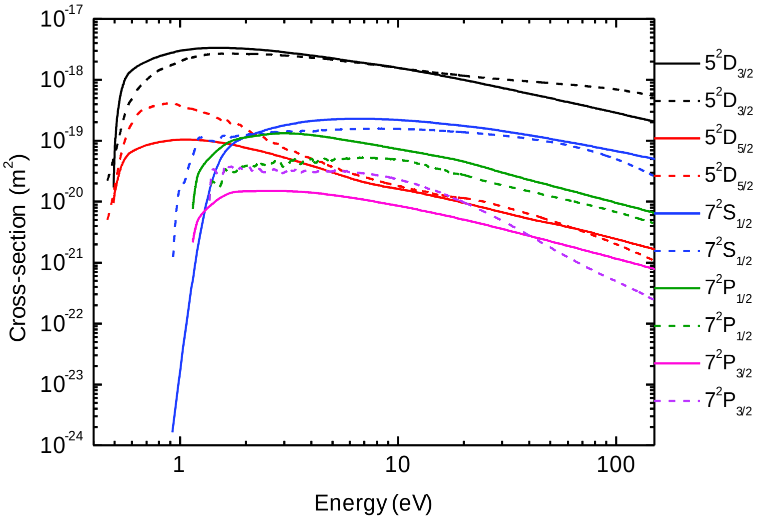

Figure 2.3: Comparison of the present RDW electron impact excitation cross sections (solid line) from the state $6^2P_{1/2}$ of cesium with the DBSR calculations of Zatsarinny *et al.* [63] (dashed line).

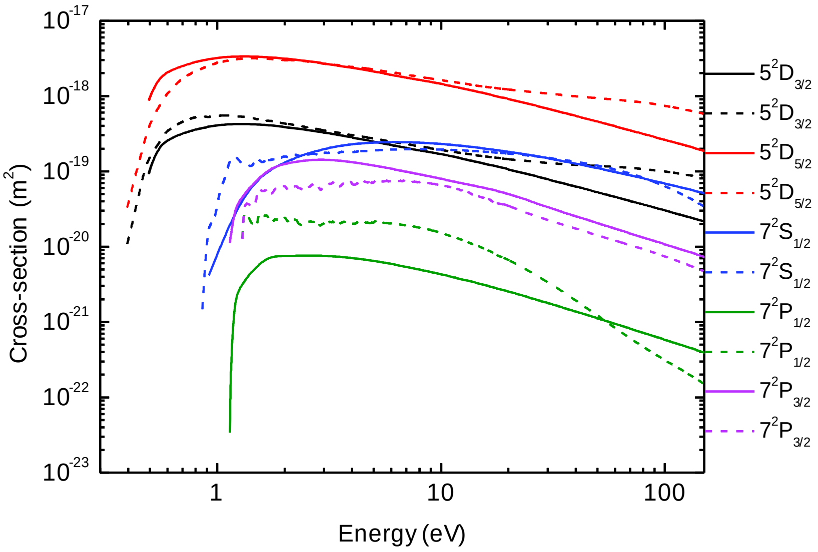

Figure 2.4: Comparison of the present RDW electron impact excitation cross sections (solid line) from the state $6^2P_{3/2}$ of cesium with the DBSR calculations of Zatsarinny *et al.* [63] (dashed line).

Through the figures 2.5-2.16, we have presented our calculated all the RDW cross sections of various fine-structure transitions from the ground state as well as excited states to the different higher lying states which are referred in the figure 2.1. In these figures along with our cross section results we have also shown in an adjacent box, the rate coefficients varying with electron temperature up to 50 eV for the same fine-structure transitions.

Figures 2.5 and 2.6 present the electron impact excitation cross sections and the rate coefficients from the ground state of cesium $6^2S_{1/2}$ to fine-structure excited states $n^2P_{1/2,\,3/2}$, $n'^2D_{3/2,\,5/2}$ and $n''^2S_{1/2}$ states(where n=6-8, n'=5-7 and n"=7 and 8). It can be seen from these figures that the cross sections for the fine-structure states with the larger *J* value are greater i.e., cross sections for the states $n^2P_{3/2}$ and $n'^2D_{5/2}$ are larger as compared to the state $n^2P_{1/2}$ and $n'^2D_{3/2}$ respectively in the entire range of electron energy. This is quite expected from the fine structure L-S coupling formula that the cross section from the same initial state ^2S to the two final states, are in the ratio of their multiplicities. Thus the ratio of the excitation cross section of the same P state with J=3/2 and J=1/2 should be in the ratio of a factor of 2 and for the excitation cross section of the same D state with J=5/2 and J=3/2 should be in the ratio of a factor of 1.5. However, we find that in our RDW results these ratios are not exactly 2 and 1.5 but they vary close to 1.9-2.2 and 1.4-1.5 respectively. The deviation in the ratio confirms the breaking down of L-S fine-structure formula and indicates the importance of the contribution of the relativistic spin-orbit interactions.

In the figures 2.7, 2.8 and 2.9, the cross sections for the excitation from $6^2P_{1/2,\ 3/2}$ to higher excited states have been shown. In absence of any available experimental data it is difficult to comment on the magnitudes of the cross section results for the different transitions. However, it can be seen that the cross sections are almost same for the excitation from $6^2P_{1/2}$ or $6^2P_{3/2}$ to $n^2S_{1/2}$ states with n=7, 8. Also, it is observed that for the excitation from $6^2P_{1/2,\ 3/2}$ to the levels $n'^2D_{3/2,\ 5/2}$ (n'=5-7) and $n''^2P_{1/2,\ 3/2}$ (n''=7,8), their cross sections show that $\sigma(6^2P_{1/2}\rightarrow n'^2D_{3/2}) > \sigma(6^2P_{1/2}\rightarrow n'^2D_{5/2})$; $\sigma(6^2P_{3/2}\rightarrow n'^2D_{5/2}) > \sigma(6^2P_{3/2}\rightarrow n'^2D_{3/2})$; $\sigma(6^2P_{1/2}\rightarrow n''^2P_{1/2}) > \sigma(6^2P_{1/2}\rightarrow n''^2P_{3/2})$ and $\sigma(6^2P_{3/2}\rightarrow n''^2P_{3/2}) > \sigma(6^2P_{3/2}\rightarrow n''^2P_{1/2})$. Such behavior of cross sections for different transitions can be easily argued on the basis of the selection rule $\Delta J=0,\pm1$ of total angular momentum J as well as the change in parity during the transition.

Further, through the figures 2.10-2.16, the cross sections for rest of the transitions considered are shown. For the excitation from the states $5^2D_{3/2,\ 5/2,}$ $7^2P_{1/2/3/2}$, $6^2D_{3/2,\ 5/2}$ and $8^2P_{1/2,\ 3/2}$ to higher excited states we find the similar behavior as seen for the excitation from the states $6^2P_{1/2,\ 3/2}$. Further, the cross section curves for the excitation from the states $7^2S_{1/2}$ and $8^2S_{1/2}$ follow same trend as observed for the excitation from $6^2S_{1/2}$ state.

It would be worth mentioning about the uncertainty of our results reported here for the application point of view. The overall numerical accuracy of the present cross sections depends on many factors. For example, the bound state wave functions calculated by the GRASP code are accurate to at least one part in 10^6, while the solution of the free particle Dirac-Fock equations converges to one part in 10^5. The accuracy of the radial integration involving these functions is governed by the accuracy of the integrands as well as the integration method used. We have accurately evaluated the oscillating long-range contribution to the direct terms in T-matrix by using contour integration so the overall error in the radial integration should not exceed one part in $10^{4.}$ In evaluating the T-matrix, we expand the free wave functions in partial waves and calculate the individual terms for increasing values of their angular momentum until the convergence is achieved to one part in 10^5. Thus, the accuracy of the reported cross sections here within the RDW approximation is at least one part in 10^4.

As far as the rate coefficients for various electron impact excitation transitions presented through all the figures are concerned these show expected behavior. There is a sharp increase in rate coefficient at very low electron temperatures and thereafter attaining the maximum value it decreases slowly at higher temperatures. Magnitudes of rate coefficients for different transitions are according to their cross sections. We have presented the rate coefficients up to 50 eV so that one can use directly accurate rate coefficients in their plasma model as some plasma models require rate coefficients as direct input instead of cross sections.

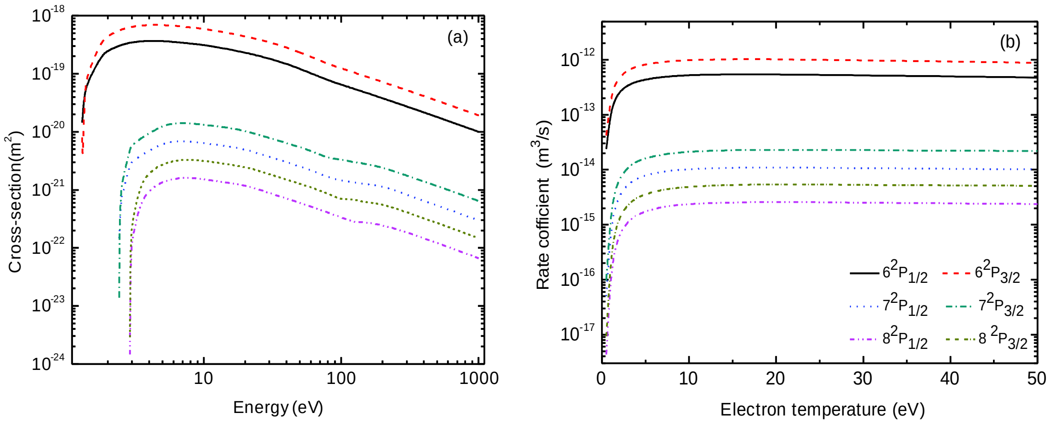

Figure 2.5: Electron-impact excitation from the ground state $6^2S_{1/2}$ to $n^2P_{1/2,3/2}$ (n=6-8) of cesium (a) Cross sections as a function of incident electron energy (b) Rate coefficients as a function of electron temperature.

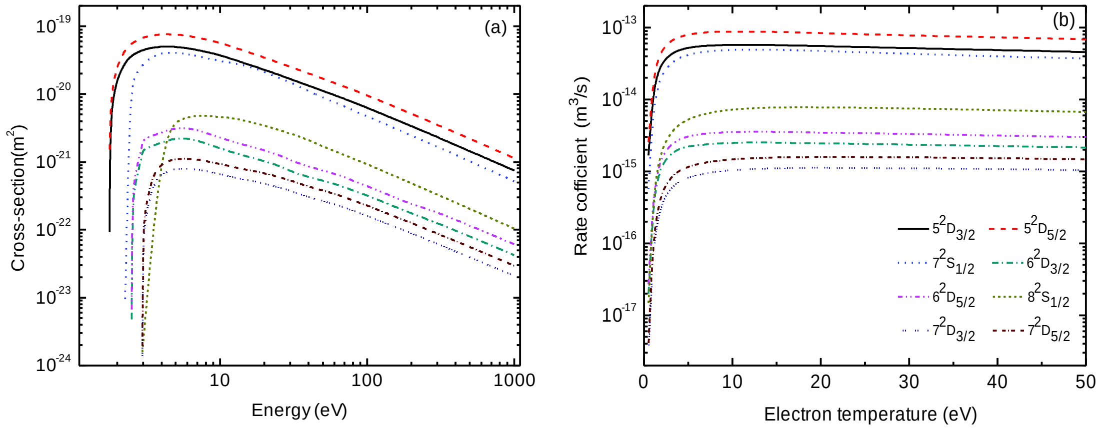

Figure 2.6: Electron-impact excitation from the ground state $6^2S_{1/2}$ to $n'^2D_{3/2,\ 5/2}$ (n'=5-7) and $n''^2P_{1/2,\ 3/2}$ (n"=7,8) of cesium (a) Cross sections as a function of incident electron energy (b) Rate coefficients as a function of electron temperature.

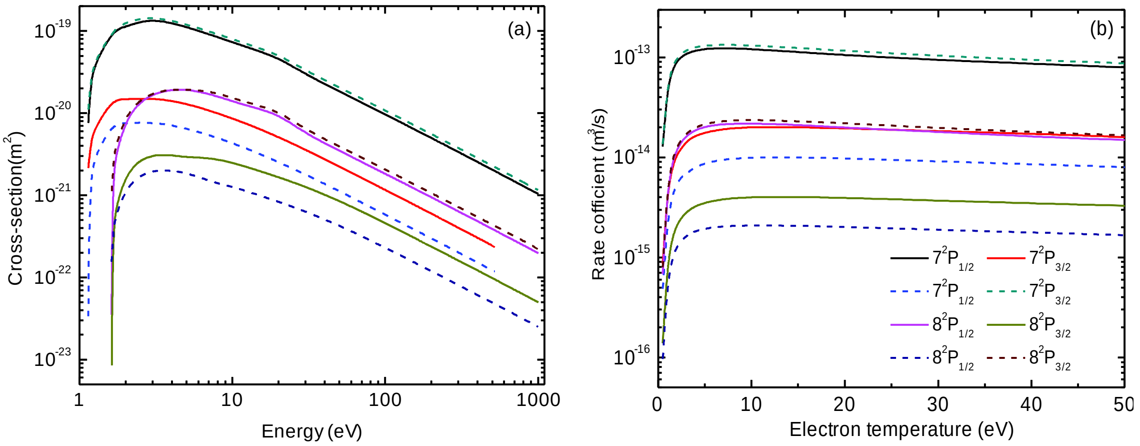

Figure 2.7: Electron-impact excitation from the excited states $6^2P_{1/2,3/2}$ of cesium (a) Cross sections as a function of incident electron energy (b) Rate coefficients as a function of electron temperature. Here solid line and dashed line present the excitation from $6^2P_{1/2}$ and $6^2P_{3/2}$ respectively.

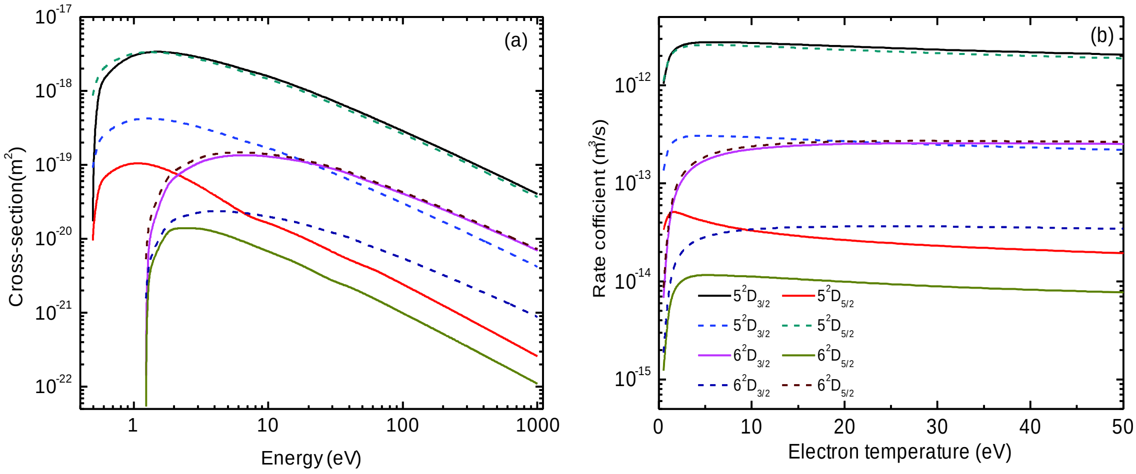

Figure 2.8: Electron-impact excitation from the excited states $6^2P_{1/2,3/2}$ of cesium (a) Cross sections as a function of incident electron energy (b) Rate coefficients as a function of electron temperature. Here solid line and dashed line present the excitation from $6^2P_{1/2}$ and $6^2P_{3/2}$ respectively.

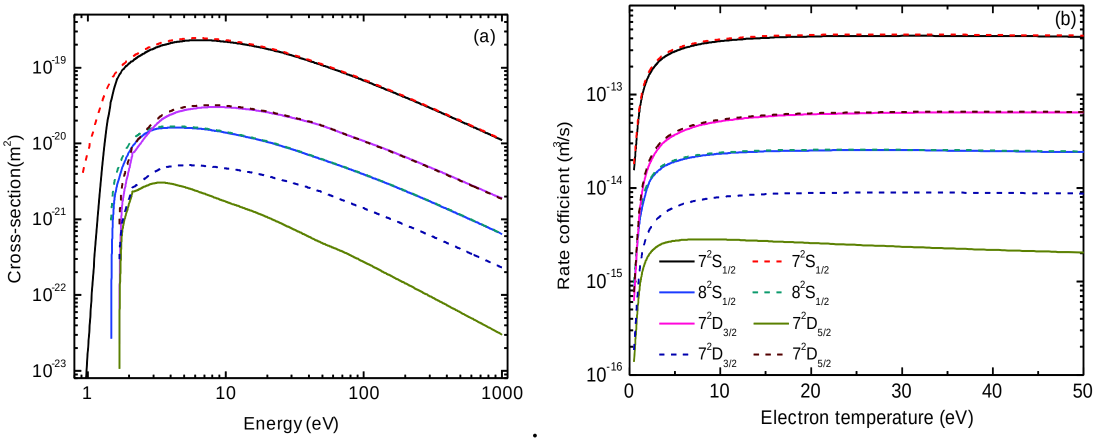

Figure 2.9: Electron-impact excitation from the excited states $6^2P_{1/2,3/2}$ of cesium (a) Cross sections as a function of incident electron energy (b) Rate coefficients as a function of electron temperature. Here solid line and dashed line present the excitation from $6^2P_{1/2}$ and $6^2P_{3/2}$ respectively.

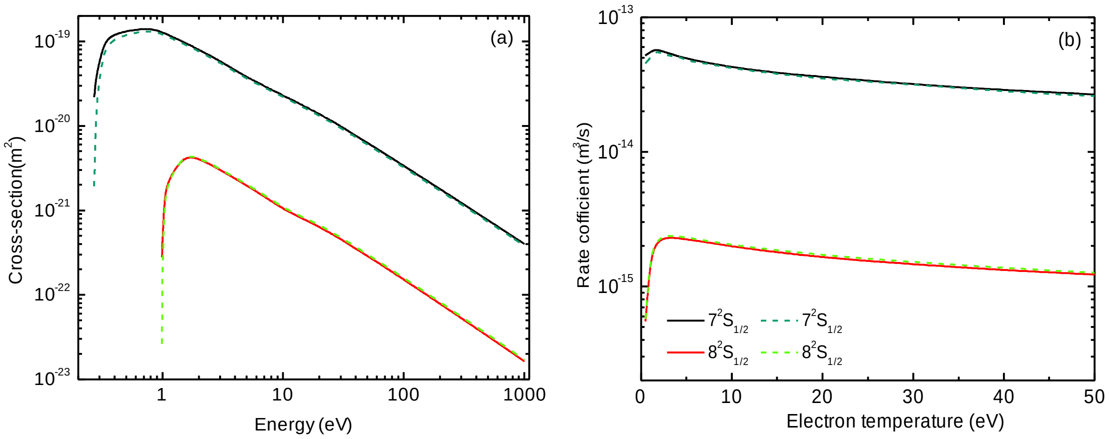

Figure 2.10: Electron-impact excitation from the excited states $5^2D_{3/2,5/2}$ of cesium (a) Cross sections as a function of incident electron energy (b) Rate coefficients as a function of electron temperature. Here solid line and dashed line present the excitation from $5^2D_{3/2}$ and $5^2D_{5/2}$ respectively.

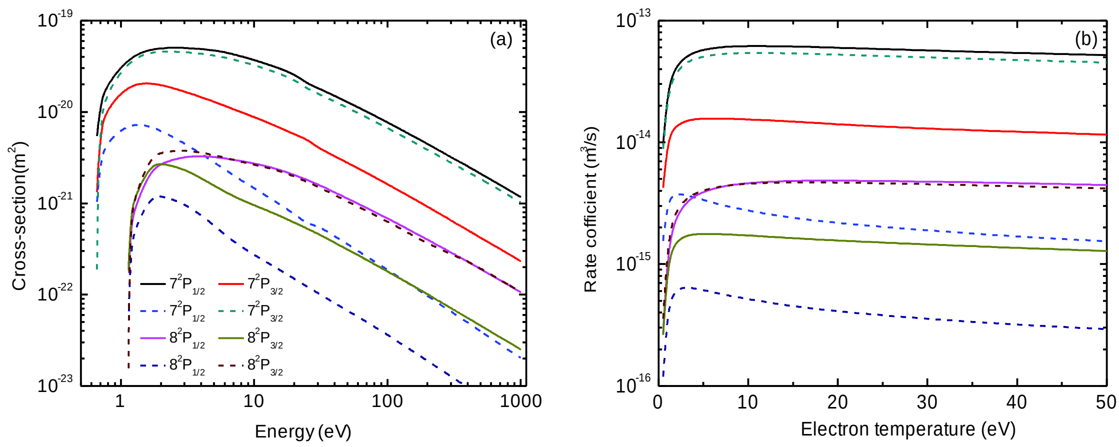

Figure 2.11: Electron-impact excitation from the excited states $5^2D_{3/2,5/2}$ of cesium (a) Cross sections as a function of incident electron energy (b) Rate coefficients as a function of electron temperature. Here solid line and dashed line present the excitation from $5^2D_{3/2}$ and $5^2D_{5/2}$ respectively.

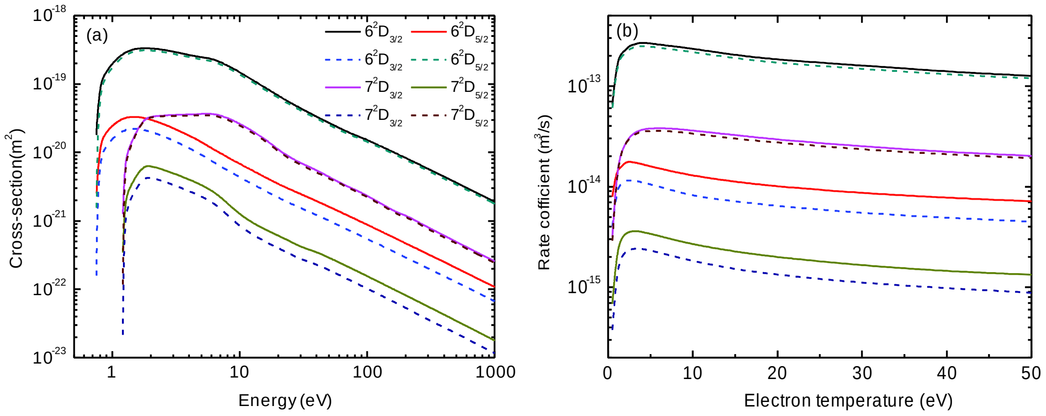

Figure 2.12: Electron-impact excitation from the excited states $5^2D_{3/2,5/2}$ of cesium (a) Cross sections as a function of incident electron energy (b) Rate coefficients as a function of electron temperature. Here solid line and dashed line present the excitation from $5^2D_{3/2}$ and $5^2D_{5/2}$ respectively.

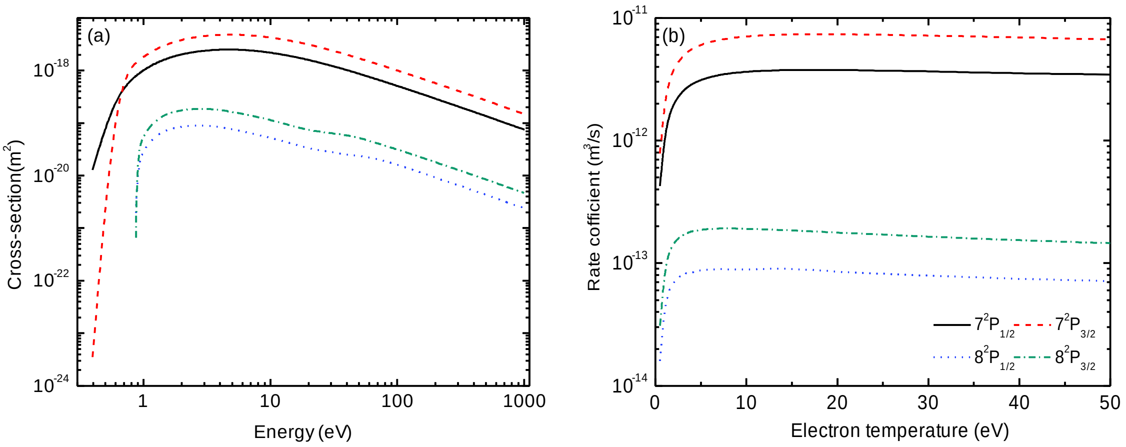

Figure 2.13: Electron-impact excitation from the excited states $7^2S_{1/2}$ of cesium (a) Cross sections as a function of incident electron energy (b) Rate coefficients as a function of electron temperature.

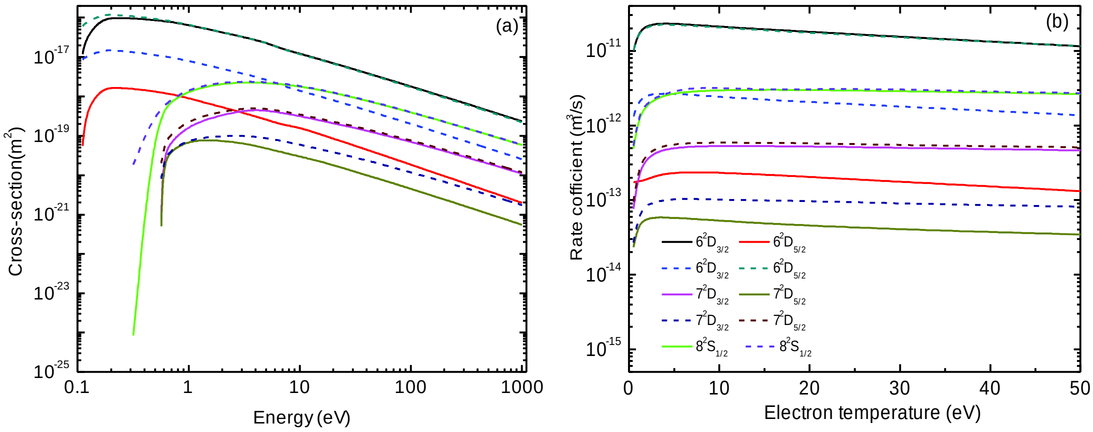

Figure 2.14: Electron-impact excitation from the excited states $7^2P_{1/2,3/2}$ of cesium (a) Cross sections as a function of incident electron energy (b) Rate coefficients as a function of electron temperature. Here solid line and dashed line present the excitation from $7^2P_{1/2}$ and $7^2P_{3/2}$ respectively.

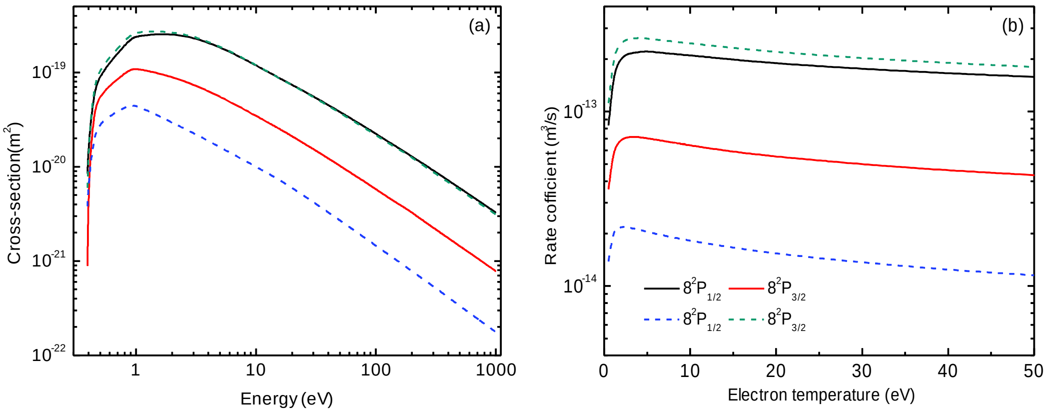

Figure 2.15: Electron-impact excitation from the excited states $6^2D_{3/2,5/2}$ of cesium (a) Cross sections as a function of incident electron energy (b) Rate coefficients as a function of electron temperature. Here solid line and dashed line present the excitation from $6^2D_{3/2}$ and $6^2D_{5/2}$ respectively.

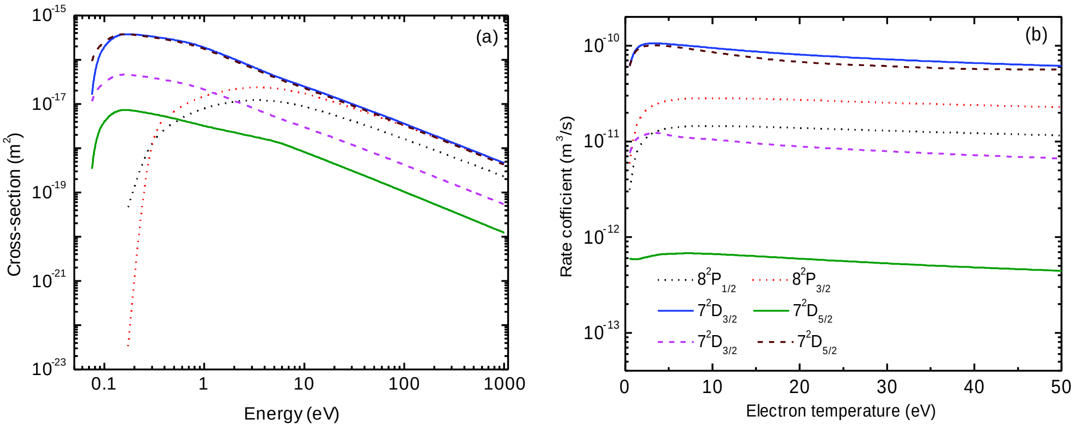

Figure 2.16: Electron-impact excitation from the excited states $8^2S_{1/2}$ and $8^2P_{1/2,3/2}$ of cesium (a) Cross sections as a function of incident electron energy (b) Rate coefficients as a function of electron temperature. Here solid line and dashed line present the excitation from $8^2P_{1/2}$ and $8^2P_{3/2}$ respectively. Dotted line denotes the excitation from $8^2S_{1/2}$ state.

2.2.3 Analytical fittings of excitation cross sections

The calculated numerical excitation cross sections for all the fine-structure transitions have been fitted through the following analytical formulae [13, 73].

$$\sigma = \frac{\sum_{i=0}^{n} b_i E^i}{c_0 + c_1 E + c_2 E^2} a_0^2 \, . \tag{2.2.2}$$

Here, σ is in units of a_0^2 (0.28e-20 m^2), E is incident electron energy in atomic units (27.211eV) and b_i, c_0, $c_1$and c_2 are fitting coefficients. Table 2.2 list the fitting coefficients for the electron impact excitation cross sections for the 82 transitions considered for Cs. The accuracy of the fitted formula is within 5% in the considered energy range from threshold to 1keV. The advantage of giving this fitting is that one can use directly the obtained expressions in the plasma models.

Table 2.2: Fitting coefficients for the electron impact excitation cross sections for the transitions considered for Cs atom. The number in the parenthesis stands for the multiplying power of 10.

Transition	**Energy Interval (in eV)**	b_0	b_1	b_2	b_3	c_0	c_1	c_2
$6\,^2S_{1/2} \rightarrow 6\,^2P_{1/2}$	E_{th}-9	-3.81054(+1)	7.54048(+2)	1.25534(+3)		1.55700(-2)	1.78717(+0)	2.21984(+1)
	9-79	-1.75894(+1)				-1.13180(-1)	1.11190(-1)	-2.1900(-2)
	79-1000	5.91161(+2)	4.63893(+1)			4.63266(+0)	6.54466(+0)	-2.94770(-1)
$6\,^2S_{1/2} \rightarrow 6\,^2P_{3/2}$	E_{th}-3.989	-7.26705(+1)	4.09312(+2)	2.32295(+4)		1.84670(-1)	-3.33583(+0)	1.05340(+2)
	3.989-10	7.93665(+1)	-2.38839(+2)	5.26072(+3)		5.97760(-1)	-4.41745(+0)	3.18780(+1)
	10-200	1.14601(+2)	-1.94563(+1)	1.92874(+0)		3.85840(-1)	3.20710(-1)	3.24000(-3)
	200-1000	2.48919(+3)	1.10249(+2)			1.37531(+1)	1.28994(+1)	3.47500(-1)
$6\,^2S_{1/2} \rightarrow 5\,^2D_{3/2}$	E_{th}-10	-3.17268(+0)	4.87372(+1)	2.6881(-1)		-1.82600(-2)	6.69300(-1)	6.48457(+0)
	10-100	-3.59404(+0)	1.15153(+1)	5.5628(-1)		-9.05400(-2)	-1.95260(-1)	1.59306(+0)
	100-1000	3.61628(+1)	1.87718(+0)			1.64331(+0)	4.10517(+0)	1.78090(-1)
$6\,^2S_{1/2} \rightarrow 5\,^2D_{5/2}$	E_{th}-10	-8.23595(+0)	1.24485(+2)	4.39487(+1)		-1.64100(-2)	8.43920(-1)	1.34987(+1)
	10-1000	6.96129(+0)	3.92645(+0)	-4.15000(-3)		9.76800(-2)	7.54580(-1)	2.50820(-1)
$6\,^2S_{1/2} \rightarrow 7\,^2S_{1/2}$	E_{th}-5.347	-2.99608(+2)	3.62361(+3)			5.70680(-1)	7.92740(+0)	6.88594(+2)
	5.347-15	6.75203(+0)	-1.33522(+1)	2.685113(+1)		3.56850(-1)	-4.30320(-1)	2.20125(+0)
	15-1000	-1.57257(+0)	2.81126(+0)			-1.36000(-2)	-2.30310(-1)	4.55550(-1)
$6\,^2S_{1/2} \rightarrow 7\,^2P_{1/2}$	E_{th}-10	-1.36731(+0)	1.64506(+1)	-1.07404(+1)		-2.42400(-2)	2.24682(+0)	4.54871(+0)
	10-40	1.05207(+0)	2.13983(+0)			4.04320(-1)	6.09090(-1)	1.19916(+0)
	40-200	1.11308(+1)	-5.09764(+0)	1.14627(+0)	-5.71700(-2)	6.11765(+0)	-1.37468(+0)	6.47940(-1)

	200-1000	-1.00681(+3)				-3.36980(+2)	-2.92537(+2)	1.27908(+0)
$6\,^2S_{1/2} \rightarrow 7\,^2P_{3/2}$	E_{th}-10	-2.21180(+0)	2.65034(+1)	-1.83647(+1)		-1.63400(-2)	1.82118(+0)	3.07782(+0)
	10-80	4.90909(+0)	-5.72509(+0)	4.88310(+0)	-7.77240(-1)	9.66290(-1)	-1.10910(+0)	1.23349(+0)
	80-1000	5.86816(+0)	1.71845(+0)			4.35925(+0)	8.63310(-1)	2.03650(-1)
$6\,^2S_{1/2} \rightarrow 6\,^2D_{3/2}$	E_{th}-20	-5.33480(-1)	5.39508(+0)	4.26812(+0)		1.39970(-1)	-3.01639(+0)	3.30188(+1)
	20-80	1.30764(+0)	4.40180(-1)	-1.54070(-1)		-8.67100(-1)	7.95181(+0)	-1.54904(+0)
	80-1000	2.23178(+0)	5.30650(-1)			9.51000(-2)	6.72701(+0)	8.79680(-1)
$6\,^2S_{1/2} \rightarrow 6\,^2D_{5/2}$	E_{th}-15	-4.22664(+0)	5.71813(+1)	-1.33953(+2)	1.14118(+2)	-9.71940(-1)	1.54700(+1)	5.05230(+0)
	15-100	1.26784(+0)	1.47192(+0)	2.02680(-1)		8.24240(-1)	2.66861(+0)	3.51356(+0)
	100-1000	1.17263(+1)	2.40641(+0)	-1.61200(-2)		-2.23973(+1)	3.47000(+1)	1.77529(+0)
$6\,^2S_{1/2} \rightarrow 8\,^2S_{1/2}$	E_{th}-34.356	-4.68611(+0)	4.26299(+1)	4.05570(+0)		2.57600(-2)	5.54742(+0)	3.50999(+1)
	34.35-1000	-1.86037(+0)	1.82753(+0)			-6.67560(-1)	-7.69210(-1)	1.34703(+0)
$6\,^2S_{1/2} \rightarrow 8\,^2P_{1/2}$	E_{th}-10	-7.61330(-1)	6.67988(+0)	4.43974(+0)		-2.97940(-1)	-2.97940(-1)	2.92917(+1)
	10-30	1.01344(+0)	-5.03590(-1)			1.40514(+0)	4.20930(-1)	-3.41200(-1)
	30-80	8.71640(-1)	5.79760(-1)			4.62160(-1)	2.72728(+0)	1.07386(+0)
	80-1000	2.12349(+1)	1.26943(+0)			1.20778(+2)	1.99868(+1)	1.54220(+0)
$6\,^2S_{1/2} \rightarrow 8\,^2P_{3/2}$	E_{th}-20	-2.37044(+0)	2.43790(+1)	-2.20524(+1)	2.05063(+1)	2.27600(-1)	2.95463(+0)	2.01650(+1)
	20-100	3.85382(+0)	-4.75970(-1)	-8.39500(-2)		1.27187(+0)	4.29951(+0)	-9.65870(-1)
	100-1000	1.12565(+0)	7.67630(-1)			9.73270(+0)	2.87170(-1)	4.17980(-1)
$6\,^2S_{1/2} \rightarrow 7\,^2D_{3/2}$	E_{th}-20	-3.50730(-1)	3.44227(+0)	-2.46232(+0)	3.34117(+0)	-1.02550(-1)	5.09350(-1)	2.26566(+1)
	20-1000	4.93400(-2)	2.12710(-1)			-5.59900(-2)	1.11488(+0)	7.77950(-1)
$6\,^2S_{1/2} \rightarrow 7\,^2D_{5/2}$	E_{th}-20	-4.54740(-1)	4.43165(+0)	-2.88731(+0)	4.16856(+0)	-1.00460(-1)	4.87700(-1)	2.12774(+1)
	20-1000	7.24800(-2)	7.26280(-1)			-2.64600(-1)	2.32223(+0)	1.88685(+0)

$6\,^2P_{1/2}\rightarrow 5\,^2D_{3/2}$	E_{th}-10	3.34325(+4)	-1.80003(+6)	-2.20691(+6)	-1.00100(+6)	2.85105(+0)	-4.30465(+2)	-1.15886(+4)
	10-1000	3.05952(+2)	6.00028(+1)			2.10280(-1)	9.57810(-1)	1.04340(-1)
$6\,^2P_{1/2}\rightarrow 5\,^2D_{5/2}$	E_{th}-10	-5.22447(+0)	3.10720(+2)	-1.01916(+3)	1.85859(+3)	1.63000(-3)	1.06660(-1)	7.94629(+1)
	10-1000	2.26774(+0)	9.94330(-1)			9.25200(-2)	8.52810(-1)	2.75050(-1)
$6\,^2P_{3/2}\rightarrow 5\,^2D_{3/2}$	E_{th}-10	-1.81659(+1)	1.04951(+3)	1.09186(+3)	9.36400(+2)	-1.10300(-2)	1.59657(+0)	6.41960(+1)
	10-1000	3.63964(+1)	7.58185(+0)			2.23660(-1)	1.09351(+0)	1.27910(-1)
$6\,^2P_{3/2}\rightarrow 5\,^2D_{5/2}$	E_{th}-10	-2.99876(+1)	1.92919(+3)	1.88665(+4)	-1.28987(+4)	2.86900(-2)	-7.93650(-1)	3.84900(+1)
	10-1000	1.01720(+2)	1.74512(+1)			7.95800(-2)	3.38820(-1)	3.27900(-2)
$6\,^2P_{1/2}\rightarrow 7\,^2S_{1/2}$	E_{th}-17.469	-6.33231(+0)	1.72429(+2)	4.49555(+2)	-1.23994(+2)	1.24310(-1)	4.36510(-1)	8.35339(+0)
	17.46-1000	2.82005(+1)	2.52613(+0)			2.45200(-1)	3.03550(-1)	1.41200(-2)
$6\,^2P_{3/2}\rightarrow 7\,^2S_{1/2}$	E_{th}-18	7.80726(+1)	-2.19120(+3)	-5.78967(+3)	1.72785(+3)	-1.37274(+0)	-5.45403(+0)	-1.02086(+2)
	18-1000	3.93319(+1)	3.75098(+0)			3.21380(-1)	4.21410(-1)	2.09200(-2)
$6\,^2P_{1/2}\rightarrow 7\,^2P_{1/2}$	E_{th}-2	-2.82682(+1)	6.84644(+2)			3.46490(-1)	-1.15744(+1)	1.94725(+2)
	2-20	-5.78802(+0)	9.76577(+1)	2.16311(+2)	-8.06914(+1)	2.82200(-2)	-8.37660(-1)	1.77880(+1)
	20-1000	8.07560(-1)	3.92818(+0)			-5.53500(-2)	1.67660(-1)	2.86260(-1)
$6\,^2P_{1/2}\rightarrow 7\,^2P_{3/2}$	E_{th}-4	-2.17447(+1)	5.37095(+2)			-2.19027(+0)	6.68373(+1)	1.51889(+2)
	4-38	-5.64840(-1)	1.28549(+1)	9.58730(-1)		5.68800(-2)	6.17730(-1)	4.87153(+0)
	38-1000	5.05736(+0)	-9.50000(-3)			4.16750(-1)	1.67218(+0)	-4.56000(-3)
$6\,^2P_{3/2}\rightarrow 7\,^2P_{1/2}$	E_{th}-4	-4.92872(+0)	1.17108(+2)			-1.07114(+0)	2.98189(+1)	6.00588(+1)
	4-38	-5.47170(-1)	1.01234(+1)	3.42590(-1)		3.46800(-2)	1.08921(+0)	7.20467(+0)
	38-1000	3.69653(+0)	1.02690(-1)			5.69960(-1)	2.48831(+0)	6.31500(-2)
$6\,^2P_{3/2}\rightarrow 7\,^2P_{3/2}$	E_{th}-10	-1.26794(+1)	3.40635(+2)	-7.44447(+2)	1.06779(+3)	2.84000(-3)	1.60920(+0)	1.25685(+1)
	10-1000	-7.20130(-1)	1.58638(+1)			5.74800(-2)	-9.17200(-2)	1.16644(+0)
$6\,^2P_{1/2}\rightarrow 6\,^2D_{3/2}$	E_{th}- 20	-7.48077(+0)	1.63003(+2)	6.00999(+1)	-8.31549(+0)	3.81300(-2)	1.78989(+0)	4.36812(+0)

	20-1000	1.64241(+1)	1.15391(+0)			2.37080(-1)	2.84530(-1)	9.31000(-3)
$6\,^2P_{1/2} \to 6\,^2D_{5/2}$	E_{th}- 20	-5.60520(-1)	1.22545(+1)	3.15319(+0)		-1.01000(-2)	1.51560(-1)	1.29998(+1)
	20-1000	-1.12070(-1)	3.45750(+0)			-3.29560(-1)	1.10875(+0)	2.32576(+0)
$6\,^2P_{3/2} \to 6\,^2D_{3/2}$	E_{th}-20	-1.15229(+0)	2.57465(+1)	8.63478(+0)		-3.75500(-2)	1.72499(+0)	5.35990(+0)
	20-1000	3.05913(+0)	2.71880(-1)			2.80170(-1)	4.22670(-1)	1.87100(-2)
$6\,^2P_{3/2} \to 6\,^2D_{5/2}$	E_{th}-20	-5.00425(+0)	1.11655(+2)	5.48587(+1)	-1.26310(+1)	1.36700(-2)	1.14937(+0)	3.07386(+0)
	20-1000	1.68845(+1)	1.15261(+0)			2.27290(-1)	2.79520(-1)	8.91000(-3)
$6\,^2P_{1/2} \to 8\,^2S_{1/2}$	E_{th}-2.77	-1.09176(+2)	2.02280(+3)			9.89772(+0)	-1.09805(+2)	1.80775(+3)
	2.77-19.74	1.18767(+0)	1.08428(+1)	1.42266(+1)		3.35360(-1)	2.62250(-1)	7.32109(+0)
	19.74-1000	2.78572(+0)	9.21280(-1)			3.16350(-1)	7.50050(-1)	1.00990(-1)
$6\,^2P_{3/2} \to 8\,^2S_{1/2}$	E_{th}-10.26	8.34850(-1)	-5.78583(+1)	8.23993(+2)	-5.32691(+2)	2.73000(-1)	-9.68456(+0)	1.17467(+2)
	10.26-1000	2.03494(+0)	4.06400(-1)			2.51430(-1)	4.63980(-1)	4.17900(-2)
$6\,^2P_{1/2} \to 8\,^2P_{1/2}$	E_{th}-7.4	-2.56162(+0)	4.85706(+1)	-9.33934(+1)		-1.22830(-1)	4.06463(+0)	-4.84345(+0)
	7.4-1000	-1.32077(+1)	1.69834(+1)	-6.42600(-1)	2.06700(-2)	-9.89970(-1)	-3.17073(+0)	5.58169(+0)
$6\,^2P_{1/2} \to 8\,^2P_{3/2}$	E_{th}-5	-2.29496(+0)	2.53410(+1)	2.19570(+2)		5.22240(-1)	-2.05712(+1)	3.75777(+2)
	5-52.66	-5.76180(-1)	5.14202(+0)	5.01476(+0)	-1.21928(+0)	9.18600(-2)	-1.07973(+0)	1.83002(+1)
	52.66-1000	4.06169(+0)	-5.29800(-2)			1.78177(+0)	6.26467(+0)	-8.46600(-2)
$6\,^2P_{3/2} \to 8\,^2P_{1/2}$	E_{th}-5	-8.61480(-1)	1.47360(+1)			-1.91400(-1)	4.14937(+0)	6.48350(+1)
	5-1000	-8.42193(+0)	4.76599(+1)			-9.58002(+0)	2.85551(+1)	1.43035(+2)
$6\,^2P_{3/2} \to 8\,^2P_{3/2}$	E_{th}-7.4	-2.82501(+0)	3.97355(+1)	1.44745(+2)		-3.75400(-2)	1.21709(+0)	3.46632(+1)
	7.4-1000	2.63920(+0)	1.59998(+0)	4.39100(-2)		2.66040(-1)	5.53000(-1)	8.00030(-1)
$6\,^2P_{1/2} \to 7\,^2D_{3/2}$	E_{th}-20	-2.10313(+0)	3.27595(+1)	1.71330(+1)		6.64000(-2)	1.29513(+0)	4.36387(+0)
	20-1000	3.66588(+0)	1.12300(-1)			2.50940(-1)	2.06710(-1)	2.65000(-3)
$6\,^2P_{1/2} \to 7\,^2D_{5/2}$	E_{th}-10	-8.37520(-1)	1.29843(+1)	7.50785(+0)		-3.90300(-2)	-1.30627(+0)	6.42257(+1)

	10-100	5.93480(-1)	1.10329(+0)	1.37770(-1)		7.33000(-1)	9.23470(-1)	4.53816(+0)
	100-1000	3.59138(+0)	2.23690(-1)			2.58975(+0)	9.58481(+0)	5.44360(-1)
$6\,^2P_{3/2} \rightarrow 7\,^2D_{3/2}$	E_{th}-10	-4.36639(+0)	8.60911(+1)	-2.49955(+2)	1.65608(+2)	-9.22490(-1)	2.838514(+1)	-6.28016(+1)
	10-1000	2.39501(+0)	9.59500(-2)			1.01691(+0)	1.13083(+0)	2.05900(-2)
$6\,^2P_{3/2} \rightarrow 7\,^2D_{5/2}$	E_{th}-20	-1.71559(+0)	2.85150(+1)	-6.53913(+0)	7.56328(+0)	2.87100(-2)	1.15020(+0)	2.03200(+0)
	20-1000	5.18489(+0)	1.41580(-1)			3.36410(-1)	2.96650(-1)	3.05000(-3)
$5\,^2D_{3/2} \rightarrow 7\,^2S_{1/2}$	E_{th}-5	-7.41063(+0)	7.70933(+2)	3.22554(+2)		-2.93000(-3)	1.15221(+0)	3.12738(+2)
	5-1000	3.01710(+0)	2.38840(-1)			9.69300(-2)	7.06720(-1)	4.12000(-2)
$5\,^2D_{5/2} \rightarrow 7\,^2S_{1/2}$	E_{th}-2	-1.36458(+1)	1.36507(+3)	9.24646(+2)		-2.78599(-4)	1.44863(+0)	5.97995(+2)
	2-5	-8.63332(+0)	8.65601(+2)	3.76108(+2)		-2.48000(-3)	1.20541(+0)	3.68284(+2)
	5-1000	2.63896(+0)	2.37130(-1)			8.82100(-2)	6.49560(-1)	4.33400(-2)
$5\,^2D_{3/2} \rightarrow 7\,^2P_{1/2}$	E_{th} -10	-1.72210(+0)	7.38337(+1)	1.12253(+1)	1.70897(+1)	-1.92600(-2)	2.30928(+0)	9.40030(+0)
	10-200	3.69596(+0)	5.25330(-1)			1.29010(-1)	4.29340(-1)	2.77800(-2)
	200-1000	1.14613(+2)	4.48626(+0)			1.03915(+1)	9.51289(+0)	2.27110(-1)
$5\,^2D_{3/2} \rightarrow 7\,^2P_{3/2}$	E_{th} -10	-1.18166(+0)	4.735687(+1)	8.16815(+1)		-5.37000(-3)	4.35030(-1)	6.47131(+1)
	10-1000	1.97650(+0)	2.15640(-1)			2.67490(-1)	1.02805(+0)	5.84600(-2)
$5\,^2D_{5/2} \rightarrow 7\,^2P_{1/2}$	E_{th} -5	-1.23312(+0)	5.37771(+1)	-6.18464(+1)		7.09000(-3)	-7.67530(-1)	1.96665(+2)
	5-1000	1.31824(+1)	2.30996(+1)			-1.95581(+0)	8.93692(+1)	8.43951(+1)
$5\,^2D_{5/2} \rightarrow 7\,^2P_{3/2}$	E_{th} -10	-1.90165(+0)	7.41776(+1)	1.74470(+2)	-9.20725(+1)	-2.11300(-2)	2.13691(+0)	2.26258(+1)
	10-1000	3.83374(+0)	4.97500(-1)			1.49370(-1)	5.11640(-1)	2.93100(-2)
$5\,^2D_{3/2} \rightarrow 6\,^2D_{3/2}$	E_{th} -7	-5.84829(+1)	2.17957(+3)	-1.56510(+3)	2.14209(+4)	-1.56800(-2)	1.70499(+0)	1.34007(+2)
	7-100	1.13806(+1)	-4.95130(-1)			-5.11300(-2)	7.48990(-1)	-6.97600(-2)
	100-1000	1.21490(+2)	1.25497(+0)			3.34702(+0)	5.24149(+0)	3.70900(-2)
$5\,^2D_{3/2} \rightarrow 6\,^2D_{5/2}$	E_{th} -7	-2.20551(+0)	7.71262(+1)	1.52091(+2)	-4.74542(+2)	2.90500(-2)	-2.28254(+0)	9.42698(+1)

	7-200	6.07820(-1)	3.40231(+0)			-2.20580(-1)	1.86932(+0)	2.56349(+0)
	200-1000	1.30279(+1)	7.05820(-1)			3.46212(+0)	1.09328(+1)	4.47750(-1)
$5\,^2D_{5/2} \to 6\,^2D_{3/2}$	E_{th} -3	-2.28019(+0)	8.31402(+1)	-1.03413(+1)		3.24900(-2)	-2.69011(+0)	1.25430(+2)
	3-20	-1.14308(+0)	4.24711(+1)	-3.50233(+1)	2.86598(+1)	9.14000(-3)	-9.30570(-1)	5.59756(+1)
	20-1000	1.60978(+0)	3.88800(-1)			3.60500(-1)	2.55015(+0)	4.32250(-1)
$5\,^2D_{5/2} \to 6\,^2D_{5/2}$	E_{th} -7	-2.88976(+1)	1.05476(+3)	-5.89435(+2)	9.88064(+3)	-7.08000(-3)	7.53360(-1)	7.12334(+1)
	7-100	1.91160(+1)	-8.61620(-1)			-8.98600(-2)	1.35104(+0)	-1.31880(-1)
	100-1000	1.21647(+2)	1.10581(+0)			3.00657(+0)	5.65834(+0)	3.22200(-2)
$5\,^2D_{3/2} \to 8\,^2S_{1/2}$	E_{th} -10	-9.63800(-1)	2.40987(+1)	7.86634(+1)	-1.04857(+2)	2.71800(-1)	-1.52150(+1)	3.06082(+2)
	10-1000	2.94998(+2)	2.03599(+2)	4.94980(-1)		3.08624(+2)	1.52242(+3)	9.99077(+2)
$5\,^2D_{5/2} \to 8\,^2S_{1/2}$	E_{th} -10	-1.97168(+0)	4.32060(+1)	3.20146(+2)	-4.51695(+2)	8.30750(-1)	-4.41944(+1)	7.86973(+2)
	10-1000	1.17820(+0)	9.20440(-1)			1.18501(+0)	5.97134(+0)	4.23247(+0)
$5\,^2D_{3/2} \to 8\,^2P_{1/2}$	E_{th} -10	-2.04412(+0)	5.12059(+1)	-4.49655(+1)	5.86830(+1)	-5.33810(-1)	2.51204(+1)	3.91611(+1)
	10-1000	9.84300(-1)	2.39900(-2)			6.43390(-1)	9.93270(-1)	7.37000(-3)
$5\,^2D_{3/2} \to 8\,^2P_{3/2}$	E_{th}-10	-6.81230(-1)	1.77519(+1)	-3.38075(+1)	7.06460(+1)	1.95000(-2)	-1.83936(+0)	1.09202(+2)
	10-1000	1.04772(+0)	2.07030(-1)			1.35044(+0)	5.12909(+0)	5.90810(-1)
$5\,^2D_{5/2} \to 8\,^2P_{1/2}$	E_{th}-10	-2.66340(-1)	7.28399(+0)	-2.28273(+1)	3.37807(+1)	-2.83000(-3)	-8.26640(-1)	7.90375(+1)
	10-1000	1.52170(-1)	8.84700(-2)			1.76130(-1)	4.11126(+0)	1.62459(+0)
$5\,^2D_{5/2} \to 8\,^2P_{3/2}$	E_{th}-10	-3.61622(+0)	7.94899(+1)	1.59553(+2)	7.51958(+1)	-3.22270(-1)	9.27644(+0)	3.75749(+2)
	10-200	1.31238(+0)	2.09400(-2)			8.41370(-1)	1.45256(+0)	-3.19000(-3)
	200-1000	-7.87000(-2)	1.09849(+0)			-7.87087(+0)	4.55774(+0)	6.48400(-1)
$5\,^2D_{3/2} \to 7\,^2D_{3/2}$	E_{th}-15	-3.54844(+0)	8.21626(+1)	-3.98165(+1)		-7.46700(-2)	2.67193(+0)	1.11355(+1)
	15-100	-8.65380(-1)	3.48944(+0)			-2.04770(-1)	1.00370(-1)	1.05356(+0)
	100-1000	-3.07445(+0)	2.07822(+0)			-1.82214(+0)	-2.31360(-1)	6.04100(-1)

$5\,^2D_{3/2} \rightarrow 7\,^2D_{5/2}$	E_{th}-5	-1.47357(+0)	3.28367(+1)	1.62633(+1)	-6.22228(+1)	9.80200(-2)	-6.03429(+0)	1.42364(+2)
	5-1000	4.04510(-1)	1.83599(+0)			-8.62890(-1)	6.51617(+0)	7.75636(+0)
$5\,^2D_{5/2} \rightarrow 7\,^2D_{3/2}$	E_{th}-5	-3.55301(+0)	8.06509(+1)	-1.60909(+1)		3.11490(-1)	-1.95893(+1)	4.72709(+2)
	5-1000	4.41010(-1)	1.17715(+0)			-1.00978(+0)	8.35644(+0)	7.43924(+0)
$5\,^2D_{5/2} \rightarrow 7\,^2D_{5/2}$	E_{th}-5	-9.62600(-2)	-3.21609(+1)	8.11083(+2)	-8.68078(+2)	4.82900(-2)	-2.69754(+0)	5.16461(+1)
	5-60	-4.04911(+0)	7.53279(+0)			-5.70700(-2)	-1.36568(+0)	2.72353(+0)
	60-1000	-6.94110(-1)	3.43766(+0)			-2.35860(-1)	2.01590(-1)	1.08731(+0)
$7\,^2S_{1/2} \rightarrow 7\,^2P_{1/2}$	E_{th}-7.1	6.06873(+0)	-2.23182(+3)	1.29277(+5)	-1.20099(+5)	8.54600(-2)	5.12820(-1)	1.00504(+2)
	7.1-1000	-7.13603(+1)	9.66725(+2)	2.81774(+1)	-4.72710(-1)	-3.17400(-2)	5.63110(-1)	1.42125(+0)
$7\,^2S_{1/2} \rightarrow 7\,^2P_{3/2}$	E_{th}-10.306	9.68591(+0)	-2.74894(+3)	1.45117(+5)	-1.20369(+5)	5.58700(-2)	9.40000(-2)	6.03657(+1)
	10.30-1000	1.91947(+3)	7.73600(+1)			7.61810(-1)	1.36563(+0)	2.71100(-2)
$7\,^2S_{1/2} \rightarrow 8\,^2P_{1/2}$	E_{th}-7	-6.18459(+0)	1.98592(+2)	-1.35508(+2)	4.75804(+2)	-1.12100(-2)	1.46048(+0)	2.34710(+1)
	7-160	9.20540(-1)	3.44851(+0)			9.17000(-3)	2.13240(-1)	2.19610(-1)
	160-1000	8.70751(+1)	4.49350(+0)			3.31753(+0)	6.11026(+0)	2.37240(-1)
$7\,^2S_{1/2} \rightarrow 8\,^2P_{3/2}$	E_{th}-10	-8.00554(+0)	2.44130(+2)	2.04260(+2)	4.18490(+1)	-4.21000(-3)	8.02140(-1)	1.80637(+1)
	10-1000	8.90326(+0)	2.00373(+0)			8.54900(-2)	3.90120(-1)	5.64200(-2)
$7\,^2P_{1/2} \rightarrow 6\,^2D_{3/2}$	E_{th}-10	3.01590(+4)	-7.05174(+6)	1.36661(+7)	-1.6008(+7)	-8.21255(+0)	-3.28379(+2)	-1.62175(+3)
	10-1000	1.50803(+3)	5.82155(+2)			6.90900(-2)	8.18900(-1)	1.91390(-1)
$7\,^2P_{1/2} \rightarrow 6\,^2D_{5/2}$	E_{th}-3.23	-4.53128(+2)	1.08874(+5)	3.10215(+5)		5.52891(+0)	-4.63543(+2)	3.15131(+4)
	3.23-40	9.29430(-1)	2.82860(+0)	1.50038(+1)	-4.40228(+0)	5.29900(-2)	-2.77990(-1)	8.52520(-1)
	40-1000	3.28018(+1)	3.06182(+0)			8.94000(-2)	1.37057(+0)	1.14550(-1)
$7\,^2P_{3/2} \rightarrow 6\,^2D_{3/2}$	E_{th}-10	9.21824(+2)	-2.42064(+5)	1.17680(+5)		-1.27035(+0)	-1.15233(+2)	-7.43667(+2)
	10-1000	1.64259(+2)	6.21643(+1)			5.79200(-2)	7.84850(-1)	1.86860(-1)
$7\,^2P_{3/2} \rightarrow 6\,^2D_{5/2}$	E_{th}-15	4.88437(+3)	-1.19547(+6)	3.03212(+5)		-1.28089(+0)	-5.77624(+1)	-5.05325(+2)

	15-1000	1.29020(+5)	3.42827(+4)			6.91858(+0)	6.86487(+1)	1.15677(+1)
$7\,^2P_{1/2}\rightarrow 8\,^2S_{1/2}$	E_{th}-6.177	1.30131(+3)	-2.34051(+5)	1.06553(+7)	-1.34349(+7)	1.32783(+0)	7.78687(+0)	8.66661(+3)
	6.177-78.60	2.27917(+2)	-3.04416(+1)			2.03790(-1)	3.95150(-1)	-6.05400(-2)
	78.60-1000	1.73077(+3)				2.71971(+0)	2.66030(+0)	-1.49400(-2)
$7\,^2P_{3/2}\rightarrow 8\,^2S_{1/2}$	E_{th}-6.177	2.24415(+1)	-4.22351(+3)	2.02601(+5)	-2.58639(+5)	3.07500(-2)	-1.36460(-1)	1.59618(+2)
	6.177-78.60	-9.14789(+1)	5.62220(+2)	3.05713(+1)		-6.81900(-2)	2.46280(-1)	1.16698(+0)
	78.60-1000	1.795320(+3)				2.72054(+0)	2.72290(+0)	-1.51700(-2)
$7\,^2P_{1/2}\rightarrow 7\,^2D_{3/2}$	E_{th}-5.0	-3.43819(+1)	1.65721(+3)			1.27340(-1)	5.94389(+0)	1.19659(+1)
	5-100	1.12278(+3)	2.25868(+3)			2.37737(+0)	3.39762(+1)	1.85896(+1)
	100-1000	1.05679(+4)	1.05417(+3)			7.38710(+1)	1.14151(+2)	6.21019(+0)
$7\,^2P_{1/2}\rightarrow 7\,^2D_{5/2}$	E_{th}-3.0	-2.69989(+1)	1.29590(+3)			-1.16000(-3)	5.45188(+0)	3.48722(+2)
	3.0-50	-2.79090(-1)	3.09408(+1)			-4.42400(-2)	1.01947(+0)	5.15359(+0)
	50-1000	1.27838(+1)	1.37920(+0)			4.56670(-1)	2.24768(+0)	1.78640(-1)
$7\,^2P_{3/2}\rightarrow 7\,^2D_{3/2}$	E_{th}-5	-1.53928(+1)	7.15356(+2)	2.36859(+3)		-3.68000(-2)	8.14815(+0)	1.36200(+2)
	5-100	3.99681(+0)	5.45012(+0)			4.77500(-2)	5.30140(-1)	2.76480(-1)
	100-1000	7.68465(+1)	5.21352(+0)			3.04636(+0)	4.68300(+0)	1.90060(-1)
$7\,^2P_{3/2}\rightarrow 7\,^2D_{5/2}$	E_{th}-5	-3.66643(+1)	1.83328(+3)			6.79600(-2)	6.34353(+0)	1.20050(+1)
	5-100	2.29302(+1)	2.36068(+1)			5.74100(-2)	4.67670(-1)	1.66950(-1)
	100-1000	8.24526(+2)	5.46920(+1)			6.13125(+0)	7.57702(+0)	2.86310(-1)
$6\,^2D_{3/2}\rightarrow 8\,^2P_{1/2}$	E_{th}-3	-3.16065(+1)	2.23519(+3)			-2.89300(-2)	1.47167(+1)	4.87025(+1)
	3-100	5.03628(+0)	1.53875(+1)			6.42000(-3)	5.14930(-1)	4.37110(-1)
	100-1000	1.58024(+2)	1.14022(+1)			3.25325(+0)	5.10711(+0)	2.25840(-1)
$6\,^2D_{3/2}\rightarrow 8\,^2P_{3/2}$	E_{th}-3	-2.15732(+1)	1.37407(+3)	8.84644(+3)		-2.92200(-2)	6.03396(+0)	6.21838(+2)

	3-100	2.26064(+0)	3.42837(+0)			2.61200(-2)	5.46410(-1)	3.87180(-1)
	100-1000	5.45463(+1)	9.63610(-1)			5.0074(+0)	6.07575(+0)	7.02400(-2)
$6\,^2D_{5/2} \rightarrow 8\,^2P_{1/2}$	E_{th}-3	-5.98379(+0)	4.17200(+2)	5.73101(+2)		1.69200(-2)	-6.48390(-1)	4.72555(+2)
	3-1000	2.11872(+0)	5.89500(-1)			1.19620(-1)	1.28598(+0)	2.51400(-1)
$6\,^2D_{5/2} \rightarrow 8\,^2P_{3/2}$	E_{th}-3	-3.03230(+1)	2.17263(+3)	-2.99295(+3)		-6.15300(-2)	1.11950(+1)	2.56480(+1)
	3-100	2.03736(+1)	2.69251(+1)			5.29100(-2)	1.27066(+0)	6.19760(-1)
	100-1000	2.47160(+2)	9.25713(+0)			5.50604(+0)	6.46856(+0)	1.59710(-1)
$8\,^2S_{1/2} \rightarrow 8\,^2P_{1/2}$	E_{th}-16.49	-1.77629(+2)	2.77388(+4)	3.56742(+2)		1.74840(-1)	2.68115(+0)	1.48315(+1)
	16.49-1000	1.07471(+4)	2.16123(+3)			1.37810(+0)	5.90059(+0)	6.72870(-1)
$8\,^2S_{1/2} \rightarrow 8\,^2P_{3/2}$	E_{th}-16.49	-2.05555(+3)	3.11322(+5)			1.07884(+0)	1.49198(+1)	8.46410(+1)
	16.49-1000	1.92194(+5)	3.93134(+4)			1.26612(+1)	5.36956(+1)	6.18089(+0)
$8\,^2P_{1/2} \rightarrow 7\,^2D_{3/2}$	E_{th}-5.270	-1.35507(+4)	7.81326(+6)	-5.80704(+6)	3.04531(+7)	1.35986(+0)	5.69190(+1)	9.85152(+2)
	5.270-1000	1.31767(+4)	4.10770(+3)	6.68893(+0)		1.47080(-1)	1.54879(+0)	3.16440(-1)
$8\,^2P_{1/2} \rightarrow 7\,^2D_{5/2}$	E_{th}-3.119	-1.02207(+2)	7.64402(+4)	-3.50116(+5)	5.79979(+6)	3.11700(-1)	-9.22361(+0)	5.43112(+3)
	3.119-72.59	1.07853(+1)	1.28208(+2)			1.05100(-1)	8.31300(-2)	1.86080(+0)
	72.59-1000	1.50245(+1)	2.74337(+1)			1.51300(-2)	2.33170(-1)	3.78580(-1)
$8\,^2P_{3/2} \rightarrow 7\,^2D_{3/2}$	E_{th}- 5.270	-1.69120(+2)	1.13364(+5)	2.51122(+4)		9.59400(-2)	9.27579(+0)	1.31871(+2)
	5.270-1000	7.21140(+2)	1.54499(+2)	4.69600(-2)		7.55200(-2)	7.48270(-1)	1.06290(-1)
$8\,^2P_{3/2} \rightarrow 7\,^2D_{5/2}$	E_{th}- 8.905	-6.90680(+4)	4.20536(+7)	4.55978(+7)	-4.04026(+7)	6.59810(+0)	3.27472(+2)	7.07566(+3)
	8.905-1000	7.49744(+3)	3.48156(+3)	1.18474(+1)		8.23300(-2)	9.90040(-1)	3.10010(-1)

2.3 Electron impact ionization cross sections of Cesium

In the present C-R model we need electron impact ionization cross section data of the ground ($6^2S_{1/2}$) as well as the excited $n^2S_{1/2}$, $n'^2P_{1/2,3/2}$, $n''^2D_{3/2,5/2}$ (where n=7,8, n'=6,7,8 and n″=5,6,7) states. Most of the available results in the literatures for ionization cross sections of cesium are either from the ground state or from fine structure unresolved excited states [138–140, 161]. Only few theoretical calculations have reported ionization cross section results for $6^2P_{1/2}$ and $6^2P_{3/2}$ fine structure states [63, 141]. Since our RDW code can calculate at present only excitation cross sections, we have used the available FAC code of Gu [143] to calculate the ionization cross sections. This code has been applied earlier also to calculate the electron impact ionization cross section for various neutral atoms [162, 163]. In the FAC code, there are three methods which one can use *viz.* Coulomb-Born-exchange (CBE) approximation, relativistic distorted wave (DW) theory and binary-encounter-dipole (BED) theory to calculate electron impact ionization cross sections. Since CBE method is simply a Born level calculation one could use the DW and BED methods. However, Gu [143] in his paper recommended the use of BED method and explained it to be the most consistent for ionization cross section results. For the present work also, we have tested and found that among all available methods in FAC, the BED results are in the best agreement with the available calculations and measurements and therefore, used it to calculate the ionization cross section of all the fine structure states considered in the C-R Model.

In figure 2.17, we have presented our calculated ionization cross section of the ground ($6^2S_{1/2}$) and ($6^2P_{1/2,3/2}$) states, where some other results are also available for comparison. In this figure we have compared our results with recently reported relativistic B-spline R-matrix (BSR-311) results of Zatsarinny *et al.* [63] and non-relativistic convergent close coupling (CCC) results of Łukomski *et al.* [141]. For $6^2S_{1/2}$ state the energy dependence of the cross section data was experimentally determined by Tate and Smith [161] long back. Łukomski *et al*. [141] *and* Zatsarinny *et al*. [63] have compared their CCC and DBRS-311 calculations with the data of Tate and Smith by normalizing it to their calculation in the low energy region (up to 10-20eV) for best fit. We have also included in figure 2.17 the available experimental results of Tate and Smith [161] which are normalized with CCC [63] calculations ($6^2S_{1/2}$).

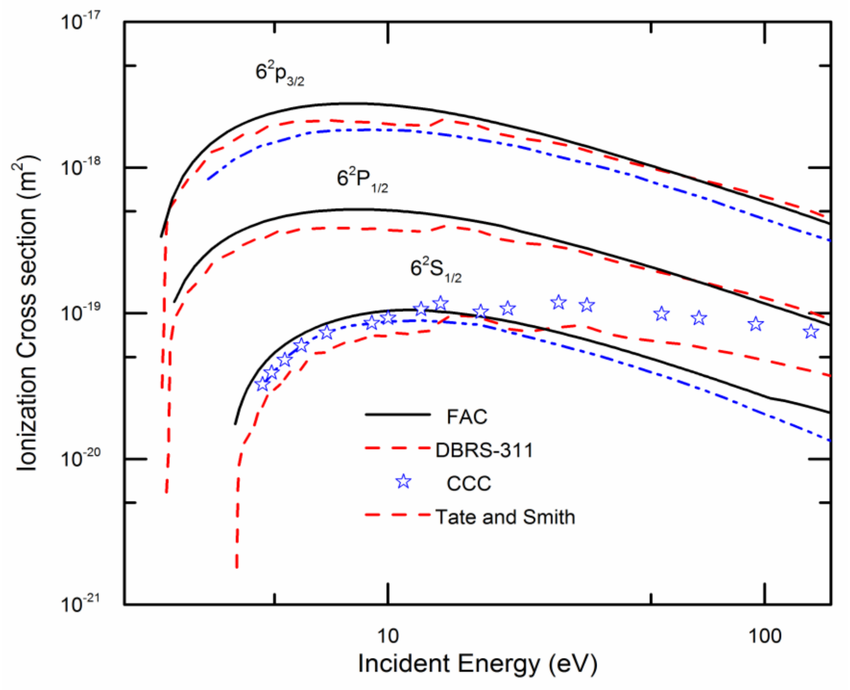

Figure 2.17: Electron impact ionization cross section of $6^2S_{1/2}$ and $6^2P_{1/2,3/2}$ states. Our FAC results are compared with the full relativistic DBRS-311 method results [63], non-relativistic convergent close coupling (CCC) approach [141] and Tate and Smith [161] normalized to CCC [141]. The cross sections presented in the figure are multiplied by a factor of 2 and 10 respectively for the $6^2S_{1/2}$ and $6^2P_{1/2,3/2}$ states.

First, we compare in the figure 2.17 the different results for the ionization of the ground $6^2S_{1/2}$ state. We observe that in the energy range up to 15-20 eV, since CCC results are normalized to the experimental result they both match completely and the BED and DBRS-311 results are higher and lower respectively nearly by a factor of 1.2 with respect to the CCC calculations. Further, in the higher energy range we find that the BED results lie between DBRS-311 and CCC calculations and the experimental results are too high (which may be due to the additional contributions of the inner shell ionizations). For the ionization of $6^2P_{1/2}$ state, the BED calculations are in close agreement with DBRS-311 results with the maximum difference of 25% up to incident energy 15 eV and within 10% at higher energies while the CCC calculations are not available. Similar behavior is observed for the ionization of $6^2P_{3/2}$ state and the CCC results appear to agree well with DBRS at ~10 eV, but differ more at lower and higher energies.

In figure 2.18, we have presented only our calculated ionization cross sections for different states as there are no other results available for comparison.

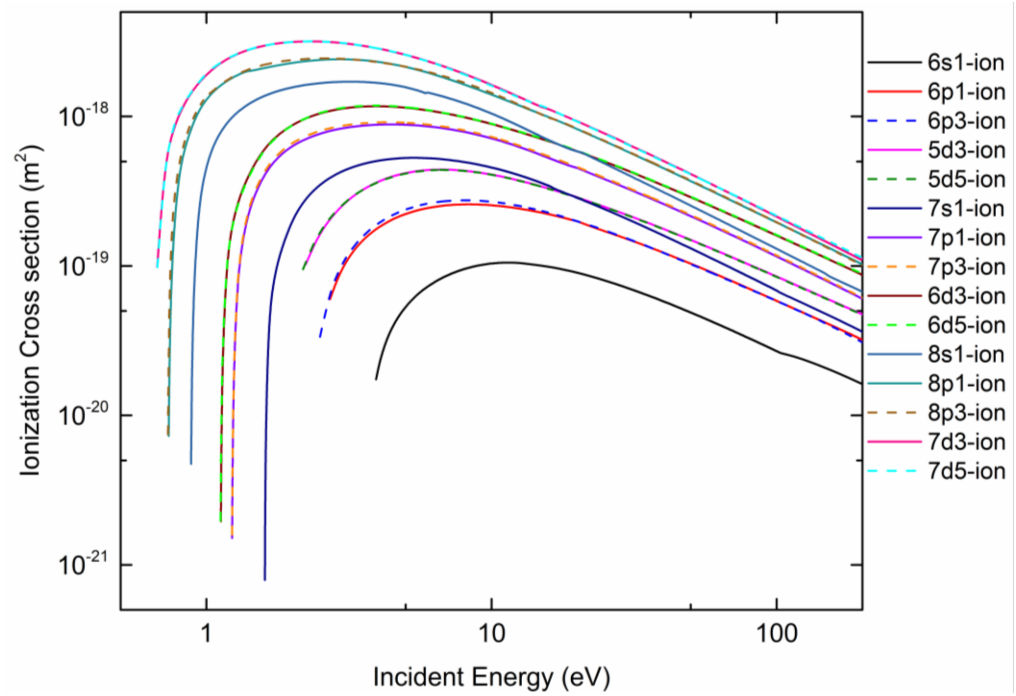

Figure 2.18: Electron impact ionization cross section of ground and all other excited states up to $7^2D_{3/2,5/2}$ calculated from FAC code.

2.4 Collisional radiative model for H_2-Cs plasma

In the previous section, we have presented our complete set of relativistic excitation cross sections for different fine structure transitions in the wide range of electron energy. As an application of these cross sections, we develop a fine structure resolved C-R model to analyze the low-pressure hydrogen cesium plasma. The model includes the 14 fine-structure levels of Cs in addition to the ground states of atom and singly charged Cs^+ ion as given in the figure 2.1. All these levels are interconnected through collisional and radiative transitions occurring in the plasma [112]. The present model includes various population transfer mechanisms among fine structure levels such as electron impact excitation, ionization, radiative decay along with their reverse processes viz. electron impact de-excitation and three body recombination. Another important process which has also been included in the present hydrogen-cesium plasma model is the mutual neutralization of Cs^+ with H^- ion. Since the mutual neutralization cross sections are expected to be quite large, it will considerably affect the population of the ground and excited states of cesium. The particle balance equation for an excited level j can be expressed as follows;

$$\sum_{\substack{i\\ i\neq j}} k_{ij}(T_e)n_i n_e + \sum_{\substack{i\\ i>j}} A_{ij}n_i - \sum_{\substack{i\\ i\neq j}} k_{ji}(T_e)n_j n_e - \sum_{\substack{i\\ i<j}} A_{ji}n_j \\ - n_j n_e k_{j+}(T_e) + n_+ n_{H^-} k_{mutual\,neut.,j} = 0 \qquad (2.4.1)$$

Various terms and symbols used here in this equation are already explained in the Chapter 1 while defining the equation (1.3.1). Additional notations n_+ and n_{H^-} represent respectively the Cs ion and H$^-$ ion densities. $k_{mutual\ neut.,j}$ is the rate coefficient for the mutual neutralization of Cs$^+$ ion with negative H$^-$ ion.

The electron impact excitation rates for different transitions have been taken as calculated in section 2.2.2 using our cross sections and Maxwellian electron energy distribution function. The required ionization cross sections from the ground as well as the excited states are taken as calculated in see section 2.3 using the relativistic FAC package [143]. Rate coefficients for ionization process k_{j+} can be calculated by replacing upper state by ionization level in the equation 2.2.1. Reverse processes such as de-excitation and three body recombination i.e. a collision between two electrons and an ion results as recombination of an electron and ion have been taken into account through the principle of detailed balance [111, 144]. The rate coefficient for the de-excitation via electron collision in terms of excitation cross section is given by

$$k_{ji} = \frac{g_i}{g_j}\sqrt{\frac{2}{m}}\int_{E_{ij}}^{\infty} \sigma_{ij}(E)\; E\; F_x(E-E_{ij})dE \qquad (2.4.2)$$

where g_i and g_j represent respectively the statistical weights for the levels i and j. We have utilized the rate coefficient for three body recombination calculated by using the Saha relation as follows [111]

$$k_{+i} = \frac{g_i}{2g_+}\left(\frac{h^2}{2\pi m T_x}\right)^{3/2}\sqrt{\frac{2}{m}}\int_{E_{i+}}^{\infty} \sigma_{i+}(E)\; E\; F_x(E-E_{i+})dE \qquad (2.4.3)$$

To include the radiative decay among the different states of Cs, the required transition probabilities are taken from the available NIST database [147] and for unavailable data, we have used the values obtained from the present Cs wave function calculations using GRASP code [99]. In the present C-R model, we have utilized the same set same set of mutual neutralization cross sections as used by Wünderlich *et al.* [134] in their C-R model in order to have a meaningful comparison with their results. They took the mutual neutralization cross sections for 6^2S, 6^2P, 7^2S and 5^2D states in the collision energy range 0.01 eV-1 keV from the recent paper by Belyaev *et al.* [164]. Thereafter, the set of coupled rate balance equations (2.4.1) are solved to obtain the population distribution of the fine-structure levels included in the C-R model as a function of input parameters. In the present case, the input parameters are T_e, n_e, n_{H^-} and the densities of Cs atom in ground $n(6^2S)$ as well as ion state $n(Cs^+)$.

The population distribution of various excited levels as a function of input plasma parameters of a C-R model is the prime and most appropriate output for comparing the various C-R models. In the present work, we have compared our all the C-R model results with the values reported by Wünderlich *et al*. [134]. Since the theoretical and experimental results reported in [134] are available for the unresolved fine-structure states, therefore in order to compare with their results we have transformed our fine-structure resolved results for the unresolved states. We have performed two set of calculations one without including mutual neutralization and the other by including it.

In the first set of calculation, we studied the variation of the population densities of 6^2P, 7^2P and 7^2D states as a function of T_e and n_e by fixing the ground state population density $n(6^2S) = 10^{15}$ m^{-3} and $n^+(Cs) = 9\times 10^{15}$ m^{-3} as well as n_{H^-} is taken to be zero. These plasma parameters represent the same ion source that was considered by Wünderlich *et al.* [134]. The dependence of the population of the fine-structure unresolved excited states 6^2P, 7^2P and 7^2D as a function of T_e (1-10 eV) by setting $n_e=10^{17}$ m^{-3} and as a function of n_e (10^{16}-10^{18} m^{-3}) for $T_e=2$ eV has been shown in the figures 2.19 and 2.20 respectively. Figure 2.19 indicates that our populations are significantly higher than Wünderlich *et al.* [134] at low T_e values and as the electron temperature increases both the results get closer in magnitude. This may be due to the fact that as T_e increases the peak of Maxwellian shifts towards higher energies, consequently the rate-coefficients gets relatively higher contributions from high impact energy cross sections. Since at very high energies the RDW cross sections approach to Born approximation results, the results of Wünderlich *et al.* [134] are expected to agree with our calculation. Further, from the figure 2.20 we observe that the population densities as a function of n_e obtained from both the models show similar nature but are very different in magnitude.

In the second set of calculation, the mutual neutralization is switched on (i.e. n_{H^-} is not taken to be zero) and its effect on the population densities is observed. Again we take the ground state population density $n(6^2S) = 10^{15}$ m^{-3} and $n^+(Cs) = 9\times 10^{15}$ m^{-3} . We further fixed the electron density $n_e = 10^{17}$ m^{-3} and electron temperature $T_e = 2$ eV. The population densities of excited states 6^2P, 7^2P and 7^2D as a function of n_{H^-} (10^{14}-10^{18} m^{-3}) are calculated and presented in the figure 2.21. For the low values of the density of negative hydrogen ions (n_{H^-}) around 10^{14}-10^{16} m^{-3}, the population densities of 6^2P, 7^2P and 7^2D states are same with or without mutual neutralization. However, the effect of mutual neutralization on the population densities of 6^2P, 7^2P and 7^2D states is found be significant when n_{H^-} is increased above 10^{16}-10^{17} m^{-3}. The density of negative hydrogen ions is order of 10^{17} m^{-3} for the present hydrogen-cesium plasma [134]. Thus, the effect of mutual neutralization of Cs$^+$ ion with H$^-$ ions should be included in the C-R model for the present study. This point is also highlighted by Wünderlich *et al.* [134].

Overall observation of the results presented in figure 2.19, 2.20 and 2.21, illustrates that the present results from our C-R model are different from the values reported by Wünderlich *et al.* [134]. This is basically due to the use of different set of cross sections by us in our model. Since our theoretical approach of calculating cross sections is more rigorous, we expect that they provide more reliable results.

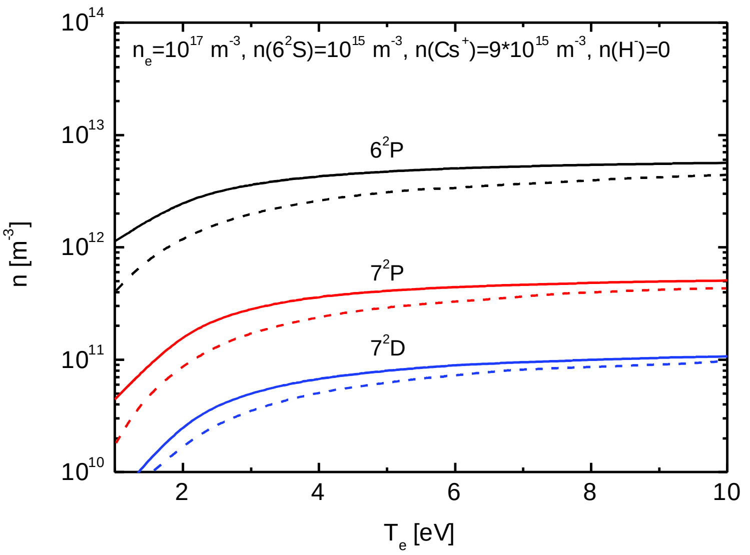

Figure 2.19: Variation of the population densities of the excited states 6^2P, 7^2P and 7^2D as a function of electron temperature. Solid line presents the represent C-R model calculations while the dashed lines are the results from C-R model calculations of Wünderlich *et al.*[134].

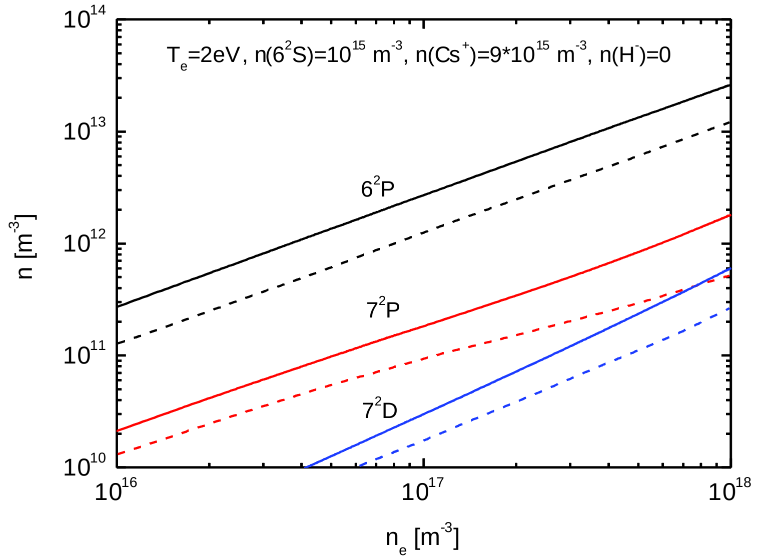

Figure 2.20: Variation of the population densities of the excited states 6^2P, 7^2P and 7^2D as a function of electron density. Solid line represents the present C-R model calculations while the dashed lines are the results from C-R model calculations of Wünderlich *et al.* [134].

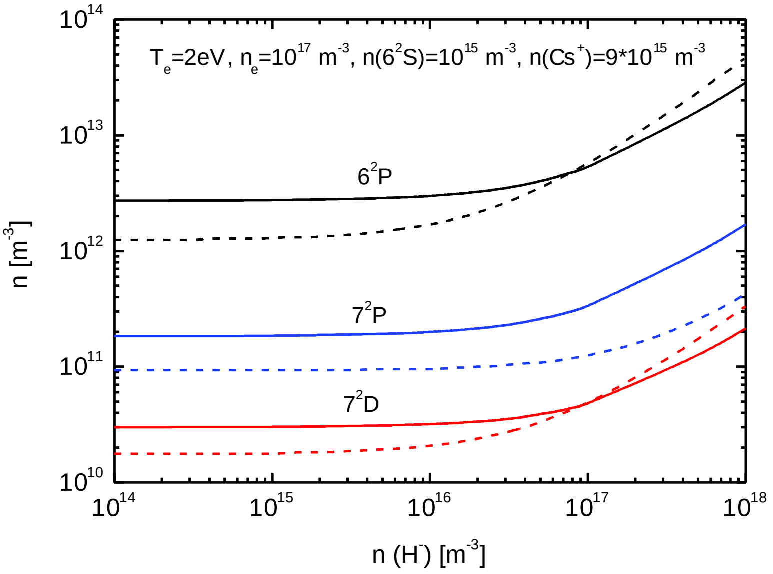

Figure 2.21: Variation of the population densities of the excited states 6^2P, 7^2P and 7^2D as a function of the density of negative hydrogen ions. Solid line represents the present C-R model calculations while the dashed lines are the results from C-R model calculations of Wünderlich *et al.*[134].

In ref [134], in order to extract various plasma parameters, the intensity of emission lines originating from the 6^2P, 7^2P and 7^2D were recorded and corresponding level densities were determined by dividing them by the respective Einstein coefficients. Most probably Wünderlich *et al.* [134] obtained the excited state population by summing the 852.1nm ($6^2P_{3/2}\rightarrow 6^2S_{1/2}$) and 894.3nm ($6^2P_{1/2}\rightarrow 6^2S_{1/2}$) for 6^2P; 459.3 nm ($7^2P_{1/2}\rightarrow 6^2S_{1/2}$) and 455.5nm ($7^2P_{3/2}\rightarrow 6^2S_{1/2}$) for 7^2P; 672.3nm ($7^2D_{3/2}\rightarrow 6^2P_{1/2}$), 698.3nm ($7^2D_{3/2}\rightarrow 6^2P_{3/2}$) and 697.3nm ($7^2D_{5/2}\rightarrow 6^2P_{3/2}$) for 7^2D. These OES measurements were performed for low temperature and pressure conditions of the plasma of the IPP prototype negative hydrogen ion source at the BATMAN test facility [165, 166]. There were two set of measurements along the horizontal line of sight (LOS) with 2.0 cm distance from the plasma grid; first without bias current flowing to the plasma grid and second with the bias potential optimized for reducing the co-extracted electron current without affecting much the extracted negative ion current. Each set further consisted measurements in two plasma regimes; one (XR1) in the upper part of the ion source and the other (XL1) in the lower part of the ion source.

The diagnostic approach of the present model as well as in [134], are coupled with the population results obtained from the OES measurements [134]. In both the cases, the C-R model populations are obtained as a function of input plasma parameters and the best fits of the population values with the OES measurements fix the final plasma parameters.

In the present case, T_e, n_e , n_{H^-} , $n(6^2S)$ and n_+ are the input parameters in our C-R model. In order to check the optimized values of the plasma parameters obtained from OES coupled C-R model approach we have compared our values with the previous measurements from various other techniques [167–171]. These measurements are the Langmuir probe which was used to measure the electron density and electron temperature under the bias and without bias conditions [134, 167] and the laser absorption spectroscopy measurements were performed to determine ground state population density $n(6^2S)$ [168]. The laser detachment [169] and cavity ring-down measurements were used to estimate the negative hydrogen ion densities [170, 171]. The ionization degree of Cs has been taken from some other OES measurements [128]. Details of these measurements can be seen in their publications [167–171]. The measured plasma parameters in the IPP prototype source [[134] and references there in] are listed in the Table 2.3 along with the OES coupled C-R model optimized values of Wünderlich *et al.*[134].

Unfortunately, Wünderlich *et al.* [134] did not report their OES measurements explicitly and therefore to extract the plasma parameters, we have to sum our C-R model fine-structure resolved population for excited 6^2P, 7^2P and 7^2D levels. Usually in these OES coupled C-R model approaches the best way is to optimize the individual emission line (or corresponding excited levels) not the summed values of the fine-structure states [8, 172]. It is due to the fact that every emission line is not equally sensitive to the plasma parameters (eg. T_e, n_e). Therefore adding the intensities reduces the overall dependence on plasma parameters. Moreover all emission lines are not equally intense thus the errors (signal-to-background ratio) will also get added.

We have taken $n_+(Cs) = 9\times n(6^2S)$ in our C-R model as used by Wünderlich *et al.* [134] in their C-R model. Two set of results for the populations of the states of Cs are obtained for each type of measurements *i.e.* with and without mutual neutralization. For the case, with mutual neutralization, electron temperature, electron density and ground state density and n_{H^-} are variables in the C-R model. We have calculated the population of 6^2P, 7^2P and 7^2D states as a function of T_e, n_e $n(6^2S)$ and n_{H^-}. The best match of the calculated population of 6^2P, 7^2P and 7^2D states with the OES measured corresponding values will give us the electron temperature, electron density ground state population and negative hydrogen ion density. Thereafter, the channel of mutual neutralization is switched off i.e n_{H^-} is set to be zero in the C-R model and results without mutual neutralization are obtained for the densities of the same excited sates. The presently obtained densities of 6^2P, 7^2P and 7^2D states along with the OES measurements of Wünderlich *et al.* [134] as well as with their C-R results are shown in the figure 2.22. From the figure, significance of mutual neutralization is observed in our calculation of the population densities in the lower LOS regime while in the upper LOS regime; the densities of the three states are almost same with and without mutual neutralization. The considerable influence of mutual neutralization in lower LOS may be attributed to the low electron density (2.6-3.8×10^{16} m^{-3}) and high density of negative hydrogen ion (4×10^{16} m^{-3}) in this regime. However, in the upper LOS, electron density (9×10^{16}-10^{17} m^{-3}) is large and density of negative hydrogen ion (10^{16} m^{-3}) is low as compared to lower LOS regime and the effect of mutual neutralization is negligible.

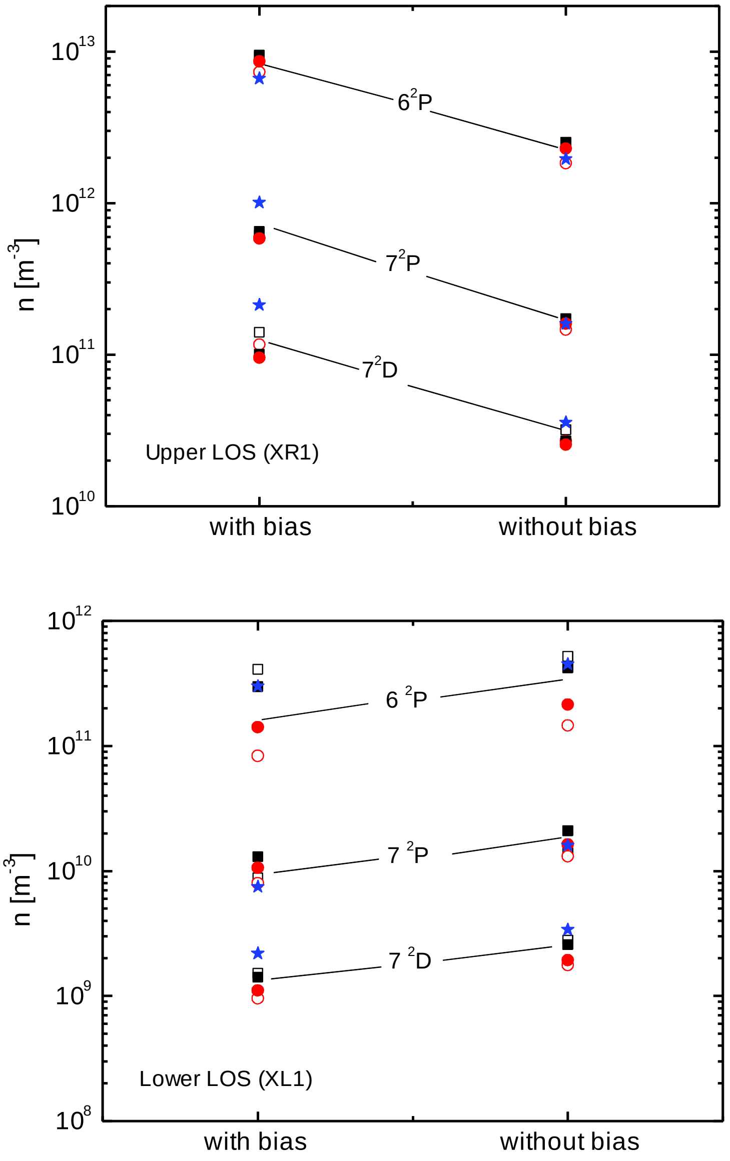

Figure 2.22: Population densities of the three excited states 6^2P, 7^2P and 7^2P. Experimentally obtained results (filled stars) [134]; squares and circles denote population densities obtained with and without mutual neutralization respectively: present C-R model results (filled) and previous C-R model results (open) [134].

The plasma parameters obtained from the best match of the calculated densities of 6^2P, 7^2P and 7^2D states with the OES measurements has been given in the Table 2.3. It may appear from Table 2.3 that our extracted plasma parameters are very similar to those of Wünderlich *et al.* [134]. However, to check this, we have also obtained the population of excited levels at their optimized plasma parameter (as given in Table 2.3) and found that these are very different from our values. Further, the electron temperature and electron density obtained from our C-R model are found within the range associated with the probe measured values [167]. However a significant discrepancies with measurements are present in “n_{H^-} density”, “n(6^2S) density” and its “n(6^2S)upper/n(6^2S)lower” ratio. Similar large deviation can be seen from the C-R model calculations of Wünderlich *et al.* [134]. This is due to the fact that the line of sight (LOS) of the OES measurements of [134] (which is coupled with both the models) is different than the LOS used in the reported other measurements for different plasma parameters [167–171] with which we compared our C-R model results. For example, the OES measurements in Ref. [134] were performed along horizontal LOS parallel to Plasma Grid at 2 cm distance from the grid while the laser absorption spectroscopy (for ground state population density) [168] and the laser detachment [169] and cavity ring-down measurements [170, 171] (for negative hydrogen ion densities) [168] were along a vertical LOS. Therefore the measured cesium densities are not directly comparable to the OES coupled C-R model results. Since, the vertical LOS averages the cesium densities in the upper and the lower part of the ion source in contrast to the two horizontal LOS used in the OES measurement. Thus due to the vertical plasma drift the Cs population distribution can change and the higher values of “n(6 2S) density” and the ratio “n(6 2S)upper/n(6 2S)lower” can be possible [134].

For meaningful comparison and to avoid arbitrariness, it is required that such measurements with the same LOS as of OES (or vice versa) be reported. The present C-R model then can significantly contribute in improving the extracted results by enabling the diagnostic with the individual emission lines rather than the summed fine-structure sub-states values. Further improvement can also be done by including the more emission lines [134] originating from the other fine-structure levels considered in the present model. These lines lie in similar wavelength range as of the emission lines used in [134] and therefore can be recorded. The inclusion of more emission lines improves the analysis by averaging out the uncertainties in the set of cross sections.

From the Table it looks that our extracted plasma parameters are not very different from results of Wünderlich *et al.* [[134]. However, if we look at the comparison of the population distributions which are the direct output of the C-R Model (with input parameters same as of [134]), significant differences from the previous results [134] has been observed through the figures 2.19, 2.20 and 2.21. Further, we also obtained the population of excited levels at the optimized plasma parameter of [134] as presented here in Table 2.3 and found that these are very different from our values.

Table 2.3: Plasma parameters deduced from the present C-R model, previous C-R model calculations of Wünderlich *et al.* [134] as well as their and other experimentally obtained values.

Parameter	**Measurements [**[134]**and references there in]**	**Present calculations**	**Previous calculations** [134]
T_e with bias [eV]			
Lower (XL1)	2.0	2.0	2.0
Upper (XR1)	2.0	2.0	2.5
T_e without bias [eV]			
Lower (XL1)	2.1	2.1	2.0
Upper (XR1)	2.1	2.1	2.2
n_e [m^{-3}]	2.8x10^{16}-10^{17}	2.6x10^{16} - 10^{17}	2.8x10^{16} - 10^{17}
$n_{e, upper}$/ $n_{e, lower}$ (without bias)	2.1	2.37	2.07
$n_{e, upper}$/ $n_{e, lower}$ (with bias)	3.6	3.85	3.57
n(6^{2}S) [m^{-3}]	6x10^{14}– 7x10^{14}	2x10^{14}–3.2x10^{15}	2.4x10^{14}–4.5x10^{15}
n(6^{2}S)$_{upper}$/ n(6^{2}S)$_{lower}$	1-2	with bias=16 without bias= 4.5	with bias= 18.7 without bias= 6.2
n_+/ n(6^{2}S)	9	9	9
n_{H^-} [m^{-3}]	~10^{17}	1-4x10^{16}	1-3x10^{16}

2.5 Conclusions

Electron impact excitation cross sections and rate coefficients have been reported for 82 fine-structure transitions in Cs using the fully relativistic distorted wave theory. Results obtained for excitation from $6^2S_{1/2}$ and $6^2P_{1/2/3/2}$ to few higher lying states when compared with the recent available DBSR-311 calculations show good agreement. Analytic expressions for the fitting of cross sections of all different excitation transitions are also given for the plasma modeling purposes. Electron impact ionization cross sections of all the considered different fine structure states of Cs have been reported. A collisional radiative model involving the complete set of obtained electron impact cross sections has been developed for the analysis of low pressure, low temperature hydrogen-cesium plasma relevant for the development of ITER-NBI system. Our collisional radiative model includes various important population and depopulation mechanisms among the fine-structure states. Since we used improved input cross section data for the dominant production channel in the model among the states in a systematic manner we expect that the various results obtained from the present C-R model should describe the real plasma in a better way. The most important aspect of the present C-R model is that it can perform the diagnostic with the intensity of individual emission lines rather than use the summed fine-structure values as was employed in the previous C-R model and consequently more reliable values of plasma parameters can be determined.

CHAPTER 3

COLLISIONAL RADIATIVE MODEL FOR Ar-O_2 MIXTURE PLASMA

3.1 Introduction

Admixture plasma of rare gas with reactive gases is widely used in many applications such as synthesis of thin films, surface cleaning and etching of metals and semiconductors, surface feature modification of materials and functionalization of carbon nanotubes[2, 173–177]. One of the most commonly used mixture plasma is Ar-O_2 which is often utilized as a source of atomic oxygen. In such plasma the production of atomic oxygen can be influenced by the excited states of argon[178, 179]. To further understand this behavior it is essential to study in more detail how the mixture of O_2 in argon influences the plasma parameters, such as the electron density (n_e) and electron temperature (T_e), which behave differently depending on the quantity of O_2 introduced in the plasma. Therefore, the aim of this Chapter is to study the variations of the plasma n_e and T_e with addition of O_2 in the mixture Ar-O_2 plasma.

Further, it is interesting to study Ar-O_2 mixture plasma as the available studies led to conflicting conclusions. Most of the earlier work [9, 180–186] has focused at low gas pressure plasmas and it was found[9, 181, 182] that the $1s_i$ population of Ar decreases with the increase in O_2 abundance which is in conflict with the other observations[183–186]. The results from reference[180] show that $1s_i$ population increases as concentration of O_2 increases and becomes maximum at 1% and then start deceasing while reference [184] shows that it reaches maximum at around 7% O_2 fraction. Similar observations can be seen in reference[185]. For Ar-O_2 mixture plasma at moderate pressure, Kutasi *et.*

al.[187] and Vries[188] have reported the plasma parameters for microwave generated plasma. Kutasi *et. al.*[187] have reported the Ar 1s_i population and T_e as a function of Ar abundance in O_2 plasma. They found that 1s_i population of Ar increases with increase in Ar fraction and T_e first deceases with growth Ar fraction and then start increasing at approximately 90% fraction of Ar. Vries[188] has estimated the n_e and the T_e of an Ar–O_2 discharge containing 5% O_2 and found a decrease in the n_e with the mixture of a small O_2 percentage while an increase in the T_e. Since the electron heating and power absorption mechanism in microwave discharges are different from radio-frequency, one can expect the behavior of T_e and n_e may be governed by different effects. Therefore, modeling of *rf* discharge Ar-O_2 mixture plasma at medium pressure is still needed to understand adequately the effect of addition of O_2 on plasma parameters T_e and n_e.

Recently, Jogi *et. al.* [179] have reported the optical emission spectroscopy (OES) measurements of Ar-O_2 mixture plasma with varying concentration of O_2. In their experiment, 40 MHz *rf* discharge was introduced in Ar-O_2 (0-5%) mixture at 2 Torr pressure in quartz tube with bore diameter 1.2 cm. Electrical properties as well as the spectra coming from plasma column between electrodes were recorded with TDS S40B oscilloscope and 4000 MDR-23 spectrometer, respectively. Utilizing the obtained electrical properties the calculation of electron density with O_2 fraction was done and it was found to decease with addition of O_2. From spectral measurement of OH rotational band (A-X, O-O), gas temperature was predicted and found increased from 300 to 900 K as O_2 content changed from 0-5%. Intensity was measured for thirteen intense lines originating from 2p_i-1s_i as given in Table 3.2. Using the line intensity ratio, the populations of 1s_i fine structure levels of Ar were obtained. Various results from spectroscopic measurements were extracted by employing simple population-kinetic models. In their model, they used cross sections/rate-coefficients which were obtained from simple approximation methods[189]. As pointed out in our previous studies on pure inert gas plasmas[13, 112, 144], this can significantly influence the accuracy of the extracted plasma parameter results. Thus in the light of their measurements to characterize their Ar-O_2 gas mixture plasma, in the present Chapter, we develop a reliable C-R model which utilizes accurate cross sections or rate coefficients.

Using our C-R model, we first extract the plasma parameters by optimizing the model simulated intensities (as a function of plasma parameters) with the measurements [179]. At these extracted parameters we also compared the population densities of 1s_i fine structure levels with the measurements [179]. Due to relatively longer lifetime, 1s_i states are significantly influenced by the trace addition of O_2 gases and therefore offer a good check for model optimization. Further, we estimated the ground, 1s_i manifolds and cascade (from higher lying states > 2p_i levels) contributions to radiating 2p_i states. Such calculations are of great importance to understand the real involvement of these processes in mixture plasma. In the sections 3.2 and 3.3 respectively, we briefly describe our C-R model and present the results as well as their comparison with the experiment [179]. The Panchen’s notation is used to describe the different atomic states of the argon.

3.2 C-R model for Ar-O_2 plasma

Our C-R Model for Ar-O_2 plasma considered 40 fine structure energy levels *viz.*1s_i, 2s_i (i=2-5), 2p_i, 3p_i (i=1-10) , 3d_i (i=1-12) in addition to the ground state and first ionization state of Ar. These levels with their electronic configurations are given in Table 3.1 in Paschen’s notation. A Graphical view of processes that are considered in the present C-R model is shown in figure 3.1. Electron impact excitations of the Ar from the ground states to excited states as well as among the excited states are considered. The population transfer among the different fine-structure levels through their radiative decay has been included using the values of the transition probabilities. The ionization from all the considered levels has also been included in the present C-R model. The inverse of the excitation and ionization processes i.e., de-excitation and three body recombination respectively has been taken into account through detailed balance principle [111] in a similar manner as described in the Chapter 2. Since we are dealing with Ar-O_2 mixture plasma, we have added the depopulation channel of argon-excited states (1*s* and 2*p* manifolds) through quenching with O_2 molecule. The particle balance equation for an excited level *j* can be expressed as follows

$$\sum_{\substack{i=1\\ i\neq j}}^{41} k_{ij}(T_e)n_i n_e + \sum_{i>j} A_{ij}^{eff} n_i + n_e n_+ n_e\, k_{+j}(T_e) - \sum_{\substack{i=1\\ i\neq j}}^{41} k_{ji}(T_e)n_j n_e$$
$$- \sum_{i<j} A_{ji}^{eff} n_j - n_j n_e k_{j+}(T_e) - n_j k_j^{diff} - n_j n_{(O_2)} k_j^{quench} = 0 \qquad (3.2.1)$$

Various symbols used here have same as explained in equation (1.3.1). $n_{(O_2)}$ is the population densities of the O_2. Last two terms of the equation (3.2.1) refer the depopulation through diffusion of excited states via chamber walls and the quenching with O_2 molecules. Diffusion is taken into account mainly for 1s_i excited states using the diffusion rate coefficients reported by Kolts *et. al.* [190]. The rate coefficients for the quenching of 1s_i and 2p_i states with O_2 molecules are taken from Velazco *et. al.* [191] and

Sadeghi *et. al.* [192]. Electron impact excitation have been considered from the ground to all selected excited fine structure levels, $1s_i$ to all $2p_i$states, $1s_3$ and $1s_5$ (metastable levels) to all $3p_i$ levels and also intra-excitations of $1s_i$ and $2p_i$ levels. The rate coefficients for electron impact excitation from a lower level *i* to an upper level *j* are calculated by using the equation (2.2.1). Since the reliability of the calculated excitation rate coefficients k_{ij} depend on the accuracy of the utilized cross sections, we have taken a complete set of reliable relativistic electron impact excitation cross sections calculated using fully relativistic distorted wave (RDW) theory as obtained earlier by our group [73, 193]. Rate coefficients for ionization process k_{j+} can be calculated by replacing upper state by ionization level in the equation (2.2.1). The ionization cross sections employed in the present model are the experimental results taken from[194, 195].

Population transfer through radiative decay has been taken into account via effective transition probability $A_{ji}^{eff} = \Lambda(K_{ji}\rho)A_{ji}$. Since we are working at 2Torr pressure, there is great probability that the radiation is reabsorbed by another atomic state before leaving the plasma. The modification in the transition probability (A_{ji}) by a factor of $\Lambda(K_{ji}\rho)$ is to incorporate the reabsorption of the radiation. $\Lambda(K_{ji}\rho)$ is the escape factor, which represent the probability that the radiation leaves the plasma without getting trapped. We have calculated the escape factor as a function of absorption coefficient K_{ji} and characteristic plasma length ρ via following expression suggested by Mewe [196, 197]

$$\Lambda\left(K_{ji}\rho\right) = \frac{2 - e^{-K_{ji}\rho/1000}}{1 + K_{ji}\rho} \tag{3.2.2}$$

This approximation holds under the assumption that the emitting and absorbing atoms have uniform distribution. In the present pressure range the absorption line profile is dominated by Doppler broadening, therefore, the absorption coefficient is taken as

$$K_{ji}\left(n_i\right) = \frac{\lambda_{ji}^3}{8\pi^{3/2}}\frac{g_j}{g_i}n_i A_{ji}\sqrt{\frac{M}{2RT_g}} \tag{3.2.3}$$

Where λ_{ji} is the wavelength of the emitted radiation from the transition *j*→*i*. n_i is the population density of the lower state *i*. *M* is the mass of the argon atom. R and T_g are the gas constant and gas temperature, respectively. We have taken 1.2 cm as the characteristic length of the plasma and T_g is an increasing function of O_2 fraction as in [179]. The transition probabilities (A_{ji}) are taken from the latest NIST database [147] as given in Table 3.2. We also note from this table that most of the values are close to the values taken in [179]. The calculated escape factors are also shown in Table 3.2. No significant changes in the values of escape factors are observed for 13 emission lines (observed in the OES measurements) as the % amount of O_2 varies from 0% to 5%. It is important to mention that the calculated escape factors here are applicable only for the plasma conditions of [179].

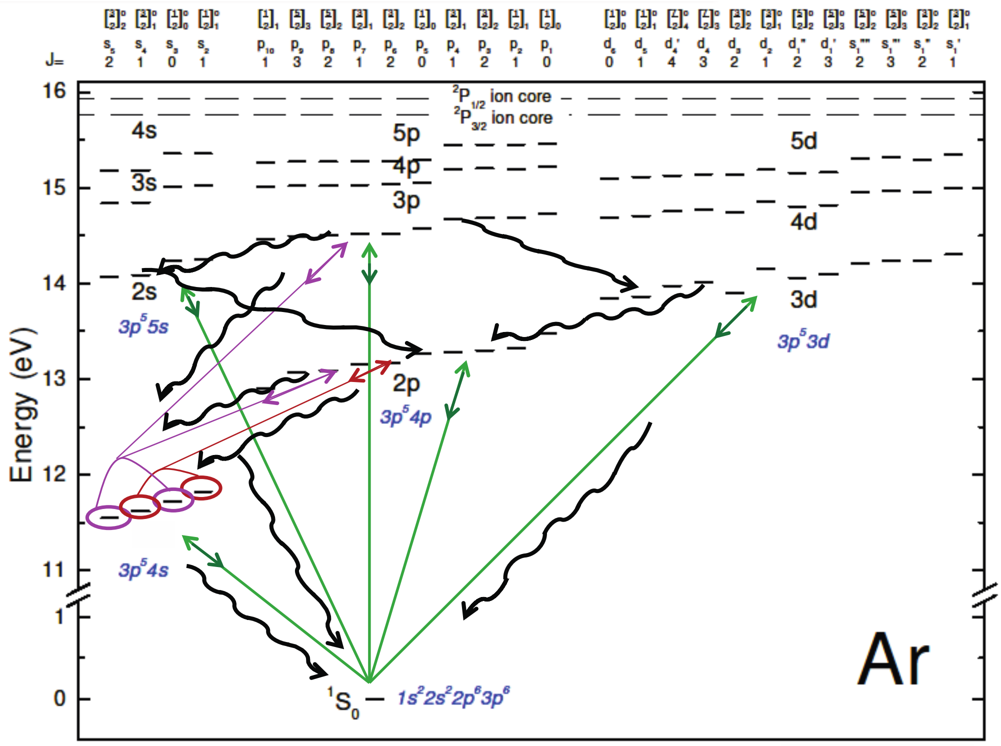

Figure3.1: Energy level diagram for Ar showing various collisional and radiative processes included in CR model. The green coloured lines represent excitations from the ground state, the purple ones show excitations from the $1s_5$ and $1s_3$ metastable states, the red color lines excitations from the $1s_2$ and $1s_4$ resonance levels while the wavy black lines represent radiative transitions.

Table3.1: Argon energy levels considered in the present model.

Level No.	Level	Paschen's notation	Excitation energy(eV)^{33}	Statistical weight
1	$[3p_{1/2}(2)3p_{3/2}(4)]_{J=0}$	$1s_0$	0	1
2	$[3p_{3/2}(3)4s_{1/2}(1)]_{J=2}$	$1s_5$	11.548	5

3	$[3p_{3/2}(3)4s_{1/2}(1)]_{J=1}$	$1s_4$	11.623	3
4	$[3p_{1/2}(1)4s_{1/2}(1)]_{J=0}$	$1s_3$	11.723	1
5	$[3p_{1/2}(1)4s_{1/2}(1)]_{J=1}$	$1s_2$	11.828	3
6	$[3p_{3/2}(3)4p_{3/2}(1)]_{J=1}$	$2p_{10}$	12.907	3
7	$[3p_{3/2}(3)4p_{3/2}(1)]_{J=3}$	$2p_9$	13.076	7
8	$[3p_{3/2}(3)4p_{1/2}(1)]_{J=2}$	$2p_8$	13.095	5
9	$[3p_{3/2}(3)4p_{1/2}(1)]_{J=1}$	$2p_7$	13.153	3
10	$[3p_{3/2}(3)4p_{3/2}(1)]_{J=2}$	$2p_6$	13.172	5
11	$[3p_{1/2}(1)4p_{1/2}(1)]_{J=0}$	$2p_5$	13.273	1
12	$[3p_{1/2}(1)4p_{1/2}(1)]_{J=1}$	$2p_4$	13.283	3
13	$[3p_{1/2}(1)4p_{3/2}(1)]_{J=2}$	$2p_3$	13.302	5
14	$[3p_{1/2}(1)4p_{3/2}(1)]_{J=1}$	$2p_2$	13.328	3
15	$[3p_{3/2}(3)4p_{3/2}(1)]_{J=0}$	$2p_1$	13.480	1
16	$[3p_{3/2}(3)3d_{3/2}(1)]_{J=0}$	$3d_{12}$	13.845	1
17	$[3p_{3/2}(3)3d_{3/2}(1)]_{J=1}$	$3d_{11}$	13.863	3
18	$[3p_{3/2}(3)3d_{5/2}(1)]_{J=2}$	$3d_{10}$	13.903	5
19	$[3p_{3/2}(3)3d_{5/2}(1)]_{J=4}$	$3d_9$	13.979	9
20	$[3p_{3/2}(3)3d_{3/2}(1)]_{J=3}$	$3d_8$	14.012	7
21	$[3p_{3/2}(3)3d_{3/2}(1)]_{J=2}$	$3d_7$	14.063	5
22	$[3p_{3/2}(3)3d_{5/2}(1)]_{J=3}$	$3d_6$	14.100	7
23	$[3p_{3/2}(3)3d_{5/2}(1)]_{J=1}$	$3d_5$	14.153	3
24	$[3p_{1/2}(1)3d_{3/2}(1)]_{J=2}$	$3d_4$	14.214	5
25	$[3p_{1/2}(1)3d_{5/2}(1)]_{J=2}$	$3d_3$	14.234	5
26	$[3p_{1/2}(1)3d_{5/2}(1)]_{J=3}$	$3d_2$	14.236	7
27	$[3p_{1/2}(1)3d_{3/2}(1)]_{J=1}$	$3d_1$	14.303	3
28	$[3p_{3/2}(3)5s_{1/2}(1)]_{J=2}$	$2s_5$	14.068	5
29	$[3p_{3/2}(3)5s_{1/2}(1)]_{J=1}$	$2s_4$	14.090	3

30	$[3p_{1/2}(1)5s_{1/2}(1)]_{J=0}$	$2s_3$	14.241	1
31	$[3p_{1/2}(1)5s_{1/2}(1)]_{J=1}$	$2s_2$	14.255	3
32	$[3p_{3/2}(3)5p_{3/2}(1)]_{J=1}$	$3p_{10}$	14.464	3
33	$[3p_{3/2}(3)5p_{3/2}(1)]_{J=3}$	$3p_9$	14.500	7
34	$[3p_{3/2}(3)5p_{1/2}(1)]_{J=2}$	$3p_8$	14.506	5
35	$[3p_{3/2}(3)5p_{1/2}(1)]_{J=1}$	$3p_7$	14.525	3
36	$[3p_{3/2}(3)5p_{3/2}(1)]_{J=2}$	$3p_6$	14.529	5
37	$[3p_{1/2}(1)5p_{1/2}(1)]_{J=0}$	$3p_5$	14.575	1
38	$[3p_{1/2}(1)5p_{1/2}(1)]_{J=1}$	$3p_4$	14.680	3
39	$[3p_{1/2}(1)5p_{3/2}(1)]_{J=1}$	$3p_3$	14.687	3
40	$[3p_{1/2}(1)5p_{3/2}(1)]_{J=2}$	$3p_2$	14.688	5
41	$[3p_{1/2}(1)5p_{1/2}(1)]_{J=0}$	$3p_1$	14.738	1
42	$3p(5)$	Ion	15.760	6

TABLE 3.2: Escape factors for the transitions originating from the upper $2p_i$ levels to lower levels at 0%, 1% and 5% O_2 mixture in Ar.

Transition	A_{fi} (s^{-1})	Wavelength (nm)	Ar-0% O_2	Ar-1% O_2	Ar-5% O_2
$2p_8$-$1s_4$	2.15e7	842.47	0.34	0.31	0.35
$2p_7$-$1s_4$	2.50e7	810.37	0.45	0.42	0.47
$2p_6$-$1s_5$	2.45e7	763.51	0.48	0.40	0.45
$2p_5$-$1s_4$	4.02e7	751.47	0.66	0.63	0.67
$2p_4$-$1s_3$	1.86e7	794.82	0.36	0.30	0.33
$2p_4$-$1s_2$	1.39e7	852.14	0.63	0.57	0.55
$2p_3$-$1s_5$	3.80e6	706.72	0.88	0.84	0.87
$2p_3$-$1s_4$	8.47e6	738.40	0.66	0.63	0.67

$2p_3$-$1s_2$	2.23e7	840.82	0.39	0.34	0.32
$2p_2$-$1s_5$	6.39e6	696.54	0.89	0.85	0.87
$2p_2$-$1s_4$	1.83e6	727.29	0.93	0.93	0.94
$2p_2$-$1s_2$	1.53e7	826.45	0.63	0.57	0.54
$2p_1$-$1s_2$	4.45e7	750.39	0.70	0.65	0.62

3.3 Results and discussions

3.3.1 Electron temperature and electron density

The coupled particle balance equations (equation (3.2.1)) for all considered states were solved simultaneously as a function of plasma parameters (T_e and n_e). The intensity (I_{ji}) of an emission line corresponding to a transition ($j \rightarrow i$) is proportional to the population of upper excited states (n_j) and can be given by the following relation

$$I_{ji} \propto n_j \frac{hc}{\lambda_{ji}} A_{ji}^{eff} \tag{3.3.1}$$

where, h and c are the usual Planck's constant and speed of light, respectively and λ_{ji} is the emitted wavelength corresponding to the transition. In the present diagnostics, we have utilized thirteen emission lines decaying from $2p_i$ (i =1-10) states to the $1s_i$ (i=2-5) states observed in the OES measurements [179] as given in Table 3.2. The normalized intensities of all these 13 lines are simulated as a function of T_e, and n_e for their various combinations of values. In order to estimate the difference of our calculated intensities with those of OES measurements, we calculate the deviation parameter (Δ) based on minimum scatter approach, as defined below [113, 198],

$$\Delta = \sum_{j=1}^{13} \left(I_{j,OES}^{normalized} - I_{j,Model}^{normalized} \right)^2 \tag{3.3.2}$$

The normalized measured and modeled intensities are obtained as below.

$$I_{j,OES(Model)}^{normalized} = \frac{I_{j,OES(Model)}}{\sum_{j=1}^{13} I_{j,OES(Model)}} \times 100 \tag{3.3.3}$$

In figure 3.2, deviation parameter is plotted as a function of T_e for different values of n_e in the case of pure Ar as if O_2 concentration is zero. The minimum value of the deviation parameter as obtained from the plots fixes the value of T_e and n_e. Similarly by plotting the deviation parameters for different concentrations of O_2 (0-5%) we have obtained the values of T_e and n_e at each concentration. In these calculations, the ground state argon population n_{Ar} are calculated from the standard gas law using the pressure and gas temperature reported by the Jogi *et. al.* [179] at each concentration of O_2. Finally, all the plasma parameters at different concentrations of O_2 are displayed in the table of figure 3.2.

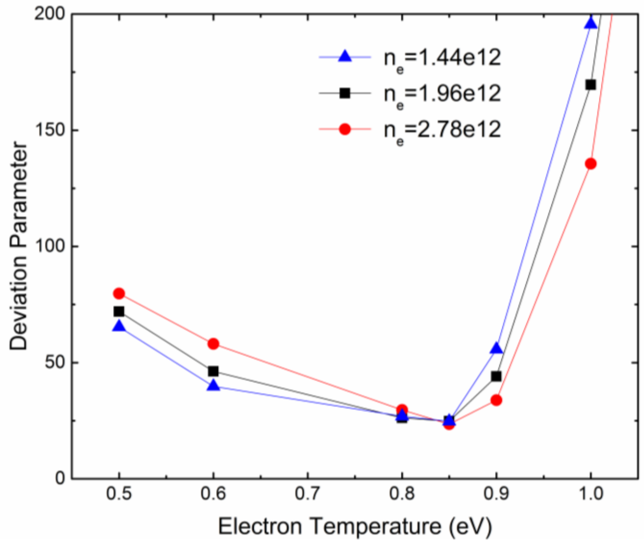

Figure 3.2: Variation of deviation parameter as a function of T_e at different n_e for Ar-0% O_2 mixture plasma at 2 Torr pressure.

We observe from the figure 3.3 that the electron temperature rises from 0.85 eV to 1.7 as the O_2 content in the Ar increases from 0 to 5%. Opposite behavior is found for electron density, which decreases from 2.76e12 cm^{-3} to 2.34e11 cm^{-3} as the O_2 increases from 0 to 5%. These results are shown in a table as given in the figure 3.3. It should be noted that the Jogi *et. al.*[179] did not explicitly obtain the value of T_e by any calculation or measurement but they took its value at 0.5 % and 5% concentration of O_2 respectively as 1.4 eV and 1.8 eV based on some discussions only. Consequently, there are no exact comparable results available with which we could compare our results directly. However, the similar trend for electron density and temperature were reported in reference[188] for microwave Ar-O_2 (0-5%) plasma at medium pressure (10mbar) which can be said to support our findings.

Further, figure 3.3 shows the comparison of our optimized model intensities with the corresponding measurements of Jogi *et. al.* [179] at 0%, 1% and 5% concentrations of O_2. It can be seen that for all the concentrations our calculated line intensities are in reasonable agreement with their corresponding experimental values, except, for the $2p_1$-$1s_2$ line (750.39nm) at 1 and 5% concentrations of the O_2. Such discrepancy can be understood by estimating the contributions of various levels to populate the 2*p* states and we have discussed this point later in the section 3.3.3.

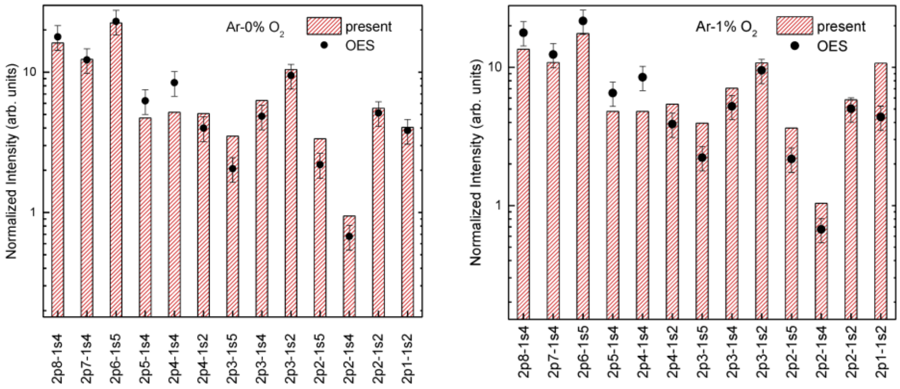

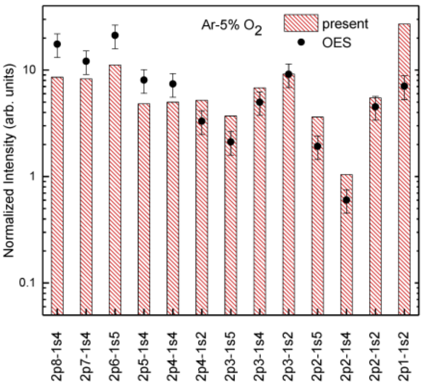

O_2 %	n_{Ar}(cm^{-3})	n_e(cm^{-3})	T_e(eV)
0	4.883e16	2.76e12	0.85
1	3.35e16	1.14e12	1.15
2	2.82e16	7.0e11	1.30
3	2.54e16	4.5e11	1.45
4	2.32e16	3.5e11	1.55
5	2.15e16	2.34e11	1.70

Figure 3.3: Comparison of the normalized intensities obtained from the C-R model with the OES measurements [179] for Ar ($3p^5 4p \rightarrow 3p^5 4s$) transition lines. Table shows the values of our extracted plasma parameters.

3.3.2. Ar-1s population densities

Jogi *et. al.* [179] observed significant discrepancy in the populations of the $1s_i$ levels that they obtained from their measurements and the calculations using a simple model (with the assumption that only the ground state excitation of Ar is the main production mechanism). They also mentioned in their paper that the cause of such discrepancy could be due to the exclusion of other processes in their model such as population transfer from upper state to 1s states as well as of not taking very accurate values of rate coefficients and T_e. In fact, Jogi *et. al.* [179] did not obtain T_e explicitly but assumed constant as 1.4 eV in the calculations. It is important to mention here that the basic or prime output of any C-R model is, in fact, the population densities of different states. Therefore, the comparison of our calculated population densities with the corresponding available measurements would also help in testing the optimization and reliability of the model. To compare with their measured populations of the 1s_i levels we have separately obtained the 1s_i level populations from our detailed CR model. In figure 3.4, we present the comparison of our calculated population densities of 1s_i states with the measurements[179] at each concentration of O_2 at the optimized values of n_e and T_e (as given in table of figure 3.3). From figure 3.4, we find that our calculated population densities are in very good agreement with the experimental results[179]. The good agreement of our 1s_i level population densities with the measurements confirms that our C-R model is well optimized for Ar with O_2 trace amount for intermediate pressure plasma (at least up to 5% trace addition) and also the extracted plasma parameters are reliable. Further, from figure 3.4 one can observe that the metastable (1s_5, 1s_3) and resonance level (1s_4, 1s_2) population densities are of the same order. This suggests that in the pressure range considered in this work, the trapping of the resonance levels is very high (~5e-5 for 0% and ~2e-4 for 5% O_2 mixture). Interestingly, all the four 1s_i level populations increase as we increase the O_2 fraction up to 1% and there after these reach to a constant value, although, the electron temperature keeps on rising till 5%. This behavior can be explained with some reasoning. Since the life time of 1s_i states are relatively longer these states can be involved in several processes such as electron impact excitation to further upper states, de-excitation to lower states, quenching with trace gas O_2 molecules, 1s_i inter-state population transfer. Now a possible conclusion can be drawn that as O_2 is added in Ar, quenching of the excited Ar atoms with O_2 causes a decrease in the 1s_i level populations and at the same time the increase in T_e compensate it by increasing the electron-impact excitation to levels. However, some studies [183, 186] claimed that the quenching only start changing the populations of 1s_i levels beyond 10% addition of O_2. Sato *et. al.*[183] reported that the net quenching rate of 1s_i states by electrons is more than an order of magnitude higher than by O_2 molecules up to 8% O_2 fraction. It is worth mentioning that their electron density was an order higher than the case considered in the present Chapter. Therefore, it is expected that both the electron and O_2 quenching is of the same order for the present case.

Overall, we find from the present study that the mechanism for population of Ar 1s_i states is very complex in the Ar-O_2 mixture plasma even for small amount of trace addition. Therefore, straightforward estimation is not appropriate and a detailed C-R model as developed here with consistent cross sections should be used to estimate the Ar-1s_i population densities.

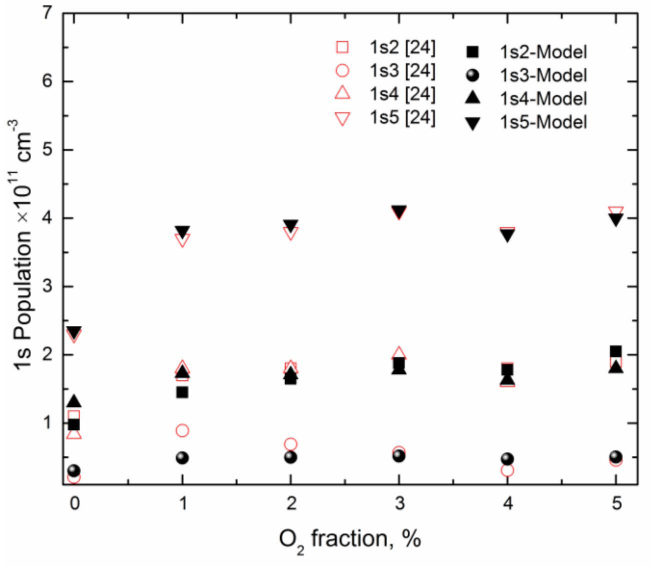

Figure 3.4: Population densities of Ar-1s_i levels as a function of O_2 content in the Ar plasma.

3.3.3. Relative contributions of the different states to the population of 2pᵢ states of Ar

At low-pressure for pure Ar plasma, Boffard *et. al.* [199] have reported the percentage contribution of electron-impact excitation from the ground, metastable and resonance states to the population of emitting Ar 2p_i levels. However, no previous studies have given the detailed contributions of the different states for radiating Ar 2p_i levels for Ar-O_2 plasma.

Using our calculated plasma parameters and the C-R model we have estimated the net contribution from the ground and 1s_i states to the 2p_i states as a function of O_2 addition and presented in figure 3.5. As we observed from figure 3.4 that the populations of all the four 1s_i levels are of the same order, therefore, we have estimated a combined contribution from the 1s_i states to the 2p_i states. For pure Ar case, the individual 1s_i state contribution dominates in populating the 2p_i states. Since for pure Ar case the electron temperature is about 0.85 eV only stepwise excitations can populate the Ar-2p_i states. As the O_2 content increases the electron temperature rises and consequently we see increase in the contribution from the ground state. Further, we observed a rapid decrease in 1s_i manifold contribution to the 2p_1 state which being a J=0 state, the electron-impact excitation from the ground (J=0) as well as 1s_5 (J=2) state is optically dipole forbidden. This particular 2p_1 state also showed some significant “other” contributions. Here the “other” contribution refers to the contribution from the higher lying levels (>2p) or from three body recombination as well as due to population transfer between 2p_i levels. The threshold energy of $2p_1$ state is (13.57 eV) the highest among the other $2p_i$ fine-structure states. Overall, this particular state appears to have complex nature of contributions as soon as the O_2 traces are added to the plasma. Perhaps this may be the reason of the overestimation of $2p_1$ population from our model. We would also like to mention here that we observed higher RDW cross section for J=0 to J=0 transitions than the measurements [73]. This may also be partially responsible for overestimation of $2p_1$ populations.

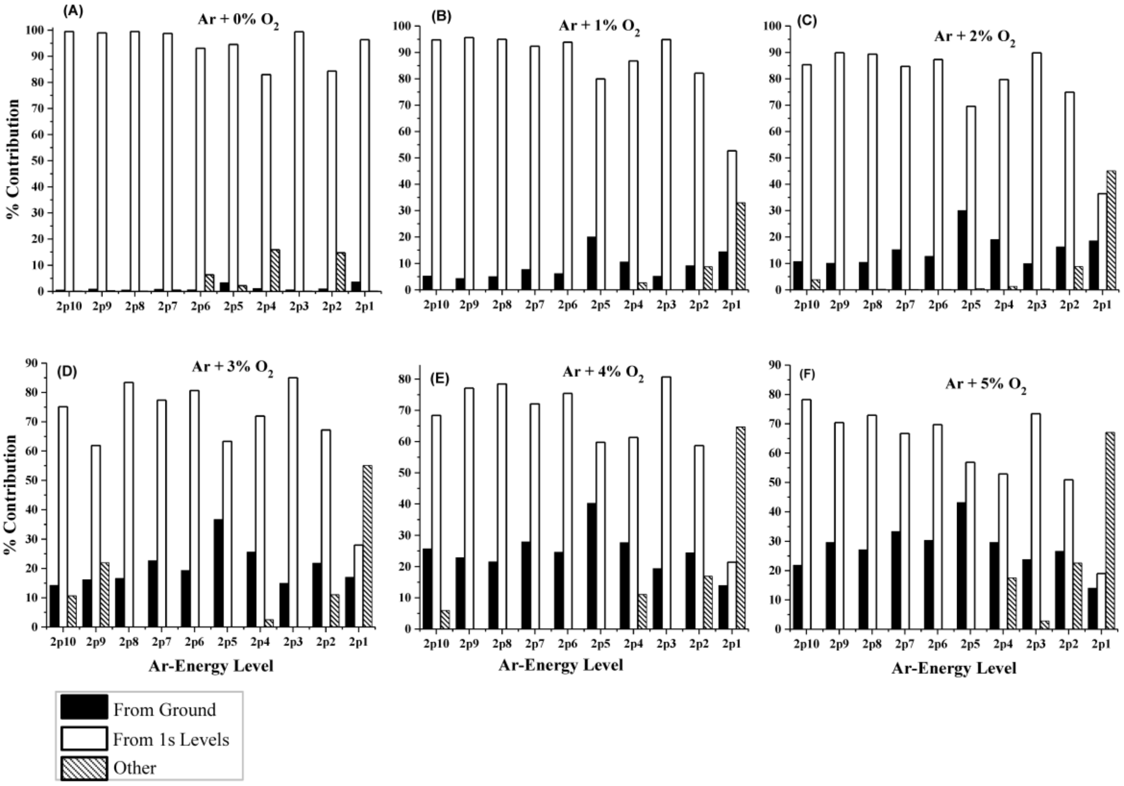

Figure 3.5: Net contributions from ground state, from 1*s* manifold and other contribution (cascade contribution from higher lying (>2*p* levels); three body recombination; population transfer among 2*p* levels etc.) to the radiating Ar-2*p* states as a function of % amount of O_2 in Ar plasma.

3.4 Conclusions

In the present work, a C-R model has been developed to characterize the Ar-O_2 mixture plasma coupled with the OES measurements[179]. Electron temperature T_e and electron density n_e are obtained by minimum scatter approach using experimental intensities of the thirteen intense lines ($2p_i \rightarrow 1s_i$ transitions) at various O_2 fractions (0-5%). Optimized T_e ranges from 0.85eV to 1.7 eV as O_2 fraction changes from 0 to 5%. Further, our reported populations of the $1s_i$ states of Ar at different O_2 fraction are in very good agreement with the experimental results[179]. This reflects that our C-R model is well optimized and with the present investigation also we can again emphasize the applicability of our reliable

RDW cross sections in developing a consistent C-R model. Furthermore, we presented the contribution from the ground and $1s_i$ levels to populate the Ar-$2p_i$ radiating states which could be quite useful in understanding the real mechanism of the various involved plasma processes. Our analysis shows a complex behavior of contributions for $2p_1$ state in the presence of O_2.

CHAPTER 4

ELECTRON EXCITATION OF XENON AND MODELING OF INDUCTIVELY COUPLED Xe PLASMA

4.1 Introduction

In the present Chapter, our aim is to obtain highly needed detailed fine-structure resolved cross sections for electron impact excitation of xenon using RDW approach and demonstrate the application of the calculated data in the modeling of low temperature xenon plasma by developing a C-R model. The xenon gas discharge is used in various plasma applications such as mercury-free light sources [200, 201], plasma displays [202] and space propulsion i.e. Hall-effect thrusters (HET) in space craft [203, 204]. In particular, xenon is used nearly in all modern HETs as propellant. Also, mixture of inert gases including xenon are added to characterize the low temperature plasmas [8].

In the literature, a number of experimental as well as theoretical studies on electron impact cross sections of xenon are reported [75, 98, 193, 204–228]. Most of them have reported the elastic total cross sections (TCS) [205, 223, 224, 226–228], differential cross sections (DCS) [205–210] and fine structure unresolved excitation cross sections [212–214, 229]. The fine structure resolved electron impact excitation cross section are available only for some transitions at certain selected electron energies [75, 98, 206, 209, 210, 215–219]. In the present work, we are interested only in the TCS results for the electron impact excitations of xenon atom. First, we see the availability of the cross sections for the excitations from the ground state. Filipovic *et al.*[209] have reported the measurement on DCS and TCS for 20 lowest excited levels at 15, 20, 30 and 80 eV. Their results for the excitation to the first excited $5p^5 6s$ configuration were only fine structure resolved and they reported cross sections for the two metastable states. Suzuki *et al.* [206] reported their experimental results for the cross sections of the four fine structure states of the $5p^5 5d$ and

$5p^57s$ configurations at 400 and 500eV incident energy using electron-energy-loss spectroscopy. Fons and Lin [216] have measured the electron-impact emission cross sections corresponding to the ten fine structure levels of the $5p^56p$ configuration in the range of incident electron energy up to 150 eV at different gas pressures between 0.1 and 2.0 m Torr. From their measurements they have extracted direct excitation cross sections by subtracting the cascade contribution coming from the upper levels. Chiu *et al.*[204] have also reported similar emission cross section for incident electron energy 10 to 70eV. Using the Breit–Pauli *R*-matrix method, Nakazaki *et al.*[215] have calculated the electron impact TCS for the nine lowest lying excited levels (four levels of $5p^56s$ and five levels of $5p^56p$ configurations) in the low incident electron energy range up to 35eV. Zatsarinny *et al.* [210] have reported electron-impact excitation of the $5p^56s$ state of Xe near the threshold using *B*-spline *R*-matrix (close-coupling) approach with non-orthogonal orbitals. More recent results for the electron impact excitations from the ground state of xenon are compiled by Pitchford *et al.* [193].

There are also few reports on the TCS for the excitation of xenon atom from an excited state to higher excited states. Jung *et al.* [217] have measured the cross sections for electron-impact excitation from the $5p^56s$ (J=2) metastable level of xenon to the six lowest lying levels of the $5p^56p$ configuration. Jung *et al.* [218], further, reported the experimental apparent cross section (includes direct plus cascade contributions) for excitation from ground and from the $5p^56s$ (J=2) metastable level into levels of the $5p^57p$ fine structure levels using the optical method. Srivastava *et al.* [98] have calculated and reported excitation cross sections from the metastable states (J=0, 2) to the ten levels of the $np^5(n+1)p$ levels of Ar (n=3), Kr (n=4) and Xe (n=5) using RDW theory. Sharma *et al.* [75, 219] have further carried out the calculations of the TCS using relativistic RDW approach for the excitations from the ground ($5p^6$) and excited metastable states $5p^56s$ (J=0,2) to the fine-structure levels of the $5p^57p$ configuration in the incident electron energy range up to 200eV. Recently Chen *et al.* [220] have also reported similar RDW excitation cross sections as reported by Sharma *et al.*[219] and compared with their results. From the above review on the electron impact excitation cross sections of xenon atom, it is obvious that there is a still lack of sufficient cross section data for the fine structure excitations from the ground and among the excited states for a reliable plasma modeling. Also the available data are not reported in the wide range of incident electron energies.

Therefore, in the present Chapter, for the sake of providing sufficient consistent cross section data, detailed calculation is carried out for the excitation cross sections in xenon involving various transitions from the ground $5p^6$ state to the excited $5p^56s$, $5p^56p$, $5p^55d$, $5p^57s$ and $5p^57p$ as well as among these excited states using the RDW method. In fact, the RDW method has been already successfully applied to study the electron impact excitation of rare gas atoms *viz.* Ar and Kr [13, 73, 74, 112]. The T-matrices for different transitions of xenon are evaluated by using equation (1.2.11). The required xenon bound state Dirac-Fock wave functions are obtained from GRASP2K code [100]. The obtained wavefunctions are employed to calculate the distortion potential (Eq. (1.2.24)) which is further used to calculate the relativistic distorted wave function for the projectile electron in the initial and final channels by solving Dirac equations (1.2.27) numerically.

In order to utilize the calculated cross section data directly for the plasma modeling, these are also fitted with suitable analytical expressions. A C-R model is developed by incorporating the obtained cross sections. Further, coupling the C-R model with the optical emission spectroscopy (OES) measurements of Czerwiec *et al*. [230], diagnostic of the low temperature inductively coupled (ICP) xenon plasma is performed. The plasma parameters *viz.* electron temperature (T_e) and electron density (n_e) are extracted for H-mode transitions of xenon discharge.

4.2 Dirac-Fock wave functions of xenon atom

From the equation (1.2.11) it is clear that the accuracy of the obtained cross section depends on the reliability of the atomic target wave function used in the calculation. As mentioned above, GRASP2K [99] code is used to calculate the multi-configuration Dirac-Fock (MCDF) bound state wave functions of xenon atom. Only those CSFs are considered which contribute significantly. The various CSF's used to represent the xenon atom wave functions in GRASP2K are $5p^5$ns (n=6-8), $5p^5$np (n=6, 8), $5p^5$nd (n=5, 6) in addition to the ground state ($5p^6$). To assure the reliability of the obtained wave functions, we have calculated the oscillator strengths for dipole allowed transitions and compared with the available experimental and theoretical results. The comparison of oscillator strengths is given in table 4.1.

Table 4.1. Our calculated oscillator strengths for various dipole allowed transitions compared with other available experimental and theoretical results. (All the levels are in Paschan's notation)

Lower level	***Upper level***	f_{present}	f_{NIST} [147]	$f_{\textit{previous}\text{(Exp.)}}$	$f_{\textit{previous}\text{(Theory)}}$
$1s_0$	$1s_4$	0.280	0.273	0.260[a] 0.220 [b] 0.273[c]	0.260[d] 0.271[e] 0.313[f]
$1s_0$	$1s_2$	0.180	0.186	0.17[a] 0.158[b] 0.186[c]	0.188[d] 0.158[e] 0.161[f]
$1s_0$	$3d_{11}$	0.010	0.0096	0.0120[a] 0.0105[c]	0.0083[d]
$1s_0$	$3d_5$	0.420	0.400	0.370[a] 0.298[g] 0.379[c]	0.303[d] 0.467[f]
$1s_0$	$3d_1$	0.510	0.205	0.191[c]	0.167[d] 0.508[f]
$1s_0$	$2s_4$	0.081	0.099	0.1000[a] 0.0738[g] 0.0859[c]	0.0791[d] 0.0646[f]
$1s_0$	$2s_4$	0.029	0.029		0.0287[f]
$1s_5$	$2p_{10}$	0.199			0.268[h]
$1s_5$	$2p_9$	0.101			0.132[h]
$1s_5$	$2p_8$	0.570		0.590[i]	0.641[h]
$1s_5$	$2p_7$	0.022			0.012[h]
$1s_5$	$2p_6$	0.304		0.300[i]	0.253[h]
$1s_5$	$2p_4$	8.09e-5			7.67e-4[h]
$1s_5$	$2p_3$	9.30e-4	6.40e-4		0.0026[h]
$1s_5$	$2p_2$	0.005	0.0011		6.56e-4[h]
$1s_4$	$2p_{10}$	0.027			0.0457[h]
$1s_4$	$2p_9$	0.415			0.483[h]
$1s_4$	$2p_7$	0.359			0.398[h]
$1s_4$	$2p_6$	0.183			0.213[h]
$1s_4$	$2p_5$	0.146			0.153[h]
$1s_4$	$2p_4$	3.93e-4			0.0044[h]

$1s_4$	$2p_3$	0.005		0.0020[j]	0.0059[h]
$1s_4$	$2p_2$	1.21e-4			1.51e-4[h]
$1s_4$	$2p_1$	7.38e-4			0.0032[h]
$1s_3$	$2p_4$	0.484			0.286[h]
$1s_3$	$2p_2$	0.706			0.382[h]
$1s_2$	$2p_5$	3.733e-5			5.53e-3[h]
$1s_2$	$2p_4$	0.221			0.124[h]
$1s_2$	$2p_3$	0.654			0.461[h]
$1s_2$	$2p_2$	0.158			0.133[h]
$1s_2$	$2p_1$	0.140			0.068[h]
$1s_5$	$3p_{10}$	2.54193e-4			3.98e-4[h]
$1s_5$	$3p_9$	0.00245			0.0048[h]
$1s_5$	$3p_8$	0.0058	0.0046	0.0043[j]	0.0169[h]
$1s_5$	$3p_7$	0.0027	0.0023	0.0020[j]	0.0160[h]
$1s_5$	$3p_6$	2.406e-4			7.74e-4[h]
$1s_4$	$3p_{10}$	1.181e-4			8.64e-5[h]
$1s_4$	$3p_9$	0.0066			0.0035[h]
$1s_4$	$3p_7$	0.0047			0.0044[h]
$1s_4$	$3p_6$	0.0073			0.0045[h]
$1s_4$	$3p_5$	0.0079			0.0059[h]
$1s_3$	$3p_{10}$	0.0138			0.0023[h]
$1s_3$	$3p_6$	0.0087			0.169[h]
$1s_2$	$3p_{10}$	0.0081			0.037[h]
$1s_2$	$3p_9$	0.0023			0.0210[h]
$1s_2$	$3p_7$	0.0019			0.0194[h]
$1s_2$	$3p_6$	0.00448			0.0305[h]
$1s_2$	$3p_5$	0.00724			0.0173[h]

[a]Molino *et al.* [231] , [b]Suzuki *et al.* [232], [c]Chan *et al.*[233], [d] Zatsarinny and Bartschat [234], [e]Dong *et al.*[235], [f]McEacharan *et al.*[236], [g]Suzuki *et al.* [206], [h]Aymar *et al.* [237], [i]jung *et al.* [217], [j] Kettlitz *et al.* [238]

For the oscillator strengths of the dipole allowed transitions from the ground state to $1s_i$, $3d_i$ and $2s_i$ fine structure levels various experimental [147, 206, 231–233] and theoretical results [234–236] are available in the literature. Molino *et al.* [231] obtained from absorption measurements, Suzuki *et al.*[206, 232] used electron energy loss spectroscopy for measurements and Chan *et al.*[233] did the measurements using photo-absorption technique. On the theoretical side, all the available studies[234–236] used multi configuration Dirac Fock wave functions for calculation of oscillator strengths. On comparison of the present oscillator strengths with the experimental as well as theoretical values from NIST, we find good agreement except for the single $1s_0 \rightarrow 3d_1$ transition. Oscillator strengths obtained from the present calculation for this transition is higher than the value reported in NIST database[147] but matches with the theoretical values reported by McEachran *et al* [236]. Experiential value of Chan *et al.*[233] and theoretical results of Zatsarinny and Bartschat [234] are lower and close to NIST value. For this particular transition, the difference may be due to the reason that in the present calculation core-core correlation from $4l$ subshells are not included. However, Zatsarinny and Bartschat [234] found that for this transition, inclusion of core-core correlation reduced the value of oscillator strength by a factor 4. Although the correlation corrections in the various excited levels are mainly due to the core–valence correlations.

Further, for the dipole allowed transitions from $1s_i \rightarrow 2p_i$ and $3p_i$ manifolds only few experimental[217, 238] and one theoretical[237] result are available for the oscillator strength. Present results are in good agreement with the experimental results of Jung *et al.* [217] and from NIST database [147] while reasonable agreement with the theoretical calculations of Aymer *et al.*[237]. This difference in the oscillator strengths obtained from the two theoretical calculations can be due to the fact that Aymer *et al.* [237] have obtained the radial part of the wave function by means of a parametric central potential and the angular part by a least-squares fit procedure on energy levels. After obtaining the wave-functions of xenon atom in various states, the electron impact excitation cross sections (Eq. (1.2.29)) for all the considered fine structure transitions of xenon are calculated for the incident electron energy in the range from the excitation threshold to 1 keV.

4.3 Electron impact excitation cross sections

The transitions *viz.* ground $5p^6$ ($1s_0$) to four fine structure levels of $5p^56s$ ($1s_i$, i=2-5), ten levels of $5p^56p$ ($2p_i$, i=1-10), twelve levels of $5p^55d$ ($3d_i$, i=1-12), four levels of $5p^57s$ ($2s_i$, i=2-5), and six levels of $5p^57p$ ($3p_i$, i=6-10) as well as excitations from$1s_i$, (i=2-5)$\rightarrow 2p_i$, (i=1-10), $3p_i$, (i=6-10) and intra transitions among $1s_i$ and $2p_i$ levels are considered. Here, fine structure levels corresponding to different configurations are written in Paschan’s notation.

Before, we present and discuss our results we would like to mention here one very important feature about the structure of xenon atom. The atomic structure of xenon is more complex than other lighter rare gases (like Ne, Ar and Kr) due to its relatively large spin orbit- interaction within ion core ($5p^5$) than the core with outer electron. Therefore, the fine structure levels of any configuration ($5p^5nl$) can be separated into two groups (as shown in figure 4.12). The lower and higher lying energy group corresponds to levels having core angular momentum j_c=3/2 and j_c=1/2, respectively. This property of core reflects in the cross sections for the different transition which we will discuss later in this section. Moreover, we explore the dependency of cross section for different transitions on various factors like angular momentum of final states, core angular momentum j_c and oscillator strengths for different allowed transitions.

First, the cross section results for the transitions from the ground ($1s_0$) to all the considered excited levels are presented through figures 4.1-4.5. Figure 4.1, shows the excitation cross section for transitions from $1s_0 \rightarrow 1s_i$ (i=1-4) levels. As expected, the dipole allowed ($1s_0 \rightarrow 1s_2$ and $1s_4$) transitions have larger cross section than the forbidden ($1s_0 \rightarrow 1s_3$ and $1s_5$) transitions. Also, for allowed transitions cross sections decay slowly with the increasing incident electron energy while for forbidden transitions it decays quickly. Present results are compared with the B-spline Breit–Pauli R-matrix (BSR) calculations of Zatsarinny *et al.*[193] available for incident energy up to 400 eV and the experimental data of Fivipovic *et al.*[209] that were reported only at three incident electron energies *viz.* 15, 20 and 30eV. On comparison of present results with the BSR calculations, one can see that both the cross section curves show similar behavior and their magnitudes differ maximum by factor of ~ 1.7 for $1s_0 \rightarrow 1s_3$, $1s_4$ and, ~1.2 for $1s_0 \rightarrow 1s_2$, $1s_5$ transitions. Further, we observe that both the calculations are in reasonable agreement with the experimental data of Filipovic *et al.*[209].

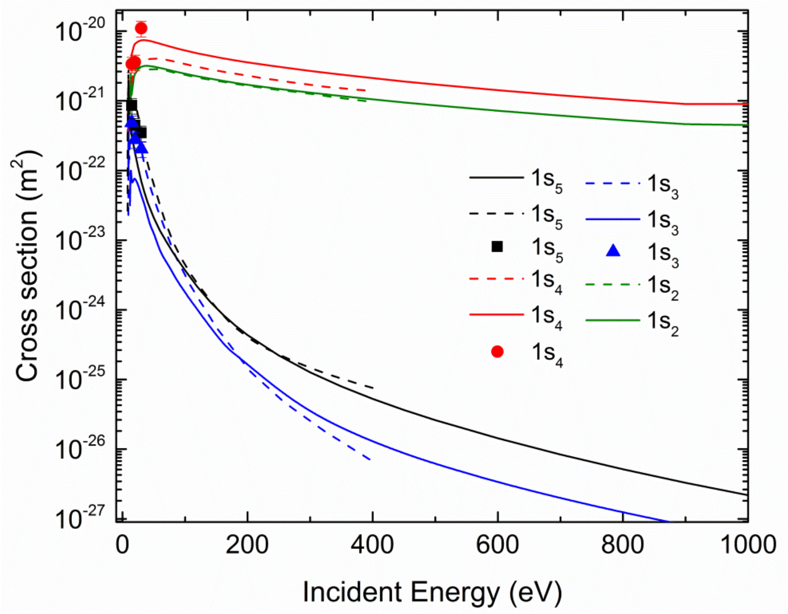

Figure 4.1. Electron impact excitation cross section for the transitions $1s_0$-$1s_i$ (i=1-4). Solid line denotes the present RDW calculation; dashed line represents the BSR calculations[193], and the symbols (square, sphere and triangle) show the experimental data of Filipovic *et al.* [209].

Figure 4.2, presents the cross sections for the transitions from ground ($1s_0$) state to ten fine structure $2p_i$ levels of $5p^5 6p$ configuration. These are forbidden transitions as the parity of both the initial and final states is even. We observe from the figure that the cross section for levels $2p_9$, $2p_8$ with J=2 and the levels $2p_5$, $2p_0$ with J=0 are larger in magnitude than other levels with J=1, 3. This can be explained on the basis that the same parity transitions with the even (J=0, 2) angular momentum states are more favorable. This is due to the fact that levels with even J value have non-zero direct T-matrix, therefore they can be excited by both the direct and exchange process whereas levels with odd J value are excited by the exchange process only. No direct excitation cross section measurements are available to compare with our results for the excitation of the ten fine structure $2p_i$ levels. However, pressure dependent emission cross sections are reported by Chiu *et al.*[204] and Fons *et al.*[216]. Since these include cascade contributions in addition to direct cross section and therefore, are not directly comparable to our calculated cross sections. However, we have compared our cross sections with the BSR calculations of Zatsarinny *et al*. [193] available for electron impact energies from threshold to 80eV. We find good agreement between these two theoretical calculations for electron impact energies greater than 2-3 times of the threshold except for the (J=0→J=0) transitions *viz.* ground to $2p_1$ and

$2p_5$ levels. We notice that the cross section for (J=0→J=0) transitions are usually large in RDW calculations which we also observed for other inert gas atoms.[73, 74]

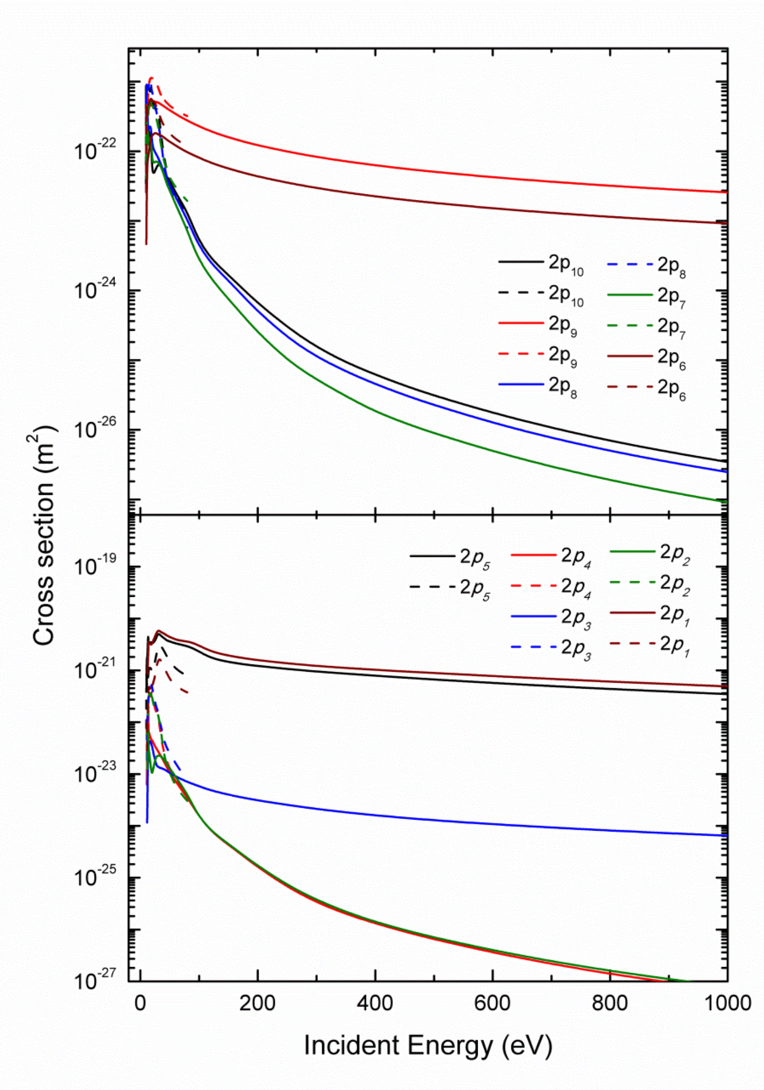

Figure 4.2. Electron impact excitation cross-section for the transitions $1s_0$-$2p_i$ (i=1-10). Solid line denotes the present RDW calculations and dashed line represents the BSR calculations[193].

Through figure 4.3, the cross section for transitions $1s_0$→$3d_i$ (i=1-12) are shown. We find typical behavior of cross sections as expected for the dipole allowed and forbidden transitions. Cross sections for the allowed transitions to the $3d_{11}$, $3d_5$ and $3d$1 (J=1) states are larger than the forbidden transitions. However, among forbidden transitions *viz.* $1s_0$ to $3d_8$, $3d_6$ and $3d_2$ have larger magnitude at higher energies due to a non-zero direct term in T-matrix. In this figure 4.3, we have also compared our cross section results with the BSR calculations of Zatsarinny *et al.*[193] available for low incident energy up to 80eV and the experimental measurements of Filipovic *et al.*[209] available for transition to $3d_8$, $3d_7$, $3d_6$

and $3d_5$ levels at 15, 20 and 30 eV incident energy as well as of Suzuki *et al.* [206] for the transition to $3d_5$ level at incident energies of 400 and 500eV. Present results are in good agreement with the BSR calculations[193] except for transition $1s_0$-$3d_1$ which quite expected as we pointed out earlier that our oscillator strength for this particular transition is relatively high. On comparison our cross sections with both the experimental results we find these are in good agreement.

In figure 4.4, cross sections for the excitation from ground to $2s_i$ (i=1-4) states are shown. The cross section curves for these transitions have similar behavior as observed for the transitions from ground state to the $1s_i$ levels in figure 4.1. Further, we have compared our results with the BSR calculations of Zatsarinny *et al.* [193] at low incident energies up to 80 eV as well as with the measurements of Suzuki *et al.* [206] at 400 and 500 eV electron energy for $1s_0$-$2s_4$ transition only. We find our results are in very good agreement with the measurement of Suzuki *et al.* [206] and also in reasonable agreement with the BSR calculations[193].

In figure 4.5, we present the cross sections for the excitation from the ground ($1s_0$) state to the only six $3p_i$ (i=5-10) levels. We have considered here only six lower lying levels of $5p^57p$ configuration because other four $3p_i$ (i=1-4) levels lie above the ionization threshold. Though there are previous RDW results reported by our group (see Sharma *et al.* [75]) for the excitation of $3p_i$ states but these were only for the incident energy up to 200eV and used lesser number of configurations in the calculation of the xenon wave functions for the $3p_i$ states. Here, we have extended our previous calculations to obtain the cross sections for incident energy up to 1000eV. It is important to mention here that although in the present calculations we have used more accurate MCDF wave functions for the ground as well as for the excited $3p_i$ states, present cross sections differ with the results of Sharma *et al.* [219] within 5%. In the figure 4.5, we have compared our results with the BSR calculations of Zatsarnny *et al.* [193] and find again reasonable agreement. The cross section curves for these transitions have similar behavior as observed for the transitions from ground state to the $2p_i$ levels in the figure 4.2.

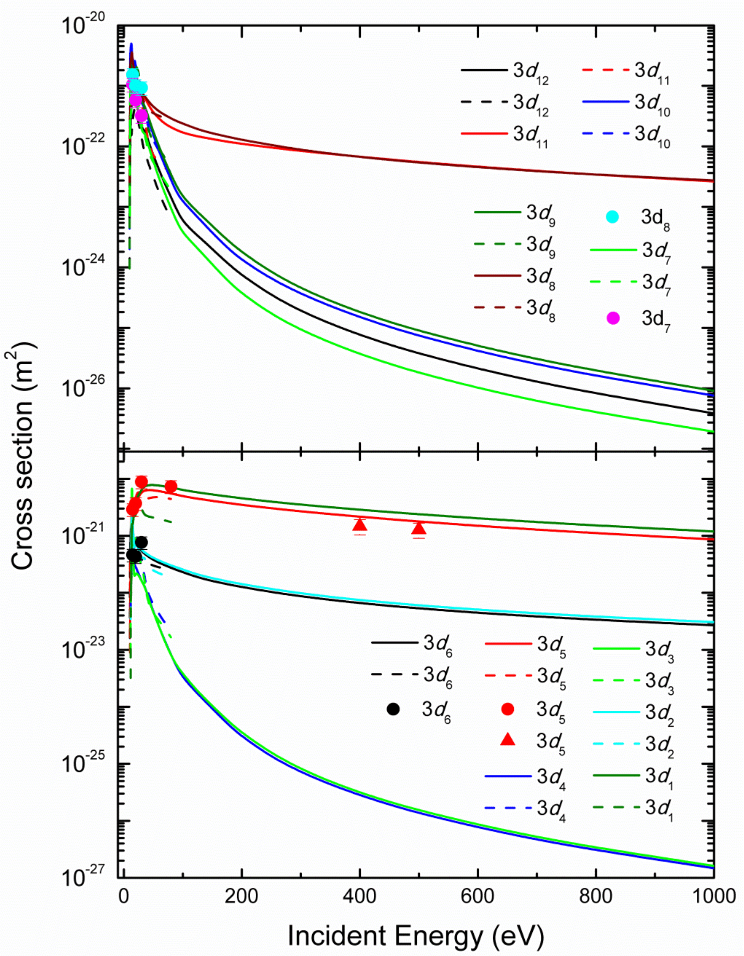

Figure 4.3. Electron impact excitation cross section for the transitions $1s_0$-$3d_i$ (i=1-12). Solid line denotes the present RDW calculations; dashed line represents the BSR calculations of Zatsarinny *et al.* [193], circle represents the experimental data of Filipovic *et al.* [209] and triangles represent the measurements of Suzuki *et al.* [206] .

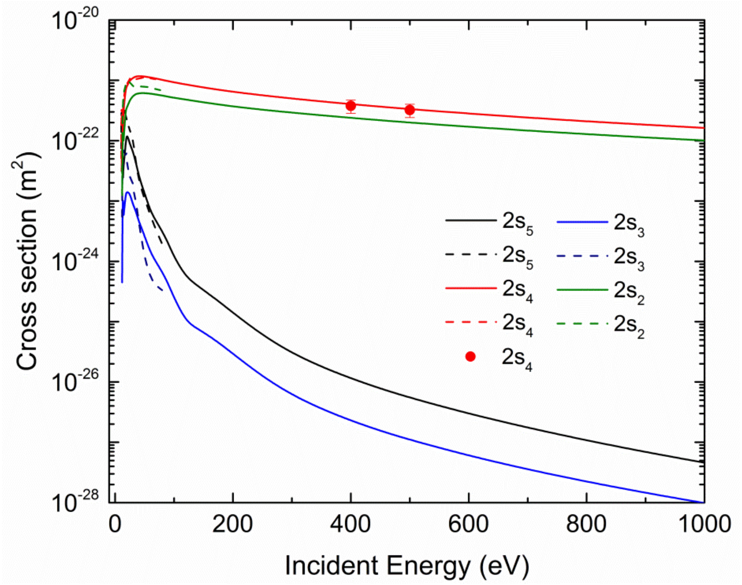

Figure4.4. Electron impact excitation cross section for the transitions $1s_0$-$2s_i$ (i=1-4). Solid line denotes the present RDW calculation; dashed line represent the BSR calculations of Zatsarinny *et al.* [193], circle represents the experimental data of Suzuki *et al.* [206] .

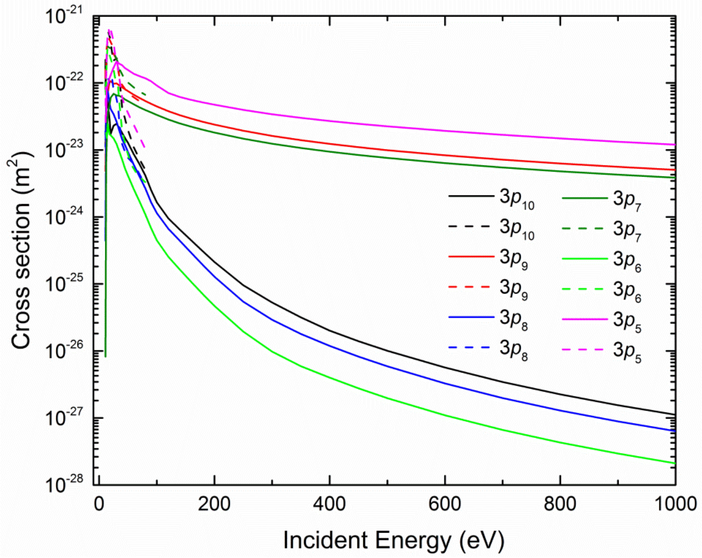

Figure4.5. Electron impact excitation cross section for the transitions 1*s*₀-3*p*ᵢ (*i*=5-10). Solid line denotes the present RDW calculations; dashed line represents the BSR calculations of Zatsarinny *et al.* [193].

Further, through figures 4.6-4.10, we present our calculated cross sections for the excitation from the four $1s_i$ levels of $5p^5 6s$ to higher excited ten $2p_i$ levels of $5p^5 6p$ and six $3p_i$ levels of $5p^5 7p$ configurations. Only experimental cross section results of Jung *et. al.*[217] are available for the $1s_5 \rightarrow 2p_6$ and $1s_5 \rightarrow 2p_8$ excitations for the impact energies up to 400 eV. In Fig. 4.6, we have compared our calculated cross sections with these experimental results and find good agreement in the entire incident energy range. Figure 4.7 show the electron impact cross section results for the excitation from the metastable states $1s_3$ and $1s_5$ to the ten ($2p_i$, i=1-10) fine structure levels of $5p^5 6p$. We find from the figure that the dipole allowed transitions ($\Delta J=0, \pm 1$), have lager cross sections as compare to the forbidden transitions which is quite expected. As we have discussed that due to spin orbit coupling, fine structure levels of $5p^5 6p$ configuration are separated into two groups. Lower lying energy levels ($6p_i$, i=5-10) have core angular momentum j_c=3/2 and higher lying levels ($6p_i$, i=1-4) have core angular momentum j_c=1/2. From the figure 4.7, we can see that the core preserving excitations have larger cross section than the core exchanging excitations. For example, cross sections for excitation from $1s_5$ (j_c=3/2) $\rightarrow 2p_i$ (i=5-10, j_c=3/2) are larger in magnitude than excitation from $1s_5$ (j_c=3/2) $\rightarrow 2p_i$ (i=1-4, j_c=3/2). Further, relative magnitude of the cross sections for allowed transitions can also be understood by the associated oscillator strengths. Transitions with greater value of oscillator strengths yield higher cross section values. For example, among all the allowed transitions from $1s_5$ to $2p_i$'s, the transition $1s_5$-$2p_8$ have largest oscillator strength (0.57) corresponds to highest cross section while $1s_5$-$2p_4$ has lowest oscillator strength (8.09e-5), corresponds to smallest cross section. We also observe that cross sections for transition from $1s_i$ to $2p_i$ are larger in magnitude than $1s_0 \rightarrow 2p_i$ transitions.

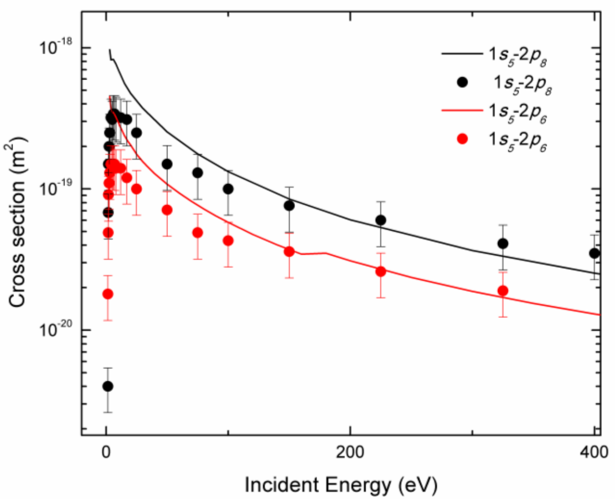

Fig.4.6. Electron impact excitation cross section for the transitions $1s_5$-$2p_6$ and $1s_5$-$2p_8$, solid lines represent the present RDW calculation and solid circles represent the experimental results of Jung *et al.*[217]

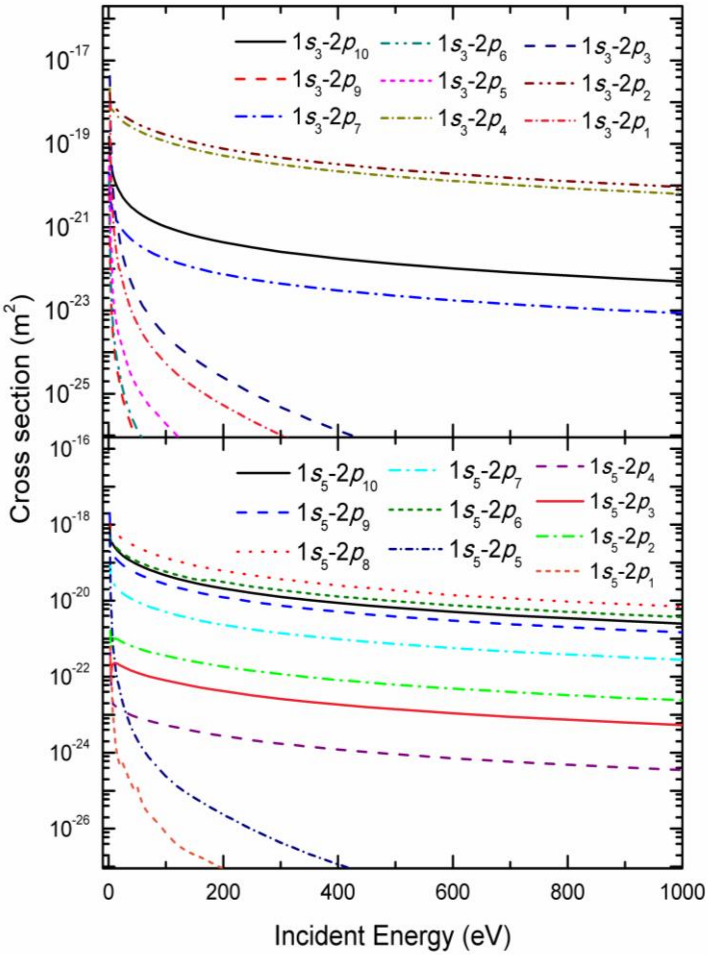

Figure 4.7: Electron impact excitation cross section for the transitions from metastable levels $1s_5$ and $1s_3 \rightarrow 2p_i$ (i=1-10).

The cross sections for the excitation from the two resonance $1s_2$ and $1s_4$ levels to the $2p_i$'s levels are also important. In fact, due to radiation trapping the population of resonance levels could be comparable to metastable state populations in the plasma; therefore, it is very essential to include these transitions in the C-R model. The calculated cross sections from resonance states ($1s_4$, $1s_2$) $\rightarrow 2p_i$ ten levels are presented in the figure 4.8 and their behavior is found to be similar as for transitions from metastable states *i.e* the cross sections for the forbidden transitions $(1s_4, 1s_2)_{J=1} \rightarrow (2p_8)_{J=3}$ have very small magnitudes in comparison to rest other dipole allowed ($\Delta J=0, \pm 1$) transitions. Also, the core preserving excitations from $1s_2$ $(j_c=1/2) \rightarrow 2p_i$ (i=1-4, j_c=1/2) are larger in magnitude than the core exchanging excitations from $1s_2$ $(j_c=1/2) \rightarrow 2p_i$ (i=5-10, j_c=3/2). There are no experimental or theoretical cross sections available for the comparison with our results of the excitation from the two resonance states to the ten $2p_i$ levels.

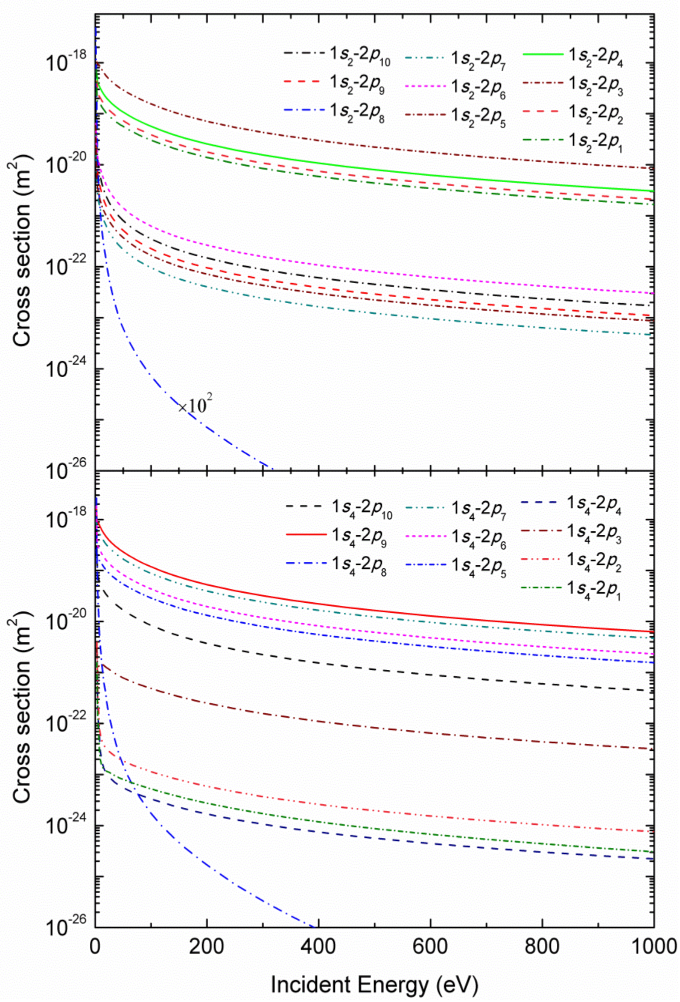

Figure 4.8. Electron impact excitation cross section for the transitions from resonance levels $1s_4$ and $1s_2 \rightarrow 2p_i$ (i=1-10).

In figures 4.9 and 4.10, we show the cross section results for the excitation from the metastable ($1s_5$, $1s_3$) and resonance ($1s_4$, $1s_2$) levels, respectively to the six $3p_i$ (i=5-10) states. Earlier, our group (Sharma *et al.* [219]) have reported the RDW cross sections for the excitations only from the metastable states to $3p_i$ levels up to incident electron energy of 300eV. Here we have revised and extended our previous calculations up to incident energy 1000 eV and obtained a complete set of cross sections results for $1s_i$ (i=1-4) $\rightarrow 3p_i$ (i=5-10) transitions. We find that the cross section curves for these transitions have similar behavior as observed for the transitions from $1s_i$ levels to the $2p_i$ levels in the figure 4.7 and 4.8. There are no measurements or theoretical calculations available for the excitation cross section of these transitions for direct comparison with our present results.

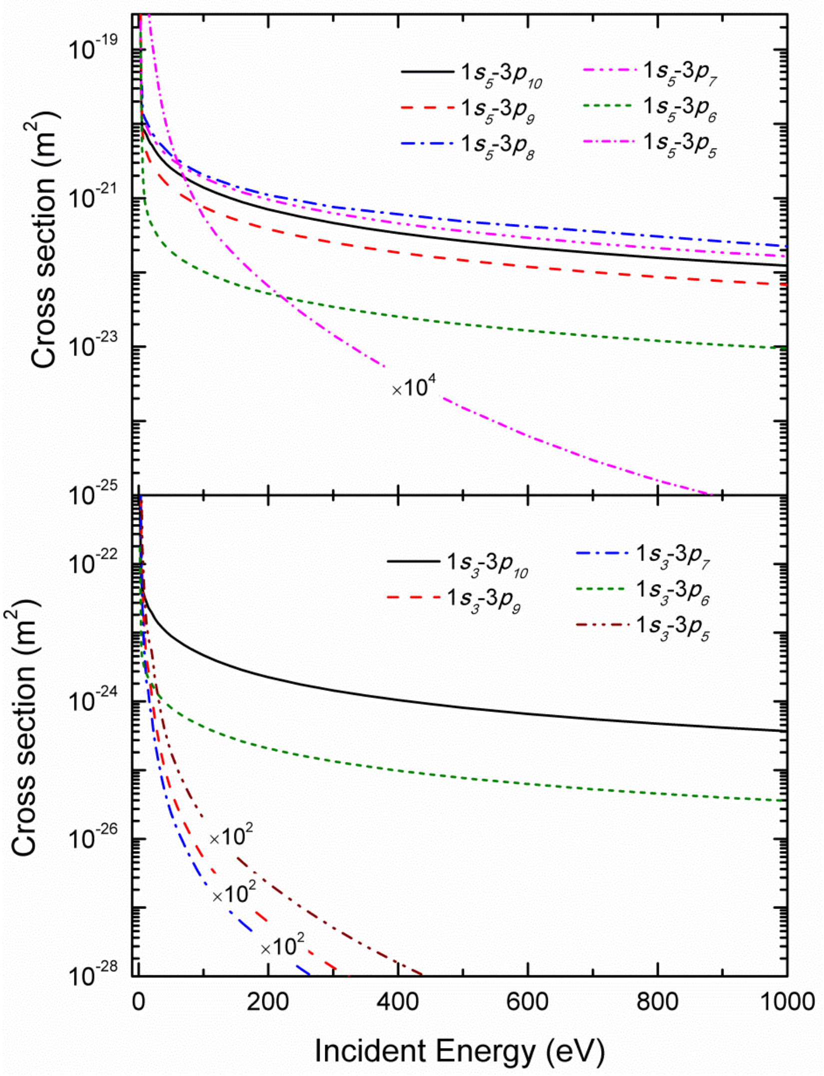

Figure 4.9. Electron impact excitation cross section for the transitions from metastable levels $1s_5$ and $1s_3 \rightarrow 3p_i$ (i=5-10).

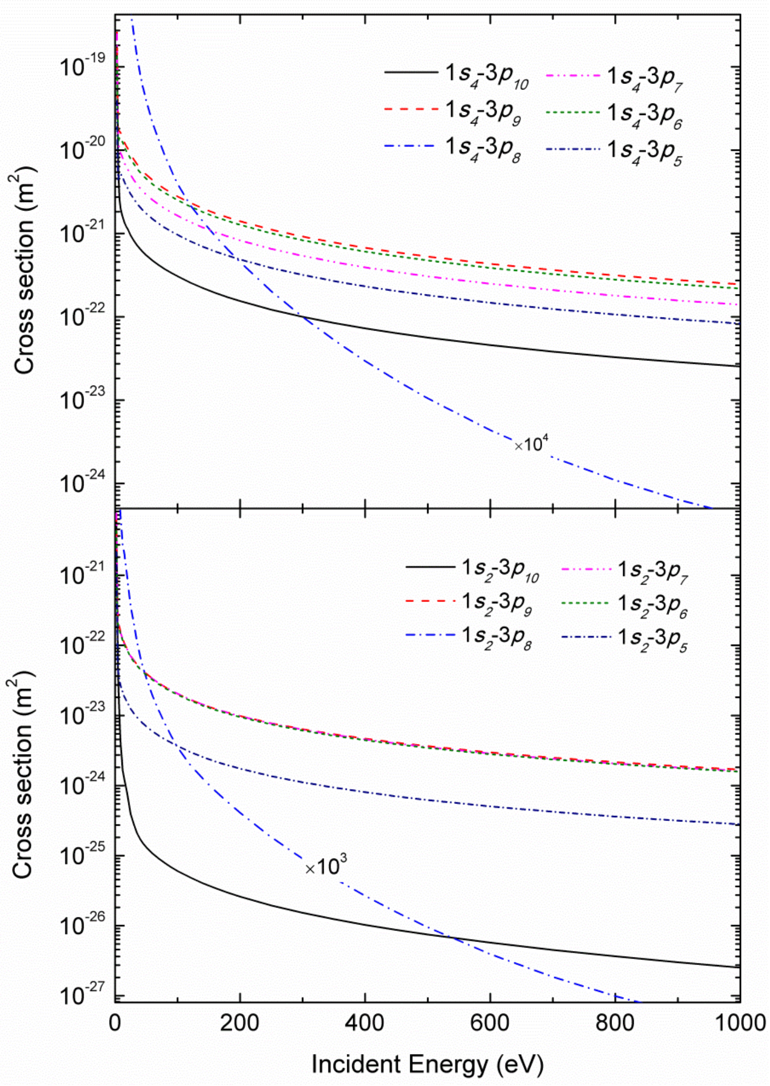

Figure4.10. Electron impact excitation cross section for the transitions from resonance levels $1s_4$ and $1s_2 \rightarrow 3p_i$ (i=5-10).

Further, through figure 4.11, we present our calculated results for intra excitations *viz.* six transitions among $1s_i$'s and 45 transitions among $2p_i$'s levels. Since transitions are taking place among the same sublevels, all the transitions are forbidden. However, their contribution can be very crucial in the modeling of xenon plasma and should be included in the model. In fact, in our earlier studies[13, 144], we have shown the significance of including these inter-excitations in the modeling of Ar and Kr plasma. From the figure 4.11, we notice that the cross section curves show the typical behavior of forbidden transitions as discussed earlier. In the absence of any experimental or other theoretical data for these transitions, it is difficult to comment on the magnitudes of the cross sections for these inter-excitation transitions.

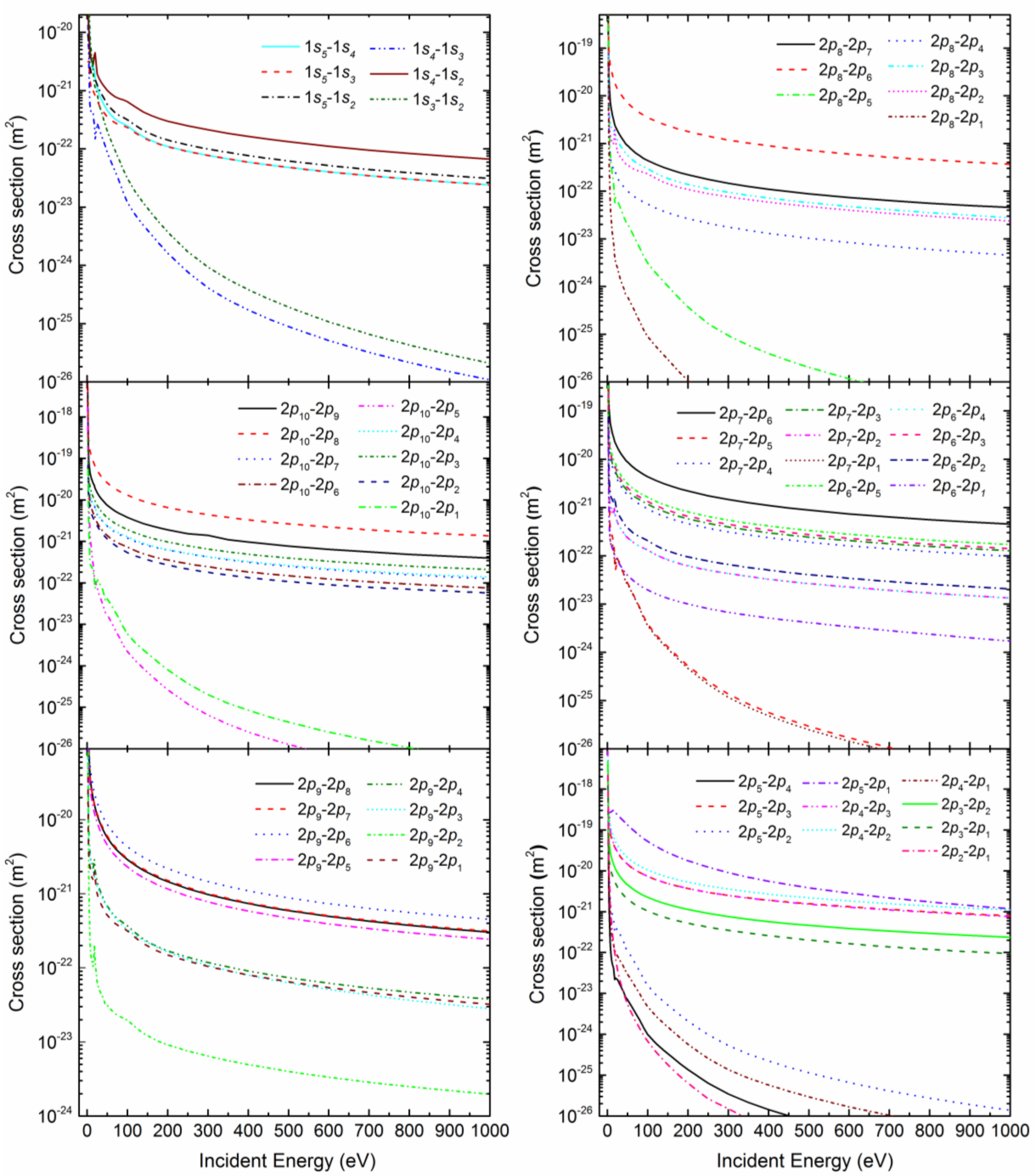

Figure 4.11. Electron impact excitation cross section for the intra-transitions among $1s_i$ (i=1-4) and $2p_i$ (i=1-10) levels.

4.4 Analytical fittings of the cross sections

In order to utilize the calculated cross section data directly in various plasma models, these are also fitted with suitable analytical expressions for electron incident energy up to 1KeV by the following expressions

$$\sigma = b_0 E^{b1} a_0^2 \tag{4.4.1}$$

$$\sigma = \frac{\sum_{i=0}^{n} b_i E^i}{c_0 + c_1 E + c_2 E^2} a_0^2 \tag{4.4.2}$$

where σ is in units of a_0^2 (0.28 × 10−20 m^2), E is the incident electron energy in atomic units (27.211 eV) and b_i, c_0, c_1 and c_2 are the fitting coefficients given in the table 4.2 The accuracy of the fitted cross sections is within 5%.

Table4.2 Fitting coefficients for the electron impact excitation cross sections. The number in the parenthesis stands for the multiplying power of 10.

Transition	***Energy Interval (eV)***	***Equation used***	***b0***	***b1***	***b2***	***b3***	***c0***	***c1***	***c2***
$1s_0 \rightarrow 1s_5$	E_{th}-90	(4.4.2)	7.88600(-2)				3.03614(+0)	-6.6126(+0)	4.01724(+0)
	90-1000	(4.4.2)	4.6820(-2)				5.28381(+1)	-3.8888(+1)	8.05832(+0)
$1s_0 \rightarrow 1s_4$	E_{th}-1000	(4.4.2)	-4.50779(+0)	1.70340(+1)	5.56969(-4)	-4.3196(+0)	1.0217(-1)	8.01800(-2)	2.5299(-1)
$1s_0 \rightarrow 1s_3$	E_{th}-40	(4.4.2)	-1.602(-1)	5.5439(-1)	-1.362(-2)	8.37878(+1)	-7.9799(+1)	3.09846(+1)	-1.8364(+2)
	40-80	(4.4.2)	6.02229(+0)				6.28576(+2)	-1.1946(+3)	8.71118(+2)
	80-1000	(4.4.1)	4.913(-2)	-3.4094(+0)					
$1s_0 \rightarrow 1s_2$	E_{th}-200	(4.4.2)	-2.4261(+0)	8.12922(+0)	3.05089e-4	-2.7220(+0)	1.3342(-1)	1.1941(-1)	3.3396(-1)
	200-1000	(4.4.2)	-2.524(-2)	-3.1378(+1)			-6.6090(+1)	-6.9982(+0)	-4.5787(+0)
$1s_0 \rightarrow 2p_{10}$	E_{th}-80	(4.4.2)	1.991(-2)	-9.7100(-3)	7.46646(-4)	-5.0700(-2)	-6.0716(+1)	1.07574(+2)	-5.1771(+1)
	80-200	(4.4.2)	1.09844(+0)				3.31885(+2)	-4.1171(+2)	1.29177(+2)
	200-1000	(4.4.2)	-3.1026(-5)	2.25904(-7)	6.89787(-5)		1.80309(+2)	-5.3398(+1)	4.18524(+0)
$1s_0 \rightarrow 2p_9$	E_{th}-100	(4.4.2)	-1.85207(+0)	1.02185(+1)	-4.2500(-3)	1.46791(+4)	-1.02890(+2)	-2.51388(+2)	-1.44089(+3)
	100-1000	(4.4.2)	1.3479(+0)				2.13171(+0)	3.92097(+0)	7.62638(-4)
$1s_0 \rightarrow 2p_8$	E_{th}-100	(4.4.2)	-5.4400(-3)	1.59156(+5)			3.26813(+6)	-6.79295(+6)	7.75208(+6)
	100-200	(4.4.2)	-6.2454(-4)	5.1328(-1)			-1.31937(+3)	3.69968(+2)	6.03261(+1)
	200-1000	(4.4.2)	-2.6894(-5)	2.01277(-7)	6.3865(-5)		1.69953(+2)	-5.35157(+1)	4.4449(+0)
$1s_0 \rightarrow 2p_7$	E_{th}-80	(4.4.2)	3.4010(-2)				1.28149(+1)	-1.81487(+1)	9.25374(+0)
	80-300	(4.4.2)	3.576(-2)	-3.56084(+0)					
	300-1000	(4.4.1)	3.011(-2)	-3.5337(+0)					

$1s_0\rightarrow2p_6$	E_{th}-50	(4.4.2)	-3.0920(-2)	-8.4500(-3)	3.47072(+1)		1.73484(+2)	-3.37690(+2)	4.97165(+2)
	50-1000	(4.4.2)	7.5561(-1)				4.50319(+0)	5.88171(+0)	1.25700(-2)
$1s_0\rightarrow2p_5$	E_{th}-70	(4.4.2)	1.08177(+0)	2.5260(-2)			9.3725(-1)	-1.57115(+0)	6.8408(-1)
	70-200	(4.4.2)	-3.8067(-1)	3.5950(-2)	8.6913(-1)		1.50116(+1)	-1.15878(+1)	2.85641(+0)
	200-1000	(4.4.2)	-2.85057(+0)	-2.1500(-3)	4.44743(+0)		3.55872(+0)	-1.58908(+0)	1.49774(+0)
$1s_0\rightarrow2p_4$	E_{th}-25	(4.4.2)	2.91056(-4)	2.984(-2)			5.15571(+0)	-1.53499(+1)	1.34244(+1)
	25-80	(4.4.2)	2.01595(+0)				2.72785(+2)	-3.67033(+2)	2.74655(+2)
	80-200	(4.4.1)	5.2600(-2)	-3.47363(+0)					
	200-1000	(4.4.1)	5.5250(-2)	-3.49995(+0)					
$1s_0\rightarrow2p_3$	E_{th}-100	(4.4.2)	2.6500(-3)	1.2460(-1)			2.23443(+0)	-1.40455(+0)	1.32645(+0)
	100-1000	(4.4.2)	1.62014(+0)				7.60978(+0)	1.07492(+1)	5.2500(-3)
$1s_0\rightarrow2p_2$	E_{th}-20	(4.4.2)	2.5758(-4)				5.43811(+0)	-2.21182(+1)	2.24981(+1)
	20-100	(4.4.2)	-1.4955(-1)	4.0044(-1)	-2.3700(-3)	3.3853(+0)	-3.70743(+0)	-1.37432(+0)	-8.99866(+0)
	100-300	(4.4.2)	-3.7367(-5)	1.1530(-2)			1.77247(+2)	-1.46118(+2)	3.18773(+1)
	300-1000	(4.4.2)	3.6810(-2)	-3.3045(+0)					
$1s_0\rightarrow2p_1$	E_{th}-50	(4.4.2)	1.9487(-1)	-1.1222(-1)	7.7131(-1)		1.16743(+0)	-1.96961(+0)	1.21951(+0)
	50-100	(4.4.2)	4.24344(+0)				1.34169(+0)	7.8567(-1)	-2.9950(-2)
	100-1000	(4.4.2)	7.2682(-1)	-2.2216(-1)	-1.20707(-5)	1.24058(+0)	-7.64686(+1)	1.45190(+1)	5.63878(+0)
$1s_0\rightarrow3d_{12}$	E_{th}-80	(4.4.2)	-9.8360(-2)	7.400(-3)	6.3340(-2)		3.5772(-1)	-1.1701(+0)	1.126(+0)
	80-200	(4.4.2)	-4.3580(-4)	1.9287(-1)			-4.23458(+1)	-9.87351(+1)	5.01666(+1)
	200-1000	(4.4.1)	2.1027(-1)	-3.3464(+0)					
$1s_0\rightarrow3d_{11}$	E_{th}-30	(4.4.2)	-1.45404(+0)	-2.09710(-1)	-9.97441(+1)		-1.52676(+1)	4.79767(+1)	-8.26163(+1)
	30-100	(4.4.2)	1.09187(+0)				6.56610(-1)	2.31191(+0)	8.71540(-1)
	100-1000	(4.4.2)	1.46058(+0)				1.27910(+1)	3.18579(+0)	1.15100(-2)

$1s_0\rightarrow 3d_{10}$	E_{th}-45	(4.4.2)	2.42800(-2)	6.45350(-1)			1.65558(+0)	-7.11242(+0)	8.60701(+0)
	45-200	(4.4.1)	4.9143(-1)	-3.59328(+0)					
	200-1000	(4.4.1)	2.7547(-1)	-3.18961(+0)					
$1s_0\rightarrow 3d_9$	E_{th}-50	(4.4.2)	-2.88100(-2)	-2.82902(+1)			-1.04465(+2)	3.17457(+2)	-3.06908(+2)
	50-200	(4.4.2)	-2.16259(+0)	-3.0900(-3)	-1.03503(+0)		1.25560(-1)	-6.17100(-2)	-4.67440(-1)
	200-1000	(4.4.2)	-1.47000(-3)	-1.40548(-6)	2.27300(-2)		-4.59088(+2)	3.64836(+1)	1.42697(+1)
$1s_0\rightarrow 3d_8$	E_{th}-20	(4.4.2)	1.120400(-1)	1.77303(+0)			9.64883(+0)	-3.71305(+1)	3.93383(+1)
	20-100	(4.4.2)	-2.6500(-2)	2.36829(+0)			-4.29194(+0)	6.75957(+0)	4.34695(+0)
	100-1000	(4.4.2)	1.5524(+0)				2.66006(+0)	4.29045(+0)	-3.0200(-3)
$1s_0\rightarrow 3d_7$	E_{th}-50	(4.4.2)	-1.1400(-2)	1.41500(-1)			1.08462(+0)	-3.84366(+0)	3.99027(+0)
	50-200	(4.4.2)	2.06980(-1)	-3.79297(+0)					
	200-1000	(4.4.1)	1.16980(-1)	-3.40313(+0)					
$1s_0\rightarrow 3d_6$	E_{th}-35	(4.4.2)	6.42880(-1)				-1.17764(+0)	6.5669(+0)	-2.11421(+0)
	35-100	(4.4.2)	1.08081(+0)				1.89827(+0)	3.53006(+0)	-1.37970(-1)
	100-1000	(4.4.2)	1.33677(+0)				3.06064(+0)	3.62464(+0)	1.2600(-3)
$1s_0\rightarrow 3d_5$	E_{th}-35	(4.4.2)	-8.0515(-1)	1.89286(+0)	2.76790(-1)		1.49686(+0)	-3.45426(+0)	2.24947(+0)
	35-200	(4.4.2)	6.0566(-1)	1.6763(+0)			8.77930(-1)	-9.18300(-2)	3.45570(-1)
	200-1000	(4.4.2)	1.57614(+2)				6.08101(+1)	8.12006(+0)	1.11670(-1)
$1s_0\rightarrow 3d_4$	E_{th}-18	(4.4.2)	3.0188(-1)				-4.09868(+0)	1.11540(+1)	-1.42798(+0)
	18-140	(4.4.2)	7.7392(-1)	-1.2600(-3)	6.8469(-1)		-2.17920(-1)	1.19130(-1)	-9.07650(-1)
	140-1000	(4.4.2)	1.3680(-2)				2.25236(+2)	-9.42161(+1)	1.10151(+1)
$1s_0\rightarrow 3d_3$	E_{th}-20	(4.4.2)	3.16690(-1)				-2.9231(+0)	8.32259(+0)	1.98020(-1)
	20-100	(4.4.2)	1.69360(-1)	-1.17160(-1)	1.1870(-2)	-2.08200(-1)	-1.26118(+2)	6.85999(+1)	-1.68232(+1)
	100-1000	(4.4.1)	9.93800(-2)	-3.28886(+0)					

$1s_0 \to 3d_2$	E_{th}-20	(4.4.2)	3.85300(-2)				1.83866(+0)	-6.38005(+0)	5.76752(+0)
	20-100	(4.4.2)	1.13857(+0)				1.76396(+0)	3.67940(+0)	-2.27180(-2)
	100-1000	(4.4.2)	1.73827(+0)				3.84003(+0)	4.17096(+0)	4.35195(-5)
$1s_0 \to 3d_1$	E_{th}-100	(4.4.2)	-1.5644(+0)	-3.1241(-1)	7.73272(+0)		8.4738(-1)	-6.1488(-1)	1.65611(+0)
	100-1000	(4.4.2)	9.79417(+3)				2.71759(+3)	4.27864(+2)	3.09543(+0)
$1s_0 \to 2s_5$	E_{th}-25	(4.4.2)	1.87500(-2)				7.98561(+0)	-1.94078(+1)	1.23603(+1)
	25-90	(4.4.2)	5.2110(-2)				1.01764(+1)	-1.91057(+1)	1.07106(+1)
	90-300	(4.4.2)	-1.8042(-4)	1.1920(-2)			-2.19808(+2)	7.83288(+1)	3.96650(-1)
	300-1000	(4.4.1)	3.4020(-2)	-3.35735(+0)					
$1s_0 \to 2s_4$	E_{th}-1000	(4.4.2)	-7.73170(-1)	2.28699(+0)	6.04454(-5)	-6.5200(-1)	1.7293(-1)	1.1387(-1)	2.8447(-1)
$1s_0 \to 2s_3$	E_{th}-45	(4.4.2)	2.039(-4)	2.5610(-2)			3.19439(+1)	-7.37374(+1)	4.82088(+1)
	45-90	(4.4.2)	0.00992				1.910001+1)	-2.70742(+1)	-2.70742(+1)
	90-250	(4.4.2)	-1.9024e-5	1.700(-3)			-1.54123(+2)	3.81556(+1)	5.52391(+0)
	250-1000	(4.4.1)	0.01362	-3.62666(+0)					
$1s_0 \to 2s_2$	E_{th}-1000	(4.4.2)	-1.63080(-1)	4.51330(-1)	1.53623(-5)	-1.1200(-1)	2.0790(-1)	1.1236(-1)	2.4748(-1)
$1s_0 \to 3p_{10}$	E_{th}-20	(4.4.2)	-1.45489(+0)				-2.17309(+3)	7.96713(+7)	7.96713(+7)
	20-100	(4.4.2)	2.80554(+0)				1.52833(+3)	-1.84701(+3)	8.35098(+2)
	100-300	(4.4.2)	1.76300(-2)				8.68011(+1)	-5.54937(+1)	1.20163(+1)
	300-1000	(4.4.1)	3.27200(-2)	-3.27681(+0)					
$1s_0 \to 3p_9$	E_{th}-50	(4.4.2)	-3.86900(-2)	4.1200(-3)	4.04266(+0)		2.70757(+1)	-7.00884(+1)	1.11882(+2)
	50-1000	(4.4.2)	4.75001(-5)	1.6928(-1)			2.38075(+0)	9.28150(-1)	3.93238(+0)
$1s_0 \to 3p_8$	E_{th}-30	(4.4.2)	1.254(-2)	-5.8200(-3)	-8.60317(+2)		-2.60438(+6)	9.26907(+6)	-8.34585(+6)
	30-120	(4.4.2)	2.038(-2)	5.1530(-2)	-1.83192(-6)	-2.321(-1)	9.86550(-1)	-1.89287(+0)	4.51669(+0)
	120-1000	(4.4.1)	1.605(-2)	-3.10058(+0)					

$1s_0\rightarrow3p_7$	E_{th}-100	(4.4.2)	-5.9930(-2)	1.8123(-1)	-2.0200(-3)	3.92581(+0)	-1.29552(+1)	-1.08862(+0)	-2.40140(+1)
	100-1000	(4.4.2)	8.2791(-1)				1.68058(+1)	2.38339(+1)	8.3900(-3)
$1s_0\rightarrow3p_6$	E_{th}-45	(4.4.2)	5.34162(+0)				2.07437(+3)	-2.95325(+3)	2.52437(+3)
	45-160	(4.4.2)	8.0700(-3)	7.6330(-2)	-2.32737(-5)	-3.400(-1)	3.21090(-1)	-6.0698(-1)	4.47756(+0)
	160-1000	(4.4.2)	-2.79271(+0)				-7.88639(+5)	2.85661(+5)	-2.89521(+4)
$1s_0\rightarrow3p_5$	E_{th}-35	(4.4.2)	1.46950(-1)				4.19827(+0)	-6.24999(+0)	2.7539(+0)
	35-100	(4.4.2)	1.64956(+0)				3.66159(+0)	3.2739(+0)	3.3790(-2)
	100-1000	(4.4.1)	2.807(-1)	-8.554(-1)					
$1s_2\rightarrow2p_{10}$	E_{th}-20	(4.4.2)	-1.93868(+0)	3.45006(+1)	-8.18927(+0)		2.4990(-2)	-3.22893(+0)	4.66562(+1)
	20-1000	(4.4.2)	2.35151(+0)	1.1469(-1)	-6.93693(-4)		-4.1698(-1)	4.05444(+0)	5.6082(-1)
$1s_2\rightarrow2p_9$	E_{th}-20	(4.4.2)	-1.79038(+0)	2.79536(+1)	-8.12065(+0)		-1.2387(-1)	-1.70753(+0)	5.32357(+1)
	20-1000	(4.4.2)	1.63445(+0)	6.9840(-2)	-3.40114(-4)		-4.1133(-1)	4.39629(+0)	5.6770(-1)
$1s_2\rightarrow2p_8$	E_{th}-20	(4.4.2)	2.33480(-1)				2.68091(+0)	-1.04710(+2)	7.59426(+2)
	20-200	(4.4.1)	1.53689(-4)	-3.25667(+0)					
	200-1000	(4.4.1)	7.88079(-4)	-4.03082(+0)					
$1s_2\rightarrow2p_7$	E_{th}-10	(4.4.2)	1.06325(+0)				-4.5634(-1)	1.24871(+1)	-1.28436(+1)
	10-100	(4.4.2)	9.63470(-1)				1.89410(-1)	5.13911(+0)	7.9036(-1)
	100-1000	(4.4.2)	1.07185(+0)				-4.62126(+0)	8.8324(+0)	2.5812(-1)
$1s_2\rightarrow2p_6$	E_{th}-18	(4.4.2)	2.6498(+0)				9.1790(-2)	2.57822(+0)	-4.4464(-1)
	18-100	(4.4.2)	1.20897(+0)				-1.3330(-2)	1.10038(+0)	1.0900(-1)
	100-1000	(4.4.2)	3.12326(+0)				-2.03712(+0)	3.9344(+0)	1.1455(-1)
$1s_2\rightarrow2p_5$	E_{th}-10	(4.4.2)	9.1161(-1)				-2.9309(-1)	7.9165(+0)	-8.93628(+0)
	10-100	(4.4.2)	9.8334(-1)				3.5007(-1)	3.04354(+0)	4.1932(-1)
	100-1000	(4.4.2)	3.5526(+0)				-8.68198(+0)	1.70321(+1)	4.2124(-1)

$1s_2 \rightarrow 2p_4$	E_{th}-50	(4.4.2)	1.87836(+0)	-3.25517(+0)	-2.16219(+9)		-5.25409(+6)	-5.34584(+6)	-3.54809(+5)
	50-200	(4.4.2)	1.39529(+2)				7.49390(-1)	1.42922(+0)	7.0000(-2)
	200-1000	(4.4.2)	-4.52210(-1)	3.05633(+5)			5.58590(+4)	-1.91020(+4)	5.90528(+3)
$1s_2 \rightarrow 2p_3$	E_{th}-100	(4.4.2)	-4.69982(+0)	3.04626(+9)			1.10467(+5)	6.01646(+6)	1.20634(+7)
	100-1000	(4.4.2)	1.85154(+3)	4.72491(+7)			-3.21260(+3)	-2.54285(+4)	-1.28085(+0)
$1s_2 \rightarrow 2p_2$	E_{th}-100	(4.4.2)	1.79815(+4)				1.44766(+2)	3.08812(+2)	-1.57991(+0)
	100-1000	(4.4.2)	1.62946(+2)				5.0563(-1)	2.73418(+0)	9.43100(-2)
$1s_2 \rightarrow 2p_1$	E_{th}-100	(4.4.2)	7.26060(-1)				8.9600(-3)	1.3660(-2)	6.74697(-4)
	100-1000	(4.4.2)	1.46527(+2)				4.8346(-1)	3.17484(+0)	1.0340(-1)
$1s_3 \rightarrow 2p_{10}$	E_{th} -10	(4.4.2)	5.2976(+1)				-4.4000(-2)	4.0975(+0)	-3.9228(+0)
	10-1000	(4.4.2)	1.4071(+1)	1.1100(-3)	7.1165(+2)		-1.9707(+0)	-5.1316(+0)	-5.0370(+1)
$1s_3 \rightarrow 2p_9$	E_{th} -20	(4.4.2)	3.9048e+0				9.0941e+2	-1.9226e+4	1.0925e+5
	20-300	(4.4.2)	2.0734e-5	-3.3033e+0					
	300-1000	(4.4.2)	3.7034e-4	-4.5519e+0					
$1s_3 \rightarrow 2p_7$	E_{th} -10	(4.4.2)	1.5408e+0				9.3580e-2	8.1152e+0	-6.9688e+0
	10-200	(4.4.2)	1.4604e+0	1.6700e-3	5.4206e+1		-1.9582e+0	-7.1655e+0	-3.6481e+1
	200-1000	(4.4.2)	1.4436e+0				-5.9308e+0	7.0601e+0	1.6550e-1
$1s_3 \rightarrow 2p_6$	E_{th}-10	(4.4.2)	3.2290(-2)				4.2454(+0)	-9.0377(+1)	5.1407(+2)
	10-300	(4.4.1)	3.7715(-5)	-2.9783(+0)					
	300-1000	(4.4.1)	6.1656(-4)	-4.5518(+0)					
$1s_3 \rightarrow 2p_5$	E_{th}-10	(4.4.1)	4.5790(-5)	-4.1147(+0)					
	10-200	(4.4.1)	2.8912(-4)	-2.7052(+0)					
	200-1000	(4.4.1)	9.3760(-4)	-3.5701(+0)					
$1s_3 \rightarrow 2p_4$	E_{th}-20	(4.4.2)	3.4357(-6)	4.8063(-7)	2.2660(-6)	2.3146(+7)	4.9307(+2)	-6.6931(+2)	-4.7232(+4)
	20-300	(4.4.2)	2.9420(+2)				9.9270(-2)	1.4493(-1)	7.1800(-3)
	300-1000	(4.4.2)	6.5692(+3)				-3.6586(+1)	4.5181(+1)	9.8724(-1)
$1s_3 \rightarrow 2p_3$	E_{th}-10	(4.4.2)	7.3481(-1)				1.7417(-1)	-2.4551(+0)	9.4552(+0)
	10-200	(4.4.1)	6.0840(-2)	-3.0874(+0)					

	200-1000	(4.4.1)	5.3314(-1)	-4.3205(+0)					
$1s_3\rightarrow 2p_2$	E_{th}-20	(4.4.2)	2.9483(-4)	2.0089(-3)	6.5456(-4)	-2.0241(+4)	-2.0241(+4)	1.31256(+0)	6.15596(+0)
	20-1000	(4.4.2)	4.8482(+1)				1.2252(-1)	1.6453(-1)	7.6500(-3)
$1s_3\rightarrow 2p_1$	E_{th}-10	(4.4.2)	-7.5782(-1)	1.1885(+1)			-1.1100(+0)	5.0443(+0)	2.43598(+1)
	10-300	(4.4.1)	1.0480(-2)	-3.2194(+0)					
	300-1000	(4.4.1)	1.8262(-1)	-4.5049(+0)					
$1s_4\rightarrow 2p_{10}$	E_{th}-8	(4.4.2)	8.1008(+0)				-3.8427(-1)	5.61968(+0)	-1.03704(+1)
	8-100	(4.4.2)	3.11615(+0)				7.6280(-2)	2.46980(-1)	9.81388(-4)
	100-1000	(4.4.2)	5.06452(+1)				-6.5874(-1)	4.26404(+0)	1.36630(-1)
$1s_4\rightarrow 2p_9$	E_{th}-200	(4.4.2)	7.30143(+3)				1.75047(+1)	3.38148(+1)	2.61519(+0)
	200-1000	(4.4.2)	1.55083(+4)				-6.01102(+2)	1.01925(+2)	2.44272(+0)
$1s_4\rightarrow 2p_8$	E_{th}-10	(4.4.2)	1.56324(+0)				1.6679(-1)	-3.41201(+0)	1.83525(+1)
	10-100	(4.4.1)	4.00300(-2)	-3.11036(+0)					
	100-200	(4.4.1)	4.31300(-2)	-3.26142(+0)					
	200-1000	(4.4.1)	1.89030(-1)	-4.03215(+0)					
$1s_4\rightarrow 2p_7$	E_{th}-20	(4.4.2)	3.16921(+2)	1.80566(+1)	2.04349(+2)	5.3340(+7)	1.12368(+2)	8.35765(+3)	-1.32047(+5)
	20-100	(4.4.2)	1.69554(+1)				6.41500(-2)	1.1017(-1)	5.0700(-3)
	100-1000	(4.4.2)	5.55142(+2)				-9.70400(-2)	4.3373(+0)	1.3799(-1)
$1s_4\rightarrow 2p_6$	E_{th}-20	(4.4.2)	2.07305(+2)	-1.84207(+3)	1.26024(+7)		5.01685(+2)	7.02169(+3)	1.8115(-1)
	20-100	(4.4.2)	7.78042(+0)				6.05800(-2)	1.0319(-1)	4.3300(-3)
	100-1000	(4.4.2)	2.07489(+2)				1.32200(-2)	3.2528(+0)	1.0482(-1)
$1s_4\rightarrow 2p_5$	E_{th}-12	(4.4.2)	-5.59063(+1)	3.04345(+3)	-1.45096(+8)		2.81348(+3)	4.43263(+4)	2.14758(+3)
	12-90	(4.4.2)	1.03012(+1)				1.13360(-1)	2.3264(-1)	8.12585(-5)
	90-1000	(4.4.2)	-3.60460(-1)	2.03815(+1)			1.8713(+0)	-9.8003(-1)	6.47030(-1)
$1s_4\rightarrow 2p_4$	E_{th}-8	(4.4.2)	1.82500(-2)	2.58170(-1)			3.00163(+0)	-5.14172(+1)	2.22968(+2)

	8-100	(4.4.2)	1.84015(+0)	8.37532(+0)		-6.69009(+2)	2.88052(+3)	1.24231(+3)
	100-1000	(4.4.2)	1.04075(+0)			1.73205(+2)	1.71234(+3)	5.48578(+0)
$1s_4\rightarrow 2p_3$	E_{th}-20	(4.4.2)	2.88800(-2)	2.78014(+0)		1.16761(+0)	-1.13390(-1)	6.68216(+0)
	20-1000	(4.4.2)	1.05361(+0)			1.52221(+0)	1.13453(+0)	3.5380(-2)
$1s_4\rightarrow 2p_2$	E_{th}-20	(4.4.2)	1.52110(-1)	-5.3315(-1)	2.0081(+0)	2.86273(+0)	-4.40240(+1)	1.85352(+2)
	20-100	(4.4.2)	8.4633(+0)			4.04477(+2)	4.75891(+2)	-1.42086(+0)
	100-1000	(4.4.2)	2.35729(+0)			1.33829(+2)	1.07166(+2)	3.78116(+0)
$1s_4\rightarrow 2p_1$	E_{th}-10	(4.4.2)	2.9136(-1)	-1.0477(+0)	1.7213(+0)	-1.13992(+0)	-1.07816(+1)	2.03993(+2)
	10-100	(4.4.2)	-1.74751(+1)	6.98075(+1)	-3.71225(+0)	-3.97648(+3)	1.25113(+4)	4.44099(+3)
	100-1000	(4.4.2)	3.0300(+0)			5.26864(+2)	2.45542(+2)	1.3986(+1)
$1s_5\rightarrow 2p_{10}$	E_{th}-1000	(4.4.2)	2.6098(+1)			1.5121(-1)	3.2918(-1)	1.6700(-2)
$1s_5\rightarrow 2p_9$	E_{th}-10	(4.4.2)	3.9755(-4)	7.2257(+5)		-3.0221(+3)	2.5272(+4)	8.0032(+4)
	10-1000	(4.4.2)	1.0122(+1)			1.0684(-1)	2.312(-1)	7.4400(-2)
$1s_5\rightarrow 2p_8$	E_{th}-1000	(4.4.2)	3.6499(+2)	1.2666(-1)	-3.9480(+4)	6.1273(+0)	6.5354(+1)	1.0580(+2)
$1s_5\rightarrow 2p_7$	E_{th}-10	(4.4.2)	7.0814(+0)			1.9165(-1)	2.3946(+0)	-2.5172(+0)
	10-1000	(4.4.2)	2.5173(+0)			1.5313(-1)	3.1449(-1)	8.6500(-3)
$1s_5\rightarrow 2p_6$	E_{th}-10	(4.4.2)	7.3764(-6)	1.8704(+8)		-2.4360(+5)	3.6945(+6)	6.2914(+6)
	10-1000	(4.4.2)	2.3404(+1)			1.3008(-1)	2.5480(-1)	4.5500(-3)
$1s_5\rightarrow 2p_5$	E_{th}-10	(4.4.2)	1.2579(+1)			4.0798(+1)	-5.4764(+2)	2.0071(+3)
	10-200	(4.4.1)	4.9200(-3)	-3.1775(+1)				
	200-1000	(4.4.1)	3.4700(-2)	-4.1720(+1)				
$1s_5\rightarrow 2p_4$	E_{th}-10	(4.4.2)	4.8510(-2)			-2.6937(+0)	2.42388(+1)	2.8147(+1)
	10-200	(4.4.2)	2.0074(+1)			2.2740(+2)	2.37348(+2)	-1.1196(+0)
	200-1000	(4.4.2)	1.4891(+2)			7.0555(+3)	1.64423(+4)	4.3993(+2)

$1s_5\rightarrow 2p_3$	E_{th}-10	(4.4.2)	1.6970(-2)	1.6418(-1)	1.2860(-2)		1.1657(+0)	-9.5431(+0)	2.0322(+1)
	10-1000	(4.4.2)	-2.1300(-3)	7.9129(+4)			4.8117(+4)	6.0709(+5)	5.5174(+5)
$1s_5\rightarrow 2p_2$	E_{th}-10	(4.4.2)	9.0160(-2)	6.7293(-1)	6.7626(-1)		1.0771(+1)	-8.7902(+1)	1.8948(+2)
	10-1000	(4.4.2)	8.2549(-1)				1.8115(+0)	1.1182(+0)	4.6650(-2)
$1s_2\rightarrow 3p_{10}$	E_{th}-10	(4.4.2)	4.1190(-2)				6.73157(+0)	-1.23997(+2)	5.72745(+2)
	10-50	(4.4.2)	1.1200(-3)	-4.22524(-5)	-2.44540(+3)		9.19987(+5)	-1.20211(+6)	2.84579(+6)
	50-1000	(4.4.2)	6.48625(+0)				-6.12401(+2)	6.95946(+4)	3.45953(+3)
$1s_2\rightarrow 3p_9$	E_{th}-100	(4.4.2)	1.7278(-1)	-3.02942(+0)			2.64576(+0)	1.77407(+1)	-4.5890(-2)
	100-1000	(4.4.2)	7.3926(-1)				-2.85083(+0)	2.76950(+1)	1.7917(-1)
$1s_2\rightarrow 3p_7$	E_{th}-100	(4.4.2)	1.7020(-1)	-6.00912(-4)	-1.45681(+0)		2.49838(-4)	1.24152(+0)	8.72649(+0)
	100-1000	(4.4.2)	5.4495(-1)				-2.20961(+0)	2.01672(+1)	1.7959(-1)
$1s_2\rightarrow 3p_6$	E_{th}-20	(4.4.2)	-1.85001(+0)				-1.14948(+1)	-7.64488(+1)	4.11644(+0)
	20-100	(4.4.2)	3.02951(+1)				1.68337(+2)	1.18069(+3)	-2.1377(+1)
	100-1000	(4.4.2)	5.07240(-1)				-1.99556(+0)	1.95167(+1)	1.5854(-1)
$1s_2\rightarrow 3p_5$	E_{th}-8	(4.4.2)	4.84890(-1)	-5.6497(+0)	1.53805(+0)	2.51120(+1)	1.41920(-1)	-3.13250(-1)	6.4305(+0)
	8-100	(4.4.2)	3.43656(+0)				1.30546(+2)	7.09336(+2)	-1.23654(+1)
	100-1000	(4.4.2)	2.74324(+0)				-5.98734(+1)	5.68025(+2)	5.69003(+0)
$1s_3\rightarrow 3p_{10}$	E_{th}-100	(4.4.2)	1.10782(+0)				2.60773(+1)	2.01954(+2)	-1.06302(+0)
	100-1000	(4.4.2)	7.52618(+2)				-1.2035(+4)	1.20939(+5)	1.10548(+3)
$1s_3\rightarrow 3p_6$	E_{th}-50	(4.4.2)	4.38093(+0)				-7.76527(+1)	1.35882(+4)	-3.39477(+3)
	50-1000	(4.4.2)	2.00475(+0)				8.10604(+2)	3.23732(+3)	3.94781(+1)
$1s_4\rightarrow 3p_{10}$	E_{th}-12	(4.4.2)	4.37030(-1)	2.28398(+0)			1.22572(+0)	-1.90919(+1)	7.33136(+1)
	12-100	(4.4.2)	1.14817(+0)				7.07280(-1)	3.03214(+0)	-1.1095(-1)
	100-1000	(4.4.2)	-2.2300(-3)	6.9560(-1)			3.29049(+0)	-1.01452(+0)	1.72933(+0)

$1s_4 \rightarrow 3p_9$	E_{th}-20	(4.4.2)	4.72796(+0)	1.32800(+1)	-2.95552(+4)		9.64402(+2)	-5.7820(+2)	1.76480(+3)
	20-100	(4.4.2)	1.62336(+0)				1.24120(-1)	4.15950(-1)	1.4000(-3)
	100-1000	(4.4.2)	1.43386(+1)				9.32110(-1)	3.56902(+0)	2.6790(-1)
$1s_4 \rightarrow 3p_7$	E_{th}-10	(4.4.2)	3.22788(+1)	-4.63340(+2)	7.62004(+3)		1.80008(+0)	1.40038(+1)	2.55131(+0)
	10-100	(4.4.2)	1.48705(+0)				2.35640(-1)	6.4454(-1)	-1.7000(-1)
	100-1000	(4.4.2)	8.65538(+0)				1.26184(+0)	3.5599(+0)	3.5450(-2)
$1s_4 \rightarrow 3p_6$	E_{th}-50	(4.4.2)	-3.12793(+0)	6.63053(+1)	-3.1337(-1)	1.25e16(+0)	-9.6585(+12)	-6.0870(+12)	-1.9248(+14)
	50-1000	(4.4.2)	4.79733(+0)				6.5170(-1)	1.2337(+0)	1.4750(-2)
$1s_4 \rightarrow 3p_5$	E_{th}-50	(4.4.2)	2.5087(-1)	1.34685(+0)			1.8342(-1)	-3.9151(-1)	2.06632(+0)
	50-1000	(4.4.2)	1.7945(+0)				6.6791(-1)	1.19249(+0)	1.5150(-2)
$1s_5 \rightarrow 3p_{10}$	E_{th}-10	(4.4.2)	1.26631(+0)				7.6023(-1)	-5.0730(-2)	8.9156(-1)
	10-100	(4.4.2)	1.23649(+0)				4.8765(-1)	9.2608(-1)	2.8600(-3)
	100-1000	(4.4.2)	4.47678(+0)				1.63997(+0)	3.19858(+0)	4.5610(-2)
$1s_5 \rightarrow 3p_9$	E_{th}-10	(4.4.2)	8.31690(-1)	5.36477(+0)			-1.534(+0)	6.80779(+0)	1.77460(+1)
	10-100	(4.4.2)	1.22165(+0)				3.5609(-1)	1.36313(+0)	-1.0080(-2)
	100-1000	(4.4.2)	3.18583(+0)				8.8656(-1)	3.36855(+0)	2.2290(-2)
$1s_5 \rightarrow 3p_8$	E_{th}-20	(4.4.2)	5.52253(+0)	-4.72701(+0)	1.47964(+2)		-8.44078(+1)	4.63367(+2)	-2.5418(+2)
	20-1000	(4.4.2)	1.2855(+0)				1.51210(-1)	4.30180(-1)	-3.5833(-4)
$1s_5 \rightarrow 3p_7$	E_{th}-100	(4.4.2)	1.87187(+0)				2.86240(-1)	6.55720(-1)	1.1090(-2)
	100-1000	(4.4.2)	8.9062(+0)				1.18647(+0)	3.16357(+0)	2.8930(-2)
$1s_5 \rightarrow 3p_6$	E_{th}-10	(4.4.2)	3.83632(+0)				-6.77063(+0)	3.85629(+1)	3.92073(+1)
	10-100	(4.4.2)	6.86120(-1)				9.01200(-2)	6.00136(+0)	-2.6719(-1)
	100-1000	(4.4.2)	1.43078(+0)				2.06997(+0)	9.86759(+0)	4.8690(-2)
$1s_3 \rightarrow 1s_2$	E_{th}-20	(4.4.2)	3.3748(-1)				-8.6620(-2)	5.4087(-1)	6.5560(-1)

	20-100	(4.4.2)	3.5794(-1)				1.54674(+0)	-2.84997(+0)	2.64151(+0)
	100-1000	(4.4.1)	5.4580(-1)	-2.98927(+0)					
$1s_4\rightarrow 1s_3$	E_{th}-15	(4.4.2)	1.27264(+1)	-1.27821(-2)	7.09719(+0)	1.23207(+3)	2.8317(-1)	1.9804(-1)	1.08992(+1)
	15-200	(4.4.2)	4.05700(-2)	4.66820(-1)	-6.74457(-4)	-9.7190(-1)	6.9214(-1)	-5.0252(-1)	2.13553(+0)
	200-1000	(4.4.2)	-8.9412(-5)	6.13028(-7)	1.817040(-4)		1.50055(+2)	-4.54663(+1)	3.68157(+0)
$1s_4\rightarrow 1s_2$	E_{th}-15	(4.4.2)	8.88810(-1)				-1.2021(-1)	2.43918(+0)	-7.4841(-1)
	15-1000	(4.4.2)	1.28114(+0)				3.2931(-1)	1.71068(+0)	-1.600(-2)
$1s_5\rightarrow 1s_4$	E_{th}-20	(4.4.2)	4.6855(-1)				-8.9910(-2)	8.2880(-1)	8.6022(-1)
	20-1000	(4.4.2)	9.01468(-4)	2.8059(+10)			-2.1069(+10)	6.00946(+9)	9.4849(+10)
$1s_5\rightarrow 1s_3$	E_{th}-10	(4.4.2)	2.0797(-1)	1.76851(+2)			9.02585(+1)	-1.16432(+3)	4.88411(+3)
	10-1000	(4.4.2)	8.4943(-1)				8.59200(-1)	2.95385(+0)	-1.2770(-2)
$1s_5\rightarrow 1s_2$	E_{th}-10	(4.4.2)	4.0006(-1)	4.96010(-1)			2.1633(-1)	-2.86437(+0)	1.08065(+1)
	10-100	(4.4.2)	1.5210(-2)	1.27852(+0)			6.9435(-1)	-1.58589(+0)	4.12191(+0)
	100-1000	(4.4.2)	1.42291(+0)				-2.75198(+0)	4.36494(+0)	-3.10400(-2)
$2p_{10}\rightarrow 2p_9$	E_{th}-20	(4.4.2)	1.77854(-2)	-3.43472(-2)	-1.3860(+11)		-2.54927(+6)	-3.92122(+7)	-8.29778(+5)
	20-1000	(4.4.2)	1.54369(+0)				-5.4500(-3)	3.2086(-1)	-1.2400(-3)
$2p_{10}\rightarrow 2p_8$	E_{th}-20	(4.4.2)	2.56531(+1)	-5.45146(+2)	-2.48434(+6)		4.64963(+2)	-5.7330(+3)	7.05562(+2)
	20-1000	(4.4.2)	1.0100(-2)	1.01873(+1)			-2.0080(-2)	3.8260(-2)	5.9100(-1)
$2p_{10}\rightarrow 2p_7$	E_{th}-9	(4.4.2)	5.4542(-1)				-1.5794(-1)	1.81463(+0)	-2.79639(+0)
	9-100	(4.4.2)	-1.2160(-2)	1.78584(+0)			4.5120(-2)	-6.2830(-2)	1.17036(+0)
	100-1000	(4.4.2)	5.65457(+0)				6.6701(-1)	3.4426(+0)	-2.1300(-3)
$2p_{10}\rightarrow 2p_6$	E_{th}-15	(4.4.2)	4.5775(-1)				-1.29710(-1)	1.39324(+0)	-1.17313(+0)
	15-1000	(4.4.2)	1.17693(+0)				3.0900(-3)	1.28793(+0)	-3.4900(-3)
$2p_{10}\rightarrow 2p_5$	E_{th}-15	(4.4.2)	9.55180(-1)				4.06640(-1)	-7.97893(+0)	4.66793(+1)

	15-100	(4.4.1)	2.12900(-2)	-2.4934(+0)					
	100-1000	(4.4.1)	3.59200(-2)	-2.92782(+0)					
$2p_{10}\rightarrow 2p_4$	E_{th}-15	(4.4.2)	2.47915(+0)				-4.6430(-2)	2.69968(+0)	-1.78087(+0)
	15-1000	(4.4.1)	1.60094(+0)	-9.8528(-1)					
$2p_{10}\rightarrow 2p_3$	E_{th}-20	(4.4.2)	3.32346(+0)				1.84500(-2)	1.77401(+0)	-6.7383(-1)
	20-1000	(4.4.1)	2.44026(+0)	-9.8581(-1)					
$2p_{10}\rightarrow 2p_2$	E_{th}-15	(4.4.2)	-1.43920(-1)	3.39197(+1)			-1.1277(+0)	1.29586(+1)	2.08905(+1)
	15-1000	(4.4.1)	7.45460(-1)	-9.84040(-1)					
$2p_{10}\rightarrow 2p_1$	E_{th}-10	(4.4.2)	3.68568(+0)				1.95667(+0)	-8.39050(+1)	6.68783(+2)
	10-70	(4.4.2)	4.72982(+5)				6.78379(+6)	-6.97858(+6)	1.15787(+7)
	70-1000	(4.4.1)	1.49660(-1)	-3.22399(+0)					
$2p_9\rightarrow 2p_8$	E_{th}-20	(4.4.2)	1.72794(+0)	3.79105(+4)			-2.04238(+1)	-9.65496(+2)	1.52014(+4)
	20-1000	(4.4.2)	1.48494(+0)				-6.6900(-3)	3.9923(-1)	-1.2000(-3)
$2p_9\rightarrow 2p_7$	E_{th}-20	(4.4.2)	1.04581(+0)	-6.75323(+0)	7.39826(+1)	-6.1924(+1)	9.7200(-3)	-4.3291(-1)	5.05290(+0)
	20-1000	(4.4.2)	1.49252(+0)				9.4100(-3)	3.6966(-1)	6.01203(-4)
$2p_9\rightarrow 2p_6$	E_{th}-15	(4.4.2)	9.93809(+0)				-1.3950(-1)	2.97715(+0)	-1.66859(+0)
	15-1000	(4.4.2)	2.02789(+0)				1.2100(-2)	3.49120(-1)	3.08198(-4)
$2p_9\rightarrow 2p_5$	E_{th}-20	(4.4.2)	5.4480(-1)				-8.200(-3)	2.6288(-1)	-7.8860(-2)
	20-1000	(4.4.2)	1.45178(+0)				6.300(-3)	4.8074(-1)	-5.4614(-4)
$2p_9\rightarrow 2p_4$	E_{th}-20	(4.4.2)	2.32750(-1)	-1.0464(+0)	1.22654(+1)		8.3080(-2)	-2.24363(+0)	1.66292(+1)
	20-1000	(4.4.2)	-1.27782(+0)	2.08734(+0)			-2.1364(-1)	-2.56294(+0)	4.51253(+0)
$2p_9\rightarrow 2p_3$	E_{th}-20	(4.4.2)	1.85050(-1)	1.4053(+0)	-1.59954(+0)		-2.9636(-1)	3.20311(+0)	-2.64971(+0)
	20-1000	(4.4.2)	1.01331(+0)				8.5540(-2)	2.29732(+0)	7.6500(-3)
$2p_9\rightarrow 2p_2$	E_{th}-20	(4.4.2)	8.4690(-2)	-4.66310(-1)	9.63690(-1)		8.10200(-2)	-1.92854(+0)	1.15997(+1)

	20-1000	(4.4.2)	3.86543(+2)	-6.92794(+2)	2.03779(+0)		1.3849(+4)	-4.86853(+3)	-2.42405(+4)
$2p_9 \rightarrow 2p_1$	E_{th}-20	(4.4.2)	3.65420(-1)	1.77074(+0)	-1.20329(+0)		-4.19740(-1)	6.59427(+0)	-5.19208(+0)
	20-1000	(4.4.2)	-1.80062(+0)	3.14766(+0)	-8.7100(-3)		-3.32332(+0)	6.60270(-1)	6.86193(+0)
$2p_8 \rightarrow 2p_7$	E_{th}-20	(4.4.2)	1.4646(-1)	-1.13513(+0)	8.57124(+0)	-7.6057(+0)	1.901(-2)	-4.8539(-1)	3.20249(+0)
	20-1000	(4.4.1)	6.000(-1)	-1.01902(+0)					
$2p_8 \rightarrow 2p_6$	E_{th}-18	(4.4.2)	1.23692(+0)	-1.15302(+1)	7.92784(+1)	-7.0466(+1)	5.8900(-3)	-2.681(-1)	3.22203(+0)
	18-1000	(4.4.1)	4.63418(+0)	-9.99570(-1)					
$2p_8 \rightarrow 2p_5$	E_{th}-20	(4.4.2)	6.2791(-1)				-6.9800(-2)	-4.3017(+0)	5.63486(+1)
	20-100	(4.4.2)	-2.1500(-3)	5.7010(-2)			3.26672(+0)	-7.03426(+0)	6.27449(+0)
	100-300	(4.4.2)	1.8010(-2)				1.8010(-2)	-3.63974(+0)	6.05211(+0)
	300-1000	(4.4.1)	4.3770(-2)	-2.99437(+0)					
$2p_8 \rightarrow 2p_4$	E_{th}-20	(4.4.2)	1.6084(-1)	-1.69962(+0)	7.23477(+0)	-5.4058(+0)	1.3715(-1)	-3.34066(+0)	2.06829(+1)
	20-200	(4.4.1)	6.4560(-2)	-9.7109(-1)					
	200-1000	(4.4.1)	7.8280(-2)	-1.05535(+0)					
$2p_8 \rightarrow 2p_3$	E_{th}-20	(4.4.2)	2.2339(-1)	5.58115(+0)			-7.3095(-1)	6.59283(+0)	1.39229(+1)
	20-1000	(4.4.2)	-1.0300(-3)	1.29507(+0)			-3.6450(-1)	3.9490(-1)	3.33331(+0)
$2p_8 \rightarrow 2p_2$	E_{th}-20	(4.4.2)	1.9724(-1)	-1.51547(+0)	7.03111(+0)		8.2990(-2)	-2.16201(+0)	1.48739(+1)
	20-1000	(4.4.2)	-9.7771(-1)	1.61585(+0)			-2.93764(+0)	1.11127(+0)	4.80864(+0)
$2p_8 \rightarrow 2p_1$	E_{th}-20	(4.4.2)	2.3316(-1)				4.72557(+0)	-8.84457(+1)	4.230161(-2)
	20-90	(4.4.2)	-5.4661(-5)	6.6500(-3)			1.12091(+1)	-2.97783(+1)	2.694808(-1)
	90-300	(4.4.2)	9.4850(-2)	-5.88388(-7)	-3.2722(-1)		3.4600(-2)	-6.95000(-3)	3.45037(+0)
	300-1000	(4.4.1)	1.3800(-3)	-3.04659(+0)					
$2p_7 \rightarrow 2p_6$	E_{th}-20	(4.4.2)	6.31909(+0)				-5.3010(-2)	1.43974(+0)	-3.38260(-1)
	20-1000	(4.4.2)	1.61158(+0)				4.5800(-3)	2.7934(-1)	1.47323e-4

$2p_7\rightarrow2p_5$	E_{th}-15	(4.4.2)	1.9638(-1)				-1.36849(+0)	1.14255(+1)	-6.0615(+0)
	15-90	(4.4.2)	-7.6100(-3)	7.0151(-1)			9.0590(-2)	-3.81566(+0)	2.35065(+1)
	90-1000	(4.4.1)	6.46800(-2)	-2.92961(+0)					
$2p_7\rightarrow2p_4$	E_{th}-20	(4.4.2)	-2.25096(+0)	3.55524(+1)			-1.8570(-1)	8.5213(-1)	2.58359(+1)
	20-1000	(4.4.2)	-2.72699(+0)	3.9441(+0)	7.3400(-3)		-1.4650(-2)	-1.4650(-2)	3.28142(+0)
$2p_7\rightarrow2p_3$	E_{th}-20	(4.4.2)	7.61807(+0)	-3.21172(+1)	-1.96084(+1)	-2.670(+6)	4.29725(+3)	-3.7429(-4)	-2.56459(-4)
	20-1000	(4.4.2)	-2.3300(-3)	4.31997(+0)			-4.75820(-1)	8.3776(-1)	2.63242(+0)
$2p_7\rightarrow2p_2$	E_{th}-10	(4.4.2)	-7.4913(-1)	-1.51334(+0)	5.53244(+3)		-9.68950(+1)	8.20642(+2)	1.92390(+3)
	10-20	(4.4.2)	6.5863(-1)				9.78130(-1)	4.04683(+0)	-2.28734(+0)
	20-1000	(4.4.2)	-1.63952(+2)	2.75411(+2)	6.76853(-1)	6.7600(-3)	-1.82417(+2)	-7.49157(+2)	1.65161(+3)
$2p_7\rightarrow2p_1$	E_{th}-20	(4.4.2)	1.3409(-1)	-1.20409(+0)	4.37758(+0)	-3.5564(+0)	1.36100(-1)	-3.32271(+0)	2.08461(+1)
	20-100	(4.4.2)	5.3800(-2)				7.36497(+0)	-1.16009(+1)	6.12043(+0)
	100-1000	(4.4.1)	5.1360(-2)	-2.83909(+0)					
$2p_6\rightarrow2p_5$	E_{th}-15	(4.4.2)	2.50681(+0)				-1.7575(-1)	2.5306(+0)	-1.6856(+0)
	15-1000	(4.4.2)	1.34603(+0)				1.4640(-2)	6.3716(-1)	8.09262(-5)
$2p_6\rightarrow2p_4$	E_{th}-15	(4.4.2)	7.1193(-1)				-4.1935(-1)	8.79019(+0)	-5.90478(+0)
	15-100	(4.4.2)	7.3802(-1)				2.1002(-1)	4.4796(+0)	-3.6800(-3)
$2p_6\rightarrow2p_3$	E_{th}-20	(4.4.2)	2.93030(+1)	-4.26774(+2)	6.37407(+3)		1.14358(+0)	1.4633(+1)	0.20358(-1)
	20-1000	(4.4.2)	1.22772(+0)				-3.65400(-2)	7.6436(-1)	-5.5500(-3)
$2p_6\rightarrow2p_2$	E_{th}-12	(4.4.2)	1.43149(+0)				-1.8895(+0)	2.18783(+1)	-2.58348(+1)
	12-100	(4.4.2)	5.9927(-1)	-4.2760(-2)	-1.4355(+6)		5.05249(+6)	-4.72775(+6)	4.77422(+6)
	100-1000	(4.4.2)	-7.4672(-4)	1.01401(+0)			-3.03670(+1)	1.03219(+1)	3.14842(+0)
$2p_6\rightarrow2p_1$	E_{th}-15	(4.4.2)	-8.2100(-2)	1.73077(+8)			-1.99364(+8)	1.93413(+9)	-3.14132(+8)
	15-1000	(4.4.2)	-5.0219(-5)	1.40998(+2)			1.45917(+2)	6.45936(+1)	5.34115(+3)

$2p_5 \rightarrow 2p_4$	E$_{th}$-11	(4.4.2)	5.2913(-1)				1.37026(+0)	-4.31227(+1)	2.61568(+2)
	11-100	(4.4.2)	7.4880(-2)	3.86486(-4)	-1.18355(+0)		3.12090(-1)	1.99130(+0)	1.50188(+1)
	100-300	(4.4.1)	1.3560(-2)	-2.79423(+0)					
	300-1000	(4.4.1)	1.7760(-2)	-3.03018(+0)					
$2p_5 \rightarrow 2p_3$	E$_{th}$-20	(4.4.2)	-1.57470(+1)	2.65679(+2)			-2.0956(-1)	1.50658(+0)	2.45135(+1)
	20-1000	(4.4.2)	2.00787(+0)				5.2500(-3)	2.1364(-1)	-8.5210(-4)
$2p_5 \rightarrow 2p_2$	E$_{th}$-20	(4.4.2)	3.4413(-1)	-1.67825(+0)	8.03235(+0)	-6.6902(+0)	9.30300(-2)	-2.23976(+0)	1.40739(+1)
	20-100	(4.4.2)	1.7954(-1)				3.18351(+0)	-4.53959(+0)	2.89155(+0)
	100-1000	(4.4.1)	2.7261(-1)	-2.9582(+0)					
$2p_5 \rightarrow 2p_1$	E$_{th}$-20	(4.4.2)	2.33947(+2)	-3.43269(+3)	1.84404(+4)	-8.3299(+3)	2.71281(+0)	-2.28978(+1)	1.12731(+2)
	20-1000	(4.4.2)	3.82941(+1)	8.80840(-1)			2.7415(-1)	1.0428(-1)	1.1400(-1)
$2p_4 \rightarrow 2p_3$	E$_{th}$-20	(4.4.2)	-1.95794(+0)	9.67333(+1)	-1.39146(+0)		-7.9760(-2)	4.0229(-1)	9.33313(+0)
	20-1000	(4.4.2)	1.92092(+0)				-7.7689(-4)	2.0258(-1)	-4.6329(-4)
$2p_4 \rightarrow 2p_2$	E$_{th}$-20	(4.4.2)	-1.43845(+1)	2.24177(+2)			-8.814(-2)	-6.2620(-2)	1.52190(+1)
	20-1000	(4.4.2)	3.05981(+0)				-1.070(-3)	2.2433(-1)	-5.1361e(-4)
$2p_4 \rightarrow 2p_1$	E$_{th}$-20	(4.4.2)	2.93245(+0)	-1.5529(+1)	3.16939(+1)	-1.9839(+1)	2.59990(-1)	-4.09315(+0)	4.61660(+1)
	20-100	(4.4.2)	1.65723(+2)	-2.89419(+1)			2.57350(+3)	2.14830(+2)	2.25792(+3)
	100-1000	(4.4.1)	7.76100(-2)	-2.93431(+0)					
$2p_3 \rightarrow 2p_2$	E$_{th}$-1000	(4.4.2)	-1.95166(+0)	3.67626(+1)			-9.1630(-2)	6.6380(-2)	1.17728(+1)
$2p_3 \rightarrow 2p_1$	E$_{th}$-20	(4.4.2)	1.02290(-1)	7.36492(+0)	-3.08933(+0)		-1.1395(-1)	1.59456(+0)	2.07966(+0)
	20-1000	(4.4.2)	1.20596(+0)				2.4990(-2)	8.9348(-1)	-2.12729(-4)
$2p_2 \rightarrow 2p_1$	E$_{th}$-45	(4.4.2)	-6.91600(+4)	-6.91600(+4)	-5.22736(+3)		-7.79975(+4)	1.03905(+6)	1.03905(+6)
	45-200	(4.4.2)	9.31245(+0)	-1.96022(+0)	1.29749(-1)		1.9701(+3)	-2.45133(+3)	1.69139(+3)
	200-1000	(4.4.1)	3.79000(-2)	-3.72372(+0)					

4.5 C-R model for xenon plasma

In the previous section, a complete set of relativistic excitation cross sections of different transitions have been presented in the wide range of incident electron energy. To test the applicability of our calculated cross sections, we develop a C-R model using these cross sections and applied to diagnose the low temperature inductively coupled xenon plasma. The model incorporates 36 fine-structure levels *viz.* $1s_i$ (i=1-4), $2p_i$ (i=1-10), $3d_i$ (i=1-12), $2s_i$ (i=1-4) and $3p_i$ (i=6-10) along with the ground state of xenon atom and the singly ionized Xe^+ ion state. Energy and weight factors of the fine structure levels (in Paschan's notation) are given in table 4.3. Present model takes into account population transfer among the various fine structure states through the electron impact excitations, ionization, diffusion though metastable states ($1s_5$,$1s_3$) and radiative decay in addition to the corresponding reverse processes such as de-excitation and three body recombination. A graphical view of processes that are considered in the present C-R model is shown in figure 4.12.

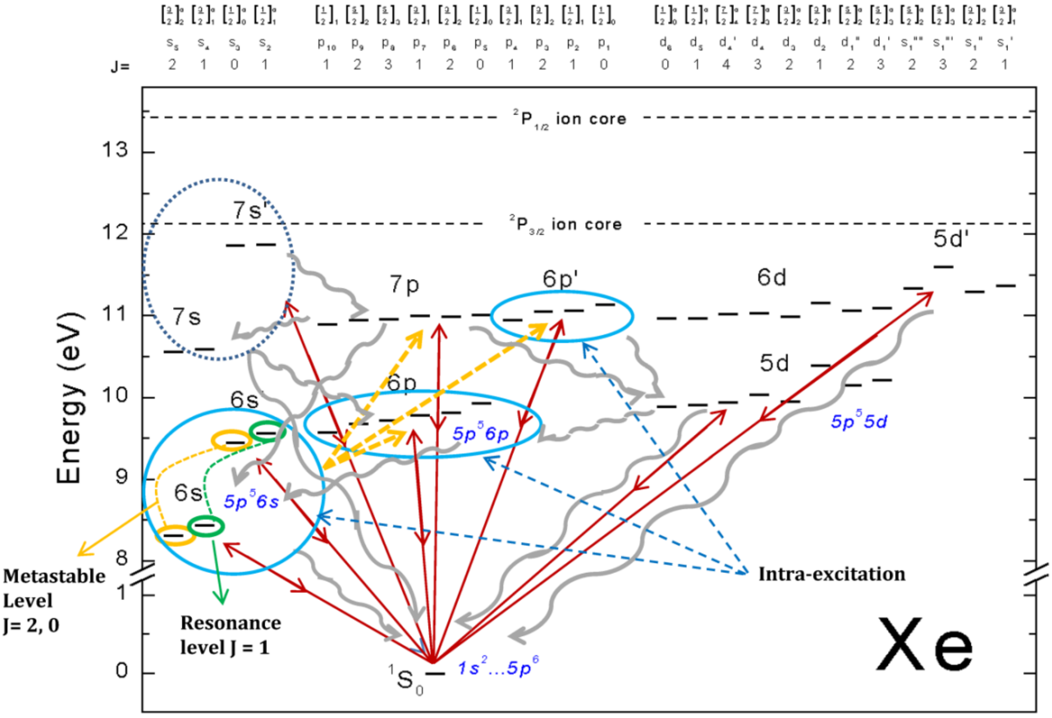

Figure4.12. Energy level diagram for a Xe atom along with considered various collisional and radiative processes in the present C-R model. The solid lines show excitations from the ground state, the dashed lines represent excitations from the $1s_i$'s (metastable as well as resonance) states while the circles and oval represent the intra-excitations. Wavy lines represent the radiative transitions.

Table 4.3. Xenon energy levels along with their statistical weights considered in our CR model.

Levels	**Excitation energy(eV)**	**Statistical weight**
$1s_0$	0	1
$1s_5$	8.315	5
$1s_4$	8.436	3
$1s_3$	9.447	1
$1s_2$	9.569	3
$2p_{10}$	9.580	3
$2p_9$	9.686	5
$2p_8$	9.721	7
$2p_7$	9.789	3
$2p_6$	9.821	5
$2p_5$	9.933	1
$2p_4$	10.957	3
$2p_3$	11.054	5
$2p_2$	11.069	3
$2p_1$	11.141	1
$3d_{12}$	9.890	1
$3d_{11}$	9.917	3
$3d_{10}$	9.943	9
$3d_9$	9.958	5
$3d_8$	10.039	7
$3d_7$	10.157	5
$3d_6$	10.220	7
$3d_5$	10.401	3
$3d_4$	11.301	5

$3d_3$	11.338	5
$3d_2$	11.375	7
$3d_1$	11.607	3
$2s_5$	10.562	5
$2s_4$	10.593	3
$2s_3$	11.867	1
$2s_2$	11.877	3
$3p_{10}$	10.901	3
$3p_9$	10.954	5
$3p_8$	10.968	7
$3p_7$	10.995	5
$3p_6$	11.002	3
$3p_5$	11.015	1
Ion	12.129	4

As already discussed in the earlier Chapters, in the steady state, the particle balance equation can be rewritten for an excited j^{th} level of Xe as,

$$\sum_{\substack{i=1 \\ i\neq j}}^{36} k_{ij}(T_e)n_i n_e + \sum_{i>j} A_{ij}^{eff} n_i + n_e n_+ n_e\, k_{+j}(T_e) - \sum_{\substack{i=1 \\ i\neq j}}^{36} k_{ji}(T_e)n_j n_e - \sum_{i<j} A_{ji}^{eff} n_j - n_j n_e k_{j+}(T_e) - n_j k_j^{diff} = 0 \tag{4.5.1}$$

Again, in the above equation, various symbols have same meaning as already discussed for equation (1.3.1). Population transfer through electron impact excitation and ionization are included through the rates k_{ij} and k_{j+}, respectively, are calculated from the equations (2.2.1). The electron energy distribution function is taken to be Maxwellian in the present work as used in previous Chapters 2 and 3. For the calculation of excitation rates [from equation (2.2.1)], the values of σ_{ij} we have taken our calculated RDW cross sections for various electron impact excitations *viz.* ground $1s_0$ to four fine structure $1s_i$, ten $2p_i$, twelve $3d_i$, four $2s_i$ and six $3p_i$ levels as well as excitations from$1s_i$, (i=2-5)→$2p_i$, (i=1-10), $3p_i$, (i=6-10) and intra transitions among $1s_i$ and $2p_i$ levels. It is important to mention here that the RDW method, being a perturbative approach, have been found sometimes to give cross sections near threshold incident electron energies different from the reliable experimental or non-perturbative theoretical results for certain transitions. This is often true for the excitations from the ground state to higher levels having large excitation thresholds but not for the excitations among the excited levels. Since the non-perturbative BSR cross sections of Zatsarinny *et al.* [193] (which can be said to be quite reliable in the low incident energy range) are available for the excitations from the ground state to considered higher excited states, we have used their results in the low incident range (2-3 times of threshold) as also considered in the previous model of Dressler *et al.*[239].

Further, for the ionization rates from the ground state we have incorporated the experimental ionization cross section of Rejoub *et al.*[240] However, the ionization cross sections from the $1s_i$ levels are calculated in the present work using Flexible Atomic Code (FAC) [143]. Reverse processes such as de-excitation and three particle recombination are taken into consideration by principle of detail balance as explained in earlier Chapters 2 and 3. Population transfer via radiative decay, are included through effective transition probabilities ($A_{ij(eff)} = \Lambda_{ij} * A_{ij}$) from level $i \rightarrow j$, as described in section 2 of Chapter 3. Λ_{ij} is escape factor calculated by equation (3.2.2), taking 1.0 cm as the characteristic length of the plasma at 600K gas temperature The required transition probabilities are taken either from the values available in the NIST database [147] or values obtained from the present calculations by GRASP2K[100]. Diffusion from metastable ($1s_5$ and $1s_3$) levels is also taken into account and rate coefficients for this are taken from the values reported by Kolts and Setzer [190]. Further, by solving the coupled linear equations simultaneously (equation 5) for the all considered fine structure levels, the atomic level population densities as a function of T_e and n_e are obtained [111]. The required ground state population of xenon in the model is calculated by the standard gas law at 460mTorr pressure and gas temperature 600K.

In order optimize the plasma parameters T_e and n_e, we compare the intensities obtained from the C-R model to the OES measured intensities of Czerwiec *et al.* [230]. We have utilized four most intense lines coming out from $2p_i$ to $1s_i$ levels (see table 4.4) measured by Czerwiec *et al.* [230] in H-mode at 460 mTorr pressure. In their experiment, 100–400W *rf* power supply at 13.56MHz coupled to a matching network were used to generate the discharge. The light coming out from the ICP discharge was collected perpendicular to the ICP source through an optical fiber and intensities were measured by PC2000-UV-VIS-ISA Optic Spectrometer. A characteristic emission spectrum between

300-870 nm for xenon ICP discharge in H-mode was recorded at 460 mTorr pressures for injected power 160W. Intensities of four most intense lines were also reported as function of injected power at same pressure 460 mTorr.

Intensity corresponding to any transition $j \rightarrow i$ can be expressed in terms of the calculated upper level population n_j and effective transition probability A_{ji}^{eff} (see the equation (3.3.1).) Now, by using our calculated population densities of $2p_i$ levels from our C-R model, intensities of the considered transitions are obtained as a function of T_e and n_e. Thereafter, we have normalized individually the intensities estimated from CR model and from the OES measurements as follows

$$I_{j,OES(Model)}^{normalized} = \frac{I_{j,OES(Model)}}{\sum_{j=1}^{4} I_{j,OES(Model)}} \times 100 \qquad (4.5.2)$$

We then calculate the difference between intensities obtained from both the C-R model and measurements and obtain the deviation parameter as a function of n_e and T_e using the following expression [13, 113],

$$\Delta = \sum_{j=1}^{4} \left(I_{j,OES}^{normalized} - I_{j,Model}^{normalized} \right)^2 \qquad (4.5.3)$$

Table 4.4. Escape factors for the emission lines considered in the diagnostic of xenon plasma.

Transition	A_{ji} (s^{-1})	Wavelength (nm)	Escape factor (Λ)
$2p_6$-$1s_5$	2.62e7	823.16	0.076
$2p_5$-$1s_4$	3.32e7	828.01	0.190
$2p_3$-$1s_2$	2.71e7	834.74	0.328
$2p_2$-$1s_3$	1.54e7	764.20	0.367

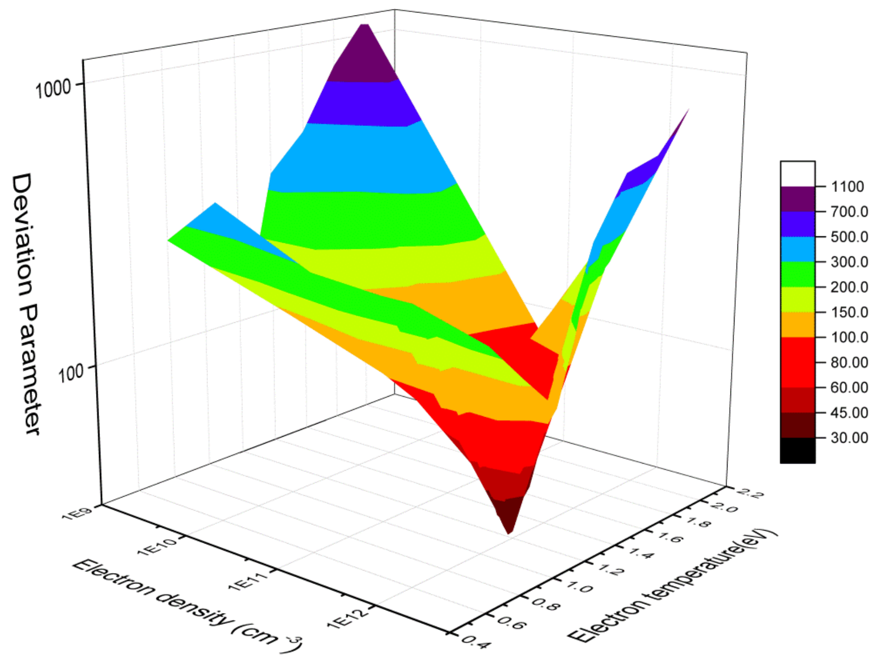

Figure 4.13. Deviation parameter as a function of T_e and n_e for injected power 130W and gas pressure 460 mTorr.

In figure 4.13, the deviation parameter is shown as a function of electron density n_e and electron temperature T_e for injected power 130W at 460 mTorr gas pressure. Minimum value of the deviation parameter corresponds to the optimized plasma parameters n_e and T_e. Similarly deviation parameter is calculated for 45W input power at the same gas pressure. We found that the extracted electron density is 9e11 cm^{-3} and electron temperature varies from 1.0 to 1.2eV as the injected power changes from 45W to 130W. Although there are no results reported by Czerwiec *et. al.* [230] to directly compare with our extracted electron temperature and electron density. However, it is worth to mention here that for Ar plasma Czerwiec *et. al.* [230] have reported the range of n_e and T_e in both E and H-mode. For H-mode n_e varied from 10^{11}-10^{12} cm^{-3} and T_e from 1-2eV for gas pressure 100-400 mTorr. Therefore, our values are well within the range expected in H-mode of Xe plasma. However, they have estimated the variation of electron temperatures as a function pressure by comparing theoretically obtained intensity ratio $I_{823.1}/I_{834.7}$ to their measurements. To obtain the intensity ratio as a function of T_e theoretically, they used the cross section data available in the literature[216, 241]. The transitions for which cross section data were not available, they have used some proportionality factor for the rates calculation *viz.* $k_{e,\mathrm{Xe}}=0.75k_{e,\mathrm{Ar}}$. They reported that their calculated T_e varies in the range 0.8-1.3eV for gas pressure 60-500mTorr [230] which is also quite close to our estimated range of 1.0 to 1.2eV.

In figure 4.14, we present the comparison of the normalized intensities obtained from the C-R model obtained using the n_e and T_e values (at minimum deviation position) with the corresponding OES measurements[230]. Overall, we see from the figure that our values are in reasonable agreement with the measurements. This gives us the confidence that our CR model is well optimized and all the necessary processes are adequately included in the model.

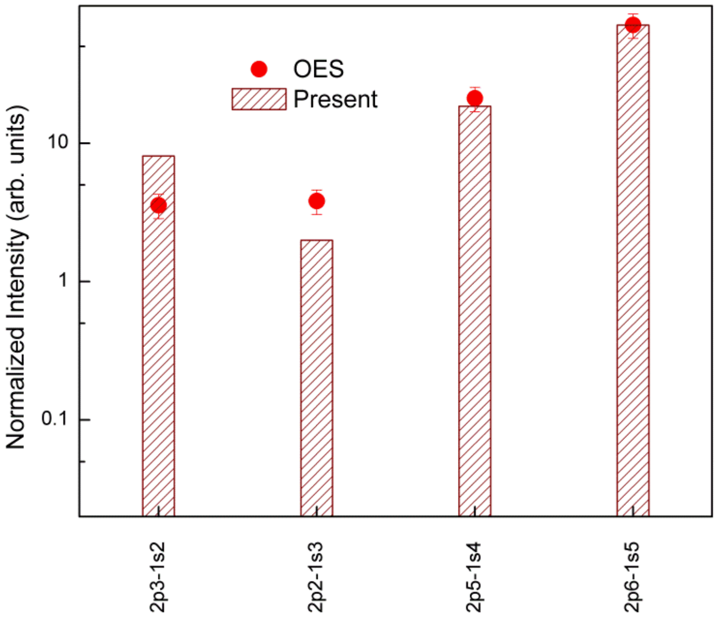

Figure 4.14. Comparison of the normalized intensities obtained from the C-R model with the OES measurements [230] of Xe ($5p^56p \rightarrow 5p^56s$) transition lines at n_e=9e11 cm^{-3} and T_e=1.2eV

Further, in figure 4.15, we have presented the ratio of 1s$_i$ (i=2-5) level population to the ground level population of xenon in the plasma as a function of T_e at our optimized value of n_e (9e11 cm^{-3}). In the paper of Czerwiec *et. al.* [230], it was found that ratio of the population of the metastable state 1s$_5$ to ground the state 1s$_0$ varies in the range 10^{-6}-10^{-3} for xenon discharge under the typical condition of H-mode and we found the similar order for the ratio from our present CR model.

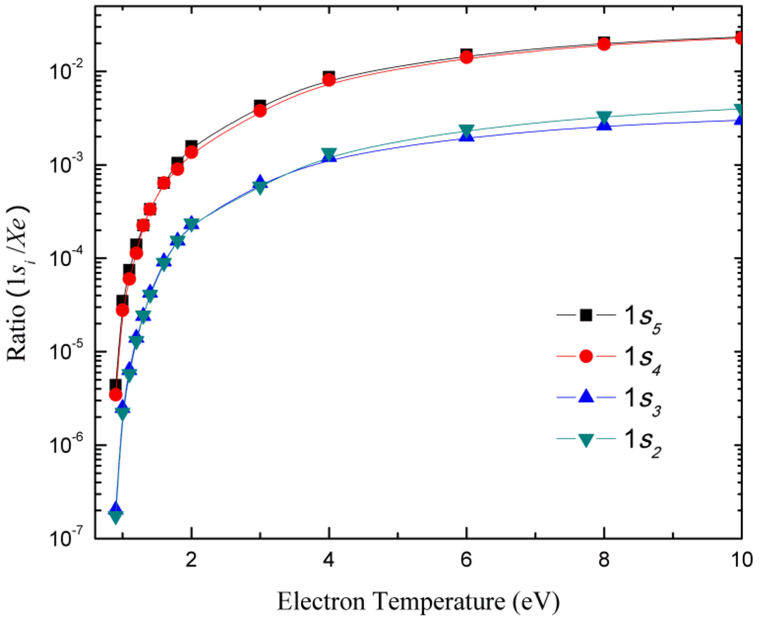

Figure 4.15. Ratio of population densities of four levels of $5p^5 6s$ to Xe ground state population density as a function of T_e at 460mTorr gas pressure and n_e= 9e11 cm^{-3}.

Further, through figures 4.16(a) and (b), population densities of $1s_i$ levels and $2p_i$ levels at our optimized parameter are presented. From the figure it can be seen that the population density of $1s_5$ and $1s_4$ levels (lower lying energy levels) are larger than $1s_3$ &$1s_2$ (higher lying energy levels). Similar distribution is observed for $1s_i$ levels population from the laser absorption spectroscopy (LAS) measurements of Zhu *et al.*[242] at power 15W and 120W for gas pressure 10-100 mTorr in xenon discharge. In the present case, the population densities of $1s_4$ (resonance level) is of the same order as $1s_5$ (metastable level). This reflects that the radiation trapping for the resonance levels is significantly high (escape factor ~ 10^{-4}) at the considered gas pressure 460 mTorr. Also, it shows that the inter excitations from the resonance levels is as important as from the metastable levels and should be properly included in the C-R model. Further, at the optimized T_e (low temperature), it is seen that $2p_i$ levels are mainly populated through electron impact excitation from the $1s_i$ levels. We have already seen from the figures 4.6-4.10 that the cross sections for transitions $1s_5$,$1s_4$→$2p_i$ (i=5-10) are larger than the $1s_5$,$1s_4$-$2p_i$ (i=1-4). This fact reflects in the population density of $2p_i$ levels shown in figure 4.16(b) where population density of $2p_i$ (i=5-10) are larger than the $2p_i$ (i=1-4).

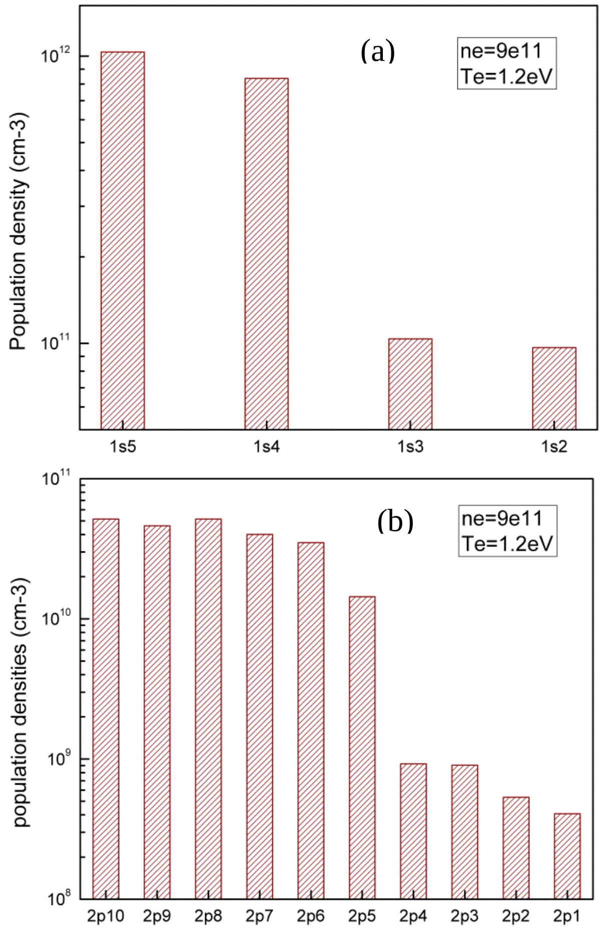

Figure 4.16. Population densities of four levels of $5p^56s^1$ and ten levels of $5p^56p^1$ configuration at obtained plasma parameters for 460mTorr gas pressure.

4.6 Conclusions

A complete data set of electron impact excitation cross sections of 116 fine structure transitions have been calculated in xenon using relativistic distorted wave theory in the wide range of incident electron energy from threshold to 1 KeV. Cross section results obtained for the transitions from the ground state show good agreement with the recent DBSR calculations and other available measurements. One observes that the cross section results for the fine structure levels $1s_i$ to $2p_i$ reflect interesting atomic structure behavior of the xenon due to strong spin orbit interaction within the core. Fitting coefficients for cross sections of all the considered excitation transitions are also provided for direct use of these cross sections in the plasma models. Utilizing the obtained complete set of cross sections, a fine-structure resolved collisional radiative model is developed for low temperature xenon plasma. Model includes all the relevant collisional and radiative processes among the fine structure levels occurring in the plasma. The plasma parameters (T_e and n_e) have been obtained by minimum scatter approach using the OES measurements for four lines ($2p_i \rightarrow 1s_i$). Population densities of fine structure level of $5p^5 6s$ and $5p^5 6p$ are also given at the obtained n_e and T_e which show the excitations from the resonance level to higher levels are as important as excitations from metastable levels. Further, our obtained plasma parameters and population densities are within the range reported in various previous studies which shows that our model is well optimized.

CHAPTER 5

ELECTRON IMPACT N-SHELL EXCITATION OF TUNGSTEN IONS AND POLARIZATION OF THEIR PHOTON EMISSION

5.1 Introduction

In the previous Chapters we have studied the electron impact excitation of neutral Cs, Ar and Xe atoms which are important for low temperature plasma modeling. In the present Chapter, we focus our attention on electron impact excitation of highly charged tungsten ions relevant to high temperature fusion plasma.

Atomic data corresponding to different tungsten ions have been in great demand in the last decade due to their application in fusion devices[243]. Special physical properties of tungsten such as its highest melting point and lowest metal pressure amongst metals make it a potential candidate in fusion engineering where tungsten can be used as a potential plasma facing material. Various charge species of tungsten are predicted to be present in the high-temperature and low-density divertor plasma of the International Thermonuclear Experiment Reactor (ITER) tokomak [243–245]. Tungsten ions, which move into a tokomak will not be completely ionized even in the hot core, thus causing strong X-ray emission over a wide range of temperatures. Since electron induced processes are anticipated to be among the dominant ones, it is likelihood that tungsten ions will get excited by collision with plasma electrons and will decay by emitting radiation. Thus information on the electron impact excitation cross sections as well as the polarization of the radiation emitted due to decay of the excited state will facilitate a thorough understanding of the spectra for plasma diagnostics. For example, the ion temperature of the ITER core plasma can be assessed with the help of such diagnostics. Polarization studies play an important role in understanding the plasma properties, as X-ray polarization spectroscopy is a useful diagnostic tool for measuring the velocity distribution of hot electrons propagating in plasma created with a high intensity laser pulse[246]. It has also been employed to measure the energy component associated with the cyclotron motion of the beam electrons in the Livermore electron beam ion trap (EBIT) [247].

The understanding and modeling of such plasma rely on the knowledge of accurate atomic data for ion species encountered in the plasma [248]. The International Atomic Energy Agency (IAEA) has constituted a committee consisting of leading scientists from all over the world in order to encourage the production and exchange of a variety of tungsten data required to facilitate the growth of ITER and other fusion applications. The initiative taken by IAEA has led to extensive experimental and theoretical investigations related to emission spectra, energy levels, transition rates, ionization, excitation, radiative recombination and dielectronic recombination etc., of highly charged tungsten ions [249]. As a coordinated effort to cater the need of atomic data of various ionic stages of tungsten, thereby assisting in the design and development of ITER, our aim is to provide reliable cross section data for excitation of various tungsten ions by electron impact.

In the present Chapter, we consider the electron impact excitations of Rb-like (W^{37+}) to Cu-like (W^{45+}) tungsten ions from their N-shell to specifically selected excited states which lead to extreme ultra violet (EUV) and Soft X-rays lines emissions on its decay back to the initial state. Recently, Utter *et al.* [250] have performed measurements on Rb-like (W^{37+}) to Cu-like (W^{45+}) tungsten ions at the Livermore electron beam ion trap (EBIT) facility and recorded spectra in the range 40-85 Å. They varied electron-beam energy systematically to produce and excite these tungsten ions and identified the individual spectra of these ions. In the light of their EBIT experiment and identified lines by them, the objective of the present work has been to study all the corresponding transitions that occurred due to the electron excitation in three tungsten ions *viz.*, Rb-like W^{37+}through Br-like W^{39+}. The excitation cross sections of these highly charged ions are crucial in order to identify and interpret the spectroscopic data.

It would be worth to first review the experimental and theoretical atomic data which has already been reported for the three W^{37+}, $W^{38+}$and W^{39+} tungsten ions of our interest. Extreme ultra violet (EUV) and Soft X-rays lines emitted from the intermediate charge states of tungsten are expected to be present in large portion of ITER spectra. Various earlier theoretical and experimental work have been reported on the study of emission spectra of such tungsten ions [251]. Neu *et al.*[252] observed X-ray spectra (7-10 Å) of

W^{37+} to W^{47+} charged tungsten ions in axially symmetric divertor experiment (ASDEX) upgrade. Further, Neu *et al.*[253] also reported X-ray spectra for W^{39+} to W^{50+} tungsten ions in the 5.5 to 19 Å spectral range from the same tokomak ASDEX upgrade. Radtke *et al.*[254] have measured spectra from I-like W^{21+} to Cu-like W^{45+} ions of tungsten in the wavelength range 45 to70 Å at an EBIT. Later Radtke *et al.* [255] used HULLAC code [256] to calculate the radiative rates and electron impact collision strengths and obtained the line intensities through collisional radiative (C-R) model. Utter *et al.*[250] reported sixty spectral lines from the intermediate charge states of tungsten in the spectral range 40 to 85 Å at the EBIT facility of Livermore. Emission lines in the range 40-140 Å for highly ionized tungsten from ASDEX Upgrade have been reported by Putterich *et al.*[257]. This spectra from ASDEX Upgrade was compared to EBIT measurements [253] in the wavelength range 40-70 Å. Putterich *et al* have also investigated temperature and energy dependence features of spectral lines between 45 – 65 Å, where they have used cross section calculated via the Cowan code [258] based on the plane-wave Born approximation. Ralchenko *et al.* [259] observed spectra of W^{39+}–W^{47+} in EUV wavelength range 12-20 nm using high-resolution EUV spectrometry at EBIT facility of the National Institute of Standards and Technology (NIST).

On theoretical side, Fournier [260] calculated the wavelengths and oscillator strengths for different transitions in Co-like W^{47+} to Rb-like W^{37+} ions and also calculated their line intensities using CR model. In their CR model, they have utilized electron excitation cross sections calculated from semi- relativistic code CROSS [261]. Bogdanovich *et al.* [262, 263] calculated the energy level spectra, transition rates, oscillator strengths and radiative life times for W^{37+} and W^{39+}. The transition energies, wavelengths and transition probabilities have been calculated by Jonauskas *et al.* [264] for different magnetic dipole (M1) transitions in W^{29+}–W^{37+} ions using the Dirac–Fock approximation. Theoretical calculations for the transition energies and radiative rates of W^{39+} Br-like tungsten ion have been reported by Aggarwal *et al.* [265] using the GRASP code [160]. Wu *et al.* [266] have performed cross sections calculations using relativistic electron impact excitation (REIE06) code [267] for the highly charged W^{46+} to W^{42+} tungsten ions. Moreover, they have reported polarization for emitted photon for W^{43+} to W^{42+} as well as dielectronic recombination rates for W^{37+} to W^{46+}.

As mentioned above, we see that the most of the earlier work on the three W^{37+}, $W^{38+}$and W^{39+} tungsten ions has been devoted to the study of different associated properties, such as excitation energies, radiative rates and dielectronic recombination rates. However, not much attention has been paid to the study of the electron-impact excitation of these ions, which is an important process involved in the fusion plasma and should be considered in detail. It is worth mentioning here that there are no reports on the direct experimental measurements of electron impact excitation cross sections for these tungsten ions and thus, theoretical predictions are of prime importance. Moreover, there is in general no experimental work available for electron excitation cross section of any tungsten ion while only few theoretical works have been performed in this connection [85, 86, 268–274]. In continuation of such effort, in the present Chapter, we consider the N-shell electron impact excitation of W^{37+} to W^{39+} tungsten ions in the framework of fully relativistic distorted wave (RDW) approximation theory [76]. The electron impact excitation cross sections as well as linear polarization of the emitted photons from the excited tungsten ions on their decay to the lower state for the electron is obtained for impact energy from threshold to 20 keV.

5.2 Theoretical considerations

5.2.1 RDW theory for the electron impact excitation of ions

In Chapter 1, the general outline of the relativistic distorted wave approach for the electron impact excitations of the neutral atoms has been discussed. Since in this Chapter we consider electron impact excitations of ions, the RDW calculations are slightly different. In the first order RDW approximation [76, 79], T-matrix for the electron impact excitation from initial state $\left|\alpha_i J_i M_i\right\rangle$ to a final state $\left|\alpha_f J_f M_f\right\rangle$ of the tungsten ion having Z nuclear charge and N electrons can be expressed as

$$T_{i\to f}^{RDW} = \left\langle \Phi_f^{rel}(\mathbf{1},\ \mathbf{2},\ \ldots,\ \mathbf{N})\mathrm{F}_{f,\mu_f}^{DW-}(\mathbf{k}_f,\mathbf{N}+\mathbf{1})\right| V - U_f(N+1) \left| \mathcal{A}\{\Phi_i^{rel}(\mathbf{1},\ \mathbf{2},\ \ldots,\ \mathbf{N})\mathrm{F}_{\mathrm{i},\mu_\mathrm{i}}^{DW+}(\mathbf{k}_i,\mathbf{N}+\mathbf{1})\}\right\rangle \qquad (5.2.1)$$

Notation used here have the same meaning as described in detail for equation (1.2.11) and (1.2.12) of Chapter 1 with the difference that the target atomic wave functions now represent that of the ion and the projectile distorted waves are obtained in the ionic field of the target which is calculated in a different manner.

We have used GRASP2K [99] code to calculate the multi-configurational Dirac-Fock (MCDF) bound state wave functions of the target tungsten ions in the initial and final states. Using the obtained target ion bound state wavefunctions, the distortion potential U_f can be calculated. It can be expressed as sum of static and exchange potential,

$$U_f(r) = V_{st}(r) + V_{ex}(r). \tag{5.2.2}$$

The static potential V_{st} is taken as the spherical average of static potential of the ion in the excited state given by

$$V_{st}(r_{N+1}) = -\frac{Z-N}{r_{N+1}} + \sum_{\substack{j\in all \\ \text{subshells}}} \omega_j \int_0^\infty \left[P^2_{n_j\kappa_j}(r) + Q^2_{n_j\kappa_j}(r) \right] \frac{1}{r_>} dr \tag{5.2.3}$$

where, ω_j is the occupation number of the j^{th} subshell and the electron in it is represented by quantum numbers $n_j\kappa_j$.

However, here instead of incorporating the non-local exchange effects as taken in the Chapter 1, for the exchange effect, we take a local potential V_{ex} which accounts the dynamics effects in the atomic potential, the following local energy dependent form [275] in terms of the static potential and charge density is used,

$$\begin{aligned} V_{ex} = \frac{1}{2}\Bigg[&\left(\frac{1}{2}k^2 - V_{st}(r) + \frac{3}{10}\left(3\pi^2\rho(r)\right)^{3/2} \right) - \\ &\left\{ \left(\frac{1}{2}k^2 - V_{st}(r) + \frac{3}{10}\left(3\pi^2\rho(r)\right)^{3/2} \right)^2 + 4\pi\rho(r) \right\}^{1/2} \Bigg] \end{aligned} \tag{5.2.4}$$

Where, charge density for the relativistic orbitals is given by

$$\rho(r) = \frac{1}{4\pi r^2} \sum_{j\in all\, subshells} \omega_j \left[P^2_{n_j\kappa_j}(r) + Q^2_{n_j\kappa_j}(r) \right]. \tag{5.2.5}$$

The continuum incident (scattered) electron distorted waves $\mathrm{F}^{DW+(-)}_{i(f),\,\mu_{i(f)}}$ can be expressed in terms of relativistic partial waves as,

$$\begin{aligned} \mathrm{F}^{DW\pm}_{i(f),\,\mu_{i(f)}}(\mathbf{k}_{i(f)},\mathbf{r}) &= \frac{1}{(2\pi)^{3/2}} \sum_{\kappa m} \mathrm{e}^{\pm i\Delta_\kappa} 4\pi i^l \left[\frac{E_{\mathbf{i}(f)} + c^2}{2E_{\mathbf{i}(f)}} \right]^{1/2} \\ &\times \sum_{\mathrm{m}_l} \left(l\ m_l\ \ \frac{1}{2}\ \mu_{\mathbf{i}(f)} \middle|\ j\ m \right) Y^*_{l\,m_l}(\hat{\mathbf{k}}_{\mathbf{i}(f)})(\hat{\mathbf{k}}_{i(f)}) \frac{1}{r} \begin{pmatrix} f_\kappa(r)\ \chi_{\kappa m}(\hat{\mathbf{r}}) \\ i g_\kappa(r)\ \chi_{-\kappa m}(\hat{\mathbf{r}}) \end{pmatrix} \end{aligned} \tag{5.2.6}$$

where, Δ_κ is the combined (Coulomb and scattering) phase shift of the partial wave and $\chi_{\pm\kappa m}$ are the spinor spherical harmonics. $E_{i(f)}$ is the relativistic energy of the projectile electron with linear momentum $\boldsymbol{k}_{i(f)}$ such that $E_{i(f)} = \sqrt{k_{i(f)}{}^2 c^2 + c^4}$ where c is the velocity of light taken to be 1/137. $f_\kappa(r)$ and $g_\kappa(r)$ are the large and small components of the radial functions of the distorted waves which can be obtained by solving the following coupled Dirac equations numerically

$$\left(\frac{d}{dr}+\frac{\kappa}{r}\right)f_\kappa(r)-\frac{1}{c}(c^2-U_f+E_{i(f)})g_\kappa(r)=0 \tag{5.2.7a}$$

$$\left(\frac{d}{dr}-\frac{\kappa}{r}\right)g_\kappa(r)+\frac{1}{c}(-c^2-U_f+E_{i(f)})f_\kappa(r)=0 \tag{5.2.7b}$$

subject to the following boundary conditions

$$f_\kappa(r)\xrightarrow[r\to\infty]{}\frac{1}{k_{i(f)}}\sin(k_{i(f)}r-\frac{l\pi}{2}+\eta\ln 2k_{i(f)}r+\Delta_\kappa) \tag{5.2.8a}$$

$$g_\kappa(r)\xrightarrow[r\to\infty]{}\frac{c}{c^2+E_{i(f)}}\cos(k_{i(f)}r-\frac{l\pi}{2}-\eta\ln 2k_{i(f)}r+\Delta_\kappa) \tag{5.2.8b}$$

In the above equation (5.2.8), η = Z/v is the Sommerfeld’s parameter, where v is the velocity of the electron. The coupled Dirac equations (5.2.7) are solved numerically.

Finally, the magnetic sublevel cross section cross section σ_{M_f} for the excitation ($i \to f$) in terms of the calculated T-matrix (5.2.1) can be obtained by using the expression (1.2.29). Summing the σ_{M_f} for all the magnetic sub levels of final state of the ion, we get the total excitation cross section.

5.2.2 Calculation of linear polarization

Tungsten ions after the excitation by the electron impact can decay subsequently to the lower level via photon emission. Under the electric dipole approximation, the degree of linear polarization of the emitted photon from excited level $|\alpha_j J_j\rangle$ to lower level $|\alpha_i J_i\rangle$ is obtained using the density matrix theory by the following formula [76, 276]

$$P(\varphi)=\frac{-\frac{3}{2}A_{20}G^{E_1}\left(\alpha_i J_i,\alpha_f J_f\right)\sin^2\varphi}{1+A_{20}G^{E_1}\left(\alpha_i J_i,\alpha_f J_f\right)P_2\left(\cos\varphi\right)} \tag{5.2.9}$$

Here choice of geometry is such that the emitted photons are detected in the direction perpendicular to the x-z plane (scattering plane) i.e. y-direction. Hence we take $\phi=90^0$ as ϕ represents direction of propagation of the emitted photon with respect to the z-axis (quantization axis). P_2 is the second order Legendre's polynomial, A_{20} is the alignment parameter which is directly related to the magnetic sub-level cross sections and can be expressed as

$$A_{20} = \frac{\sqrt{(2J_f + 1)}}{\sigma\left(\alpha_f J_f\right)} \sum_{M_f} (-1)^{J_f - M_f} \left\langle J_f M_f \quad J_f - M_f \middle| 2\,0 \right\rangle \sigma_{M_f} \tag{5.2.10}$$

In equation (5.2.10), G^{E_1} is the structure function given by

$$G^{E_1}\left(\alpha_i J_i, \alpha_f J_f\right) = (-1)^{J_i + J_f + 1} \begin{Bmatrix} 1 & 1 & 2 \\ J_f & J_f & J_i \end{Bmatrix} \sqrt{\frac{3}{2}\left(2J_f + 1\right)} \tag{5.2.11}$$

Using the equations (5.2.10) and (5.2.11) we obtain the simplified expressions for the polarization for different J_i and J_f values which are applicable to the transitions considered in the present work. These polarization formulae are listed in table 5.1.

Table5.1: Formulae for the linear polarization in terms of magnetic sub level cross sections for various electric dipole allowed transitions

Transition	Polarization	Transition	Polarization
1→0	$\frac{\sigma_0 - \sigma_1}{\sigma_0 + \sigma_1}$	3/2→1/2	$\frac{3(\sigma_{1/2} - \sigma_{3/2})}{3\sigma_{3/2} + 5\sigma_{1/2}}$
1→2	$\frac{\sigma_0 - \sigma_1}{7\sigma_0 + 13\sigma_1}$	3/2→3/2	$-\frac{3(\sigma_{1/2} - \sigma_{3/2})}{6\sigma_{3/2} + 4\sigma_{1/2}}$
2→1	$-\frac{3(2\sigma_2 - \sigma_1 - \sigma_0)}{6\sigma_2 + 9\sigma_1 + 5\sigma_0}$	3/2→5/2	$\frac{3(\sigma_{1/2} - \sigma_{3/2})}{19\sigma_{3/2} + 21\sigma_{1/2}}$
2→2	$\frac{3(2\sigma_2 - \sigma_1 - \sigma_0)}{10\sigma_2 + 7\sigma_1 + 3\sigma_0}$	5/2→3/2	$-\frac{(5\sigma_{5/2} - \sigma_{3/2} - 4\sigma_{1/2})}{5\sigma_{5/2} + 7\sigma_{3/2} + 8\sigma_{1/2}}$
2→3	$\frac{-3(2\sigma_2 - \sigma_1 - \sigma_0)}{26\sigma_2 + 29\sigma_1 + 15\sigma_0}$	5/2→5/2	$\frac{2(5\sigma_{5/2} - \sigma_{3/2} - 4\sigma_{1/2})}{15\sigma_{5/2} + 11\sigma_{3/2} + 9\sigma_{1/2}}$
3→2	$\frac{-3(5\sigma_3 - 3\sigma_1 - 2\sigma_0)}{15\sigma_3 + 20\sigma_2 + 23\sigma_1 + 12\sigma_0}$	7/2→5/2	$-\frac{3(7\sigma_{7/2} + \sigma_{5/2} - 3\sigma_{3/2} - 5\sigma_{1/2})}{21\sigma_{7/2} + 27\sigma_{5/2} + 31\sigma_{3/2} + 33\sigma_{1/2}}$
3→3	$\frac{3(5\sigma_3 - 3\sigma_1 - 2\sigma_0)}{21\sigma_3 + 16\sigma_2 + 13\sigma_1 + 6\sigma_0}$	7/2→9/2	$\frac{-3(7\sigma_{7/2} + \sigma_{5/2} - 3\sigma_{3/2} - 5\sigma_{1/2})}{53\sigma_{7/2} + 59\sigma_{5/2} + 63\sigma_{3/2} + 65\sigma_{1/2}}$
3→4	$\frac{-3(5\sigma_3 - 3\sigma_1 - 2\sigma_0)}{43\sigma_3 + 48\sigma_2 + 51\sigma_1 + 26\sigma_0}$	9/2→9/2	$\frac{3(12\sigma_{9/2} + 4\sigma_{7/2} - 2\sigma_{5/2} - 6\sigma_{3/2} - 8\sigma_{1/2})}{45\sigma_{9/2} + 37\sigma_{7/2} + 31\sigma_{5/2} + 27\sigma_{3/2} + 25\sigma_{1/2}}$

4→3	$\frac{-(28\sigma_4+7\sigma_3-8\sigma_2-17\sigma_1-10\sigma_0)}{28\sigma_4+35\sigma_3+40\sigma_2+43\sigma_1+22\sigma_0}$	11/2→11/2	$\frac{55\sigma_{11/2}+25\sigma_{9/2}+\sigma_{7/2}-17\sigma_{5/2}-29\sigma_{3/2}-35\sigma_{1/2}}{66\sigma_{11/2}+56\sigma_{9/2}+48\sigma_{7/2}+42\sigma_{5/2}+38\sigma_{3/2}+36\sigma_{1/2}}$
4→4	$\frac{28\sigma_4+7\sigma_3-8\sigma_2-17\sigma_1-10\sigma_0}{36\sigma_4+29\sigma_3+24\sigma_2+21\sigma_1+10\sigma_0}$	5→4	$\frac{-3(15\sigma_5+6\sigma_4-\sigma_3-6\sigma_2-9\sigma_1-5\sigma_0)}{45\sigma_5+54\sigma_4+61\sigma_3+66\sigma_2+69\sigma_1+35\sigma_0}$

5.3 Results and Discussion

We study electron impact N-shell excitations of $W^{37+,}$ W^{38+} and W^{39+}ions. The ground states of these ions are having configurations $[4d_{3/2}]_{J=3/2}$ $[4p^4_{3/2}]_{J=0}$ and $[4p^3_{3/2}]_{J=3/2}$ respectively. Most of the excitations that we have considered are from the outer sub-shell of the ground state but few are from inner sub-shells. Corresponding to all transitions of the different ions, the initial and final states are mentioned in table 5.3 with their designated notation.

5.3.1 Dirac-Fock wave functions for Rb-like W^{37+} through Br-like W^{39+} ions

To obtain the electron impact excitation cross section (equation (5.2.1)) for each transition, we have calculated the initial and final state wave function of the tungsten ions using GRASP2K [99]. First, we performed calculations by considering maximum possible number of configuration state functions in the linear expansion of the bound state wavefunctions of the target each ion. Thereafter we examined the contribution of all the CSFs and neglect those which do not have significant contribution. In fact, removing the CSFs having very small contribution did not affect the excitation energies and oscillator strengths. The various CSFs which we have used for each tungsten ions are given in table 5.2.

Table 5.2. Various CSF's used in GRASP2K [99] to represent the target ion wave function in the initial and the final states of Rb-like W^{37+} through Br-like W^{39+} ions

Rb-like (W^{37+})	Kr-like (W^{38+})	Br-like (W^{39+})
$4s^2\ 4p^6\ 4d^1$	$3d^{10}\ 4s^2\ 4p^6$	$3d^{10}\ 4s^2\ 4p^5$
$4s^2\ 4p^5\ 4d^2$	$3d^{10}\ 4s^2\ 4p^5\ 4d^1$	$3d^{10}\ 4s^2\ 4p^4\ 4d^1$
$4s^2\ 4p^6\ 4f^1$	$3d^{10}\ 4s^2\ 4p^5\ 5p^1$	$3d^{10}\ 4s^1\ 4p^6$

$4s^2\,4p^6\,5f^1$	$3d^{10}\,4s^2\,4p^5\,5d^1$	$3d^{10}\,4p^6\,4d^1$
$4s^2\,4p^5\,4d^1\,5d^1$	$3d^9\,4s^2\,4p^6\,4f^1$	$3d^{10}\,4s^1\,4p^5\,4d^1$
$4s^2\,4p^4\,4d^2\,4f^1$	-	$3d^{10}\,4s^2\,4p^4\,5p^1$
$4s^2\,4p^5\,4d^1\,4f^1$	-	$3d^{10}\,4s^1\,4p^5\,4f^1$
-	-	$3d^{10}\,4s^1\,4p^5\,5p^1$
-	-	$3d^9\,4s^2\,4p^5\,4f^1$
-	-	$3d^9\,4s^2\,4p^4\,4d^2$
-	-	$3d^9\,4s^2\,4p^5\,4f^1$

All the transitions considered in the present work are dipole allowed. In order to check the accuracy of our calculated wavefunctions we have compared our calculated excitation energies and oscillator strengths with the available experimental and other theoretical calculations (see table 5.3). The available experimental excitation energy results are from Utter *et al.* and Radtke *et al.* [250, 254]. It can be seen from the table 5.3 that our calculated excitation energies are in good agreement with their results with the maximum relative difference less than 1%. Also our energies are in overall good agreement with the available other theoretical calculations [257, 260, 262, 265, 277–279]. For oscillator strengths, there are no experimental results available and hence we have compared in table 5.3 our results, only with the other available theoretical calculations. Fully relativistic calculations are available from Fournier [260] for all the three ions, Fisher *et al.* [277] for W^{37+}, Gaigalas *et al.*[279] for W^{38+}, Aggarwal *et al.*[265] and Putterich *et al.* [257] for W^{39+} ion. We have taken the oscillator strengths calculated in Babushkin (length) gauge. In contrast to our calculation, Fournier [260] reported the Coulomb gauge (velocity gauge) oscillator strengths calculated by RELAC code [280]. Fisher and Gaigalas [277, 279] reported the oscillator strengths in length gauge but they have considered single and double both excitations from a multi reference set (SD-MR) to generate expansions for the MCDHF approximation while we have considered only single excitations. Aggarwal *et al.* [265] and Putterich *et al.* [257] used different GRASP [108, 160] code to calculate the oscillator strengths. On comparison of our results with their calculations we find overall good agreement with the maximum deviation of less than 15% for most of the transitions. This difference among the various theoretical results can be said to be due to different methods and gauges used in the calculations.

Table 5.3: Different considered transitions of Rb-like W^{37+} through Br-like W^{39+} ions and comparison of our calculated excitation energies (eV) and oscillator strengths with the other available experimental and theoretical values.

Ion	*Notation used for the transition*	*Lower Level*	*Upper Level*	*Brief representation of transition*	*Energy*			*f*	
					Present	*Experiment*	*theory*	*present*	*Other*
W^{37+}	Rb-1	$[4d_{3/2}]_{J=3/2}$	$[4p_{1/2}(4d_{3/2}^2)_2]_{J=3/2}$	$(p_{1/2} \rightarrow d_{3/2})$	273.35	270.82[a]	276.79[b] 272.52[c] 276.96[d]	1.170	0.993[c] 1.198[d]
	Rb-2	$[4d_{5/2}]_{J=5/2}$	$[(4p_{1/2}4d_{3/2})_2 4d_{5/2}]_{J=3/2}$	$(p_{1/2} \rightarrow d_{5/2})$	269.20	269.16[a]	268.73[c] 272.62[d]	0.467	0.451[c] 0.523[d]
	Rb-3	$[4d_{5/2}]_{J=5/2}$	$[(4p_{1/2}4d_{3/2})_2 4d_{5/2}]_{J=7/2}$	$(p_{1/2} \rightarrow d_{5/2})$	268.42	269.46[a]	268.25[c] 272.19[d]	0.952	0.811[c] 1.030[d]
	Rb-4	$[4d_{3/2}]_{J=3/2}$	$[4p_{1/2}(4d_{3/2}^2)_2]_{J=5/2}$	$(p_{1/2} \rightarrow d_{3/2})$	249.32	249.76[a] 250.37[b]	252.74[b] 250.36[c] 252.87[d]	0.685	0.619[c] 0.795[d]
	Rb-5	$[4d_{3/2}]_{J=3/2}$	$[4f_{5/2}]_{J=5/2}$	$(d_{3/2} \rightarrow f_{5/2})$	219.06	217.98[a] 218.05[b]	221.22[b] 218.77[c] 221.18[d]	0.573	0.427[c] 0435[d]

Rb-6	$[4d_{3/2}]_{J=3/2}$	$[(4p^3_{3/2})_{3/2}(4d^2_{5/2})_4]_{J=5/2}$	$\left(p_{3/2} \to d_{5/2}\right)$	216.72	214.69[a] 214.73[b]	218.60[b] 215.75[c] 218.74[d]	0.318	0.328[c] 0.349[d]
Rb-7	$[4d_{5/2}]_{J=5/2}$	$[4f_{7/2}]_{J=7/2}$	$\left(d_{5/2} \to f_{7/2}\right)$	201.28	200.23[a]	203.57[b] 201.18[c] 203.51[d]	0.502	0.433[c] 0.445[d]
Rb-8	$[4d_{5/2}]_{J=5/2}$	$[4f_{5/2}]_{J=5/2}$	$\left(d_{5/2} \to f_{5/2}\right)$	199.93	200.23[a]	202.16[b] 199.63[c] 202.13[d]	0.114	0.137[c] 0.144[d]
Rb-9	$[4d_{5/2}]_{J=5/2}$	$[(4p^3_{3/2})_{3/2}(4d^2_{5/2})_4]_{J=5/2}$	$\left(p_{3/2} \to d_{5/2}\right)$	196.21	195.46[a]	199.53[b] 196.61[c] 199.68[d]	0.360	0.294[c] 0.33[d]
Rb-10	$[4d_{5/2}]_{J=5/2}$	$[(4p^3_{3/2})_{3/2}(4d^2_{5/2})_2]_{J=3/2}$	$\left(p_{3/2} \to d_{5/2}\right)$	194.85	195.46[a]	196.86[c] 199.53[d]	0.280	0.251[c] 0.261[d]
Rb-11	$[4d_{3/2}]_{J=3/2}$	$[((4p^3_{3/2})_{3/2}4d_{3/2})_3 4d_{5/2}]_{J=3/2}$	$\left(p_{3/2} \to d_{5/2}\right)$	191.68	191.26[a]	191.95[c] 194.39[d]	0.317	0.288[c] 0.323[d]
Rb-12	$[4d_{3/2}]_{J=3/2}$	$[((4p^3_{3/2})_{3/2}4d_{3/2})_2 4d_{5/2}]_{J=5/2}$	$\left(p_{3/2} \to d_{5/2}\right)$	186.17	187.03[a]	187.38[c] 188.70[d]	0.174	0.163[c] 0.182[d]
Rb-13	$[4d_{3/2}]_{J=3/2}$	$[(4p^3_{3/2})_{3/2}(4d^2_{3/2})_2]_{J=1/2}$	$\left(p_{3/2} \to d_{3/2}\right)$	152.33	152.21[c]	152.50[d]	1.73e-3	1.67e-3[d]

	Rb-14	$[4d_{3/2}]_{J=3/2}$	$[(4p^{3}_{3/2})_{3/2}(4d^{2}_{3/2})_{2}]_{J=3/2}$	$(p_{3/2}\rightarrow d_{3/2})$	152.33	152.21[c]	151.44[c] 152.39[d]	1.26e-3	1.20e-3[c] 1.24e-3[d]
W^{38+}	Kr-1	$[4p^{4}_{3/2}]_{J=0}$	$[4p_{1/2}4d_{3/2})]_{J=1}$	$(p_{1/2}\rightarrow d_{3/2})$	268.82	265.66[a] 267.21[b]	269.16[b] 268.67[d] 265.70[e] 266.92[f]	2.570	2.565[d] 2.182[f]
	Kr-2	$[4p^{4}_{3/2}]_{J=0}$	$[(4p^{3}_{3/2})_{3/2}4d_{5/2})]_{J=1}$	$(p_{3/2}\rightarrow d_{5/2})$	195.72	194.08[a] 193.79[b]	196.03[b] 195.79[d] 194.10[e] 194.82[f]	1.290	1.294[d] 1.141[f]
	Kr-3	$[4p^{4}_{3/2}]_{J=0}$	$[(4p^{3}_{3/2})_{3/2}4d_{3/2})]_{J=1}$	$(p_{3/2}\rightarrow d_{3/2})$	153.21	153.75[a]	153.26[b] 153.28[d] 153.70[e] 153.67[f]	7.53e-3	7.66e-3[d] 7.36e-3[f]
W^{39+}	Br-1	$[4p^{3}_{3/2}]_{J=3/2}$	$[(4p_{1/2}(4p^{3}_{3/2})_{3/2})_{1}4d_{5/2}]_{J=5/2}$	$(p_{1/2}\rightarrow d_{5/2})$	270.11	269.80[a]	271.50[b] 271.48[d]	0.096	0.091[d]
	Br-2	$[4p^{3}_{3/2}]_{J=3/2}$	$[(4p_{1/2}(4p^{3}_{3/2})_{3/2})_{2}4d_{3/2}]_{J=1/2}$	$(p_{1/2}\rightarrow d_{3/2})$	267.61	264.77[a]	269.74[b] 269.13[d] 269.77[g]	0.502	0.473[d] 0.426[g]
	Br-3	$[4p^{3}_{3/2}]_{J=3/2}$	$[(4p_{1/2}(4p^{3}_{3/2})_{3/2})_{2}4d_{3/2}]_{J=3/2}$	$(p_{1/2}\rightarrow d_{3/2})$	267.13	264.77[a] 264.87[b]	268.81[b] 268.47[d]	0.562	0.584[d]

						268.83[g]		0.316[g],0.538[i]
Br-4	$[4p^3_{3/2}]_{J=3/2}$	$[(4p_{1/2}(4p^3_{3/2})_{3/2})_2\,4d_{3/2}]_{J=5/2}$	$\left(p_{1/2}\rightarrow d_{3/2}\right)$	267.15	264.77[a] 264.87[b]	268.84[b] 268.43[d] 268.77[g]	1.05	1.017[d] 0.918[g]
Br-5	$[4p^3_{3/2}]_{J=3/2}$	$[(4p_{1/2}(4p^3_{3/2})_{3/2})_1\,4d_{3/2}]_{J=5/2}$	$\left(p_{1/2}\rightarrow d_{3/2}\right)$	246.89	244.74[a]	247.90[b] 247.92[d] 249.52[g]	0.027	0.028[d] 0.026[g]
Br-6	$[4p^3_{3/2}]_{J=3/2}$	$[4s_{1/2}]_{J=1/2}$	$\left(s_{1/2}\rightarrow p_{3/2}\right)$	203.85	203.09[a]	205.67[b] 205.32[d] 209.11[g]	0.192	0.160[d] 0.152[g]
Br-7	$[4p^3_{3/2}]_{J=3/2}$	$[(4p^2_{3/2})_2\,4d_{5/2})]_{J=5/2}$	$\left(p_{3/2}\rightarrow d_{5/2}\right)$	192.92	191.75[a] 191.51[b] 192.02[j]	194.34[b] 194.10[d] 194.94[g] 193.63[h]	0.563	0.563[d] 0.519[g] 0.553[i]
Br-8	$[4p^3_{3/2}]_{J=3/2}$	$[(4p^2_{3/2})_2\,4d_{5/2})]_{J=3/2}$	$\left(p_{3/2}\rightarrow d_{5/2}\right)$	189.97	188.83[a] 188.54[b]	191.18[b] 191.04[d] 191.78[g]	0.301	0.321[d] 0.265[g]
Br-9	$[4p^3_{3/2}]_{J=3/2}$	$[(4p^2_{3/2})_2\,4d_{3/2})]_{J=5/2}$	$\left(p_{3/2}\rightarrow d_{3/2}\right)$	152.20	152.78[a]	153.27[b] 153.27[d] 155.49[g]	2.42e-3	2.37e-3[d] 2.25e-3[g]

[a]Utter *et al.*[250], [b]Radtk *et al.*[254], [c]Fischer [277], [d]Fournier [260], [e]Kramida *et al.*[278], [f]Gaigalas *et al.*[279], [g]Aggarwal *et al.* [265], [h]Putterich *et al.*[281]

5.3.2 Electron impact excitation cross sections

In Figure 5.1 we have shown electron impact excitation cross section results for all the considered transitions in the wide range of incident electron energy up to 20 keV. Nature of the cross section curves for all ions is similar as expected for the dipole allowed transitions. Total cross section decreases continuously with the increasing impact energy, in fact near threshold it decreases faster and then decreases steadily in high energy regimes. We observe a common characteristic in all the ions that the cross sections for the transitions $4p_{1/2} \rightarrow 4d_{3/2}$ are larger than those for $4p_{3/2} \rightarrow 4d_{3/2}$. Further, the relative magnitude of the cross sections can also be understood by comparing the oscillator strengths of the transitions in question[282, 283]. For a particular ion, as oscillator strength increases the cross sections also increases. For example, Rb-1, Kr-1, Br-4 transitions having the maximum oscillator strengths, correspond to the largest cross sections whereas Rb-13, Rb-14, Kr-3, and Br-9 transitions with the lowest oscillator strengths correspond to the smallest cross sections. It can be seen that the nearly same oscillator strength for Rb-6, Rb-10 and Rb-11, transitions may be accountable for the similar cross section for these transitions.

5.3.3 Analytic fitting of the cross sections

In plasma models the analytical form of the cross section in terms of incident electron energy is very convenient and often used as input which can easily provide electron impact excitation cross sections at any arbitrary value of energy. We have fitted our calculated cross sections for all the considered transitions up to 20 keV by the analytic form (equation (4.4.2)). The fitted cross sections are accurate to 5%

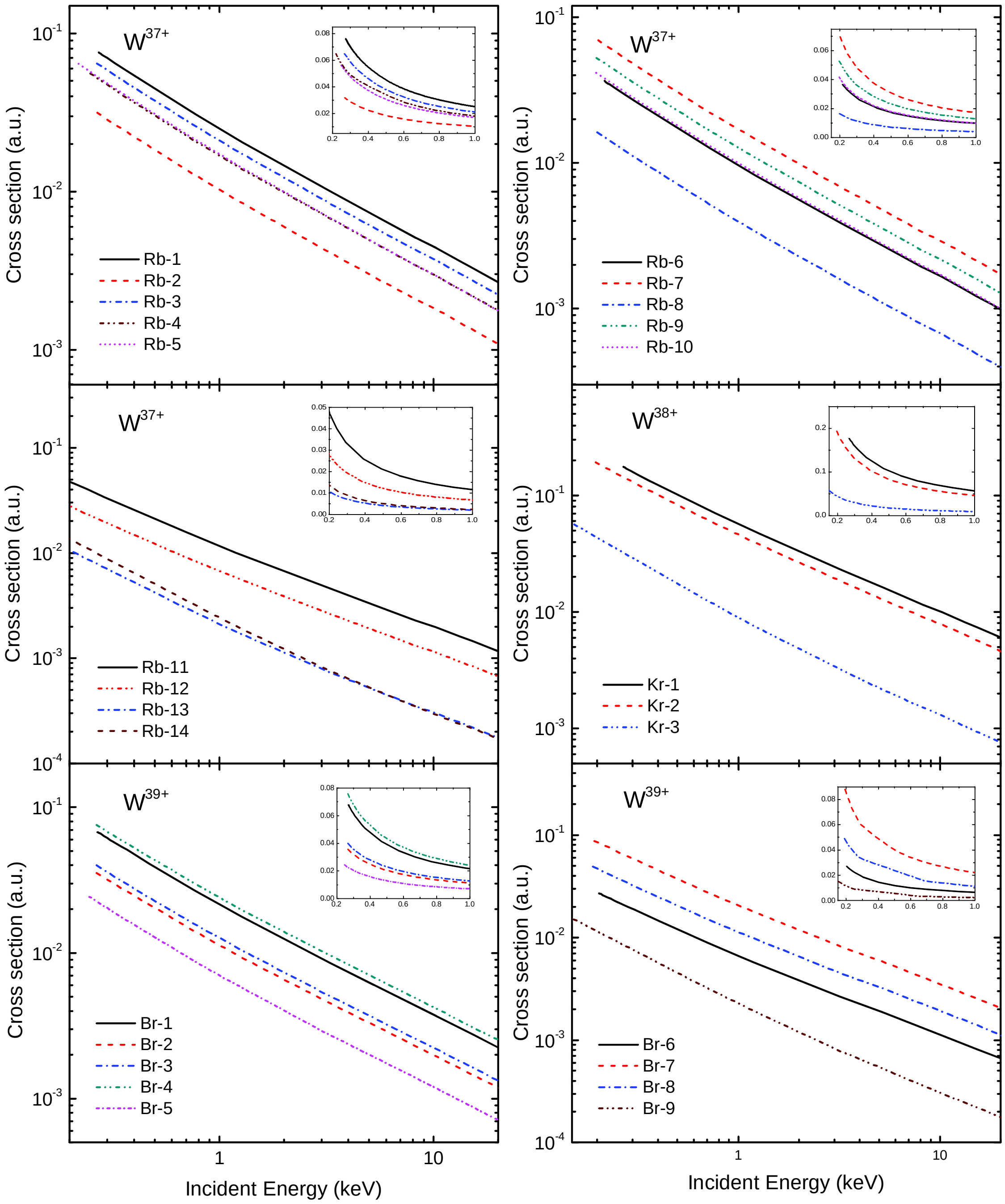

Figure5.1: Electron-impact excitation cross sections (in atomic units) for different transitions as given in Table 3 for Rb-like, Kr-like and Br-like tungsten ions as a function of incident electron energy. In this figure., cross sections for the transitions Rb-13, Rb-14, Kr-3 are multiplied by a factor of 20 and Br-1, Br-5, Br-9 are multiplied by a factor 10.

Table 5.4: Fitting coefficients of the electron impact excitation cross section for all the transitions considered in table 5.3.

Ion	***Key***	b_0	b_1	b_2	***b3***	c_0	c_1	c_2
W^{37+}	Rb-1	6.93546e+1	1.21075e+0	4.55392e-4		1.25855e+1	9.84906e+1	6.93710e-1
	Rb-2	1.22212e+2	2.13987e+0	8.08785e-4		4.92680e+1	4.23145e+2	3.00770e+1
	Rb-3	3.43770e+2	6.03654e+0	2.28144e-3		6.64628e+1	5.82524e+2	4.15455e+0
	Rb-4	1.10096e+2	2.38658e+0	2.05882e-3	-9.65398e-7	5.14259e+0	2.34191e+2	2.39672e+0
	Rb-5	6.87764e+1	1.24615e+1	4.74317e-4		6.01542e+0	1.41666e+2	1.09498e+0
	Rb-6	4.59225e+1	8.44660e-1	3.27192e-4		6.89888e+0	1.69118e+2	1.32837e+0
	Rb-7	3.40037e+1	6.25930e-1	2.39633e-4		2.01751e+0	7.06350e+1	5.64330e-1
	Rb-8	9.43133e+2	1.66554e+1	6.21000e-3		1.72783e+2	8.39904e+3	6.46934e+1
	Rb-9	8.32868e+1	1.57106e+0	6.40496e-4		5.35766e+0	2.32134e+2	1.93430e+0
	Rb-10	6.87093e+1	1.29906e+0	5.33131e-4		5.66746e+0	2.44208e+2	2.04475e+0
	Rb-11	1.86910e+2	4.28370e+0	3.81368e-3	-1.89651e-6	-5.97289e+0	5.75385e+2	6.57631e+0
	Rb-12	1.95215e+1	3.48690e-1	1.34269e-4		1.76337e+0	1.01289e+2	8.08970e-1
	Rb-13	[a]6.93288e+1	4.00677e+0	8.85098e-3		3.05479e+2	1.70606e+4	1.13014e+3
		[b]4.93951e+1	2.12441e-1			-2.59643e+4	1.42622e+4	2.38227e+1
	Rb-14	-1.22945e+2	-4.62492e+0	-7.85916e-3	4.88261e-6	-2.06012e+3	-2.20484e+4	-1.24630e+3
W^{38+}	Kr-1	1.38763e+2	2.29571e+0	8.22255e-4		1.09197e+1	8.58127e+1	5.76980e-1
	Kr-2	5.94617e+1	1.09121e+0	4.22758e-4		4.49300e-1	4.56001e+1	3.67710e-1
	Kr-3	2.39446e+1	2.94500e-2	-3.80501e-5		-2.18666e+2	1.55184e+3	-8.65980e-1
W^{39+}	Br-1	1.92229e+1	2.75630e-1	8.15538e-5		3.13928e+1	3.05701e+2	1.75754e+0
	Br-2	1.47101e+2	2.25895e+0	7.08164e-4		5.32525e+1	4.52117e+2	2.78163e+0

Br-3	5.67661e+2	8.77650e+0	2.77717e-3		1.82077e+2	1.82077e+2	9.65294e+0
Br-4	5.54987e+1	8.60470e-1	2.73494e-4		9.34857e+0	8.02609e+1	4.98880e-1
Br-5	2.89540e+2	3.71407e+0	9.39230e-4		7.15560e+2	1.38743e+4	7.22722e+1
Br-6	4.77551e+1	7.43440e-1	2.14117e-4		9.86197e+0	2.49522e+2	1.62373e+0
Br-7	2.94642e+1	4.84930e-1	1.47152e-4		1.27200e+0	5.00300e+1	3.47260e-1
Br-8	4.12807e+1	6.79580e-1	2.05480e-4		2.88350e+0	1.27633e+2	8.88780e-1
Br-9	1.04000e-2	7.14142e-4	1.35192e-6	-9.58995e-10	7.48100e-2	1.16879e+0	9.29400e-2

5.3.4 Linear polarizations

In figure 5.2, we have shown the linear polarization results of the emitted radiation due to decay of the electron excited states as a function of incident electron energy for all the three ions (W^{37+} - W^{39+}). The linear polarization of the photon emitted from the excited state with J_f =1/2 is zero. It is due to the fact that the excited state with J_f =1/2 is not aligned as $\sigma(1/2) = \sigma(-1/2)$. Therefore, the linear polarization for the transitions Rb-13, Br-2 and Br-6 are not shown in the figure. 5.2. From the figure 5 2 we find that all the curves show common expected behavior i.e., the polarization decreases with the increasing electron impact energy and becomes negative at around 3-5 keV for most of the transitions. Positive (or negative) linear polarization represents that the electric vector of the emitted radiation is parallel (or transverse) to the incident electron beam. Variation of the polarization can be understood as, near the threshold momentum transfer takes place along the direction of electron motion and at higher energies momentum transfer is transverse to the electron motion. We observe that the transitions from J_f =1 to J_i = 0 viz. Kr-1, Kr-2, Kr-3 have maximum polarization nearly 30 % to 35 % near the threshold. We find that transitions for which ΔJ = -1, have nearly zero polarization. For example, polarization for Rb-2, Rb-10 transition is less than 0.6%. For remaining transitions, polarization is higher for the transitions with ΔJ = 0 than the transitions with ΔJ = 1.

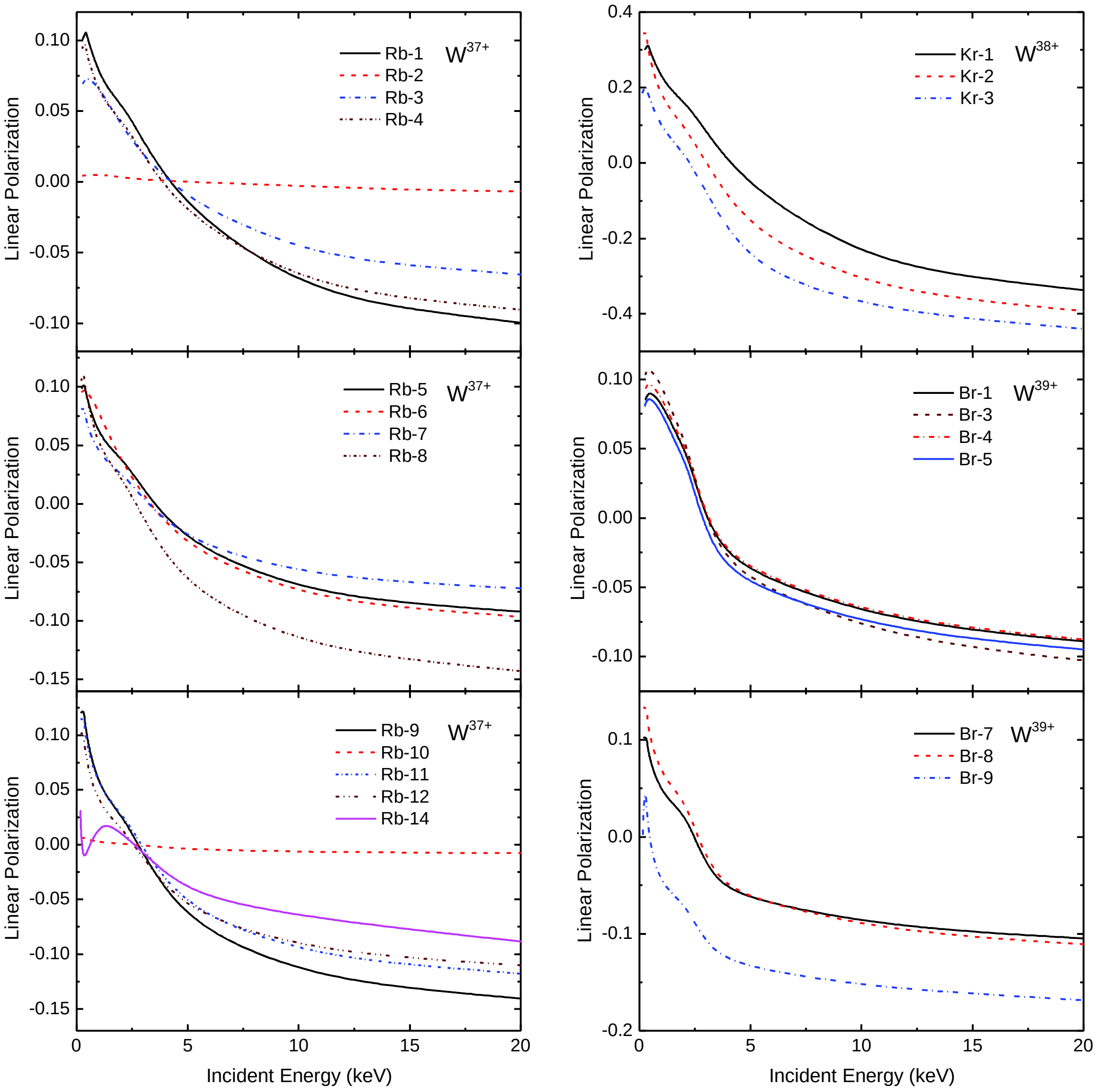

Figure 5.2: Degree of linear polarization of the photon emitted from different anisotropic excited states as given in table 5.1 for Rb-like, Kr-like and Br-like tungsten ions as a function of incident electron energy.

5.4 Conclusions

In the present Chapter, we have studied electron impact excitation of the W^{37+} to W^{39+} tungsten ions. Special attention has been focused on the strong lines which have been identified by Utter *et al.* [250] in soft X-ray range for these ions. The RDW theory has been employed to calculate the excitation cross sections for the electron impact energy ranging from threshold to 20 keV. The degree of linear polarization of the characteristic photons emitted from various anisotropic excited states has also been reported. A good agreement is found when our results for excitation energies and oscillator strengths are compared with the available experimental and other theoretical results. This ensures the accuracy of the target wavefunctions used in our calculations. Finally, we have fitted our calculated cross sections through an analytic formula for their direct application in plasma modelling. To date, there are no experimental or theoretical results available for electron excitation cross sections and polarization of photons for W^{37+} to W^{39+} ions. We believe that the present work is very useful as both the cross sections and polarizations can be applied to the diagnostics of the ITER plasmas.

CHAPTER 6

ELECTRON IMPACT M-SHELL EXCITATION OF TUNGSTEN IONS AND POLARIZATION OF THEIR PHOTON EMISSION

6.1 Introduction

In the previous Chapter we have studied electron impact N-shell excitations of tungsten ions. In this the present Chapter we consider electron impact M-shell excitation of tungsten ions. X-ray spectroscopy utilizing emissions from L-shell as well as M-shell tungsten ions is an attractive option for tokomak plasma diagnostics [281, 284–294]. There has been interest in the study of emissions from M-shell charged states of tungsten, which will be present in considerable amount in the ITER core under ohmic plasma operations. The electron excitation processes corresponding to these lines are studied in detail due to the importance of the cross section data to identify and interpret the spectroscopic data of the tungsten ions. Also anticipating the importance of information about the polarization [295] of the subsequent emission arising from electron impact anisotropically excited states of tungsten ions, results are obtained for polarization of the photon emissions utilizing the calculated magnetic sublevel excitation cross sections. In this context, let us first review the literature available for various M-shell transitions.

A significant amount of theoretical [85, 268, 270, 296–300] and experimental [286, 292–294, 301] work has been performed on M-shell spectra of various ion charge species of tungsten. For the electron impact excitation studies, Zhang *et al.* [296, 302] reported their relativistic distorted wave collision strengths for Ni-like and Cu-like tungsten ions. Xie *et al.* [270] reported magnetic sublevel excitation cross sections and polarization of

Ni-like through Ge-like tungsten ions. Das *et. al* [85] and Dipti *et. al.*[268] have reported electron impact excitation RDW cross sections and polarization of emitted photon for Co-like through Zn-like and Fe-like through Al-like tungsten ions, respectively. Though one can find a great deal of scattered literature on different ionic stages of tungsten ions, the existing electron impact excitation cross section data is still insufficient.

In the present Chapter we consider the $n = 3 \rightarrow 3$ transitions in K-like through Ne-like tungsten ions. Wavelength measurements performed at Super EBIT facility at Livermore for the $n = 3 \rightarrow 3$ transitions in 19–25 Å soft X-ray range for these ions were reported by Clementson *et al.* [294]. In particular, we studied electron impact excitation due to $3s_{1/2}$-$3p_{3/2}$ and $3p_{1/2}$-$3d_{3/2}$ transitions in potassium like W^{55+}through neon like W^{64+}ions. Magnetic sub-level excitation cross sections and summed cross sections as well as polarization of photon after excitation were calculated for the incident electron energies up to 20 keV within the framework of our RDW approach.

The RDW method has already been described in the earlier Chapter and the same has been adopted here in the present Chapter for the entire calculations. In Section 6.2 provide results and discussion for electron impact excitation cross section and polarization of emitted photon. Conclusion is given in section 6.3.

6.2. Results and Discussion

6.2.1. Dirac-Fock wave functions for W^{48+} through W^{64+} ions

We performed tungsten ion structure calculations within multi-configuration Dirac-Fock framework using GRASP2k [99]. A number of CSF's, corresponding to the configurations displayed in table 6.1, were included to describe the initial and final states of the tungsten ions. We also calculated the wavefunctions excitation energies and oscillator strengths for all the transitions considered. In table 6.2, we compare our values with the available measurements and the theoretical results obtained using FAC and GRASP2k by Clementson *et al.* [294] as well as other calculations [147, 303–307]. Among other calculations are the MCDF calculations of Huang and co-workers[303–306, 308] for Cl-like W^{57+} through Al- like W^{61+} ions. In case of Al-3 and Al-4 transitions, Safronova *et. al.* [307] used the relativistic many-body perturbation theory (RMBPT) theory. Excitation energies for transitions Cl-3, S-3, P-1 and P-2, are also available from the NIST database [147]. On comparison of excitation energies from the table 6.2, we find that our calculations show an overall good agreement with measurements of Clementson *et al.*

[294] and their reported FAC calculations [294] for all the ions. It can further be seen from table 6.2 that our values for oscillator strengths are within 5% of the only available MCDF calculations for all the transitions except in case of transitions Cl-1 and Cl-3, where the difference between the two theoretical results is, respectively, 14% and 7% [303–306, 308]. We hope that the forthcoming measurements as well as other better theoretical calculations will provide more meaningful comparisons.

Table 6.1.CSF's used in GRASP2K [99] code for the representation of target ion wave function for the initial and the final states in K-like W^{55+} through Ne-like W^{64+} ions.

K-like W^{55+}	***Ar-like W^{56+}***	***Cl-like W^{57+}***	***S-like W^{58+}***	***P-like W^{59+}***
$3s^2 3p^6 3d$ $3s^2 3p^5 3d^2$ $3s 3p^6 3d^2$ $3p^6 3d^3$ $3s^2 3p^5 4p 4d$ $3s 3p^5 3d^3$	$3s^2 3p^6$ $3s^2 3p^5 3d$ $3s^2 3p^5 4s$ $3s^2 3p^5 4d$ $3s^2 3p^5 5s$	$3s^2 3p^5$ $3s 3p^5 3d$ $3p^5 3d^2$ $3s^2 3p^4 3d$ $3s^2 3p^4 4s$ $3s^2 3p^4 4d$ $3s 3p^6$ $3p^6\ 3d$	$3s^2 3p^4$ $3s^2 3p^3 3d$ $3s^2 3p^2 3d^2$ $3s 3p^3 3d^2$ $3s 3p^5$ $3p^5 3d$	$3s^2 3p^3$ $3s^2 3p^2 3d$ $3s^2 3p 3d^2$ $3s 3p^3 3d$ $3s 3p^2 3d^2$ $3p^5$ $3s 3p^4$ $3p^4 3d$
Si-like W^{60+}	***Al-like W^{61+}***	***Mg-like W^{62+}***	***Na-like W^{63+}***	***Ne-like W^{64+}***
$3s^2 3p^2$ $3s^2 3p 3d$ $3s^2 3d^2$ $3s 3p^3$ $3s 3p 3d^2$	$3s^2 3p$ $3s 3p 3d$ $3s^2 3d$ $3s 3p^2$ $3p^2 3d$ $3p^3$	$2p^6 3s^2$ $2p^6 3s 3p$ $2p^6 3s 3d$ $2p^6 3p^2$ $2p^5 3s^2 3p$	$2p^6 3s$ $2p^6 3p$ $2p^5 3p^2$ $2p^5 3s 3d$	$2s^2 2p^6$ $2s^2 2p^5 3s$ $2s^2 2p^5 3p$ $2s^2 2p^5 4p$ $2s^2 2p^4 3s 3d$ $2s^2 2p^4 3p^2$ $2s^2 2p^4 3d^2$ $2s 2p^6 3s$ $2p^6 3s^2$ $2p^6 3p^2$

Table6.2. Comparison of our calculated excitation energies (in eV) and the oscillator strengths (*f*) of the transitions in K-like W^{55+} through Ne-like W^{64+} ions with the available measurements and the other theoretical calculations.

Ion	*Key*	*Lower Level*	*Upper Level*	$E_{Present}$	$E_{Measured}$ [294]	E_{FAC} [294]	E_{GRASP2} [294]	$E_{Previous}$	$f_{Present}$	$f_{Previous}$
W^{55+}	K-1	$\left[3s^2 3p^6 3d_{3/2}\right]_{J=3/2}$	$\left[3s^2\left(3p_{1/2}3p_{3/2}^4\right)_{1/2} 3d_{3/2}^2\right]_{J=3/2}$	647.19	646.2	647.67	649.88		1.441	
	K-2	$\left[3s^2 3p^6 3d_{3/2}\right]_{J=3/2}$	$\left[3s^2\left(3p_{1/2}3p_{3/2}^4\right)_{1/2} 3d_{3/2}^2\right]_{J=5/2}$	601.23	603.27	603.74	602.60		0.385	
W^{56+}	Ar-1	$\left[3s^2 3p^6\right]_{J=0}$	$\left[3s^2\left(3p_{1/2}3p_{3/2}^4\right)_{1/2} 3d_{3/2}\right]_{J=1}$	631.80	630.03	631.41	632.35		0.722	
W^{57+}	Cl-1	$\left[3s^2 3p_{1/2}^2 3p_{3/2}^3\right]_{J=3/2}$	$\left[3s^2\left(3p_{1/2}3p_{3/2}^3\right)_2 3d_{3/2}\right]_{J=1/2}$	631.01	631.93	633.54	637.71	636.6[a]	0.217	0.190
	Cl-2	$\left[3s^2 3p_{1/2}^2 3p_{3/2}^3\right]_{J=3/2}$	$\left[3s^2\left(3p_{1/2}3p_{3/2}^3\right)_2 3d_{3/2}\right]_{J=3/2}$	624.90	625.74	626.63	628.53	631.7[a]	0.203	0.196
	Cl-3	$\left[3s^2 3p_{1/2}^2 3p_{3/2}^3\right]_{J=3/2}$	$\left[3s^2\left(3p_{1/2}3p_{3/2}^3\right)_2 3d_{3/2}\right]_{J=5/2}$	622.10		624.07	626.53	628.9[a] 622.9[b]	0.315	0.294
W^{58+}	S-1	$\left[3s^2 3p_{1/2}^2 3p_{3/2}^2\right]_{J=2}$	$\left[3s^2\left(3p_{1/2}\left(3p_{3/2}^2\right)_2\right)_{5/2} 3d_{3/2}\right]_{J=1}$	628.44	627.7	629.30	632.83	629.76[c]	0.173	0.177[c]
	S-2	$\left[3s^2 3p_{1/2}^2 3p_{3/2}^2\right]_{J=2}$	$\left[3s^2\left(3p_{1/2}\left(3p_{3/2}^2\right)_2\right)_{5/2} 3d_{3/2}\right]_{J=2}$	622.54		623.57	627.61	623.92[c]	0.256	0.254[c]
	S-3	$\left[3s^2 3p_{1/2}^2 3p_{3/2}^2\right]_{J=0}$	$\left[3s^2\left(3p_{1/2}\left(3p_{3/2}^2\right)_0\right)_{1/2} 3d_{3/2}\right]_{J=1}$	623.39		622.35	624.54	622.19[b]	0.158	

	S-4	$\left[3s^2 3p_{1/2}^2 3p_{3/2}^2\right]_{J=2}$	$\left[3s^2\left(3p_{1/2}\left(3p_{3/2}^2\right)_2\right)_{5/2} 3d_{3/2}\right]_{J=3}$	615.23	615.40	616.35	619.74	618.29[c]	0.263	0.262[c]
	S-5	$\left[3s^2 3p_{1/2}^2 3p_{3/2}^2\right]_{J=2}$	$\left[3s_{1/2} 3p_{1/2}^2\left(3p_{3/2}^3\right)_{3/2}\right]_{J=2}$	530.35	530.98	531.10	533.33		0.072	
W^{59+}	P-1	$\left[3s^2 3p_{1/2}^2 3p_{3/2}\right]_{J=3/2}$	$\left[3s^2\left(3p_{1/2} 3p_{3/2}\right)_2 3d_{3/2}\right]_{J=3/2}$	621.48		622.54	626.53	622.28[d] 621.20[b]	0.388	0.364[d]
	P-2	$\left[3s^2 3p_{1/2}^2 3p_{3/2}\right]_{J=3/2}$	$\left[3s^2\left(3p_{1/2} 3p_{3/2}\right)_2 3d_{3/2}\right]_{J=1/2}$	619.41		621.72	624.73	620.85[d] 619.00[b]	0.125	0.129[d]
	P-3	$\left[3s^2 3p_{1/2}^2 3p_{3/2}\right]_{J=3/2}$	$\left[3s^2\left(3p_{1/2} 3p_{3/2}\right)_1 3d_{3/2}\right]_{J=5/2}$	609.11	610.19	611.21	614.18	610.72[d]	0.311	0.309[d]
	P-4	$\left[3s^2 3p_{1/2}^2 3p_{3/2}\right]_{J=3/2}$	$\left[3s_{1/2} 3p_{1/2}^2\left(3p_{3/2}^2\right)_2\right]_{J=5/2}$	515.43	515.70	515.78	516.67	517.83[d]	0.042	0.043[d]
W^{60+}	Si-1	$\left[3s^2 3p_{1/2}^2\right]_{J=0}$	$\left[3s^2 3p_{1/2} 3d_{3/2}\right]_{J=1}$	611.60	611.6	612.90	613.78	611.86[e]	0.923	0.880[e]
	Si-2	$\left[3s^2 3p_{1/2}^2\right]_{J=0}$	$\left[3s_{1/2}\left(3p_{1/2}^2\right)_0 3p_{3/2}\right]_{J=1}$	543.63	543.96	544.60	544.65	546.09[e]	0.172	0.174[e]
W^{61+}	Al-1	$\left[3s^2 3p_{1/2}\right]_{J=1/2}$	$\left[3s^2 3d_{3/2}\right]_{J=3/2}$	597.40	597.34	598.35	600.79	597.88[f]	0.490	0.476[f]
	Al-2	$\left[3s^2 3p_{1/2}\right]_{J=1/2}$	$\left[3s_{1/2}\left(3p_{1/2} 3p_{3/2}\right)_1\right]_{J=1/2}$	550.99	549.99	550.89	552.76	553.10[f]	0.212	0.215[f]
	Al-3	$\left[3s^2 3p_{1/2}\right]_{J=1/2}$	$\left[3s_{1/2}\left(3p_{1/2} 3p_{3/2}\right)_1\right]_{J=3/2}$	540.19	539.98	540.24	542.48	542.10[f] 539.53[g]	0.116	0.124[f] 0.103[g]
	Al-4	$\left[3s^2 3p_{1/2}\right]_{J=1/2}$	$\left[3s_{1/2}\left(3p_{1/2} 3p_{3/2}\right)_0\right]_{J=3/2}$	500.60	500.34	500.54	499.65	502.92[f]	0.0020	0.0021[f]

								500.34[g]		0.0019[g]
W^{62+}	Mg-1	$\left[3s_{1/2}3p_{1/2}\right]_{J=1}$	$\left[3s_{1/2}3d_{3/2}\right]_{J=2}$	579.87	580.12	580.45	573.42		0.322	
	Mg-2	$\left[3s^2\right]_{J=0}$	$\left[3s_{1/2}3p_{3/2}\right]_{J=1}$	545.03	545.35	546.16	544.87		0.641	
W^{63+}	Na-1	$\left[3s_{1/2}\right]_{J=1/2}$	$\left[3p_{3/2}\right]_{J=3/2}$	533.27	533.20	533.56	533.28		0.283	
W^{64+}	Ne-1	$\left[2s^2 2p_{1/2}^2 2p_{3/2}^3 3s_{1/2}\right]_{J=1}$	$\left[2s^2 2p_{1/2}^2 2p_{3/2}^3 3p_{3/2}\right]_{J=0}$	588.02	588.51	591.27	591.10		0.052	

[a]Huang *et al* [303]; [b] NIST [147]; [c] Chou *et al* [306]; [d] Huang [304]; [e] Huang [305]; [f] Huang [308]; and [g] Safronova and Safronova [307].

6.2.2 Electron impact excitation cross sections

In figure 6.1, we display different magnetic sublevel cross sections $\sigma(\alpha_f J_f M_f)$ along with the total cross sections for K-like and Ar-like tungsten ions. This figure shows that for K-1 transition, magnetic excitation cross section curve for the sublevel M_f = ±3/2 lies above than that for the corresponding sublevel with M_f = ±1/2 in the incident electron energy range up to ~8 keV and thereafter the behavior is reversed. For K-2 transition where the excitation takes place from the same lower state with J_i= 3/2, the cross sections for the sublevel M_f = ±1/2 are highest followed by excitation to the sublevels with M_f = ±3/2 and M_f = ±5/2 up to an incident electron energy around 8 keV and then the order is reversed. In case of Ar-1, the cross section for the sublevel with M_f= 0 is higher compared to M_f= ±1 up to an energy of 8 keV and then it becomes less. Thus, we observe a general feature, i.e. for each transition, the magnetic sublevels which are more populated in the range of incident energy from the threshold to 8 keV become less populated afterwards. This interesting behavior of the variation of magnetic sublevel cross sections play an important role in the study of the polarization of the radiation emitted following the decay of the excited states. We will see this later when we discuss figure 6.3 for our polarization results corresponding to K-1, K-2 and Ar-1 transitions.

Since we are considering many transitions in different tungsten ions with varying values of J_i and J_f, there would be too many corresponding magnetic sublevel cross section results for each set of J_i and J_f values. Consequently, to avoid crowding of the figures, we only show the total cross sections for all the transition in figure 6.2(a, b).These figures show that all the cross section for different transitions decreases right from the threshold to the higher incident electron energies. We also see the general feature that the cross section for $3s_{1/2}\rightarrow 3p_{3/2}$ transition is always lower than the cross section for the transition $3p_{1/2}\rightarrow 3d_{3/2}$ for each ion except for Mg-like W^{62+} ion where the reverse is seen.

6.2.3 Analytic fitting of the cross sections

Analytic fitting of the obtained cross sections were done using the equation (4.4.2). The calculated fitting coefficients are given in the Table 6.3. These coefficients provide values of cross sections within an accuracy of 5% right from the excitation threshold impact energy.

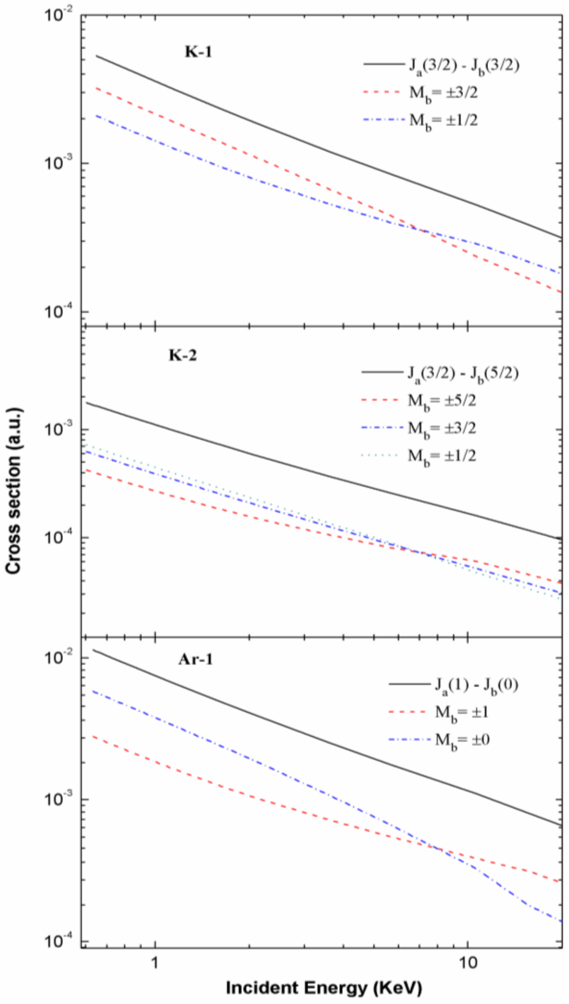

Figure 6.1: Electron impact magnetic sublevel and total excitation cross sections (in atomic units) for K-like and Ar-like tungsten ions as a function of incident electron energy.

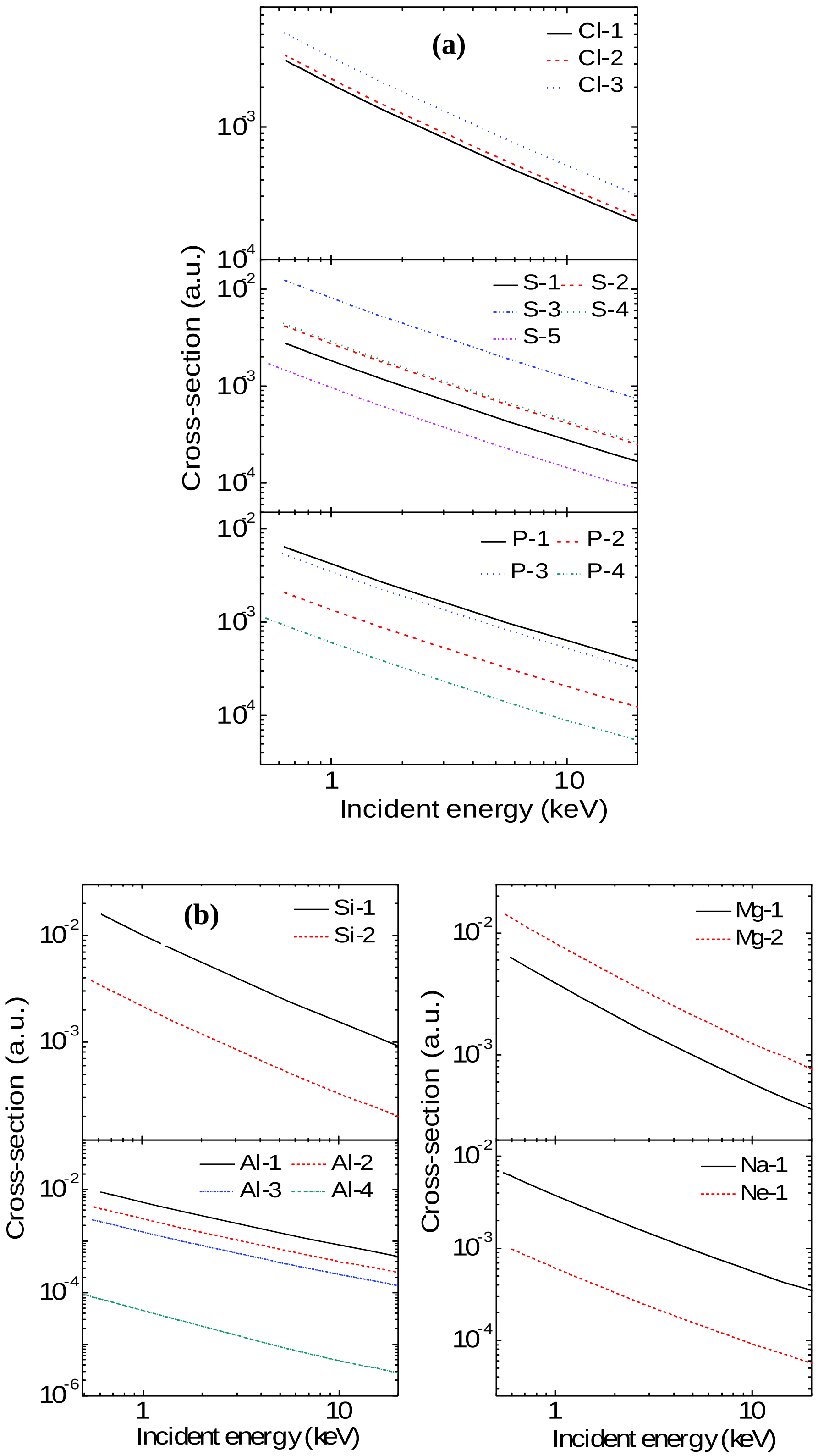

Figure6.2. (**a**) Electron-impact excitation cross sections (in atomic units) for different transitions as given in Table 6 for Cl-like, S-like and P-like tungsten ions as a function of incident electron energy; (**b**) Electron-impact excitation cross sections (in atomic units) for different transitions as given in Table 6 for Si-like, Al-like, Mg-like, Na-like and Ne-like tungsten ions as a function of incident electron energy.

Table6.3. Coefficients for the fitting function given in equation (4.4.2) for electron impact excitation cross sections for all the transitions in K-like W^{55+} through Ne-like W^{64+} ions. The number in the bracket represents the power of 10 by which the quantity has been multiplied.

Ion	***Key***	b_0	b_1	b_2	b_3	c_0	c_1	c_2
W^{55+}	K-1	3.11677(-1)	2.23638(-3)	8.52164(-7)		5.85249(+1)	2.71204(+0)	9.80664(-3)
	K-2	4.48806(-2)	1.73784(-4)			2.53707(+1)	1.16952(+0)	7.96291(-2)
W^{56+}	Ar-1	1.13969(-2)	4.47742(-4)	5.95543(-10)	3.55779(-5)	7.01913(-1)	1.90273(+0)	7.96291(-2)
W^{57+}	Cl-1	9.25517(-2)	3.81140(-4)			2.88522(+1)	1.27190(+0)	1.90158(-5)
	Cl-2	1.02397(-1)	4.21701(-4)			2.88731(+1)	1. 28580(+0)	1.93272(-5)
	Cl-3	1.50742(-1)	6.21858(-4)			2.89651(+1)	1.29560(+0)	1.95184(-5)
W^{58+}	S-1	1.90654(-2)	1.07145(-4)	2.43210(-8)		6.81444(+0)	3.13430(-1)	8.18660(-4)
	S-2	2.88122(-2)	1.61719 (-4)	3.63116(-8)		6.81449(+0)	3.16108(-1)	8.23966(-4)
	S-3	8.51184(-2)	4.83359 (-4)	1.11054(-7)		6.81631(+0)	3.16292(-1)	8.37729(-4)
	S-4	2.67276(-1)	1.51345(-3)	3.44237(-7)		5.93855(+1)	2.78957(+0)	7.38151(-3)
	S-5	1.02681(-1)	7.06571(-4)	2.65752(-7)		5.93142(+1)	3.29168(+0)	1.18559(-2)
W^{59+}	P-1	8.05453(-2)	3.25370(-4)			1.25106(+1)	5.60198(-1)	8.27364(-4)
	P-2	1.40812(-2)	8.06080(-5)	1.92106(-8)		6.68179(+0)	3.12933(-1)	8.45658(-4)
	P-3	3.64642(-2)	2.10421(-4)	5.02610(-8)		6.68194(+0)	3.18220(-1)	8.69310(-4)
	P-4	3.84554(-3)	3.78456(-5)	3.25047(-8)	1.05095(-11)	3.42358(+0)	2.06440(-1)	1.28072(-3)

W^{6o+}	Si-1	4.04866(-1)	1.62130(-3)			2.52737(+1)	1.15084(+0)	1.69347(-3)
	Si-2	9.68220(-2)	3.63716(-4)			2.53397(+1)	1.28431(+0)	1.65007(-3)
W^{61+}	Al-1	9.04079(-3)	2.48386(-7)	1.16146(-3)		3.36091(-3)	3.04110(+0)	1.34588(-1)
	Al-2	4.64005(-3)	1.12413(-7)	6.48106(-4)		2.40066(-3)	3.04169(+0)	1.45958(-1)
	Al-3	2.63551(-3)	1.23729(-4)	9.72385(-11)	1.30408(-5)	3.73498(-1)	2.13835(+0)	1.05531(-1)
	Al-4	9.14755(-5)	4.86592(-6)	3.16316(-12)	3.54016(-7)	1.35241(+0)	1.37690(+0)	7.26933(-2)
W^{62+}	Mg-1	1.61410(-1)	5.05668(-4)			2.53830(+1)	1.16343(+0)	1.22164(-3)
	Mg-2	3.76691(-1)	1.39624(-3)			2.60676(+1)	1.31803(+0)	1.67008(-3)
W^{63+}	Na-1	2.05206(-2)	7.74583(-5)			3.02309(+0)	1.56720(-1)	2.10181(-4)
W^{64+}	Ne-1	3.02868(-3)	1.05254(-5)			3.02448(+0)	1.41603(-1)	1.66132(-4)

6.2.4 Linear polarizations

Magnetic sub-level excitation cross sections are further utilized to calculate the polarization of emitted photons following the decay of electron impact excited states using the formulae given in table 6.1. Results obtained for polarization due to the decay from the final state with J_b to a lower level with J_0 are shown in the figure 6.3(a, b). According to the density matrix theory it is clearly evident that if the polarization of incoming electrons is not accounted for, $\sigma\left(\alpha_b J_b M_b\right)$ will be equal for the two magnetic substates with the same mod value of M_b *i.e.* $\sigma(M_b)=\sigma(-M_b)$. Thus, the excited state with J_b = 1/2 is not aligned; consequently, the degree of linear polarization of the photon emission would be zero. Hence, the polarization for the transitions *viz.* Cl-1, P-2, Al-2 decaying from the excited states with J_b= 1/2 are not displayed in these figures. Another transition Ne-1 following the decay from J_b = 0 to J_0 = 1 give an isotropic photon emission, and its polarization is also zero. The two Figures 3a and b illustrate a general expected behavior *i.e.*, polarization decreases with the increase of incident electron energy for all the transitions considered. For most of the transitions, polarization attains negative values around 8 keV. The two types of decay transitions considered *viz.* $3p_{3/2} \rightarrow 3s_{1/2}$ and $3d_{3/2} \rightarrow 3p_{1/2}$, exhibit different shapes of polarization curves for all the ions. We find that for the decay from J_b = 1 to J_0 = 0 in transitions *viz.*, Ar-1, Si-1, Si-2, S-3 and Mg-2, the polarization near threshold is quite large and nearly 40%.

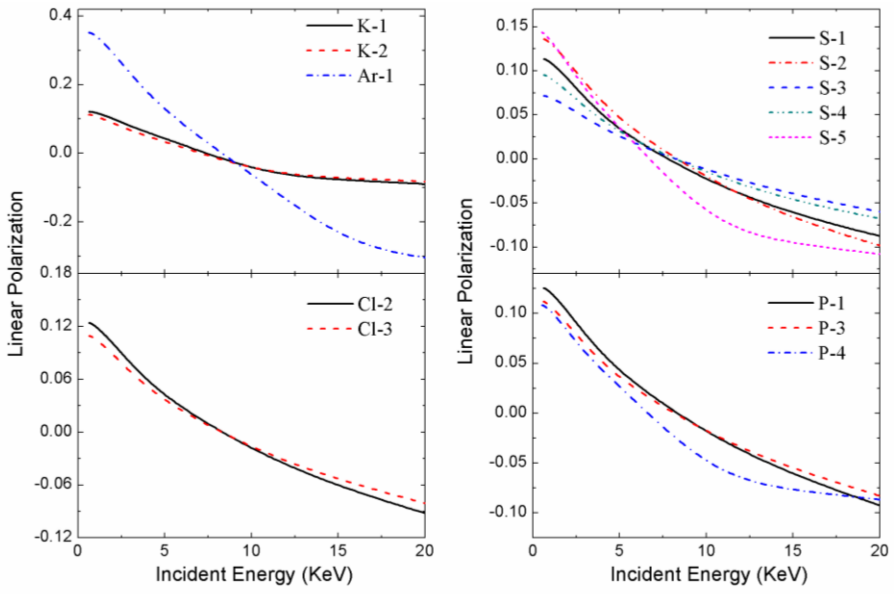

(a)

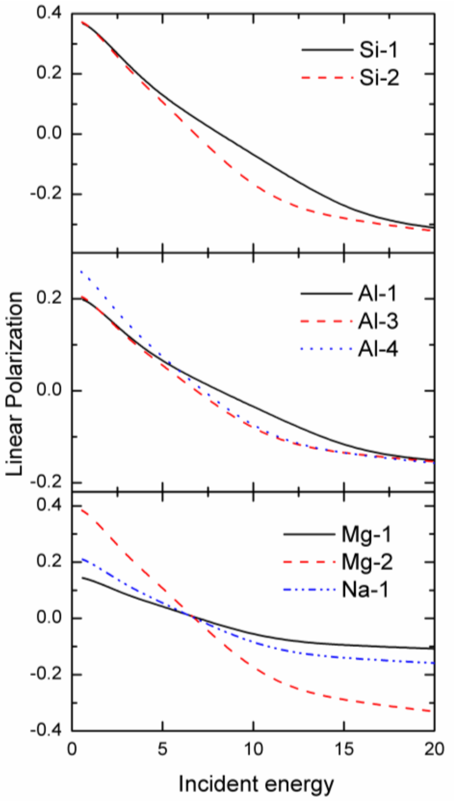

(b)

Figure 6.3(**a**) Polarization for the photon emission from anisotropic excited states through different transitions (as given in Table 6.2) for K-like, Ar-like, Cl-like, S-like and P-like tungsten ions as a function of incident electron energy; (**b**) Polarization for the photon emission from anisotropic excited states through different transitions (as given in Table 6.2) for Si-like, Al-like, Mg-like and Na-like tungsten ions as a function of incident electron energy.

6.3 Conclusions

In the present Chapter, we studied electron impact M-shell excitations of highly charged. Electron impact excitation cross section and polarization of the emitted photon for various transitions in K-like through Ne-like tungsten ions are obtained and reported in the wide range of incident electron energies up to 20 keV. Fitting of the new cross section results is also provided to fulfill the purpose of serving atomic data for fusion plasma diagnostics.

CHAPTER 7

SUMMERY, CONCLUSIONS AND COMMENTS

Present thesis has aimed to theoretically study the electron impact excitations of various fine structure transitions in different atoms and ions which play crucial role in the diagnostics of variety of plasmas. Consequently, electron impact excitation cross sections have been obtained for few important atoms *viz.* cesium, argon and xenon using RDW approach. Further, the applicability of the obtained cross sections has been explored in developing the C-R models to diagnose low temperature plasmas which are useful in many applications such as for neutral beam injectors for ITER and in the studies of different industrial aspect. Another aim has been to perform the calculations of electron impact excitation cross sections and polarization of emitted photon by the subsequent decay of the excited tungsten ions. These obtained cross sections and polarizations are very important in modeling of high temperature ITER fusion plasma thereby assisting in the design and development of ITER. Though the concluding remarks of the work presented in each Chapter has already been added at the end of the Chapters, here, the overall conclusion of entire work presented in this thesis is briefly described below:

In the order to understand the thesis work a general motivation was given and RDW theory used throughout for the cross sections calculation is outlined. A general overview of the collisional radiative (C-R) model used to diagnose plasma is presented.

Electron impact excitations of Cs play dominant role in the low pressure hydrogen-cesium plasma, which is relevant to the negative ion based neutral beam injectors for the ITER project. The existing electron impact data of Cs were not adequate and sufficient for a reliable modeling. For this purpose, a complete set of electron impact excitation cross sections and rate coefficients have been calculated using fully relativistic distorted wave theory for several fine-structure transitions from the ground as well as excited states of cesium atom in the wide range of incident electron energy. Thereafter, the calculated detailed cross sections are used to construct a reliable collisional radiative (C-R) model to characterize the hydrogen-cesium plasma. It is expected that the various results obtained from the present C-R model can describe the real plasma in a better way if the suitable experimental observations are made available.

One of the most commonly used mixture plasma is Ar-O_2 which is often utilized as a source of atomic oxygen. In such plasma the production of atomic oxygen can be influenced by the excited states of argon. It is interesting to study Ar-O_2 mixture plasma as the available studies on population of 1s excited state led to conflicting conclusions. Therefore, a suitable C-R model has been developed for Ar-O_2 mixture plasma and the variations of the plasma n_e and T_e with addition of O_2 is studied by using the reliable complete set of relativistic electron impact excitation cross section data. The model was coupled to the optical spectroscopic measurements reported by Jogi *et al.* [*J. Phys. D: Appl. Phys. 47, 335206 (2014)*]. It is found that as the content of O_2 in Ar increases from 0%–5%, T_e increases in the range 0.85–1.7 eV while the electron density decreases from 2.76e12–2.34e11 cm^{-3}. The Ar-$3p^5 4s$ ($1s_i$) fine-structure level populations at our extracted plasma parameters are found to be in very good agreement with those obtained from the measurements.

The xenon gas discharge is used in various plasma applications. In particular, xenon is used nearly in all modern HETs as propellant. From the literature on the electron excitation cross sections of xenon atom, one observes that there is still lack of sufficient cross section data for the fine structure excitations from the ground and among the excited states for a reliable plasma modeling. Even more recent results for the electron impact excitations are only from the ground state of xenon. Also the available data are not reported in the wide range of incident electron energies. Therefore, for the sake of providing sufficient consistent cross section data, detailed calculations are carried out for the excitation cross sections in xenon involving various transitions from the ground state to the excited as well as among these excited states using the RDW method. As an application, using the obtained cross sections, a collisional Radiative (C-R) model coupled with an optical emission measurement from the inductively coupled Xe plasma is developed and the extracted plasma parameters are obtained. Population densities are found within the range reported in various previous studies which shows that our model is well optimized.

Finally, a systematic study of the electron impact N- and M-shell excitations of highly charged Rb-like through Br-like (W^{37+}-W^{39+}) and K-like through Ne-like (W^{55+}-W^{64+}) tungsten ions have been done using fully relativistic distorted wave theory. The cross sections are calculated and reported for various transitions in the electron impact energy range from the excitation threshold to 20 keV. Analytic fitting of the calculated cross sections are also provided so that these can be directly used in any plasma model. Linear polarization of the emitted photons, due to decay of the different electron excited states of the tungsten ions has also been obtained and reported.

Finally, it would be worth mentioning some of the improvements which can be made on the work presented in the thesis. An improvement can be done by including the second order term to our first order RDW T-matrix. Though, it would be very challenging task to evaluate both the second order direct and exchange *T*-matrices in an exact manner. Further, the relativistic distorted wave method which uses the distortion potential only due to static potential can be made better if one could add an additional suitable polarization potential to it. However, for this, suitable polarization potential needs to be calculated separately which a separate research topic to work is in itself. These suggested improvements might make our results more reliable at low incident electron energies. Regarding the collisional radiative model developed in this work, one could improve the model by taking and exploring non-Maxwellian electron energy distribution function and possibly consider few more processes like atom-atom collisions and many higher excitations in addition to the processes presently incorporated. However, these suggestions can be work of another thesis.

References

---

1. Samukawa S, Hori M, Rauf S, Tachibana K, Bruggeman P, Kroesen G, Whitehead JC, Murphy AB, Gutsol AF, Starikovskaia S, Kortshagen U, Boeuf JP, Sommerer TJ, Kushner MJ, Czarnetzki U, Mason N (2012) The 2012 plasma roadmap. J Phys D Appl Phys 45:253001 . doi: 10.1088/0022-3727/45/25/253001
2. Adamovich I, Baalrud SD, Bogaerts A, Bruggeman PJ, Cappelli M, Colombo V, Czarnetzki U, Ebert U, Eden JG, Favia P, Graves DB, Hamaguchi S, Hieftje G, Hori M, Kaganovich ID, Kortshagen U, Kushner MJ, Mason NJ, Mazouffre S, Thagard SM, Metelmann H-R, Mizuno A, Moreau E, Murphy AB, Niemira BA, Oehrlein GS, Petrovic ZL, Pitchford LC, Pu Y-K, Rauf S, Sakai O, Samukawa S, Starikovskaia S, Tennyson J, Terashima K, Turner MM, van de Sanden MCM, Vardelle A (2017) The 2017 Plasma Roadmap: Low temperature plasma science and technology. J Phys D Appl Phys 50:323001 . doi: 10.1088/1361-6463/aa76f5
3. Epy T (2007) Plasma Science: Advancing Knowledge in the National Interest, The National Academies Press: Washington, DC
4. Campbell L, Brunger MJ (2013) Modelling of plasma processes in cometary and planetary atmospheres. Plasma Sources Sci Technol 22:013002 doi: 10.1088/0963-0252/22/1/013002
5. Von Woedtke T, Metelmann HR, Weltmann KD (2014) Clinical Plasma Medicine: State and Perspectives of in Vivo Application of Cold Atmospheric Plasma. Contrib to Plasma Phys 54:104–117 doi: 10.1002/ctpp.201310068
6. Hutchinson IH (2002) Principles of Plasma Diagnostics: Second Edition. Plasma Phys Control Fusion 44:2603 doi: 10.1088/0741-3335/44/12/701
7. Fantz U (2006) Basics of plasma spectroscopy. Plasma Sources Sci Technol 15:S137 doi: 10.1088/0963-0252/15/4/S01
8. Donnelly VM (2004) Plasma electron temperatures and electron energy distributions measured by trace rare gases optical emission spectroscopy. J Phys D Appl Phys 37:R217 doi: 10.1088/0022-3727/37/19/R01
9. Wang S, Wendt AE, Boffard JB, Lin CC, Radovanov S, Persing H (2013) Noninvasive, real-time measurements of plasma parameters via optical emission spectroscopy. J Vac Sci Technol A 31:021303 doi: 10.1116/1.4792671
10. Boffard JB, Jung RO, Lin CC, Aneskavich LE, Wendt AE (2011) Optical diagnostics for characterization of electron energy distributions: argon inductively

coupled plasmas. Plasma Sources Sci Technol 20:055006 doi: 10.1088/0963-0252/20/5/055006

11. Hans-Joachim Kunze (2009) Introduction to Plasma Spectroscopy. Springer Series on atomic, optical, and plasma physics Springer New York
12. Ralchenko Y (2016) Modern Methods in Collisional-Radiative Modeling of Plasmas. Springer Series on atomic, optical, and plasma physics 90
13. Gangwar RK, Dipti, Srivastava R, Stafford L (2016) Spectroscopic diagnostics of low-pressure inductively coupled Kr plasma using a collisional-radiative model with fully relativistic cross sections. Plasma Sources Sci Technol 25:35025 doi: 10.1088/0963-0252/25/3/035025
14. Boffard JB, Lin CC, DeJoseph CA (2004) Application of excitation cross sections to optical plasma diagnostics. J Phys D Appl Phys 37:R143 doi: 10.1088/0022-3727/37/12/R01
15. Boffard JB, Lin CC, Wendt AE (2017) Application of Excitation Cross-Section Measurements to Optical Plasma Diagnostics. In: Advances in Atomic, Molecular and Optical Physics, 1st ed. Elsevier Inc., p 005
16. Ralchenko Y (2013) Collisional-radiative modeling for highly-charged ions of tungsten. Plasma Fusion Res 8:1–6 doi: 10.1585/pfr.8.2503024
17. Bespamyatnov IO, Rowan WL, Liao KT, Marchuk O, Ralchenko Y, Granetz RS (2013) Benchmark of collisional-radiative models for ITER beams at the Alcator C-Mod tokamak. Nucl Fusion 53:123010 doi: 10.1088/0029-5515/53/12/123010
18. Beiersdorfer P, Clementson J, Safronova U (2015) Tungsten Data for Current and Future Uses in Fusion and Plasma Science. Atoms 3:260 doi: 10.3390/atoms3020260
19. Bartschat K, Kushner MJ (2016) Electron collisions with atoms, ions, molecules, and surfaces: Fundamental science empowering advances in technology. Proc Natl Acad Sci 113:7026–7034 doi: 10.1073/pnas.1606132113
20. Afanas’ev VP, Smirnov BM, Zhilyaev DA (2014) Excited atoms in argon gas discharge plasma. J Exp Theor Phys 119:138–145 doi: 10.1134/S1063776114060089
21. Zatsarinny O, Bartschat K (2018) Molecular and Optical Physics To cite this article: Klaus Bartschat. J Phys B At Mol Opt Phys 51:50 doi: 10.1088/1361-6455/aac5aa
22. Keeler ML, Anderson LW, Lin CC (2000) Electron-Impact Ionization Cross Section Measurements Out of the 5^2P Excited State of Rubidium. Phys Rev Lett 85:3353 doi: 10.1103/PhysRevLett.85.3353

23. Ullrich J, Moshammer R, Dorn A, Dörner R, Schmidt LPH, Schmidt-Böcking H (2003) Recoil-ion and electron momentum spectroscopy: reaction-microscopes. Reports Prog Phys 66:1463 doi: 10.1088/0034-4885/66/9/203
24. Allan M (2004) Threshold Phenomena in Electron-Molecule Scattering. Phys Scr 110:161 doi: 10.1238/Physica.Topical.110a00161
25. Ren X, Jabbour Al Maalouf E, Dorn A, Denifl S (2016) Direct evidence of two interatomic relaxation mechanisms in argon dimers ionized by electron impact. Nat Commun 7:11093 doi: 10.1038/ncomms11093
26. Agnihotri AN, Kasthurirangan S, Nandi S, Kumar A, Champion C, Lekadir H, Hanssen J, Weck PF, Galassi ME, Rivarola RD, Fojón O, Tribedi LC (2013) Absolute total ionization cross sections of uracil ($C_4H_4N_2O_2$) in collisions with MeV energy highly charged carbon, oxygen and fluorine ions. J Phys B At Mol Opt Phys 46:185201 doi: 10.1088/0953-4075/46/18/185201
27. Biswas S, Monti JM, Tachino CA, Rivarola RD, Tribedi LC (2015) Differential electron emission in the ionization of Ne and Xe atoms under fast bare carbon ion impact. J Phys B At Mol Opt Phys 48:115206 doi: 10.1088/0953-4075/48/11/115206
28. Chatterjee S, Agnihotri AN, Stia CR, Fojón OA, Rivarola RD, Tribedi LC (2010) Bethe binary-encounter peaks in the double-differential cross sections for high-energy electron-impact ionization of H_2 and He. Phys Rev A 82:052709 doi: 10.1103/PhysRevA.82.052709
29. Bartschat K (2013) Computational methods for electron-atom collisions in plasma applications. J Phys D Appl Phys 46:334004 doi: 10.1088/0022-3727/46/33/334004
30. Walters HRJ (1984) Perturbative methods in electron- and positron-atom scattering. Phys Reports (Review Sect Phys Lett) 116:1
31. Yukikazu I (1986) Distorted-wave methods in electron-impact excitation of atoms and ions. Phys Reports (Review Sect Phys Lett) 143:69
32. Madison DH, Bartschat K (1996) The Distorted-Wave Method for Elastic Scattering and Atomic Excitation. In: Computational Atomic Physics. Springer Berlin Heidelberg, Berlin, Heidelberg, pp 65
33. Srivastava R, Sharma L (2013) New Trends in Atomic and Molecular Physics. Springer series on atomic, optical and plasma Physics, Springer-Verlag Berlin Heidelberg, Springer-Verlag
34. Campeanu RI (2007) Electron impact ionization of He, Ne and Ar. Phys Lett A 365:122 doi: 10.1016/J.PHYSLETA.2007.01.003

35. Khajuria Y, Kumar SS, Deshmukh PC (2009) Triple differential cross section in (e,2e) collisions for atomic potassium. Phys Lett A 373:4442 doi: 10.1016/J.PHYSLETA.2009.10.001
36. Aarthi G, Jose J, Deshmukh S, Radojevic V, Deshmukh PC, Manson ST (2014) Photoionization study of Xe 5s: ionization cross sections and photoelectron angular distributions. J Phys B At Mol Opt Phys 47:025004 doi: 10.1088/0953-4075/47/2/025004
37. Philip G. Burke (2011) R-Matrix Theory of Atomic Collisions. Springer Series on atomic, optical, and plasma physics The, Springer Heidelberg Dordrecht London New York
38. Bartschat K, Hudson ET, Scott MP, Burke PG, Burke VM (1996) Electron - atom scattering at low and intermediate energies using a pseudo-state R-matrix basis. J Phys B At Mol Opt Phys 29:115 doi: 10.1088/0953-4075/29/1/015
39. Zatsarinny O, Bartschat K (2013) The B-spline R-matrix method for atomic processes: Application to atomic structure, electron collisions and photoionization. J Phys B At Mol Opt Phys 46:112001 doi: 10.1088/0953-4075/46/11/112001
40. Berrington KA, Eissner WB, Norrington PH (1995) RMATRX1: Belfast atomic R-matrix codes. Comput Phys Commun 92:290 doi: 10.1016/0010-4655(95)00123-8
41. Zatsarinny O (2006) BSR: B-spline atomic R-matrix codes. Comput Phys Commun 174:273 doi: 10.1016/j.cpc.2005.10.006
42. Burke VM, Noble CJ (1995) Farm-A flexible asymptotic R-matrix package. Comput Phys Commun 85:471 doi: 10.1016/0010-4655(94)00178-5
43. Bray I (1992) Explicit Demonstration of the Convergence of the Close-Coupling Method for a Coulomb Three-Body Problem. Phys Rev Lett 69:53 doi: 10.1103/PhysRevLett.69.53
44. Bostock CJ (2011) The fully relativistic implementation of the convergent close-coupling method. J Phys B At Mol Opt Phys 44:083001 doi: 10.1088/0953-4075/44/8/083001
45. Fursa D V., Bray I (2009) Relativistic Convergent Close-Coupling method for excitation and ionization processes in electron collisions with atoms and ions. J Phys Conf Ser 100:113201 doi: 10.1088/1742-6596/194/4/042005
46. Bray I, Fursa D V., Kheifets AS, Stelbovics AT (2002) Electrons and photons colliding with atoms: Development and application of the convergent close-coupling method. J Phys B At Mol Opt Phys 35:R117 doi: 10.1088/0953-4075/35/15/201

47. Bartschat K, Zatsarinny O (2015) Close-coupling calculations for electron-atom collisions: Benchmark studies and uncertainty estimates. Phys Scr 90:054006 doi: 10.1088/0031-8949/90/5/054006

48. Campeanu RI, Nagy L (1985) Distorted wave cross sections for electron-impact ionization of the lithium-like ions. Zeitschrift fur Phys A Atoms Nucl 321:371 doi: 10.1007/BF01411966

49. Campeanu RI, Nagy L (1986) Electron-impact ionization of helium-like ions. Phys Lett A 114:13 doi: 10.1016/0375-9601(86)90332-4

50. Bray I, Stelbovics AT (2002) Comment on “Status of the convergent close-coupling method within the framework of the rigorous Coulomb scattering theory.” Phys Rev A 66:036701 doi: 10.1103/PhysRevA.66.036701

51. Henry RJW (1993) Applying large computers to problems in physics: Electron collision cross sections in atomic physics. Reports Prog Phys 56:327 doi: 10.1088/0034-4885/56/2/003

52. Bartschat K, Zatsarinny O, Bray I, Fursa D V., Stelbovics AT (2004) On the convergence of close-coupling results for low-energy electron scattering from magnesium. J Phys B At Mol Opt Phys 37:2617 10.1088/0953-4075/37/13/001

53. Bray I, Abdurakhmanov IB, Bailey JJ, Bray AW, Fursa D V, Kadyrov AS, Rawlins CM, Savage JS, Stelbovics AT, Zammit MC (2017) Convergent close-coupling approach to light and heavy projectile scattering on atomic and molecular hydrogen. J Phys B At Mol Opt Phys 50:202001 doi: 10.1088/1361-6455/aa8a23

54. Bray I, Fursa D V., Stelbovics AT (2001) Close-coupling approach to electron-impact ionization of helium. Phys Rev A 63:040702 doi: 10.1103/PhysRevA.63.040702

55. Chen GX (2011) Breit-Pauli R-matrix method for electron-impact excitation to magnetic sublevels and x-ray-line polarization of ions. Phys Rev A 84:012705 doi: 10.1103/PhysRevA.84.012705

56. Hudson CE, Ramsbottom CA, Norrington PH, Scott MP (2009) Breit-Pauli R-matrix calculation of fine-structure effective collision strengths for the electron impact excitation of Mg V. Astron Astrophys 494:729 doi: 10.1051/0004-6361

57. Tayal SS, Zatsarinny O (2005) B-spline R-matrix with pseudostates approach for electron impact excitation of atomic nitrogen. J Phys B At Mol Opt Phys 38:3631 doi: 10.1088/0953-4075/38/20/001

58. Wang Y, Zatsarinny O, Bartschat K (2014) B -spline R -matrix-with-pseudostates calculations for electron-impact excitation and ionization of nitrogen. Phys Rev A

89:062714 doi: 10.1103/PhysRevA.89.062714

59. Zatsarinny O, Wang Y, Bartschat K (2013) Relativistic B-spline R-matrix calculations for electron collisions with lead atoms: Differential cross sections and spin asymmetries. J Phys B At Mol Opt Phys 46:035202 doi: 10.1088/0953-4075/46/3/035202
60. Zatsarinny O, Bartschat K (2012) Electron-impact excitation of neon at intermediate energies. Phys Rev A 86:022717 doi: 10.1103/PhysRevA.86.022717
61. Zatsarinny O, Bartschat K (2017) B-spline R-matrix with pseudo-states calculations for electron-impact excitation and ionization of magnesium. J Phys Conf Ser 875:052011 doi: 10.1088/1742-6596/875/6/052004
62. Zatsarinny O, Bartschat K (2008) Relativistic B -spline R -matrix method for electron collisions with atoms and ions: Application to low-energy electron scattering from Cs. Phys Rev A 77:062701 doi: 10.1103/PhysRevA.77.062701
63. Zatsarinny O, Bartschat K, Babaeva NY, Kushner MJ (2014) Electron collisions with cesium atoms-Benchmark calculations and application to modeling an excimer-pumped alkali laser. Plasma Sources Sci Technol 23:035011 doi: 10.1088/0963-0252/23/3/035011
64. Antony BK, Joshipura KN, Mason NJ, Tennyson J (2004) R-matrix calculation of low-energy electron collisions with LiH. J Phys B At Mol Opt Phys 37:1689 doi: 10.1088/0953-4075/37/8/010
65. Gupta D, Choi H, Kwon D-C, Yoon J-S, Antony B, Song M-Y (2017) Cross sections for electron collision with difluoroacetylene. J Phys B At Mol Opt Phys 50:085202 doi: 10.1088/1361-6455/aa6325
66. Zatsarinny O, Bartschat K (2009) Fully relativistic B-spline R-matrix calculations for electron collisions with mercury. Phys Rev A 79:042713 doi: 10.1103/PhysRevA.79.042713
67. Bray I, Fursa D V, Stelbovics AT (2009) Electron-impact ionisation of atoms and ions. J Phys Conf Ser 185:012003 doi: 10.1088/1742-6596/185/1/012003
68. Zhang HL, Sampson DH (1989) Relativistic distorted wave collision strengths for excitation to the 88 n = 3 and n = 4 levels in all 71 neon-like ions with 22 less than or equal to Z less than or equal to 92. Atom. data Tables 43:1 doi.org/10.1016/0092-640X(89)90014-4
69. Srivastava R, Zuo T, McEachran RP, Stauffer AD (1992) Excitation of the 1,3P1 states of calcium, strontium and barium in the relativistic distorted-wave approximation. J Phys B At Mol Opt Phys 25:021 doi: 10.1088/0953-

4075/25/17/021

70. Sharma L, Srivastava R, Stauffer AD (2007) Excitation of the 3p55p levels of argon from the 3p54s metastable states. Phys Rev A 76:024701 doi: 10.1103/PhysRevA.76.024701

71. Srivastava R, Gangwar RK, Stauffer AD (2009) Excitation of the $6P^1_{1,3}$ states of mercury by spin-resolved electron impact. Phys Rev A 80:022718 doi: 10.1103/PhysRevA.80.022718

72. Sharma L, Surzhykov A, Inal MK, Fritzsche S (2010) Polarization transfer in the inner-shell photoionization of sodiumlike ions. Phys Rev A 81:023419 doi: 10.1103/PhysRevA.81.023419

73. Gangwar RK, Sharma L, Srivastava R, Stauffer AD (2010) Electron-impact excitation of argon: Cross sections of interest in plasma modeling. Phys Rev A 81:052707 doi: 10.1103/PhysRevA.81.052707

74. Gangwar RK, Sharma L, Srivastava R, Stauffer AD (2010) Electron-impact excitation of krypton: Cross sections of interest in plasma modeling. Phys Rev A 82:032710 doi: 10.1103/PhysRevA.82.032710

75. Sharma L, Srivastava R, Stauffer AD (2011) Excitation of the $5p^57p$ levels of xenon by electron impact. Eur Phys J D 62:399 doi: 10.1140/epjd/e2011-10644-0

76. Sharma L, Surzhykov A, Srivastava R, Fritzsche S (2011) Electron-impact excitation of singly charged metal ions. Phys. Rev. A 83:062701 doi: 10.1103/PhysRevA.83.062701

77. Pravica L, Williams JF, Cvejanović D, Samarin S, Bartschat K, Zatsarinny O, Stauffer AD, Srivastava R (2011) Unexpected effects in spin-polarized electron-impact excitation of the (3d10 4s5s) 3S1 state in zinc. Phys Rev A 83:040701 doi: 10.1103/PhysRevA.83.040701

78. Piwiński M, Kłosowski Ł, Dziczek D, Chwirot S, Das T, Srivastava R, Stauffer AD, Bostock CJ, Fursa D V., Bray I (2012) Electron excitation of the 4^1P_1 state of a zinc atom. Phys Rev A 86:052706 doi: 10.1103/PhysRevA.86.052706

79. Dipti, Srivastava R (2016) Electron-impact excitation rate-coefficients and polarization of subsequent emission for Ar^+ ion. J Quant Spectrosc Radiat Transf. 176:12 doi: 10.1016/j.jqsrt.2016.02.015

80. Srivastava R, Zuo T, McEachran RP, Stauffer AD (1992) Relativistic distorted-wave calculation of electron excitation of cadmium. J Phys B At Mol Opt Phys 25:1073 doi: 10.1088/0953-4075/25/5/018

81. Sampson DH, Zhang HL, Fontes CJ (2009) A fully relativistic approach for

calculating atomic data for highly charged ions. Phys Rep 477:111 doi: 10.1016/j.physrep.2009.04.002

82. Das T, Srivastava R, Stauffer AD (2011) Electron impact excitation of the resonance transition 5p2P1/2-6s2S1/2in indium atoms at small scattering angles. Phys Lett Sect A Gen At Solid State Phys 375:568 doi: 10.1016/j.physleta.2010.12.037
83. Das T, Dipti, Srivastava R (2014) Stokes parameters for the electron-impact excitation of the $4P^1{}_1$ state of zinc atom. Phys Lett Sect A Gen At Solid State Phys 378:641 doi: 10.1016/j.physleta.2013.12.034
84. Das T, Sharma L, Srivastava R (2015) Electron impact excitation and polarization studies of Fe-like. Can J Phys 93:888 doi: 10.1139/cjp-2014-0636
85. Das T, Sharma L, Srivastava R (2012) Electron impact excitation of the M-shell electrons from Zn-like through Co-like tungsten ions. Phys Scr 86:035301 doi: 10.1088/0031-8949/86/03/035301
86. Dipti, Das T, Sharma L, Srivastava R (2014) L-shell electron excitations of Mg- through O-like tungsten ions. Phys Scr 89:085403 doi: 10.1088/0031-8949/89/8/085403
87. Das T, Sharma L, Srivastava R, Stauffer AD (2012) Electron-impact excitation of zinc and ytterbium atoms. Phys Rev A 86:022710 doi: 10.1103/PhysRevA.86.022710
88. Campeanu RI, Walters HRJ, Whelan CT (2018) Electron- and positron-impact ionization of inert gases. Phys Rev A 97:062702 doi: 10.1103/PhysRevA.97.062702
89. Tóth I, Nagy L, Campeanu RI (2014) Triple differential cross sections for the ionization of water by electron impact. Eur Phys J D 68:369 doi: 10.1140/epjd/e2014-50643-y
90. Keller S, Whelan CT, Ast H, Walters HRJ, Dreizler RM (1994) Relativistic distorted-wave Born calculations for (e ,2 e) processes on inner shells of heavy atoms. Phys Rev A 50:3865 doi: 10.1103/PhysRevA.50.3865
91. Kaur S, Srivastava R, McEachran RP, Stauffer AD (1998) Electron impact excitation of the states of Ar , Kr and Xe atoms. J Phys B At Mol Opt Phys 31:4833 doi: 10.1088/0953-4075/31/21/015
92. Bartschat K, Madison DH (1987) Electron impact excitation of rare gases: differential cross sections and angular correlation parameters for neon, argon, krypton and xenon. J Phys B At Mol Phys 20:5839 doi: 10.1088/0022-3700/20/21/029

93. Kaur S and Srivastava R (1999) Excitation of the lowest autoionizing np5(n + 1)s2, 2P3=2;1=2 states of Na(n = 2), K(n = 3), Rb(n=4) and Cs(n=5) by electron impact. J Phys B At Mol Opt Phys 32:2323 doi:10.1088/0953-4075/32/10/303
94. Khakoo MA, Wrkich J, Larsen M, Kleiban G, Kanik I, Trajmar S, Brunger MJ, Teubner PJO, Crowe A, Fontes CJ, Clark REH, Zeman V, Bartschat K, Madison DH, Srivastava R, Stauffer AD (2002) Differential cross sections and cross-section ratios for the electron-impact excitation of the neon 2p53s configuration. Phys Rev A 65:062711 doi: 10.1103/PhysRevA.65.062711
95. Khakoo MA, Vandeventer P, Childers JG, Kanik I, Fontes CJ, Bartschat K, Zeman V, Madison DH, Saxena S, Srivastava R, Stauffer AD (2004) Electron impact excitation of the argon 3p54s configuration: differential cross-sections and cross-section ratios. J Phys B At Mol Opt Phys 37:247 doi: 10.1088/0953-4075/37/1/016
96. Srivastava R, Stauffer AD (2005) Inelastic electron scattering from excited barium atoms. Phys Rev A 71:052715 doi: 10.1103/PhysRevA.71.052715
97. Chauhan RK, Srivastava R, Stauffer AD (2005) Electron impact excitation of the 41P1 state of calcium. J Phys B At Mol Opt Phys 38:2385 doi: 10.1088/0953-4075/38/14/005
98. Srivastava R, Stauffer AD, Sharma L (2006) Excitation of the metastable states of the noble gases. Phys Rev A 74:012715 doi: 10.1103/PhysRevA.74.012715
99. Jönsson P, He X, Fischer CF, Grant IP (2007) The grasp2K relativistic atomic structure package. Comput Phys Commun 177:597 doi: 10.1016/j.cpc.2007.06.002
100. Jönsson P, Gaigalas G, Bieroń J, Fischer CF, Grant IP (2013) New version: Grasp2K relativistic atomic structure package. Comput Phys Commun 184:2179 doi: 10.1016/j.cpc.2013.02.016
101. P. Jönsson, J. Biero, T. Brage, J. Ekman, C. Froese Fischer, G. Gaigalas, M. Godefroid, I.P. Grant JG, C (2015) A practical guide to Grasp2K. Comput At Struct Group 2015 doi: http://dx.doi.org/10.1016/j.omega.2014.12.006
102. Chattopadhyay S, Mani BK, Angom D (2012) Perturbed coupled-cluster theory to calculate dipole polarizabilities of closed-shell systems: Application to Ar, Kr, Xe, and Rn. Phys Rev A 86:062508 doi: 10.1103/PhysRevA.86.062508
103. Mani BK, Angom D (2010) Atomic properties calculated by relativistic coupled-cluster theory without truncation: Hyperfine constants of Mg+, Ca+, Sr+, and Ba +. Phys Rev A 81:042514 doi: 10.1103/PhysRevA.81.042514
104. C J Joachain (1975) Quantum collision theory. Elsevier Science Ltd; Reprint edition
105. Zuo T (1991) Thesis, Yark University.

106. Grant IP (1970) Relativistic calculation of atomic structures. Adv Phys 19:747 doi: 10.1080/00018737000101191
107. I.P. Grant (2007) Relativistic Quantum Theory of Atoms and Molecules. Springer Series on Atomic, optical, and plasma physics 40, New York, NY 10013, USA
108. Dyall KG, Grant IP, Johnson CT, Parpia FA, Plummer EP (1989) GRASP: A general-purpose relativistic atomic structure program. Comput Phys Commun 55:425 doi: 10.1016/0010-4655(89)90136-7
109. M E rose (1961) Relativistic electron theory. New York london, jolin wiley & sons.
110. Fujimoto T (2004) Plasma Spectrocopy, first. Oxford University Press Inc., New York
111. Hartgers A, Dijk J van, Jonkers J, Mullen JAM van der (2001) CRModel: A general collisional radiative modeling code. Comput Phys Commun 135:199 doi: 10.1016/S0010-4655(00)00231-9
112. Dipti, Gangwar RK, Srivastava R, Stauffer AD (2013) Collisional-radiative model for non-Maxwellian inductively coupled argon plasmas using detailed fine-structure relativistic distorted-wave cross sections. Eur Phys J D 67:203 doi: 10.1140/epjd/e2013-40244-9
113. Zhu X-M, Pu Y-K, Celik Y, Siepa S, Schüngel E, Luggenhölscher D, Czarnetzki U (2012) Possibilities of determining non-Maxwellian EEDFs from the OES line-ratios in low-pressure capacitive and inductive plasmas containing argon and krypton. Plasma Sources Sci Technol 21:024003 doi: 10.1088/0963-0252/21/2/024003
114. X M Zhu,YKPu NB and RB (2009) Measurement of the electron density in atmospheric-pressure low-temperature argon discharges by line-ratio method of optical emission spectroscopy X. J Phys D Appl Phys 42:142003 doi: 10.1088/0022-3727/42/14/142003
115. ITER the way to new enrgy. https://www.iter.org/
116. Speth E (1989) Neutral beam heating of fusion plasmas. Reports Prog Phys 52:57 doi: 10.1088/0034-4885/52/1/002
117. Hemsworth RS, Tanga A, Antoni V (2008) Status of the ITER neutral beam injection system. Rev Sci Instrum 79:02C109 doi: 10.1063/1.2814248
118. Hemsworth R, Decamps H, Graceffa J, Schunke B, Tanaka M, Dremel M, Tanga A, De Esch HPL, Geli F, Milnes J, Inoue T, Marcuzzi D, Sonato P, Zaccaria P (2009) Status of the ITER heating neutral beam system. Nucl Fusion 49:045006 doi:

10.1088/0029-5515/49/4/045006

119. Development of ITER’s diagnostic neutral beam. https://www.iter. org/newsline /139/330
120. External heating systems. https://www.iter.org/mach/Heating
121. Wang C, Wang C (2010) Surface pretreatment of polyester fabric for ink jet printing with radio frequency O2 plasma. Fibers Polym 11:223 doi: 10.1007/s12221-010-0223-5
122. Bacal M, Wada M (2015) Negative hydrogen ion production mechanisms. Appl Phys Rev 398:021305 doi: 10.1063/1.4921298
123. Bacal M (2012) Negative hydrogen ion production in fusion dedicated ion sources. Chem Phys 398:3 doi: 10.1016/j.chemphys.2011.04.002
124. Masiello A, Agarici G, Bonicelli T, Simon M, Alonso J, Bigi M, Boilson D, Chitarin G, Day C, Franzen P, Hanke S, Heinemann B, Hemsworth R, Luchetta A, Marcuzzi D, Milnes J, Minea T, Pasqualotto R, Pomaro N, Serianni G, Rigato W, Sonato P, Toigo V, Waldon C, Zaccaria P (2011) The European contribution to the development of the ITER NB injector. Fusion Eng Des 86:860 doi: 10.1016/j.fusengdes.2011.03.035
125. Fantz U, Heinemann B, Wünderlich D, Riedl R, Kraus W, Nocentini R, Bonomo F (2016) Towards 20 A negative hydrogen ion beams for up to 1 h: Achievements of the ELISE test facility (invited). Rev Sci Instrum 87:02B307 doi: 10.1063/1.4932560
126. Gutser R, Wimmer C, Fantz U (2011) Work function measurements during plasma exposition at conditions relevant in negative ion sources for the ITER neutral beam injection. Rev Sci Instrum 82:023506 doi: 10.1063/1.3541790
127. Gutser R, Wünderlich D, Fantz U (2011) Dynamics of the transport of ionic and atomic cesium in radio frequency-driven ion sources for ITER neutral beam injection. Plasma Phys Control Fusion 53:105014 doi:10.1088/0741-3335/53/10/105014
128. Fantz U, Falter HD, Franzen P, Bandyopadhyay M, Heinemann B, Kraus W, McNeely P, Riedl R, Speth E, Tanga A, Wilhelm R (2005) Diagnostics of the cesium amount in an RF negative ion source and the correlation with the extracted current density. Fusion Eng Des 74:299 doi: 10.1016/j.fusengdes.2005.06.184
129. Friedl R, Fantz U (2013) Influence of cesium on the plasma parameters in front of the plasma grid in sources for negative hydrogen ions. AIP Conf Proc 1515:255 doi: 10.1063/1.4792792
130. Swanson LW, Sirayer RW (1968) Field-electron-microscopy studies of cesium

layers on various refractory metals: Work function change. J Chem Phys 48:2421 doi: 10.1063/1.1669464

131. Norcross DW, Stone PM (1968) Recombination, radiative energy loss and level populations in nonequilibrium cesium discharges. J Quant Spectrosc Radiat Transf 8:655 doi: 10.1016/0022-4073(68)90181-7
132. Sayer B, Jeannet JC, Lozingot J, Berlande J (1973) Collisional and radiative processes in a cesium afterglow. Phys Rev A 8:3012 doi: 10.1103/PhysRevA.8.3012
133. Vogel JS (2013) Neutral resonant ionization in the high-intensity cesium sputter source. In: AIP Conference Proceedings. p 1515:89
134. Wünderlich D, Wimmer C, Friedl R (2014) A collisional radiative model for low-pressure hydrogen-caesium plasmas and its application to an RF source for negative hydrogen ions. J Quant Spectrosc Radiat Transf 149:360 doi: 10.1016/j.jqsrt.2014.09.002
135. Sobelman II, Vainshtein LA, Yukov EA (1995) Excitation of atoms and broadening of spectral lines. Sringer series on Atoms and Plasma seccond ed.
136. Krishnan U, Stumpf B (1992) Calculated electron excitation cross sections for excited state-excited state transitions in alkali atoms. At Data Nucl Data Tables 51:151 doi: 10.1016/0092-640X(92)90016-B
137. Gryziński M (1965) Classical theory of atomic collisions. I. Theory of inelastic collisions. Phys Rev 138:A336 doi: 10.1103/PhysRev.138.A336
138. McFarland RH (1965) Gryziński electron-impact ionization cross-section computations for the alkali metals. Phys Rev 139:A40 doi: 10.1103/PhysRev.139.A40
139. Nygaard KJ (1968) Electron-Impact Ionization Cross Section in Cesium. J Chem Phys 49:1995 doi: 10.1063/1.1670359
140. McGuire EJ (1997) Systematics of ns subshell electron ionization cross sections. J Phys B At Mol Opt Phys 30:1563 doi: 10.1088/0953-4075/30/6/022
141. Łukomski M, Sutton S, Kedzierski W, Reddish TJ, Bartschat K, Bartlett PL, Bray I, Stelbovics AT, Mcconkey JW (2006) Electron-impact ionization cross sections out of the ground and 6 2 P excited states of cesium. Phys Rev A 74:032708 doi: 10.1103/PhysRevA.74.032708
142. Fursa D V., Bostock CJ, Bray I (2009) Relativistic convergent close-coupling method: Calculations of electron scattering from cesium. Phys Rev A 80:022717 doi: 10.1103/PhysRevA.80.022717

143. Gu MF (2008) The flexible atomic code. Can J Phys 86:675 doi: 10.1139/p07-197

144. Gangwar RK, Sharma L, Srivastava R, Stauffer AD (2012) Argon plasma modeling with detailed fine-structure cross sections. J Appl Phys 111:053307 doi: 10.1063/1.3693043

145. Rafac RJ, Tanner CE, Livingston AE (1994) Precision lifetime measurements of the 6p$P_{1/23/2}$ states in atomic cesium. Phys Rev A 50:R1976 doi: 10.1103/PhysRevA.50.R1976

146. Rafac R, Tanner C, Livingston A, Berry H (1999) Fast-beam laser lifetime measurements of the cesium $6p^2P_{1/2,3/2}$ states. Phys Rev A 60:3648 doi: 10.1103/PhysRevA.60.3648

147. Kramida A, Ralchenko Y, Reader J (2015) Atomic Spectra Database NIST. In: NIST At. Spectra Database, Version 5.3. http//physics.nist.gov/asd

148. Derevianko A and Porsev SG (2002) Determination of lifetimes of 6PJ levels and ground-state polarizability of Cs from the van der Waals coefficient C6. Phys Rev A 65:053403 doi: 10.1103/PhysRevA.65.053403

149. Zilitis VA (2014) Oscillator Strengths and Lifetimes Calculated by the Dirac–Fock Method for the Levels of Ions of the Cesium Isoelectronic Sequence. Opt Spectrosc 117:513 doi: 10.1134/S0030400X14100245

150. Głowacki L (2015) Relativistic configuration-interaction calculations for atoms with one valence electron based on altering hydrogenlike or Dirac-Fock spin orbitals. Phys Rev A 92:062505 . doi: 10.1103/PhysRevA.92.062505

151. Bostock CJ, Fursa D V., Bray I (2014) Relativistic convergent close-coupling calculation of inelastic scattering of electrons from cesium. Phys Rev A 89:032712 . doi: 10.1103/PhysRevA.89.032712

152. Vasilyev AA, Savukov IM, Safronova MS and Berry HG (2002) Measurement of the 6s-7p transition probabilities in atomic cesium and a revised value for the weak charge QW. Phys Rev A 66:020101

153. Morton DC (2000) Atomic Data for Resonance Absorption Lines. II. Wavelengths Longward of the Lyman Limit for Heavy Elements. Astrophys J Suppl Ser 130:403 doi: 10.1086/317349

154. Safronova MS, Clark CW (2004) Inconsistencies between lifetime and polarizability measurements in Cs. Phys Rev A 69:040501(R) doi: 10.1103/PhysRevA.69.040501

155. DiBerardino D, Tanner CE, Sieradzan A (1998) Lifetime measurements of cesium 5d 2D(5/2,3/2) and 11s 2S(1/2) states using pulsed-laser excitation. Phys Rev A

57:4204 doi: 10.1103/PhysRevA.57.4204

156. Kim YK (2001) Scaling of plane-wave Born cross sections for electron-impact excitation of neutral atoms. Phys Rev A 64:032713 doi: 10.1103/PhysRevA.64.032713
157. Bartschat K, Bray I (1996) Calculation of electron-Cs scattering at intermediate energies. Phys Rev A 54:1723 doi: 10.1103/PhysRevA.54.1723
158. Chen ST, Gallagher AC (1978) Electron excitation of the resonance lines of the alkali-metal atoms. Phys Rev A 17:551 doi: 10.1103/PhysRevA.17.551
159. Zeman V, McEachran RP and Stauffer AD (1994) Relativistic distorted-wave caIculation of electron impact excitation of caesium. Phys B At Mol Opl phys 20:3175
160. Grant IP, McKenzie BJ, Norrington PH, Mayers DF (1980) An atomic multiconfigurational Dirac-Fock package. Comput Phys Commun 21:207 doi:10.1016/0010-4655(80)90041-7
161. Tate JT, Smith PT (1934) Ionization potentials and probabilities for the formation of multiply charged ions in the alkali vapors and in krypton and xenon. Phys Rev 46:773 doi: 10.1103/PhysRev.46.773
162. https://www-amdis.iaea.org/FAC/
163. Roman V, Kupliauskiene A, Borovik A (2015) The single ionization cross-section of Rb atoms by electron impact. J Phys Conf Ser 635:052004 doi: 10.1088/1742-6596/635/5/052004
164. Belyaev AK, Lepetit B, Gadéa FX (2014) Theoretical study of electronic excitation, ion-pair formation, and mutual neutralization in cesium-hydrogen collisions. Phys Rev A 90:062701 doi: 10.1103/PhysRevA.90.062701
165. Fantz U, Franzen P, Kraus W, Berger M, Christ-Koch S, Falter H, Fröschle M, Gutser R, Heinemann B, Martens C, McNeely P, Riedl R, Speth E, Stäbler A, Wünderlich D (2009) Physical performance analysis and progress of the development of the negative ion RF source for the ITER NBI system. Nucl Fusion 49:125007 doi: 10.1088/0029-5515/49/12/125007
166. Speth E, Falter HD, Franzen P, Fantz U, Bandyopadhyay M, Christ S, Encheva A, Fröschle M, Holtum D, Heinemann B, Kraus W, Lorenz A, Martens C, McNeely P, Obermayer S, Riedl R, Süss R, Tanga A, Wilhelm R, Wünderlich D (2006) Overview of the RF source development programme at IPP Garching. Nucl Fusion 46:S220 doi: 10.1088/0029-5515/46/6/S03
167. Schiesko L, McNeely P, Franzen P, Fantz U (2012) Magnetic field dependence of

the plasma properties in a negative hydrogen ion source for fusion. Plasma Phys Control Fusion 54:105002 doi: 10.1088/0741-3335/54/10/105002

168. Fantz U, Wimmer C (2011) Optimizing the laser absorption technique for quantification of caesium densities in negative hydrogen ion sources. J Phys D Appl Phys 44:335202 doi: 10.1088/0022-3727/44/33/335202
169. Christ-Koch S, Fantz U, Berger M (2009) Laser photodetachment on a high power, low pressure rf-driven negative hydrogen ion source. Plasma Sources Sci Technol 18:025003 doi: 10.1088/0963-0252/18/2/025003
170. Berger M, Fantz U, Christ-Koch S (2009) Cavity ring-down spectroscopy on a high power rf driven source for negative hydrogen ions. Plasma Sources Sci Technol 18:025004 doi: 10.1088/0963-0252/18/2/025004
171. Wimmer C, Fantz U (2013) Cesium dynamics and H- density in the extended boundary layer of negative hydrogen ion sources for fusion. In: AIP Conference Proceedings. p 1515:246
172. Zhu X-M, Pu Y-K (2010) Optical emission spectroscopy in low-temperature plasmas containing argon and nitrogen: determination of the electron temperature and density by the line-ratio method. J Phys D Appl Phys 43:403001 doi: 10.1088/0022-3727/43/40/403001
173. Barreca D, Gasparotto A, Maccato C, Tondello E, Rossetto G (2008) A soft Plasma Enhanced-Chemical Vapor Deposition process for the tailored synthesis of SiO2 films. Thin Solid Films 516:7393 doi: 10.1016/j.tsf.2008.02.029
174. Graves DB (2012) The emerging role of reactive oxygen and nitrogen species in redox biology and some implications for plasma applications to medicine and biology. J Phys D Appl Phys 45:263001 doi: 10.1088/0022-3727/45/26/263001
175. Walkiewicz-Pietrzykowska A, Cotrino J, González-Elipe AR (2005) Deposition of thin films of SiOxCyH in a surfatron microwave plasma reactor with hexamethyldisiloxane as precursor. Chem Vap Depos 11:317 doi: 10.1002/cvde.200506374
176. Kylián O, Rauscher H, Gilliland D, Brétagnol F, Rossi F (2008) Removal of model proteins by means of low-pressure inductively coupled plasma discharge. J Phys D Appl Phys 41:095201 doi: 10.1088/0022-3727/41/9/095201
177. Zhao B, Zhang L, Wang X, Yang J (2012) Surface functionalization of vertically-aligned carbon nanotube forests by radio-frequency Ar/O 2 plasma. Carbon N Y 50:2710 doi: 10.1016/j.carbon.2012.02.029
178. Chung TH, Ra Kang H, Keun Bae M (2012) Optical emission diagnostics with

electric probe measurements of inductively coupled Ar/O 2 /Ar-O 2 plasmas. Phys Plasmas 19:113502 doi: 10.1063/1.4765357

179. Jõgi I, Raud J, Hein K, Laan M (2014) Spectral characterization of medium-pressure RF discharge in argon–oxygen mixture. J Phys D Appl Phys 47:335206 doi: 10.1088/0022-3727/47/33/335206
180. Xue C, Wen D-Q, Liu W, Zhang Y-R, Gao F, Wang Y-N (2017) Experimental and numerical investigations on time-resolved characteristics of pulsed inductively coupled O2/Ar plasmas. J Vac Sci Technol A Vacuum, Surfaces, Film 35:021301 .doi: 10.1116/1.4967913
181. Rauf S, Kushner MJ (1997) Argon metastable densities in radio frequency Ar, Ar/O_2 and Ar/CF_4 electrical discharges. J Appl Phys 82:2805 doi: 10.1063/1.366111
182. Etemadi R, Godet C, Perrin J (1997) Phenomenology of a dual-mode microwave/RF discharge used for the deposition of silicon oxide thin layers. Plasma Sources Sci Technol 6:323 doi: 10.1088/0963-0252/6/3/009
183. Sato T, Makabe T (2008) A numerical investigation of atomic oxygen density in an inductively coupled plasma in O $_2$ /Ar mixture. J Phys D Appl Phys 41:035211 doi: 10.1088/0022-3727/41/3/035211
184. Hayashi Y, Hirao S, Zhang Y, Gans T, O’Connell D, Petrović ZL, Makabe T (2009) Argon metastable state densities in inductively coupled plasma in mixtures of Ar and O $_2$. J Phys D Appl Phys 42:145206 doi: 10.1088/0022-3727/42/14/145206
185. Kitajima T, Nakano T, Makabe T (2006) Increased O (1D) metastable density in highly Ar-diluted oxygen plasmas. Appl Phys Lett 88:3 doi: 10.1063/1.2180871
186. Gudmundsson JT, Thorsteinsson EG (2007) Oxygen discharges diluted with argon: dissociation processes. Plasma Sources Sci Technol 16:399 doi: 10.1088/0963-0252/16/2/025
187. Kutasi K, Guerra V, Paulo SA (2010) Theoretical insight into Ar-O2 surface-wave microwave discharges. J Phys D Appl Phys 43:175201 doi: 10.1088/0022-3727/43/17/175201
188. Vries N de (2008) Spectroscopic study of microwave induced plasmas exploration of active and passive methods. AIP Conference Proceedings 740:199 doi:10.6100/IR637283
189. Ashida S, Lee C, Lieberman MA (1995) Spatially averaged (global) model of time modulated high density argon plasmas. J Vac Sci Technol A Vacuum, Surfaces, Film 13:2498 doi: 10.1116/1.579494
190. Kolts JH, Setser DW (1978) Decay rates of Ar(4s,$^3P_2$), Ar(4s',$^3P_0$), Kr(5s, $^3P_2$), and Xe(6s, $^3P_2$) atoms in argon. J Chem Phys 68:4848 doi: 10.1063/1.435638

191. Velazco JE, Kolts JH, Setser DW, Velazco JE, Kolts JH, Setser DW (1978) Rate constants and quenching mechanisms for the metastable states of argon , krypton , and xenon Rate constants and quenching mechanisms for the metastable states of argon , krypton, and xenon. J Chem Phys 69:10 doi: 10.1063/1.436447
192. Sadeghi N, Setser DW, Francis A, Czarnetzki U, Döbele HF (2001) Quenching rate constants for reactions of Ar(4p′ [1/2]0, 4p[1/2]0, 4p[3/2]2, and 4p[5/2]2) atoms with 22 reagent gases. J Chem Phys 115:3144 doi: 10.1063/1.1388037
193. Pitchford LC, Alves LL, Bartschat K, Biagi SF, Bordage MC, Bray I, Brion CE, Brunger MJ, Campbell L, Chachereau A, Chaudhury B, Christophorou LG, Carbone E, Dyatko NA, Franck CM, Fursa D V., Gangwar RK, Guerra V, Haefliger P, Hagelaar GJM, Hoesl A, Itikawa Y, Kochetov I V., McEachran RP, Morgan WL, Napartovich AP, Puech V, Rabie M, Sharma L, Srivastava R, Stauffer AD, Tennyson J, de Urquijo J, van Dijk J, Viehland LA, Zammit MC, Zatsarinny O, Pancheshnyi S (2017) LXCat: an Open-Access, Web-Based Platform for Data Needed for Modeling Low Temperature Plasmas. Plasma Process Polym 14:1–17 doi: 10.1002/ppap.201600098
194. Straub HC, Renault P, Lindsay BG, Smith KA, Stebbings RF (1995) Absolute partial and total cross sections for electron-impact ionization of argon from threshold to 1000 eV. Phys Rev A 52:1115 doi: 10.1103/PhysRevA.52.1115
195. Ali MA, Stone PM (2008) Electron impact ionization of metastable rare gases: He, Ne and Ar. Int J Mass Spectrom 271:51 doi: 10.1016/j.ijms.2007.10.006
196. Mewe R (1970) On the positive column of discharges in helium at intermediate pressures. II. Plasma particle balance and discharge characteristics. Physica 47:398 doi: 10.1016/0031-8914(70)90272-7
197. Boffard JB, Jung RO, Lin CC, Wendt AE (2009) Measurement of metastable and resonance level densities in rare-gas plasmas by optical emission spectroscopy. Plasma Sources Sci Technol 18:035017 doi: 10.1088/0963-0252/18/3/035017
198. M. V. Malyshev and V. M. Donnelly (1999) Trace rare gases optical emission spectroscopy: nonintrusive method for measuring electron temperatures in low-pressure, low-temperature plasmas. Phys Rev E Stat Phys Plasmas Fluids Relat Interdiscip Topics 60:6016 doi: 10.1103/PhysRevE.60.6016
199. Boffard JB, Jung RO, Lin CC, Wendt AE (2010) Optical emission measurements of electron energy distributions in low-pressure argon inductively coupled plasmas. Plasma Sources Sci Technol 19:065001 . doi: 10.1088/0963-0252/19/6/065001
200. Shiga T, Pitchford LC, Boeuf J, Mikoshiba S (2003) Study of efficacy in a mercury-

free flat discharge fluorescent lamp using a zero-dimensional positive column model. J Phys D Appl Phys 36:512 doi:10.1088/0022-3727/36/5/314

201. Golubovskii YB, Porokhova IA, Lange H, Gortchakov S (2005) Metastable and resonance atom densities in a positive column : II . Application to light source modelling. Plasma Sources Sci Technol 14:45 doi: 10.1088/0963-0252/14/1/006
202. Hayashi D, Heusler G, Hagelaar G, Kroesen G (2004) Discharge efficiency in high-Xe-content plasma display panels Discharge efficiency in high-Xe-content plasma display panels. J Appl Phys 95:1656 doi: 10.1063/1.1641961
203. Karabadzhak GF, Chiu YH, Dressler RA (2006) Passive optical diagnostic of Xe propelled Hall thrusters. II. Collisional-radiative model. J Appl Phys 99:113305 doi: 10.1063/1.2195019
204. Chiu Y, Austin BL, Williams S, Dressler RA, Karabadzhak F george (2006) Passive optical diagnostic of Xe-propelled Hall thrusters . I . Emission cross sections Passive optical diagnostic of Xe-propelled Hall thrusters . I . Emission cross sections. J Appl Phys 99:113304 doi: 10.1063/1.2195018
205. Register D, Vuskovic L, Trajmar S (1986) Elastic electron scattering cross sections for Xe in the 1-100 eV impact energy region. J Phys B At Mol Phys 19:1685 doi: 10.1088/0022-3700/19/11/022
206. Suzuki TY, Suzuki H, Currell FJ, Ohtani S, Takayanagi T, Wakiya K (1996) Measurements of cross sections and oscillator strengths by electron impact for the 5d and 7s levels of Xe. Phys Rev A 53:4138 doi: 10.1103/PhysRevA.53.4138
207. Zuo T, McEachran RP, Stauffer AD (1991) Relativistic distorted-wave calculation of electron impact excitation of xenon. J Phys B At Mol Opt Phys 24:2853 doi: 10.1088/0953-4075/24/12/008
208. Ester T, Kessler J (1994) Absolute elastic and inelastic electron scattering cross sections for xenon in the 15-100 ev impact-energy region. J Phys B At Mol Opt Phys 27:4295 doi: 10.1088/0953-4075/27/18/024
209. Filipović D, Marinković B, Pejcev V, Vusković L (1988) Electron-impact excitation of xenon at incident energies between 15 and 80 eV. Phys Rev A 37:356 doi: 10.1103/PhysRevA.37.356
210. Zatsarinny O, Bartschat K (2010) Benchmark calculations for near-threshold electron-impact excitation of krypton and xenon atoms. J Phys B At Mol Opt Phys 43:074031 doi: 10.1088/0953-4075/43/7/074031
211. Allan M, Zatsarinny O, Bartschat K (2006) Near-threshold absolute angle-differential cross sections for electron-impact excitation of argon and xenon. Phys

Rev A 74:030701(R) doi: 10.1103/PhysRevA.74.030701

212. Mason NJ, Newell WR (1987) Total cross sections for metastable excitation in the rare gases. J Phys B At Mol Phys 20:1357 doi: 10.1088/0022-3700/20/6/020

213. Puech V, Mizzi S (1991) Collision cross sections and transport parameters in neon and xenon. J Phys D Appl Phys 24:1974 doi: 10.1088/0022-3727/24/11/011

214. Zeman V, Bartschat K, Norén C, McConkey JW (1998) Near-threshold electron-impact excitation of the vacuum-ultraviolet resonance transitions in Ne, Ar, Kr, and Xe. Phys Rev A 58:1275 doi: 10.1103/PhysRevA.58.1275

215. Nakazaki S, Berrington KA, Eissner WB, Itikawa Y (1997) Excitation of xenon by electron impact. J Phys B At Mol Opt Phys 30:5805 doi: 10.1088/0953-4075/30/24/017

216. Fons JT, Lin CC (1998) Measurement of the cross sections for electron-impact excitation into the $5p^56p$ levels of xenon. Phys Rev A 58:4603 doi: 10.1103/PhysRevA.58.4603

217. Jung RO, Boffard JB, Anderson LW, Lin CC (2005) Electron-impact excitation cross sections from the xenon J=2 metastable level. Phys Rev A 72:022723 doi: 10.1103/PhysRevA.72.022723

218. Jung RO, Boffard JB, Anderson LW, Lin CC (2009) Excitation into 5 p5 7p levels from the ground level and the J=2 metastable level of Xe. Phys Rev A 80:062708 doi: 10.1103/PhysRevA.80.062708

219. Sharma L, Srivastava R, Stauffer AD (2009) Electron impact excitation of the $5p^57$ p levels of xenon from $5p^56s$ metastable states. J Phys Conf Ser 185:012042 doi: 10.1088/1742-6596/185/1/012042

220. Chen Z-B, Dong C-Z, Xie L-Y, Jiang J (2014) Electron Impact Excitation of Xenon from the Ground State and the Metastable State to the 5p57p Levels. Chinese Phys Lett 31:033401 doi: 10.1088/0256-307X/31/3/033401

221. Vinodkumar M, Limbachiya C, Antony B, Joshipura KN (2007) Calculations of elastic, ionization and total cross sections for inert gases upon electron impact: threshold to 2keV. J Phys B At Mol Opt Phys 40:3259 doi: 10.1088/0953-4075/40/16/007

222. Khajuria Y, Deshmukh PC (2006) Xe(4d) triple differential cross section: modified semiclassical exchange approximation in electron–atom collision. J Phys B At Mol Opt Phys 39:569 doi: 10.1088/0953-4075/39/3/010

223. de Heer FJ, Jansent RHJ, van der Kaay W (1979) Total cross sections for electron scattering by Ne and Ar and Kr and Xe. J Phys B Atom Molec Phys 12:979 doi:

10.1088/0022-3700/12/6/016

224. Hayashi M (1983) Determination of electron-xenon total excitation cross- sections, from threshold to 100 eV, from experimental values of Townsend's alpha. J Phys D Appl Phys 16:581 doi: 10.1088/0022-3727/16/4/018
225. J C Nickelt, K Imre Register DF and Trajmer S (1985) Total electron scattering cross sections. I. He, Ne, Ar, Xe. J Phys B At Mol Phys 18:125 doi: 10.1088/0022-3700/18/1/015
226. McEachran RP, Stauffer AD (1987) Relativistic low-energy elastic and momentum transfer cross sections for electron scattering from xenon. J Phys B At Mol Phys 20:3483 doi: 10.1088/0022-3700/20/14/020
227. Zecca A, Karwaszt G, Brusa1 RS, Grisenti1 R (1991) Absolute total cross section measurements for intermediate-energy electron scattering: Iv. kr and xe. J Phys B At Mol Opt Phys 24:2737 doi: 10.1088/0953-4075/24/11/014
228. Kitajima M, Kurokawa M, Kishino T, Toyoshima K, Odagiri T, Kato H, Anzai K, Hoshino M, Tanaka H, Ito K (2012) Ultra-low-energy electron scattering cross section measurements of Ar, Kr and Xe employing the threshold photoelectron source. Eur Phys J D 66:130 doi: 10.1140/epjd/e2012-20629-0
229. Blagoev A, Ivanov IV, Mishonov T and Popov Tc (1984) Absolute calibration of arbitrary total cross sections for electron impact excitation of Xe metastable states in the near-threshold region. J. Phys. B: At. Mol. Opt. Phys. 17: L647
230. Czerwiec T, Graves DB (2004) Mode transitions in low pressure rare gas cylindrical ICP discharge studied by optical emission spectroscopy. J Phys D Appl Phys 37:2827 doi: 10.1088/0022-3727/37/20/009
231. Garcia JCM, Bötticher W, Kock M (1996) Oscillator strengths of Kr I and Xe I resonance lines. J Quant Spectrosc Radiat Transf 55:169 doi: 10.1016/0022-4073(95)00154-9
232. Suzuki TY, Sakai Y, Min BS, Takayanagi T, Wakiya K, Suzuki H, Inaba T, Takuma H (1991) Measurement of cross sections and oscillator strengths for Xe by electron impact. Phys Rev A 43:5867 doi: 10.1103/PhysRevA.43.5867
233. Chan WF, Cooper G, Guo X, Burton GR, Brion CE (1992) Absolute optical oscillator strengths for the electronic excitation of atoms at high resolution. III. The photoabsorption of argon, krypton, and xenon. Phys Rev A 46:149 doi: 10.1103/PhysRevA.46.149
234. Zatsarinny O, Bartschat K (2009) B-spline calculations of oscillator strengths in noble gases. Phys Scr T134:014020 doi: 10.1088/0031-8949/2009/T134/014020

235. Dong CZ, Fritzsche S, Fricke B (2006) Theoretical study of the 5p56s - 5p6 spectra of neutral xenon. Eur Phys J D 40:317 doi: 10.1140/epjd/e2006-00172-5

236. McEachran RP, Vos M (2012) Large-angle scattering of energetic electrons from Xe: A combined theoretical and experimental approach. Phys Rev A 85:032703 doi: 10.1103/PhysRevA.85.032703

237. Aymar M, Coulombe M (1978) Theoretical transition probabilities and lifetimes in KrI and XeI spectra. At Data Nucl Data Tables 21:537 doi: 10.1016/0092-640X(78)90007-4

238. Kettlitz M, Radtke R, Spanke R, Hitzschke L (1985) Shift and oscillator strength of Xe I lines. J Quant Spectrosc Radiat Transf 34:275 doi: 10.1016/0022-4073(85)90008-1

239. Dressler RA, Chiu Y, Zatsarinny O, Bartschat K, Srivastava R, Sharma L (2009) Near-infrared collisional radiative model for Xe plasma electrostatic thrusters: the role of metastable atoms. J Phys D Appl Phys 42:185203 doi:10.1088/0022 3727/42/18/185203

240. Rejoub R, Lindsay BG, Stebbings RF (2002) Determination of the absolute partial and total cross sections for electron-impact ionization of the rare gases. Phys Rev A 65:042713 doi: 10.1103/PhysRevA.65.042713

241. Malyshev M V, Donnelly VM (1997) Determination of electron temperatures in plasmas by multiple rare gas optical emission , and implications for advanced actinometry Determination of electron temperatures in plasmas by multiple rare gas optical emission , and implications for advanced act. J Vac Sci Technol A 15:550 doi: 10.1116/1.580682

242. Zhu XM, Cheng ZW, Pu YK, Czarnetzki U (2016) Escape factors for Paschen 2p-1s emission lines in low-temperature Ar, Kr, and Xe plasmas. J Phys D Appl Phys 49:225204 doi: 10.1088/0022-3727/49/22/225204

243. Neu R, Dux R, Kallenbach A, Pütterich T, Balden M, Fuchs JC, Herrmann A, Maggi CF, O’Mullane M, Pugno R, Radivojevic I, Rohde V, Sips ACC, Suttrop W, Whiteford A (2005) Tungsten: An option for divertor and main chamber plasma facing components in future fusion devices. Nucl Fusion 45:209 doi: 10.1088/0029-5515/45/3/007

244. Ikeda K (2010) ITER on the road to fusion energy. Nucl Fusion 50:014002 doi: 10.1088/0029-5515/50/1/014002

245. Merola M, Loesser D, Martin A, Chappuis P, Mitteau R, Komarov V, Pitts RA, Gicquel S, Barabash V, Giancarli L, Palmer J, Nakahira M, Loarte A, Campbell D,

Eaton R, Kukushkin A, Sugihara M, Zhang F, Kim CS, Raffray R, Ferrand L, Yao D, Sadakov S, Furmanek A, Rozov V, Hirai T, Escourbiac F, Jokinen T, Calcagno B, Mori S (2010) ITER plasma-facing components. Fusion Eng Des 85:2312 doi: 10.1016/j.fusengdes.2010.09.013

246. Inubushi Y, Kai T, Nakamura T, Fujioka S, Nishimura H, Mima K (2007) Analysis of x-ray polarization to determine the three-dimensionally anisotropic velocity distributions of hot electrons in plasma produced by ultrahigh intensity lasers. Phys Rev E 75:026401 doi: 10.1103/PhysRevE.75.026401

247. Beiersdorfer P, Slater M (2001) Measurement of the electron cyclotron energy component of the electron beam of an electron beam ion trap. Phys Rev E 64:066408 doi: 10.1103/PhysRevE.64.066408

248. Skinner CH (2009) Atomic physics in the quest for fusion energy and ITER. Phys Scr 134:014022 doi: 10.1088/0031-8949/2009/T134/014022

249. CRP on Spectroscopic and Collisional Data for Tungsten. https://www-amdis.iaea.org/CRP/Tungsten/

250. Utter SB, Beiersdorfer P, Trabert E (2002) Electron-beam ion-trap spectra of tungsten in the EUV. Can J Phys 80:1503 doi: 10.1139/p02-132

251. Aggarwal S, Jha AKS, Mohan M (2013) REVIEW Multiconfigurational Dirac-Fock energy levels and radiative rates for Br-like tungsten. Can J Phys 91:394 doi: 10.1139/cjp-2013-0013

252. Neu R, Fournier KB, Schlögl D, Rice J (1997) Observations of x-ray spectra from highly charged tungsten ions in tokamak plasmas. J Phys B At Mol Opt Phys 30:5057 doi: 10.1088/0953-4075/30/21/036

253. Neu R, Fournier KB, Bolshukhin D, Dux R (2001) Spectral Lines from Highly Charged T ungsten Ions in the Soft-X-Ray Region for Quantitative Diagnostics of Fusion Plasmas. Phys Scr T92:307 doi: 10.1238/Physica.Topical.092a00307

254. Radtke R, Biedermann C, Schwob JL, Mandelbaum P, Doron R (2001) Line and band emission from tungsten ions with charge 21+ to 45+ in the 45–70Å range. Phys Rev A 64:012720 doi: 10.1103/PhysRevA.64.012720

255. R. Radtke, C. Biedermann, G. Fussmann, J. Schwob P, Mandelbaum RD (2007) Measured line spectra and calculated atomic physics data for highly charged tungsten ions. At Plasma-Material Interact Data Fusion (IAEA, Vienne) 13:45

256. Bar-Shalom A, Klapisch M, Oreg J (2001) Hullac, an integrated computer package for atomic processes in plasmas. J Quant Spectrosc Radiat Transf 71:169 doi: 10.1016/S0022-4073(01)00066-8

257. Pütterich T, Neu R, Biedermann C, Radtke R, Team AU (2005) Disentangling the emissions of highly ionized tungsten in the range 4–14 nm. J Phys B At Mol Opt Phys 38:3071 doi: 10.1088/0953-4075/38/16/017

258. Cowan R (1981) The theory of atomic structure and spectra. University of California Press.

259. Ralchenko Y, Reader J, Pomeroy JM, Tan JN, Gillaspy JD (2007) Spectra of W39+-W47+ in the 12-20 nm region observed with an EBIT light source. J Phys B At Mol Opt Phys 40:3861 doi: 10.1088/0953-4075/40/19/007

260. Fournier KB (1998) Atomic data and spectral line intensities for highly ionized tungsten (Co-like W47+to Rb-like W37+) in a high-temperature, low-density plasma. At Data Nucl Data Tables 61:1 doi: 10.1006/adnd.1997.0756

261. Bar-Shalom A, Klapisch M, Oreg J (1988) Electron collision excitations in complex spectra of ionized heavy atoms. Phys Rev A 38:1773 doi: 10.1103/PhysRevA.38.1773

262. Bogdanovich P, Kisielius R (2012) Theoretical energy level spectra and transition data for $4p^64d$, $4p^64f$ and $4p^54d^2$ configurations of W37+ion. At Data Nucl Data Tables 98:557 doi: 10.1016/j.adt.2011.11.004

263. Bogdanovich P, Karpuškienė R, Kisielius R (2015) Quasirelativistic calculation of $4s^24p^5$, $4s^24p^44d$ and $4s^4p^6$ configuration spectroscopic parameters for the W39+ ion. Phys Scr 90:035401 doi: 10.1088/0031-8949/90/3/035401

264. Jonauskas V, Gaigalas G, Kučas S (2012) Relativistic calculations for M1-type transitions in 4dN configurations of $W29^+$–$W37^+$ ions. At Data Nucl Data Tables 98:19 doi: 10.1016/J.ADT.2011.08.001

265. Aggarwal KM, Keenan FP (2014) Energy levels, radiative rates, and lifetimes for transitions in W XL. At Data Nucl Data Tables 100:1399 doi: 10.1016/J.ADT.2014.02.006

266. Wu Z, Fu Y, Ma X, Li M, Xie L, Jiang J, Dong C (2015) Electron Impact Excitation and Dielectronic Recombination of Highly Charged Tungsten Ions. Atoms 3:474 doi: 10.3390/atoms3040474

267. Jiang J, Dong C-Z, Xie L-Y, Wang J-G (2008) Resonance electron-impact excitation and polarization of the magnetic quadrupole line of neonlike Ba 46^+ ions. Phys Rev A 78:022709 doi: 10.1103/PhysRevA.78.022709

268. Dipti, Das T, Sharma L, Srivastava R (2015) Electron impact excitation and polarization studies of Fe-like W48+ to Al-like W61+ ions. Can J Phys 93:888 doi: 10.1139/cjp-2014-0636

269. Aggarwal K, M. K (2016) Electron Impact Excitation of F-Like W LXVI. Atoms 4:24 doi: 10.3390/atoms4030024

270. Xie LY, Ma XY, Dong CZ, Wu ZW, Shi YL, Jiang J (2014) Polarization of the nf → 3d (n=4, 5, 6) x-rays from tungsten ions following electron-impact excitation and dielectronic recombination processes. J Quant Spectrosc Radiat Transf 141:31–39 . doi: 10.1016/J.JQSRT.2014.02.027

271. Ballance CP, Loch SD, Pindzola MS, Griffin DC (2013) Electron-impact excitation and ionization of $W3^+$ for the determination of tungsten influx in a fusion plasma. J Phys B At Mol Opt Phys 46:055202 doi: 10.1088/0953-4075/46/5/055202

272. Ballance CP, Griffin DC (2007) Electron-impact excitation of $W44^+$ and $W45^+$. J Phys B At Mol Opt Phys 40:247 doi: 10.1088/0953-4075/40/2/001

273. Ballance CP, Griffin DC (2006) Relativistic radiatively damped R-matrix calculation of the electron-impact excitation of $W46^+$. J Phys B At Mol Opt Phys 39:3617 doi: 10.1088/0953-4075/39/17/017

274. Zeng J, Zhong J, Zhao G, Yuan J (2005) Electron impact collision strengths and oscillator strengths for Ni-like Nd, Sm, Eu, Gd, Ta, and W ions. At Data Nucl Data Tables 90:259 doi: 10.1016/J.ADT.2005.07.003

275. F A Gianturco and S Scialla (1987) Local approximations of exchange interaction in electron-molecule collisions: the methane molecule. J Phys B At Mol Phys 20:3171 doi: 10.1088/0022-3700/20/13/024

276. Balashov V V., Grum-Grzhimailo AN, Kabachnik NM (2000) Polarization and Correlation Phenomena in Atomic Collisions. Springer US, Boston, MA

277. Froese Fischer C, Gaigalas G (2012) Multiconfiguration Dirac-Hartree-Fock energy levels and transition probabilities for Wxxxviii. Phys Rev A 85:042501 doi: 10.1103/PhysRevA.85.042501

278. Kramida AE, Shirai T (2009) Energy levels and spectral lines of tungsten, W III through W LXXIV. At Data Nucl Data Tables 95:305 doi: 10.1016/J.ADT.2008.12.002

279. Gaigalas G, Rynkun P, Fischer CF (2015) Lifetimes of 4p54d levels in highly ionized atoms. Phys Rev A 91:022509 doi: 10.1103/PhysRevA.91.022509

280. Klapisch M, Schwob JL, Fraenkel BS, Oreg J (1977) The 1s-3p Kβ-like x-ray spectrum of highly ionized iron. J Opt Soc Am 67:148 doi: 10.1364/JOSA.67.000148

281. Pütterich T, Neu R, Dux R, Whiteford AD, O’Mullane MG, Team the AU (2008) Modelling of measured tungsten spectra from ASDEX Upgrade and predictions for

ITER. Plasma Phys Control Fusion 50:085016 doi: 10.1088/0741-3335/50/8/085016

282. Regemorter H Van (1962) Rate of collisional excitation in stellar atmospheres Astrophys. J 136:906

283. Seaton MJ (1962) The Impact Parameter Method for Electron Excitation of Optically Allowed Atomic Transitions. Proc Phys Soc 79:1105 doi: 10.1088/0370-1328/79/6/304

284. Ralchenko Y, Draganic IN, Tan JN, Gillaspy JD, Pomeroy JM, Reader J, Feldman U, Holland GE (2008) EUV spectra of highly-charged ions $W54^+$–$W63^+$ relevant to ITER diagnostics. J Phys B At Mol Opt Phys 41:021003 doi: 10.1088/0953-4075/41/2/021003

285. Beiersdorfer P, Lepson JK, Schneider MB, Bode MP (2012) L -shell x-ray emission from neonlike $W64^+$. Phys Rev A 86:012509 doi: 10.1103/PhysRevA.86.012509

286. Lennartsson T, Clementson J, Beiersdorfer P (2013) Experimental wavelengths for intrashell transitions in tungsten ions with partially filled 3p and 3d subshells. Phys Rev A 87:062505 doi: 10.1103/PhysRevA.87.062505

287. Peacock NJ, O’Mullane MG, Barnsley R, Tarbutt M (2008) Anticipated X-ray and VUV spectroscopic data from ITERwith appropriate diagnostic instrumentation. Can J Phys 86:277 doi: 10.1139/p07-140

288. Biedermann C, Radtke R, Seidel R, Pütterich T (2009) Spectroscopy of highly charged tungsten ions relevant to fusion plasmas. Phys Scr T134:014026 doi: 10.1088/0031-8949/2009/T134/014026

289. Clementson J, Beiersdorfer P, Brown GV, Gu MF, Lundberg H, Podpaly Y, Träbert E (2011) Tungsten spectroscopy at the Livermore electron beam ion trap facility. Can J Phys 89:571 doi: 10.1139/p11-028

290. Kramida A (2011) Recent progress in spectroscopy of tungsten. Can J Phys 89:551 doi: 10.1139/p11-045

291. Beiersdorfer P, Brown G V., Graf AT, Bitter M, Hill KW, Kelley RL, Kilbourne CA, Leutenegger MA, Porter FS (2012) Rest-wavelength fiducials for the ITER core imaging x-ray spectrometer. Rev Sci Instrum 83:10E111 doi: 10.1063/1.4733318

292. Gillaspy JD, Osin D, Ralchenko Y, Reader J, Blundell SA (2013) Transition energies of the D lines in Na-like ions. Phys Rev A 87:062503 doi: 10.1103/PhysRevA.87.062503

293. Clementson J, Beiersdorfer P, Brown G V, Gu MF (2010) Spectroscopy of M-shell x-ray transitions in Zn-like through Co-like W. Phys Scr 81:015301 doi: 10.1088/0031-8949/81/01/015301

294. Clementson J, Beiersdorfer P (2010) Wavelength measurement of n=3 to n=3 transitions in highly charged tungsten ions. Phys Rev A 81:052509 doi: 10.1103/PhysRevA.81.052509

295. Fujimoto T Plasma Polarization Spectroscopy. Springer series on atomic, optical and plasma physics 44

296. Zhang HL, Sampson DH, Fontes CJ (1990) Relativistic distorted wave collision strengths and oscillator strengths for the 33 Cu-like ions with $60 \leq Z \leq 92$. At Data Nucl Data Tables 44:273 doi: 10.1016/0092-640X(90)90015-C

297. Zhang HL, Sampson DH, Fontes CJ (1991) Relativistic distorted-wave collision strengths and oscillator strengths for the 33 Ni-like ions with $60 \leq Z \leq 92$. At Data Nucl Data Tables 48:91 doi: 10.1016/0092-640X(91)90024-X

298. Mohan M, Aggarwal S, Singh N (2014) REVIEW Multiconfigurational Dirac-Fock atomic structure calculations for Cl-like tungsten. Can J Phys 92:177 doi: 10.1139/cjp-2013-0348

299. Aggarwal S, Jha AKS, Khatri I, Singh N, Mohan M (2015) Relativistic atomic data for W XLVII. Chinese Phys B 24:053201 doi: 10.1088/1674-1056/24/5/053201

300. Goyal A, Sharma R, Singh AK, Mohan M (2017) ARTICLE Fully relativistic atomic structure calculations for W XLIV for determination of plasma diagnostic terms. Can J Phys 95:950 doi: 10.1139/cjp-2016-0812

301. Clementson J, Beiersdorfer P, Gu MF (2010) X-ray spectroscopy of E2 and M3 transitions inNi-like W. Phys Rev A 81:012505 doi: 10.1103/PhysRevA.81.012505

302. Zhang HL, Sampson DH (2002) Relativistic distorted-wave collision strengths and oscillator strengths for the 45δn=0 transitions with n=2 in the 79 o-like ions with $14 \leq Z \leq 92$. At Data Nucl Data Tables 82:357 doi: 10.1006/ADND.2002.0888

303. Huang K-N, Kim Y-K, Cheng KT, Desclaux JP (1983) Energy-level scheme and transition probabilities of Cl-like ions. At Data Nucl Data Tables 28:355 doi: 10.1016/0092-640X(83)90022-0

304. Huang K-N (1984) Energy-level scheme and transition probabilities of P-like ions. At Data Nucl Data Tables 30:313 doi: 10.1016/0092-640X(84)90020-2

305. Huang K-N (1985) Energy-level scheme and transition probabilities of Si-like ions. At Data Nucl Data Tables 32:503 doi: 10.1016/0092-640X(85)90022-1

306. Chou H-S, Chang J-Y, Chang Y-H, Huang K-N (1996) Energy-level scheme and

transition probabilities of S-like ions. At Data Nucl Data Tables 62:77 doi: 10.1006/ADND.1996.0003

307. Safronova UI, Safronova AS (2010) Wavelengths and transition rates for nl–n’l’ transitions in Be-, B-, Mg-, Al-, Ca-, Zn-, Ag- and Yb-like tungsten ions. J Phys B At Mol Opt Phys 43:074026 doi: 10.1088/0953-4075/43/7/074026

308. Huang K-N (1986) Energy-level scheme and transition probabilities of Al-like ions. At Data Nucl Data Tables 34:1 doi: 10.1016/0092-640X(86)90008-2